PhD PROCEEDINGS

ANNUAL ISSUES OF THE DOCTORAL SCHOOL

FACULTY OF INFORMATION TECHNOLOGY & BIONICS

2016

PhD PROCEEDINGS

ANNUAL ISSUES OF THE DOCTORAL SCHOOL

FACULTY OF INFORMATION TECHNOLOGY & BIONICS
PÁZMÁNY PÉTER CATHOLIC UNIVERSITY

PhD PROCEEDINGS

ANNUAL ISSUES OF THE DOCTORAL SCHOOL

FACULTY OF INFORMATION TECHNOLOGY & BIONICS

2016

PÁZMÁNY UNIVERSITY *e*PRESS
BUDAPEST, 2016

HU ISSN 2064-7271

Kiadja a Pázmány Egyetem eKiadó
Budapest, 2016

Felelős kiadó
Ft. Dr. Szuromi Szabolcs Anzelm O. Praem.
a Pázmány Péter Katolikus Egyetem rektora

Támogató: Emberi Erőforrások Minisztériuma
Támogatáskezelő: Emberi Erőforrás Támogatáskezelő
NTP-FKT-M-15-0006

Cover image by Sándor Földi: *Continuous wavelet spectrum of a pulse signal segment.*

Contents

Introduction

It is our pleasure to publish this Annual Proceedings again to demonstrate the genuine interdisciplinary research done at the Jedlik Laboratories by young talents working in the Roska Tamás Doctoral School of Sciences and Technology of the Faculty of Information Technology and Bionics at Pázmány Péter Catholic University. The scientific results of our PhD students show the main recent research directions in which our faculty is engaged. Thanks are also due to the supervisors and consultants, as well as to the five collaborating National Research Laboratories of the Hungarian Academy of Sciences, the Semmelweis Medical School and the University of Pannonia. The collaborative work with the partner universities, especially, Katolieke Universiteit Leuven, Politecnico di Torino, Technische Universität München, University of California at Berkeley, University of Notre Dame, Universidad de Sevilla, Universita di Catania is gratefully acknowledged.

As an important development of this special collaboration, we were able to jointly accredit a new undergraduate curriculum on Molecular Bionics with the Semmelweis Medical School, the first of this kind in Europe.

We acknowledge the many sponsors of the research reported here. Namely,

- the Hungarian National Research Fund (OTKA),
- the Hungarian Academy of Sciences (MTA),
- the National Development Agency (NFÜ),
- the Gedeon Richter Co.,
- the Office of Naval Research (ONR) of the US,
- NVIDIA Ltd.,
- Eutecus Inc., Berkeley, CA,
- MorphoLogic Ltd., Budapest,
- Analogic Computers Ltd., Budapest,
- AnaFocus Ltd., Seville,

and some other companies and individuals.

Needless to say, the resources and support of the Pázmány Péter Catholic University is gratefully acknowledged.

Budapest, June 2016.

GÁBOR PRÓSZÉKY

Chairman of the Board of the Doctoral School

PÉTER SZOLGAY

Head of the Doctoral School
Head of the Jedlik Laboratory

Program 1

BIONICS, BIO-INSPIRED WAVE COMPUTERS, NEUROMORPHIC MODELS

Heads: Tamás FREUND, György KARMOS, Zsolt LIPOSITS, Sándor PONGOR

Creating a structural ensemble for the electron transport protein Azurin

Sándor Babik
(Supervisor: Zoltán Gáspári)
Pázmány Péter Catholic University, Faculty of Information Technology and Bionics
50/a Práter street, 1083 Budapest, Hungary
babik.sandor@itk.ppke.hu

***Abstract*—Azurin is a bacterial protein found in Pseudomonas aeruginosa where it is a member of the electron transport chain and participates in denitrification processes. Azurin is known as a blue copper protein, the Cu ion located at the "top" of the protein is key player in electron transport (ET). This is due to the fact that Cu can convert easily between redox states. The rate-limiting step of the ET process in azurin is thought to be a conformational rearrangement, leading to a so-called gated ET mechanism. My goal is to create a structural ensemble of the protein to help understanding the structural changes leading to ET.**

***Keywords*-Electron transport; structural ensembles; molecular dynmaics**

I. Introduction

Electron transport (ET) reactions play a key role in the metabolism of living organisms. During oxidation of nutrients, electrons with low redox potential are generated that pass through a chain of proteins known as the electron transport or respiratory chain [1]. Azurin (Az) is a bacterial blue copper protein that carries electrons from cytochrome c551 (Cyt II) to cytochrome oxidase (Cyt(III)).

$$Az(II) + Cyt(II) \leftrightarrow Az(I) + Cyt(III)$$

Electrons can be transferred in both directions at a very fast rate ($k_(1,2)$, $k_(2,1) = 6 * 10^6 M^-1 s^-1$) however this is dependent on a slow mononuclear reaction. This slow process has been identified as a conformation equilibrium between two forms of reduced azurin, this process is known as gated electron transfer [2]. The protein is comprised of 128 amino acids arranged into an eight-stranded β-barrel and a single α-helix (figure 1). The north surface of the molecule where the copper ion is located is made up of a group of amino acids called the hydrophobic patch [3]. The ET properties of azurin arise from the redox properties of the Cu ion that can easily convert between Cu(I) or Cu(II) redox state. Copper ions play an important role in several biological functions, like ET, that are related to its redox properties. Cu ion containing proteins have been divided into several different types: type 1, type 2, type 3, CuA, CuB and CuZ [4, 5]. Out of these type 1 is also known as blue copper site, which is surrounded by a protein envelope sometimes referred to as the cupredoxin fold. The common feature in all cupredoxins are two His residues that coordinate Cu with their $N\epsilon 2$ imidazol nitrogen atoms as well as a $S\gamma$ sulfate of a Cys. These three atoms establish strong interactions with the ion and are considered as a minimal requirement for copper coordination [6, 7]. Other ligands may coordinate the Cu center as in the case of azurin, $S\delta$ sulfur atom from Met and a backbone carbonyl O atom of Gly. Out of the five coordinating atoms found in the cupredoxin fold of Azurin the first three are considered strong while the last two weak ligands (figure 2). His 117 is one of the strong ligands coordinating Cu ion, it is also positioned in the center of the hydrophobic patch. The patch is responsible for binding partner proteins of azurin and also for mediating ET between the two proteins. Since azurin can bind to several proteins the surface reorganization of this region is of great importance for ET [8, 9]. A nuclear magnetic resonance (NMR) spectroscopy study has shown His 117 to be involved in restricted nanosecond motions, as well as other residues located at and around the hydrophobic patch. These data suggest several low energy conformers separated by low energy barriers that my be important for binding different partners [9,10]. Two possible pathways have been suggested for ET in azurin, one involves 21 covalent bonds, two hydrogen bonds along the residues 31, 48-50 and 111-112, which includes a 4 Å jump from Val 31 to Trp 48. The other pathway also shows the importance of residues 47-49 along with 111-112 with the flow of electrons directed toward His 83 or a disulfide bridge formed between residues Cys 3 – Cys 26. However it should be noted that theoretical and experimental models suggest multiple coupled ET pathways [9].

Fig. 1. Azurin shown in ribbon representation, with the Cu ion colored orange, located at the top. The beta strands forming the β-barrel can be found under Cu while the alpha-helix is located to the right of the ion.

S. BABIK, "Creating a structural ensemble for the electron transport protein Azurin" in *PhD Proceedings Annual Issues of the Doctoral School, Faculty of Information Technology and Bionics, Pázmány Péter Catholic University – 2016.* G. Prószéky, P. Szolgay Eds. Budapest: Pázmány University ePress, 2016, pp 13– 15.

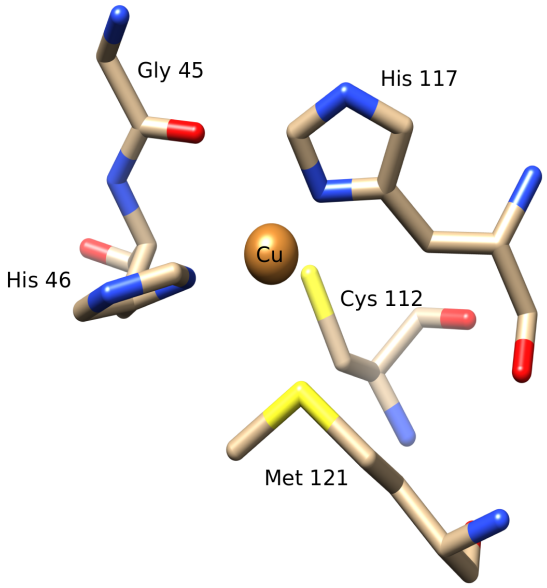

Fig. 2. Cu binding site of azurin in ball and stick representation. Cu in the middle and surrounded by its five ligands: Gly 45, His 46, Cys 112, His 117 and Met 121.

The gated ET mechanism and accompanying structural rearrangements can be investigated using computational methods such as molecular dynamics. Creating a structural ensemble of azurin that represents the experimentally observed motions of the protein may help to understand the mechanics behind gated ET.

II. Molecular Dynamics

Molecular dynamics (MD) is a computer simulation method to study the behavior and interactions of atoms and molecules. Similar simulation methods that have been applied to such systems are Monte Carlo simulations and Simulated Annealing. In the case of proteins MD is able to sample the conformational space of a given molecule and provide information about the energy landscape. The dynamic behavior of a system is investigated for a given time frame usually at an order of a few to several hundred nanoseconds, depending on available computational resources. Interactions between atoms are calculated by taking into account the bonded (atomic bonds, angles and dihedral angles) and non-bonded (electrostatic and Van der Waals) interactions that are described by an energy function known as a force field [11]. Force fields use a predefined set of parameters to calculate interaction energies such as charge, Van der Waals radius etc., that are derived either by quantum mechanics calculations or measured experimentally [11]. Different parameter sets are used to describe molecules with different chemical properties therefore one can choose from many different force fields. One example is Amber99SB-ildn that was designed for the simulation of biomolecules like proteins and nucleic acids [12]. The force field of choice must be parametrized for the molecules of our interest. Solvent is also a crucial factor when dealing with biomolecules, most often water is used as solvent either in an implicit (no actual atoms involved) or explicit (water is represented by H_2O molecules) form.

III. Structural Ensembles

In order to accurately describe and understand key molecular mechanisms such as enzymatic catalysis or molecular recognition protein flexibility has to be taken into account [13, 14]. Protein flexibility can be represented by using several structures in different conformations that show the most important changes in the structure at a given timescale. The collection of these structures is the structural ensemble of a protein. Out of the two most widely used methods for structure determination, X-ray crystallography and NMR spectroscopy, only the latter is able to capture information about the dynamic nature of proteins. During structure determination by NMR spectroscopy a penalty is applied to a molecular simulation if it does not adhere to experimental restraints, most often distance restraints derived form Nuclear Overhauser effect [15]. Structures produced by this method fulfill all experimental restrains, however NMR measurements are derived as averages from an ensemble of molecules over time. Thus, conventionally determined NMR structures This average structure or more commonly for NMR several structures do not represent the conformational flexibility of a protein. This can be a problem if a protein adopts multiple conformers during structural fluctuations [16]. MD simulations that integrate experimental data about the dynamics of proteins have been used in the past to produce conformational ensembles of proteins. Using MD simulations the NMR restraints can be applied as averages over several copies or replicas of the protein [15].

IV. Simulations

During my work I have conducted MD simulations of azurin to investigate conformational changes on the nanosecond picosecond timescales. I have applied NMR restraint over several replicas of this system, similarly as described for the MUMO procedure [15]. My goal is to create an ensemble of azurin conformations that reflect the experiments and might be used to shed light on the subtle structural rearrangements that lead to ET. Although it is expected to occur at a slower timescale. I obtained the structure of azurin from the Protein Data Bank (PDB) deposited under the PDB ID: 4azu.pdb. The structure was solved by X-ray crystallography at a resolution of 1.9 Å, the unit cell contained four chains of azurin, out of which I have used chain A. I performed MD simulations of azurin using Amber99SB-ildn as well as all OPLS force field with a four point explicit water model using the GROMACS molecular dynamics program package. Special considerations must be taken during the setup of the simulation, like choosing the proper protonation states of His residues and the nontrivial disulfide bridge between Cys 3 – Cys 26. The Cu^{+1} ion also requires special treatment, although the Amber force field is designed for simulating biomolecules interactions between the ion on protein residues tend to violate the proximity requirements of the cupredoxin fold. This behavior is even more apparent when using the OPLS force field. Therefore I have implemented distance restraints between Cu^{+1} and its ligands, lower and upper bounds for the restraints were determined from the four chains found in the crystal structure. Simulations were conducted using eight replicas, whit a simulation time of 5 ns for each replica. The S2 order parameter was used as NMR restraint over all replicas. The NMR order parameters were obtained form the Biological Magnetic Resonance Data bank (BMRB) where it was deposited for two temperatures

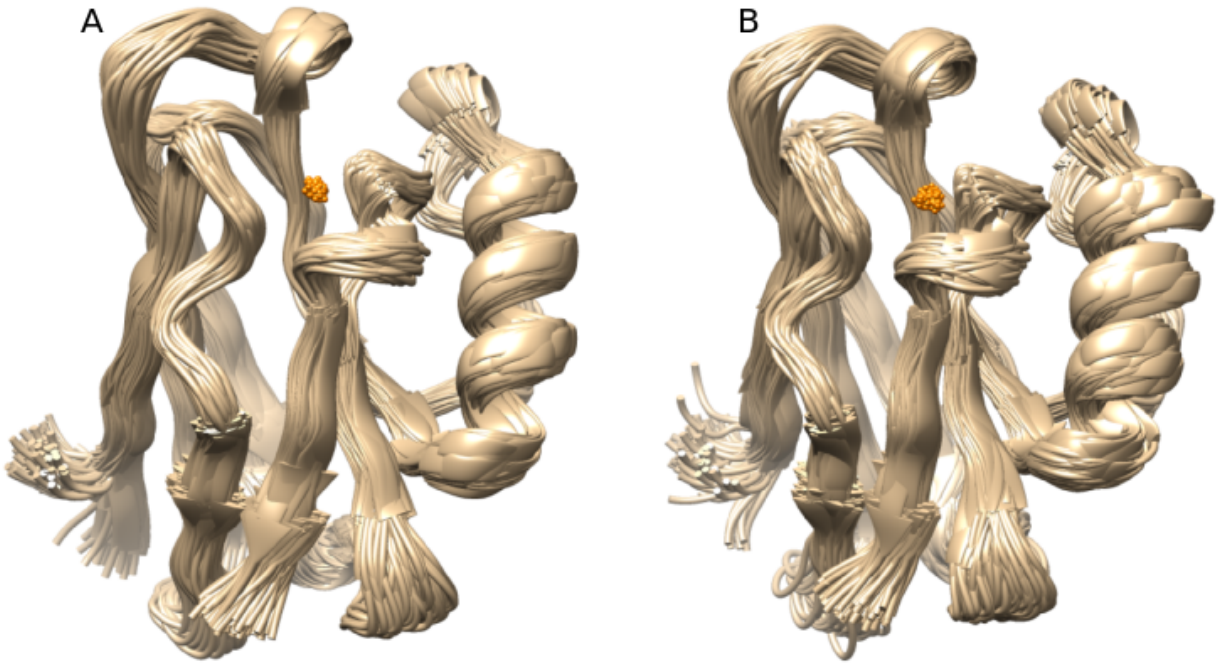

Fig. 3. Ensembles of azurin taken from exploratory simulations performed at 289 K (A) and 317 K (B).

289 K and 317 K. I have conducted exploratory runs for parameter optimization on the two temperatures and created two structural ensembles (figure 3).For validation of the ensemble I have used the ConsensX web server, developed and maintained by our group. Further analysis of the ensemble will follow using methods such as, but not limited to, principal component analysis, C_α – C_α correlations.

V. Conclusions

The structural changes associated with the gated ET mechanism in azurin is a prime candidate for analysis with structural ensembles. Selection of the force field is a crucial component for proper treatment of interactions between Cu+1 and its five ligands. The differences between force fields were apparent between Amber99SB-ildn and OPLS, showing the former to be more effective. It turned out I had to use distance restraints in combination with the Amber force field in order to preserve the geometry of Cu coordination. The preliminary structural ensembles show no significant structural fluctuations compared to each other or to the starting structure. Detailed sampling of the conformational space of azurin is the topic of ongoing investigations.

References

[1] B. Alberts, A. Johnson, J. Lewis, M. Raff, K. Roberts, and P. Walter, *Electron-Transport Chains and Their Proton Pumps*: Molecular Biology of the Cell 4th edition Garland Science, New York, 2002.

[2] H. Nar, A. Messerschmidt, R. Huber, M. van de Kamp, and Gerard W. Canters *Crystal structure analysis of oxidized Pseudomonas aeruginosa azurin at pH 5· 5 and pH 9· 0: A pH-induced conformational transition involves a peptide bond flip.*: Journal of Molecular Biology vol. 221, no. 3, pp. 765-772, 1991.

[3] E. N. Baker *Structure of azurin from Alcaligenes denitrificans refinement at 1· 8 Å resolution and comparison of the two crystallographically independent molecules.*: Journal of Molecular Biology vol. 203, no. 4, pp. 1071-1095, 1988.

[4] I. W. Sutherland, J. F. Wilinson *Azurin, a blue bacterial protein.*: Biochemical Journal vol. 84, no. 2, pp. 43-59 1962.

[5] S. A. Pérez-Henarejos, L. A. Alcaraz, and A. Donaire *Blue Copper Proteins: A rigid machine for efficient electron transfer, a flexible device for metal uptake.*: Archives in Biochemistry and Biophysics vol. 584, pp. 134-148, 2015.

[6] H. B. Gray, B. G. Malmström, and R. J. P. Williams *Gray, Harry B., Bo G. Malmström, and R. J. P. Williams. "Copper coordination in blue proteins.*: Journal of Biological Inorganic Chemistry vol. 5, no. 5, pp. 551-559, 2000.

[7] E. I. Solomon, D. E. Heppner, E. M. Johnston, J. W. Ginsbach, J. Cirera, M. Qayyum, M. T. Kieber-Emmons, C. H. Kjaergaard, R. G. Hadt, and L. Tian *Copper active sites in biology.*: Chemical Reviews vol. 114, no. 7, pp. 3659-3853, 2014.

[8] M. Kamp, M. C. Silvestrini, M. Brunori, J. Beeumen, F. C. Hali, and G. W. Canters *Involvement of the hydrophobic patch of azurin in the electron transfer reactions with cytochrome c551 and nitrite reductase.*: European Journal of Biochemistry vol. 194, no. 1, pp. 109-118, 1990.

[9] A. V. Zahuravleva, D. M. Korzhnev, E. Kupce, A. S. Arseniev, M. Billeter, and V. Y. Orekhov *Gated electron transfers and electron pathways in azurin: a NMR dynamic study at multiple fields and temperatures.*: Journal of Molecular Biology vol. 342, no. 5, pp. 1599-1611, 2004.

[10] F. Cutruzzolà, M. Arese, G. Ranghino, G. van Pouderoyen, G. Canters, and M. Brunori *Pseudomonas aeruginosa cytochrome c 551: probing the role of the hydrophobic patch in electron transfer.*: Journal of Inorganic Biochemistry vol. 88, no. 3, pp. 353-361, 2002.

[11] D. van der Spoel, E. Lindahl, B. Hess, A. R. van Buuren, E. Apol, P. J. Meulenhoff, D. P. Tieleman, A. L. T. M. Sijbers, K. A. Feenstra, R. van Drunen and H. J. C. Berendsen *Gromacs User Manual*: version 4.5.6 www.gromacs.org, 2010.

[12] K. Lindorff Larsen, S. Piana, K. Palmo, P. Maragakis, J. L. Klepeis, R. O. Dror, and D. E. Shaw *Improved side chain torsion potentials for the Amber ff99SB protein force field.*: Proteins: Structures, Function and Bioinformatics vol. 78, no. 8, pp. 1950-1958, 2010.

[13] M. Karplus and G. A. Petsko *Molecular dynamics simulations in biology.*: Nature vol. 347, no. 6294, pp. 631-639, 1990.

[14] M. Karplus and J. Kuriyan. *Molecular dynamics and protein function.*:Proceedings of the National Academy of Sciences of the United States of America vol. 102, no. 19, pp. 6679-6685, 1995.

[15] B. Richter, J. Gsponer, P. Várnai, X. Salvatella, and M. Vendruscolo *The MUMO (minimal under-restraining minimal over-restraining) method for the determination of native state ensembles of proteins.*: Journal of biomolecular NMR vol. 37, no. 2, pp. 117-135, 2007.

[16] B. Zagrovic, and F. W. van Gunsteren *Comparing atomistic simulation data with the NMR experiment: how much can NOEs actually tell us?.*: Proteins: Structure, Function and Bioinformatics vol. 63, no. 1, pp. 210-218, 2006.

Estrogen Receptor Beta and 2-arachidonoylglycerol Mediate the Suppressive Effects of Estradiol on Frequency of Postsynaptic Currents in Gonadotropin-Releasing Hormone Neurons of Metestrous Mice

Flóra BÁLINT
(Supervisor: Dr. Imre FARKAS, Prof. Zsolt LIPOSITS)
Pázmány Péter Catholic University, Faculty of Information Technology and Bionics
50/a Práter street, 1083 Budapest, Hungary
balint.flora@itk.ppke.hu

***Abstract*—The hypothalamic gonadotropin-releasing hormone (GnRH) neurons play a key role in the control of reproduction. *In vivo*, 17β-estradiol (E2) controls GnRH release in concentration and estrus cycle dependent manner. *In vitro* patch-clamp electrophysiological data on GnRH neurons of ovariectomized female mice demonstrated that low concentration (10 pM) of E2 decreased spontaneous firing rate which was eliminated by blocking fast synaptic neurotransmission [1], suggesting a pivotal role of the GABAergic excitation in the phenomenon. In the present study, we examined the effect of low concentration of E2 on GABAergic postsynaptic currents (PSCs) in GnRH neurons of acute brain slices obtained from metestrous female mice. It has been demonstrated that activation of the retrograde endocannabinoid machinery inhibits the GABAergic synaptic neurotransmission in GnRH neurons [2], therefore, we analyzed the putative involvement of endocannabinoid signaling mechanisms in the evoked effect of E2. Our loose-patch and whole-cell patch clamp results indicate that an interaction exists between estradiol and endocannabinoid signaling mechanisms which represents a novel regulatory machinery in the execution of the negative estradiol feedback to GnRH neurons.**

***Keywords*-GnRH; endocannabinoid; electrophysiology; estradiol**

I. Introduction

Gonadotropin-releasing hormone (GnRH) neurons form the final common pathway for the central regulation of reproduction. These neurons are located in the preoptic area (POA) of the hypothalamus and secrete GnRH into the hypophysial portal circulation. The hormone regulates the synthesis and secretion of gonadotropins, such as follicle-stimulating hormone (FSH) and luteinizing hormone (LH). FSH and LH are released into the systemic circulation and act on the gonads to stimulate gonadal steroid hormone secretion. The sexual steroid hormone, 17β-estradiol (E2) also has effect on GnRH secretion via classical feedback actions. Both negative and positive E2 feedback mechanisms take part in the control via classical genomic and fast, membrane actions. Nevertheless, the mechanisms underlying the feedback events are not clear. Thus, our goal was to examine the effects of E2 on GnRH neurons under the negative feedback. E2 controls GnRH release in a concentration and estrus cycle dependent manner. *In vitro* patch-clamp electrophysiological studies on GnRH neurons of ovariectomized female mice showed that low concentration (10 pM) of E2 decreased spontaneous firing rate which could be eliminated by blocking fast synaptic neurotransmission [1]. The retrograde endocannabinoid signaling was hypothesized to be involved in the mediation of the E2 effect. Endocannabinoids are synthesized in neurons and control the neurotransmitter release from the presynaptic axon terminals. It was previously shown that GABAergic terminals to GnRH neurons are under the control of the endocannabinoid system as endocannabinoids decreased the frequency of the GABAergic postsynaptic currents in these neurons [2]. In the present study, we hypothesized that the suppressive effect of E2 applied at low physiological concentration on GnRH neurons requires the activation of estrogen receptor/s and the activation of a subsequent retrograde endocannabinoid signaling mechanism resulting in the repression of GABAergic neurotransmission onto these neurons. To test this hypothesis, a series of electrophysiological studies has been carried out in acute slices obtained from intact, metestrous female mice.

II. Materials and methods

A. Animals

Adult, gonadally intact female mice were used from local colonies bred at the Medical Gene Technology Unit of the Institute of Experimental Medicine (IEM). They were maintained in 12h light/dark cycle (lights on at 06:00h) and temperature controlled environment ($22 \pm 2\,^{\circ}\mathrm{C}$), with standard rodent chow and tap water available *ad libitum*. All mice were housed in the same room under same environmental conditions. GnRH-green-fluorescent protein (GnRH-GFP) transgenic mice were used for electrophysiological experiments. In this animal model, a GnRH promoter segment drives selective GFP expression in the majority of GnRH neurons [3]. Phase of the estrous cycle was checked by both evaluating vaginal smear and visual observation of the vaginal opening. All studies were carried out with permissions from the Animal Welfare Committee of the Institute of Experimental Medicine Hungarian Academy of Sciences and in accordance with legal requirements of the European Community.

B. Brain slice preparation and recording

Mice were deeply anesthetized by Isoflurane inhalation. After decapitation brain was removed rapidly and immersed in ice-cold Na-free cutting solution which had been extensively

F. BÁLINT, "Estrogen Receptor Beta and 2-arachidonoylglycerol Mediate the Suppressive Effects of Estradiol on Frequency of Postsynaptic Currents in Gonadotropin-Releasing Hormone Neurons of Metestrous Mice" in *PhD Proceedings Annual Issues of the Doctoral School, Faculty of Information Technology and Bionics, Pázmány Péter Catholic University – 2016.* G. Prószéky, P. Szolgay Eds. Budapest: Pázmány University ePress, 2016, pp 17– 20.

bubbled with a mixture of 95% O_2 and 5% CO_2. Hypothalamic blocks were dissected, and 250μm-thick coronal slices were prepared from the medial septum/preoptic area (POA) with a VT-1000S vibratome in the ice-cold oxygenated cutting solution. The slices containing POA were transferred into artificial cerebrospinal fluid (aCSF) saturated with O_2/CO_2 and kept in it for 1 h to equilibrate. Equilibration started at 33 °C and the aCSF was allowed to cool to room temperature. Electrophysiological recordings were carried out at 33 °C, during which the brain slices were oxygenated by bubbling the aCSF with O_2/CO_2. Axopatch 200B patch-clamp amplifier, Digidata-1322A data acquisition system, and pCLAMP 10.4 software were used for recording. Cells were visualized with a BX51WI IR-DIC microscope located on an anti-vibration table. The patch electrodes (OD=1.5 mm, thin wall) were pulled with a Flaming-Brown P-97 puller and polished with an MF-830 microforge. GnRH-GFP neurons were identified by brief illumination at 470 nm using an epifluorescent filter set, based on their green fluorescence, typical fusiform shape, and topographic location in the POA. After control recording (5 min), the slices were treated with various agonists and the recording continued for a subsequent 10 min. Each neuron served as its own control when drug effects were evaluated.

C. Whole-cell patch clamp experiments

The cells were voltage clamped at -70mV holding potential. Pipette offset potential, series resistance (Rs) and capacitance were compensated before recording. Only cells with low holding current (<50 pA) and stable baseline were used. Input resistance (Rin), Rs, and membrane capacity (Cm) were also measured before each recording by using 5 mV hyperpolarizing pulses. To ensure consistent recording qualities, only cells with Rs<20 MΩ, Rin>500 MΩ, and Cm >10 pF were accepted. The resistance of the patch electrodes was 2-3 MΩ.

D. Statistical analysis

Each experimental group contained 8-18 recorded cells from six to nine animals. Mean firing rate and postsynaptic current (PSC) frequency were calculated as number of spikes divided by the length of the respective period. Percentage changes resulting from drugs were calculated by dividing the value to be analyzed before (5 min) and after (the subsequent 10 min) the respective agonist administration. Event detection was performed using the Clampfit module of the PClamp 10.4 software. Group data were expressed as mean±SEM and percentage change in the frequency of the PSCs due to the application of various drugs was calculated. Statistical analyses were carried out using Prism 3.0. Statistical significance was analyzed using Kruskal-Wallis test followed by Dunns post-test for comparison of groups whereas cumulative probabilities were analyzed with Kolmogorov-Smirnov test and considered as significant at $p<0.05$

III. Results

First the effect of the estradiol at low concentration was tested. Measurements were carried out with an initial control recording (5 min), then E2 (10 pM) was administered onto the brain slices (n=18) and the recording continued for a subsequent 10 min. The whole-cell patch clamp recordings revealed that E2 significantly diminished frequency of the PSCs (49±7% of the control) (Fig. 1, 4). As this effect occurred within minutes, we can conclude that the inhibition of PSCs was a result of the non-genomic effects of the hormone.

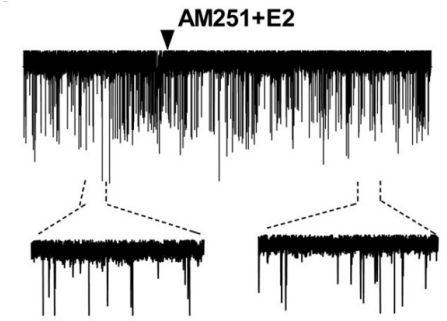

Fig. 1. Involvement of endocannabinoid receptor in the effect of E2. Pretreatment of the brain slice with the CB1 antagonist AM251 (1 μM) inhibits effect of the E2 (86±4%). Arrow shows application of E2. n=12

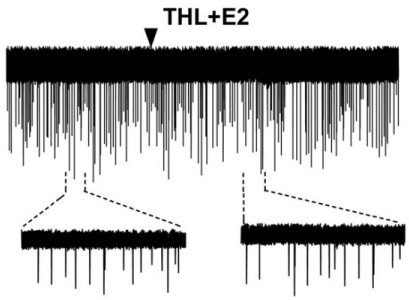

Fig. 2. Involvement of endocannabinoid synthesis in the effect of E2. Intracellular application of THL (10 μM) into the GnRH neurons attenuated the effect of E2 (67±5%). Arrow shows application of E2. n=13

There are two main types of endocannabinoids in the central nervous system: the anandamide (AEA) and the 2-arachidonoylglycerol (2-AG). We used tetrahydrolipstatin (THL, 10 μM) to determine which endocannabinoid plays a role in this mechanism and which cell synthesizes it. The diacylglycerol (DAG) lipase is an important component in the synthesis of 2-AG and since THL is a DAG lipase inhibitor, it was added into the intracellular solution in order to block 2-AG synthesis exclusively in the measured GnRH neuron. THL was allowed to enter into the intracellular milieu of the measured cell for 15 min before control recording. After 5 min control recording E2 (10 μM) was administered onto the brain slices (n=13). Intracellular application of THL in the GnRH neurons eliminated the action of E2 (67±5%) (Fig. 3, 4). These results suggest that 2-AG is involved in this mechanism and it is synthesized by GnRH neurons.

Most of the hormones execute their effects on neuron directly and/or indirectly. The direct effects can be detected by using tetrodotoxin (TTX). TTX inhibits the firing of neurons by binding to the voltage sensitive sodium channels in cell membranes and therefore, the spike-mediated transmitter release is blocked. Thus, only miniature postsynaptic currents (mPSCs) can be measured, since the measured cell can no longer receive any action potential related input signal. For mPSC recordings TTX (650 nM) was added to the aCSF 10 minutes before start. After 5 min control recording E2 (10 pM) was administered onto the brain slices (n=12). The estradiol significantly decreased the frequency of the mPSCs (50±9%, Fig. 7), indicating that the effect of the E2 is direct

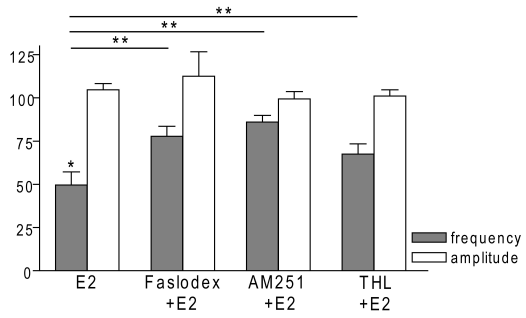

Fig. 3. Bar graph summarizing the percentage changes in the frequency and the amplitude of the sPSCs. E2 significantly decreased the frequency of sPSCs. Inhibition of its effect could be achieved by antagonizing the ERs, CB1 receptors or blocking the intracellular 2-AG endocannabinoid synthesis. The amplitude of the mPSCs did not change in any of the treatments. $\star$ $p<0.05$ as compared to the control; $\star\star$ $p<0.05$ as compared to the change evoked by E2 treatment.

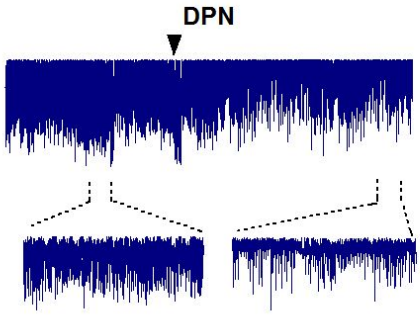

Fig. 4. ERβ is involved in the effect of E2. The ERβ agonist DPN (10 pM) decreases the frequency of the mPSCs (60$\pm$5%). Arrow shows application of DPN. n=10

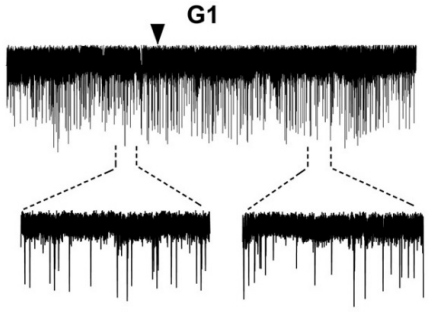

Fig. 5. GPR30 is not involved in the effect of E2. The GPR30 receptor agonist G1 (10 pM) did not modify the frequency of the mPSCs. Arrowhead shows the onset of drug administration. n=5

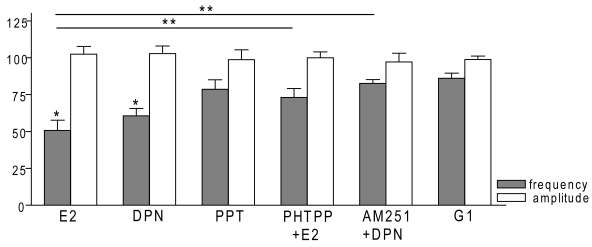

Fig. 6. Bar graph summarizing the percentage changes in the frequency and the amplitude of the mPSCs. The E2 and the selective ERβ agonist DPN significantly decreased the frequency of mPSCs. Effect of DPN was eliminated by the pretreatment with CB1 inverse agonist AM251. Effect of E2 could be inhibited by antagonizing selectively the ERβ by PHTPP. The selective ERα agonist PPT and the GPR30 receptor agonist G1 had no significant effect on the frequency of mPSCs. The amplitude of the mPSCs presented no change in any of the treatments. $\star$ $p<0.05$ compare to the control; $\star\star$ $p<0.05$ as compared to the change caused by E2 treatment.

on the GnRH neurons. In order to demonstrate involvement of cannabinoids and of the ERs in the direct action of E2 on GnRH neurons, the non-selective ER antagonist Faslodex (1 mM) and THL (10 μM) was used in the presence of TTX. The intracellularly applied THL (n=5) also eliminated the action of E2 on mPSCs (88$\pm$2%, Fig.7). The effect of E2 was blocked by Faslodex, too (Fig.7). In the presence of the antagonist, after E2 administration the mean frequency of mPSCs (84$\pm$4%) was significantly higher compared to the value measured with E2 alone. Estradiol exerts its effects via estrogen receptors (ERs). These classical receptors are ERα and ERβ. To examine which receptor type is involved in the rapid action of the estradiol on the GnRH neurons, subtype selective ER agonists were used in the presence of TTX. After 5 min control recording, the agonists were administered onto the brain slices. First ERα agonist PPT (10 pM) was added (n=10), but it had no significant effect on mPSCs (78$\pm$6%, Fig. 7). Next ERβ agonist DPN (10 pM) was used (n=10) and we observed a decrease in the frequency of the mPSCs (60$\pm$5%) (Fig. 5, 7).

In line with this observation, the effect of E2 was significantly blocked (73$\pm$6%, Fig. 7) by the specific ERβ antagonist PHTPP (1 mM) administration. These results indicate that ERβ is required for the observed rapid effect of E2 in GnRH neurons. We also addressed the putative role of the membrane associated G-protein coupled estrogen receptor GPR30 in this process. Application of the GPR30 selective agonist G1 (10 pM) had no significant effect (Fig.6, 7) on the frequency of the mPSCs (86$\pm$3%). These data show that ERα and GPR30 have no role in mediating the observed rapid effect of the E2 on GnRH neurons.

Finally, the effect of estradiol was tested in the presence of cannabinoid type-1 (CB1) inverse agonist AM251 (1 μM) and TTX in order to confirm our previous results showing that endocannabinoid signaling is involved in the mediation of the effect of E2 on suppression of fast neurotransmission onto GnRH neurons. After 5 min control recording the E2 was administered onto the brain slices (n=12) and the recording continued for a subsequent 10 min. The AM251 attenuated the effect of DPN on the mPSCs (86$\pm$9%) (Fig. 7), supporting our results.

IV. Conclusions

Endocannabinoid system is involved in the mediation of the effect of E2 on suppression of fast neurotransmission onto GnRH neurons (Fig. 8). In this effect, 2-AG plays a fundamental role. ERβ is required for the observed rapid effect of E2 in GnRH neurons. The interaction of estradiol and endocannabinoid signaling mechanisms represents a novel regulatory machinery in the execution of the negative estrogen feedback to GnRH neurons.

Acknowledgements

The author wishes to acknowledge Dr. Imre Farkas and Prof. Zsolt Liposits for their excellent supervision. This research was supported by the National Science Foundation of Hungary (OTKA K100722, K115984).

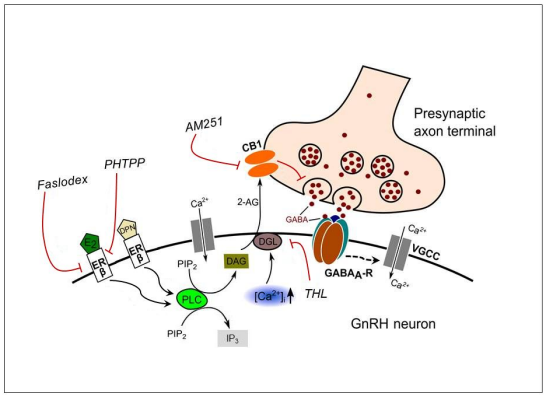

Fig. 7. Schematic illustration of the interaction between E2 and endocannabinoid signaling in GnRH neuron of the metestrous female mice. Binding of E2 to ERβ activates synthesis and release of 2-AG in the GnRH neuron. The released endocannabinoid 2-AG then binds to CB1 expressed in the presynaptic terminal of GABAergic afferents and causes suppression of GABA release into the synaptic cleft. This effect of E2 was blocked when the non-selective ER antagonist (Faslodex) or the selective ERβ receptor antagonist (PHTPP) was administered. The signaling was also inhibited when the CB1 inverse agonist (AM251) or the DAG lipase inhibitor (THL) was applied. Dashed arrow denote putative action.

REFERENCES

[1] Z. Chu, J. Andrade, M. Shupnik and S Moenter, *Differential regulation of gonadotropin-releasing hormone neuron activity and membrane properties by acutely applied estradiol: dependence on dose and estrogen receptor subtype*, J. Neurosci;2 9(17):5616-27. Apr 2009

[2] Farkas I., Kalló I., Deli L., Vida B., Hrabovszky E., Fekete C., Moenter S. M., Watanabe M., Liposits Zs., *Retrograde endocannabinoid signaling reduces GABAergic synaptic transmission to gonadotropin-releasing hormone neurons*, Endocrinology. 151(12):5818-5829.

[3] K. J. Suter, W. J. Song, T. L. Sampson, J. P. Wuarin, J. T. Saunders, F. E. Dudek, *Genetic targeting of green fluorescent protein to gonadotropinreleasing hormone neurons: characterization of whole-cell electrophysiological properties and morphology*, EEndocrinology 141, 412–419. 1.412. 2000

Short latency electrically evoked high frequency activity in the human hippocampus in vivo

Virág BOKODI
(Supervisor: Dániel FABÓ, István ULBERT)
Pázmány Péter Catholic University, Faculty of Information Technology and Bionics
50/a Práter street, 1083 Budapest, Hungary
National Institute of Clinical Neurosciences
57 Amerikai street, 1145 Budapest, Hungary
bokodi.virag@itk.ppke.hu

***Abstract*—Cortical electrical stimulation (CES) can evoke epileptic, spike-like responses in seizure onset zone areas. Spontaneous high frequency oscillations (HFO) can be more specific for epileptic brain areas, than interictal spikes. HFOs participate in memory consolidation and epileptogenic processes predominantly in and around the hippocampal formation (HcF). CES evoked high frequency oscillations (eHFO) in the HcF of eight temporal lobe epilepsy (TLE) patients were recorded under general anaesthesia. Analysis of these eHFOs may help to characterize the epileptic involvement of the human hippocampus.**

***Keywords*-epilepsy, in vivo, human, hippocampus, cortical electrical stimulation, high frequency oscillations**

I. Introduction

Epilepsies are the most frequent primary neurological diseases. The largest subgroup of the focal epilepsies is the mesial temporal lobe epilepsy (mTLE), where the hippocampus is often affected. Patients with mTLE may benefit from surgical removal of this area.

In some cases, difficult to precisely define the area responsible for seizure generation. Not only preoperative techniques (e.g. EEG, fMRI) but also other biomarkers, such as interictal spikes, spontaneous high frequency oscillations (HFO) are used to determine the epileptogenic zone. [1] High frequency oscillations – including ripples (80-200 Hz) and fast ripples (250-600 Hz) – can be registered from hippocampal formation (HcF), entorhinal cortex (EC), neocortex of patients with focal epilepsy and experimentally induced epileptic animals [2,3,4]. Higher HFO rates are significantly correlated with higher seizure frequency [2,5], and HFOs seem to be more specific biomarker than interictal spikes to identifying the epileptic zone. [2] Human epilepsy study have shown, that total removal of HFO generating area correlate well with good surgical outcome. [6] At the same time, the occurrence of the HFO is unpredictable, furthermore their visual detection is very time-consuming. [4]

The detection time of spontaneous spikes, HFOs and seizures can cause long invasive monitoring, therefore more complication and discomfort to the patients. Valentín et al. demonstrated, that in human epilepsy patients, electrical stimulation can evoke cortical, delayed responses with single pulse stimulation, which are similar to EEG spikes, and their locations are related to the seizure onset zone. [7] Single pulse electrical stimulation can also evoke epileptic high-frequency oscillations in animal model (tetanus toxin injected rats) [8]. Van't Klooster et al. investigated the frequency distribution of simulation evoked spikes and found slow and fast ripples in human cortex. [1]

Our aim was to characterize the waveforms, frequency, time duration and latency of the stimulus-evoked, short latency high frequency oscillations (eHFO) in the human hippocampus, in vivo in temporal lobe epilepsy patients.

II. Methods

A. Surgery and recording

The intrahippocampal recordings were performed under general anaesthesia, before anterior temporal lobectomy of 8 medically intractable mTLE patients with unilateral seizure starting. During the epilepsy surgery, before the temporal pole resection we recorded evoked potentials from the human hippocampus. The technique was previously described in [9,10]. In briefly, an eight contact strip electrode was placed around the temporal pole to stimulate the temporal input pathways of the hippocampus and a microelectrode was used to record in vivo evoked responses (EP) from the hippocampus.

The non-invasive epilepsy monitoring was done in the Epilepsy Centre of the National Psychiatry and Neurological Institution (2004-2007), the electrode implantation, invasive video-EEG monitoring and the resective surgery were done in the National Institution of Clinical Neurosciences (NICN). The permission to the experimental process was given from the Hungarian Medical Research Council, in accordance with the Declaration of Helsinki.

B. Electrical stimulation

The used deep microelectrode (dME) was described previously [9,10]. The 24 contacted dME (linearly arranged contacts, ø: 25 µm platinum-iridium wires, 100 µm or 200 µm center to center distance, first contact is 5 mm far from the tip) is a 10 cm long, 350 µm diameter, stainless steel needle. One or two dME was used.

Systematic bipolar stimulation of each pair of adjacent point of strip electrodes was administered with single pulses of electrical current (5,10,15 mA, 0.5 Hz, 0.2 ms pulse width, 5, 10, 25 and 50 trials per electrode pair). The sampling rate was 2000 Hz.

C. Data preprocessing

Electrophysiological data analyses were performed with Edit module of Neuroscan (Neuroscan Inc.) and Matlab (Mathworks Inc.). We used free accessible, open source Matlab

V. BOKODI, "Short latency electrically evoked high frequency activity in the human hippocampus in vivo" in *PhD Proceedings Annual Issues of the Doctoral School, Faculty of Information Technology and Bionics, Pázmány Péter Catholic University – 2016.* G. Prószéky, P. Szolgay Eds. Budapest: Pázmány University ePress, 2016, pp 21– 24.

packages, (EEGLAB [11]), previously described [12] script package developed by our laboratory and self-written Matlab scripts.

A shifting value calculation was improved to eliminate the slow electrode slipping, based on that presumption that the spike like waveform generation is stable in the cell layers. Current Source Density (CSD) analysis was used to determine the spike generating layers.

The movement of these sources in time resulted the mm/ms value of the sliding. We used those recording parts, where the slipping was less than one channel between the beginning and the end of the session. To avoid the probable side effect of the stimulation artefact, we replaced it with spline interpolation -4 ms to 4 ms around the artefact transient signal.

Hippocampal regions were reconstructed based on histological assessment of the removed HcFs, and subregions were determined as follows: Cornu Ammonis 2-3 (CA2-3), Dentate Gyrus (DG), Subiculum (Sub).

D. Analysis of evoked responses

We improved automated methods for the analysis of the evoked responses. In a [-500 + 500 ms] window around every stimulation the hippocampal local field potential data was filtered between 80-500 Hz (2nd order Butterworth) in order to measure the evoked high frequency activity (eHFA). Root Mean Square (RMS) calculation was applied in an 11 ms window 5 times. The maximal amplitude between 10-100 ms after stimulation was measured on the RMS data and converted to statistical Z-score value using the mean and standard deviation of the baseline (-450 ms to -50 ms before stimulation). (Eq.1 Standard z-score, where x is the evoked response amplitude, μis the mean of the data baseline (-450 ms to -50 ms), and σ is the standard deviation of the data baseline.)

$$z = \frac{x - \mu}{\sigma} \tag{1}$$

Since a simple amplitude threshold does not characterize well the evoked high frequency oscillations, hence stricter discrimination was employed. Two expert researchers revised the evoked potentials and selected events from every stimulation session, where the 80-500 Hz bandpass filtered eHFA were similar to the ripple oscillations with at least 4 cycle described previously in the literature. We described these evoked activity as evoked ripples (eR).

The frequency of every eR was measured with event related spectral perturbation (ERSP from EEGLAB [13]). The analysis was carried out in a -450 ms to +150 ms window around the stimulation. The ERSP baseline was -450 ms to -50 ms, and the maximal frequency was 500 Hz. The highest peak after the stimulation on the time averaged ERSP counted as the middle of the evoked event. The power of the ERSP was averaged around this time point in a 50 ms window. The highest amplitude frequency on this averaged curve was counted as the frequency of the evoked ripple. Frequency distributions was drawn according to the subregions of the hippocampal formation (CA2-3, DG, Sub).

Cross frequency coupling was calculated to measure the interaction between the frequency components. The phase-amplitude coupling (PAC) was determined by calculating the modulation index (MI) [13]. This MI characterize the strength of the phase-amplitude coupling by measuring the distance of the phase-amplitude histogram of two given frequencies from the uniform distribution by means of the Kullback-Leibler divergence. The PAC values were calculated from the complex Morlet wavelet of the 10-100 ms data after every stimulation from one session. The phase-amplitude histograms were determined on every possible frequency pairs from 11-968 Hz, the phase were discretized into 36 bins and the mean of the corresponding amplitudes were calculated. Finally, the Kullback-Leibler divergence between the resulted mean histogram and the uniform distribution yield the MI value for the given frequency pair and the resulted MI values were organized into an upper triangle matrix. From area (CA2-3, DG, Sub) averaged modulation index (MI) matrices, the maximal MI value was determined to designate one MI curve from the phase and one from the amplitude. These frequency-MI curves was signed as probability density functions, whereof mean and standard deviation were calculated. The frequencies lied within the mean in one standard deviation were considered as modulating (for phase) or modulated (for amplitude) frequencies. As we collected the MI matrices for all regions, we calculated paired t-tests ($p < 0.001$) for significant modulating-modulated frequency pairs.

III. Results

All together 131 cortical-hippocampal evoked potentials sessions containing 2275 stimuli was included. From every region the best channel was identified where evoked potentials were analysed. Based on automatic detection methods, above five z-score 1196 events fell in different Hc regions that eHFA. Evoked ripples were detected by manually. The analysis resulted 865 ripple events out of the above mentioned 1196 eHFAs, from which 241 were registered in CA2-3, 104 in DG and 520 in Sub. Amplitude, latency, duration, frequency and cross frequency coupling was calculated for all these evoked ripples.

A. Waveforms

We found oscillatory events in all sampled regions (CA2-3, DG, and Sub). The ones in the Sub were the most similar to ripples, CA2-3 and DG contains oscillatory events with fewer cycles. Figure 1 represents the most typical oscillatory events in hippocampus subregions.

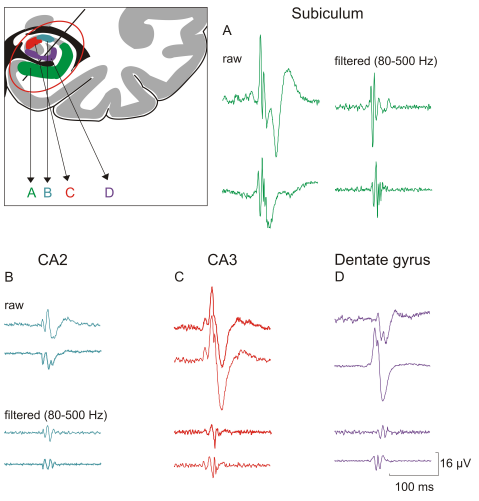

Fig. 1. Result of the most typical raw and filtered waveforms in hippocampus subregions (CA2-3, DG, Sub).

B. Latency and time duration

Peak latency and duration time of the evoked ripples were measured event by event, then mean and standard deviation were calculated. The peak latency was bimodal in DG (22.81 $\pm$ 2.49 ms; 37.11 $\pm$ 1.71 ms) and Sub (15.24 $\pm$ 6.7 ms; 39.57 $\pm$ 4.736 ms) while CA2-3 showed unimodal distribution (20.27 $\pm$ 5.935 ms). The duration of the evoked ripples was 18.33 $\pm$ 4.53ms, which remained fairly stable regardless to the subregions of the hippocampal formation.

C. Frequency

We identified three relatively distinct frequency band (27.3 $\pm$ 1.8 Hz, range 20-65 Hz; 84.7 $\pm$ 2.9 Hz, range 70-165 Hz and 192.4 $\pm$ 2.4 Hz, range 170-250 Hz) in the CA2-3 region. This result shows similarities to previous research on mice [14]. In DG, the largest amount frequency fell in gamma range (46.6 $\pm$ 2.9 Hz, range 20-80 Hz) and in the lower ripple range (87.4 $\pm$ 2.1 Hz, range 80-140 Hz). The frequency distribution of the events in Subiculum showed a peak around 41.8 $\pm$ 3.5 Hz (range 20-120 Hz) and 164.9 $\pm$ 6.1 Hz (range 125-360 Hz).

Interestingly the highest frequencies were present in the Subiculum, which may be explained by the side effect of the epilepsy. This analysis can also highlight the importance of the Subiculum.

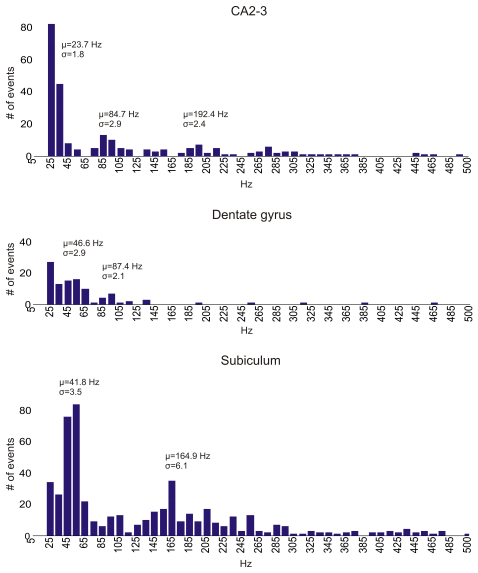

Fig. 2. Result of distribution of frequencies in the hippocampal regions. The x axes show the different frequency values (20-500 Hz), y axes show the number of events.

D. Cross frequency coupling

We analysed the interaction of the frequencies calculating phase-amplitude coupling. Fig 3 illustrates the mean modulation index (MI) between the frequencies from 11 to 968 Hz grouped by the regions CA, DG, Subiculum and all. The left column contains the results of the evoked ripples, while the right column shows the frequency coupling of the background activity. The three regions show slightly different coupling pattern. In CA, the most influential frequencies are between 11-33.4 Hz (peak 20 Hz), affecting frequencies in the range of 14.6-322.7 Hz (n=2). In DG the interaction is between 11-57.3 Hz and 47-478.9 Hz (peak 400Hz). The Sub is very similar to DG, with 11-35.9Hz influencing the 46.3-507.7 Hz range (peak 230 Hz). The volume of this effect is the highest in the DG (max MI values: 0.4), followed by the Sub (max MI: 0.25), and the lowest is in the CA (max MI: 0.14). The background activity reveals poor MI values in all areas with an interesting, but very small coupling between gamma band (15-80 Hz) and the multiple unit activity range (684-968 Hz). Statistical analysis resulted significant difference between active and background activity in terms of interaction of 11-60 Hz range modulating the 30-814 Hz range during the active phase. Interestingly significantly increased modulation was measured as [85-160 Hz and 575-968 Hz] ranges modulated the [814-968Hz] range during resting condition (Fig 3. bottom right grey stripped areas).

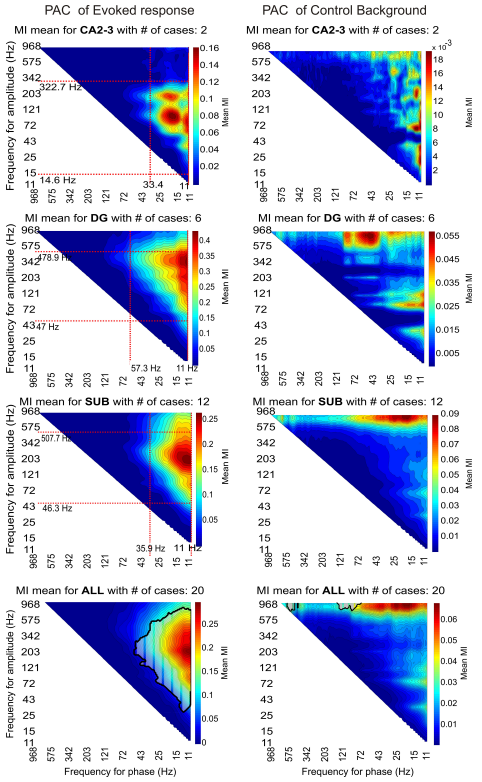

Fig. 3. Result of phase-amplitude coupling of evoked responses (left columns) and control background (right columns) in hippocampal regions and in all cases.

IV. Conclusion

We could detect short latency ripple oscillations in all region of hippocampus (CA2-3, DG, Sub) under general anaesthesia.

The frequency of the evoked ripple events consist of large amount gamma oscillation with slower and higher HFO frequencies components.

The frequency distribution in CA (27.3 $\pm$ 1.8 Hz, 84.7 $\pm$ 2.9 Hz and 192.4 $\pm$ 2.4 Hz) shows similarities with previous findings of 3 gamma band in CA1 regions: 30-80 Hz, 60-150 Hz and 120-250 Hz [14].

Regarding the interaction of the frequency ranges, we found that slow gamma [11-50 Hz] had significant effect on the high gamma-ripple [30-400 Hz] activity, similar to other research group [13]. During baseline condition this effect was missing, instead gamma [11-90 Hz] affected multi-unit activity [680-1000 Hz] ranges.

ACKNOWLEDGEMENTS

This study was supported by the Hungarian Brain Research Program (KTIA_NAP_13-1-2013_0001). We are grateful to Lucia Wittner and Zsófia Maglóczky for providing help with histology and to Loránd Erőss and László Entz for surgery.

REFERENCES

[1] Van't Klooster MA, Zijlmans M, Leijten FS, Ferrier CH, Van Putten MJ, Huiskamp GJ, *Time-frequency analysis of single pulse electrical stimulation to assist delineation of epileptogenic cortex*, Brain, vol 10, pp. 2855-66, 2011.

[2] Maxime Levesque, Aleksandra Bortel, Jean Gotman, Massimo Avoli, *High-frequency (80-500 Hz) oscillations and epileptogenesis in temporal lobe epilepsy*, Neurobiology of Disease, vol 42, pp. 231-241, 2011.

[3] Bragin A, Wilson CL, Staba RJ, Reddick M, *Interictal high-frequency oscillations (80-500 Hz) in the human epileptic brain: entorhinal cortex*, Ann. Neurol, vol 52, pp. 407-15, 2002.

[4] Jacobs J, LeVan P, Chander R, Hall J, Dubeau F, Gotman J, *Interictal high-frequency oscillations (80-500 Hz) are an indicator of seizure onset ares independent of spikes in the human epileptic brain*, Epilepsia, vol. 49, pp. 1893-907 2008.

[5] Ziljmans M, Jacobs J, Zelmann R, Dubeau F, Gotman J, *High frequency oscillations and seizure frequency in patients with focal epilepsy*, Epilepsy Res, vol. 85, pp.287-292, 2009.

[6] Jacobs J, Zijlmans M, Zelmann R, Chatillon CE, Hall J, Olivier A, Dubeau F, Gotman J, *High-frequency electroencephalographic oscillations coorelate with outcome of epilepsy surgery*, Ann Neurol, vol. 67, pp. 209-220, 2010.

[7] A. Valentín, M. Anderson, G. Alarcón, J. J. García Seoane, R. Selway, C. D. Binnie, C. E. Polkey, *Responses to single pulse electrical stimulation identify epileptogenesis in the human brain in vivo*, Brain, vol. 125, pp. 1709-1718, 2002.

[8] John D. Rolston, Nealen G. Laxpati, Claire-Anne Gutekunst, Steve M. Potter, Robert E. Gross, *Spontaneous and evoked high frequency oscillations in the tetanus toxin model of epilepsy*, Epilepsia, vol. 51, pp. 2289-2296, 2010.

[9] I. Ulbert, E. Halgren, G. Heit, and G. Karmos, *Multiple microelectrode-recording system for human intracortical applications*, J. Neurosci Methods, vol. 106, pp. 69-79, 2001.

[10] I. Ulbert, Z. Magloczky, L. Eross, S. Czirjak, J. Vajda, L. Bognar, S. Toth, Z. Szabo, P. Halasz, D. Fabo, E. Halgren, T. F. Freund, G. Karmos, *In vivo laminar electrophysiology co-registered with histology in the hippocampus of patients with temporal lobe epilepsy*, ExpNeurol, vol. 187, pp. 310-318, 2004.

[11] G. Liu, H. Guo, C. Guo, S. Zhao, D. Gong, and Y. Zhao, *Involvement of IRE1α signaling in the hippocampus in patients with mesial temporal lobe epilepsy*, Brain Res Bull, 2010.

[12] D. Fabo, *Properties of spontaneous and evoked discharges in the human subiculum*, Ph. D. Thesis, Doctoral School, Semmelweis University, Budapest, Hungary, 2007.

[13] A. B. L. Tort, R. Komorowski, H. Eichenbaum, and N. Kopell, *Measuring Phase-Amplitude Coupling Between Neuronal Oscillations of Different Frequencies*, Neurophysiology, vol. 104, pp. 1195-1210, 2010.

[14] E. W. Schomburg, A. Fernandez-Ruiz, K. Mizuseki, A. Berenyi, C. A. Anastassiou, C. Koch, *Theta phase segregation of input-specific gamma patterns in entorhinal-hippocampal networks*, Neuron, vol. 84, pp. 470-85, 2011.

Analysis of the genetic background of type 2 diabetes mellitus using a robust, high-throughput genotyping method

Réka SZALKAI-DÉNES
(Supervisors: Zoltán Gáspári PhD, Zsolt Rónai MD, PhD)
Pázmány Péter Catholic University, Faculty of Information Technology and Bionics
50/a Práter street, 1083 Budapest, Hungary
denes.reka@itk.ppke.hu

***Abstract*—Type 2 diabetes mellitus is a chronic metabolic disorder that can be characterized by the defects of both the action and secretion of insulin. It is a multifactorial disease, one of the most important environmental risks is overweight. This fact (among others) suggests the investigation of lipases in connection with the disease, as these enzymes play a major role in the fat metabolism. Certain genetic variants in the genes encoding lipases can influence the amount of the generated proteins at the level of transcription or translation, thus might modulate the efficiency of fat metabolism. Discovering the genetic alterations in the lipase genes can be used to elaborate more efficient therapeutic approaches and can contribute to primary and secondary prevention.**

***Keywords*-lipase; diabetes mellitus; genetics**

I. Introduction

Type 2 diabetes mellitus is a complex disease, being determined by both environmental and genetic factors as well as by their interactions. The disease is characterized by high blood sugar level, insulin resistance, and relative lack of insulin [1]. While the exact causes of diabetes are still not fully understood, it is known that there are certain risk factors of developing different types of diabetes mellitus. For type 2 diabetes, this includes overweight or obesity (having a body mass index – BMI – of 30 or greater) [2]. In fact, obesity is believed to account for 80–85% of the risk of developing type 2 diabetes, and recent research suggests that obese people are up to 80 times more likely to develop type 2 diabetes than those with a BMI of less than 22 [3].

The aim of this PhD project is to analyze the association between single nucleotide polymorphisms (SNP) in several candidate genes and type 2 diabetes, using molecular genetic and computational approaches.

Although the Human Genome Project was completed more than a decade ago, and the sequence of the whole genome is available since [4], identification of the genetic background of complex diseases and traits is still challenging [5]. Two substantially different approaches are available to detect genetic risk factors of polygenic diseases. Genome wide association studies (GWAS) do not require any a priori hypothesis ensuring the analysis of all biologically significant genetic components. However, genome-wide studies always include the investigation of irrelevant targets, and multiple testing requires appropriate correction of the statistical analysis.

Consequently, significance threshold is usually defined between 10^{-8} and 10^{-6} [6], which is often too stringent for the identification of biologically relevant genetic variants with statistically small effect. Candidate gene studies on the other hand focus on the investigation of selected polymorphic loci, providing the possibility of more sensitive analysis of the given polymorphisms. These two complementary techniques possess similar effect sizes, however, being rather different, thus may often provide somewhat contradictory results. According to a recent comprehensive meta-analysis, 7.1% of candidates were confirmed by both methods [7]. Candidate gene study and GWAS share one common aspect: they both require the analysis of large populations necessitating efficient, high throughput genotyping techniques.

Genome wide association studies identified several loci associated with diabetes mellitus, which data, however, need verification and may serve as starting point for further genetic and functional analyses [8].

Polymorphisms are genetic variants structurally similar to mutations. They can affect just one (SNP – single nucleotide polymorphism) or several (VNTR – variable number of tandem repeats) nucleotides. They can be located in the coding and also in the regulatory regions of the genes. Their minor allele frequency is usually higher than 5%, and they cause susceptibility to a certain complex disease or property.

Based on *in silico* data, 32 SNPs were chosen for subsequent genetic study. They are located in a number of genes, which were previously suggested to be in connection with fat metabolism. Malfunctions in fat metabolism can cause serious disorders, such as arteriosclerosis, hyperlipidemia and diabetes mellitus [9].

Lipases are enzymes that break down fats, produced by the liver, pancreas, and other digestive organs. They are part of the family of hydrolases that act on carboxylic ester bonds. The physiologic role of lipases is to hydrolyze triglycerides into diglycerides, monoglycerides, fatty acids and glycerol.

Hepatic lipase is encoded by the LIPC gene, which is located in the 15th chromosome. The hepatic lipase is a lipolytic enzyme that contributes to the regulation of plasma triglyceride (TG) levels [10].

Hormone-sensitive lipase is an enzyme that, in humans, is encoded by the LIPE gene. The enzyme is responsible for hydrolysis of triglyceride molecules and therefore release of free fatty acids and glycerol. This lipase is activated by glucagon produced by the pancreas [11].

The LIPF gene (located in the 10th chromosome) encodes gastric lipase, an enzyme involved in the digestion of dietary triglycerides in the gastrointestinal tract, and responsible for 30% of fat digestion processes occurring in human [12].

R. DÉNES, "Analysis of the genetic background of type 2 diabetes mellitus using a robust, high-throughput genotyping method" in *PhD Proceedings Annual Issues of the Doctoral School, Faculty of Information Technology and Bionics, Pázmány Péter Catholic University – 2016.* G. Prószéky, P. Szolgay Eds. Budapest: Pázmány University ePress, 2016, pp 25– 27.

The endothelial lipase protein encoded by the LIPG gene has substantial phospholipase activity and may be involved in lipoprotein metabolism and vascular biology. The enzyme is synthesized by endothelial cells and functions at the site where it is synthesized [13].

The lipoprotein lipase, encoded by the LPL gene, plays a key role in breaking down triglycerides present in chylomicrons and very low-density lipoprotein (VLDL) particles, releasing their fatty acids for entry into tissue cells [14].

The PNLIP gene encodes the pancreatic lipase that hydrolyzes insoluble, emulsified triglycerides, and is essential for the efficient digestion of dietary fats. This gene, located in the 10th chromosome is expressed specifically in the pancreas [15].

The protein encoded by the colipase (CLPS) gene is a cofactor needed by pancreatic lipase for efficient dietary lipid hydrolysis. The colipase gene is located in the 6th chromosome [16].

II. Materials and Methods

Buccal DNA samples were collected and purified from 350 diabetic and 450 control people. All participants got written information about the study and signed informed consent. SNPs were genotyped using the TaqMan® OpenArray® genotyping platform (Figure 1).

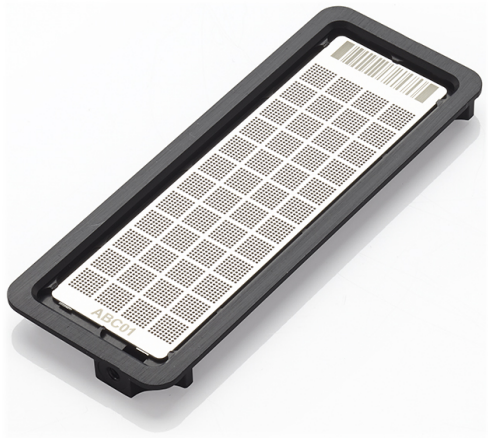

Fig. 1. OpenArray® chip

The TaqMan® OpenArray® technique is a miniaturized real-time PCR method. As the name suggests, real-time PCR is a technique used to monitor the progress of a PCR reaction in real time. Unlike the traditional methods, which requires gel electrophoresis, it is based on the detection of the fluorescence produced by a reporter molecule which produces increasing signal, as the reaction proceeds. Two allele-specific fluorescent probes labeled with different dyes (e.g. VIC, FAM) are applied to determine the genotype of the samples. The OpenArray® technique is a robust method and it employs a low-density array: one OpenArray® slide offers the analysis of 32 SNPs of 96 samples. The primers are designed and fixed on the surface of the slide. It is very fast and sensitive, but also expensive compared to traditional methods.

For this project, 10 OpenArray® plates were used. Each chip contained technical parallels from the same as well as from different plates to continuously verify reliability of the genotyping procedure. 776 technically successful parallels resulted in concordant genotype results in 757 cases. This data corresponded to as high as 97.55% reproducibility.

III. Results

Genotype call was based on the fluorescence intensity data, using the TaqMan® Genotyper Software. In the software the samples can be classified according to the intensity of the VIC (x-axis) and FAM (y-axis) dyes (Figure 2).

Out of the 32 SNPs, we could not evaluate 9 SNPs due to technical reasons, therefore these measurements were excluded from further analyses. The average call rate was 84.6%.

Hardy-Weinberg equilibrium was calculated for each SNP in the control group. The model describes and predicts genotype and allele frequencies in a non-evolving population. If there is a significant deviation from the Hardy-Weinberg model in the control population, the observed significant result could be a genetic drift and not the effect of the genetic variation. Two SNPs showed significant discrepancy from the Hardy-Weinberg model in the control group, therefore two more SNPs were excluded.

χ^2-statistical method (SPSS 17.0) was employed to compare allele frequencies of the two populations to assess genotype–phenotype association. To avoid false positive results, Bonferroni correction for multiple testing was also applied.

Several SNPs showed nominally significant difference ($p<0.05$) between the control and the diabetic population, whereas two of these results (LDL rs11570892 and LIPG rs3786248) were still significant after the Bonferroni correction. The two SNPs are both located in the 3' untranslated (UTR) regulatory region of the LDL and LIPG genes, respectively. The 3' UTR contains binding sites for both regulatory proteins and microRNAs (miRNAs). MicroRNAs constitute a class of non-coding RNAs that play key roles in the regulation of gene expression. MicroRNAs usually induce gene silencing by binding to target sites found within the 3' UTR of the target mRNA. The LDL rs11570892 and LIPG rs3786248 may influence the binding sites of certain miRNAs and thus alter the expression level of the LDL and LIPG genes, respectively. According to the PolymiRTS Database, there are several candidate microRNAs for further investigation.

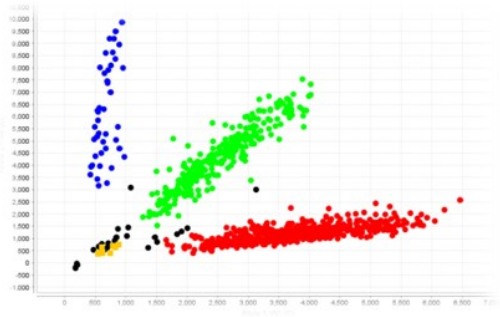

Fig. 2. Classification using the TaqMan® Genotyper Software

IV. Conclusion and Future Plan

We successfully applied the TaqMan® OpenArray® Genotyping System for genotyping SNPs in the genes of numerous lipase enzymes. Besides genotyping, further plans include the investigation of microRNA binding sites and expression of lipase genes using molecular biological methods. Our aim at

the end of the PhD project is to get more information about the genetic background of type 2 diabetes mellitus.

ACKNOWLEDGMENT

I would like to thank to my supervisors dr. Zsolt Rónai and dr. Zoltán Gáspári for their help and support.

REFERENCES

[1] International Diabetes Federation. IDF Diabetes Atlas, 6th edn. Brussels, Belgium:International Diabetes Federation, 2013. http://www.idf.org/diabetesatlas

[2] Meigs JB, Wilson PW, Fox CS, Vasan RS, Nathan DM, Sullivan LM, D'Agostino RB. Body mass index, metabolic syndrome, and risk of type 2 diabetes or cardiovascular disease. J Clin Endocrinol Metab. 2006 Aug;91(8):2906-12. Epub 2006 May 30. PubMed PMID: 16735483.

[3] http://www.diabetes.co.uk/diabetes-and-obesity.html

[4] Venter et al. The sequence of the human genome. Science. 2001 Feb 16;291(5507):1304-51. Erratum in: Science 2001 Jun 5;292(5523):1838. PubMed PMID: 11181995.

[5] Maher, B. Personal genomes: The case of the missing heritability. Nature. 2008 Nov 6;456(7218):18-21. doi: 10.1038/456018a. PubMed PMID: 18987709.

[6] Mansiaux, Y., Carrat, F. Contribution of genome-wide association studies to scientific research: a bibliometric survey of the citation impacts of GWAS and candidate gene studies published during the same period and in the same journals. PLoS One. 2012;7(12):e51408. doi: 10.1371/journal.pone. 0051408. Epub 2012 Dec 11. PubMed PMID: 23240019; PubMed Central PMCID: PMC3519865.

[7] Chang, C. Q., Yesupriya, A., Rowell, J. L., Pimentel, C. B., Clyne, M., Gwinn, M., Khoury, M. J., Wulf, A., Schully, S. D. A systematic review of cancer GWAS and candidate gene meta-analyses reveals limited overlap but similar effect sizes. Eur J Hum Genet. 2014 Mar;22(3):402-8. doi: 10.1038/ejhg.2013.161. Epub 2013 Jul 24. PubMed PMID: 23881057; PubMed Central PMCID: PMC3925284.

[8] Sanghera, D. K., Blackett, P. R., Type 2 Diabetes Genetics: Beyond GWAS. J Diabetes Metab. 2012 Jun 23;3(198). pii: 6948. PubMed PMID: 23243555; PubMed Central PMCID: PMC3521576.

[9] Carr MC, Brunzell JD. Abdominal obesity and dyslipidemia in the metabolic syndrome: importance of type 2 diabetes and familial combined hyperlipidemia in coronary artery disease risk. J Clin Endocrinol Metab. 2004 Jun;89(6):2601-7. Review. PubMed PMID: 15181030.

[10] Perret B, Mabile L, Martinez L, Tercé F, Barbaras R, Collet X. Hepatic lipase: structure/function relationship, synthesis, and regulation. J Lipid Res. 2002 Aug;43(8):1163-9. Review. PubMed PMID: 12177160.

[11] Kraemer FB, Shen WJ. Hormone-sensitive lipase: control of intracellular tri-(di-) acylglycerol and cholesteryl ester hydrolysis. J Lipid Res. 2002 Oct;43(10):1585-94. Review. PubMed PMID: 12364542.

[12] Gargouri Y, Pieroni G, Rivière C, Lowe PA, Saunière JF, Sarda L, Verger R. Importance of human gastric lipase for intestinal lipolysis: an in vitro study. Biochim Biophys Acta. 1986 Dec 5;879(3):419-23. PubMed PMID: 3778930.

[13] Edmondson AC, Brown RJ, Kathiresan S, Cupples LA, Demissie S, Manning AK, Jensen MK, Rimm EB, Wang J, Rodrigues A, Bamba V, Khetarpal SA, Wolfe ML, Derohannessian S, Li M, Reilly MP, Aberle J, Evans D, Hegele RA, Rader DJ. Loss-of-function variants in endothelial lipase are a cause of elevated HDL cholesterol in humans. J Clin Invest. 2009 Apr;119(4):1042-50. doi: 10.1172/JCI37176. Epub 2009 Mar 16. PubMed PMID: 19287092; PubMed Central PMCID: PMC2662558.

[14] Mead JR, Irvine SA, Ramji DP. Lipoprotein lipase: structure, function, regulation, and role in disease. J Mol Med (Berl). 2002 Dec;80(12):753-69. Epub 2002 Oct 24. Review. PubMed PMID: 12483461.

[15] Lowe ME. Structure and function of pancreatic lipase and colipase. Annu Rev Nutr. 1997;17:141-58. Review. PubMed PMID: 9240923.

[16] Lindner I, Helwig U, Rubin D, Li Y, Fisher E, Boeing H, Möhlig M, Spranger J, Pfeiffer A, Hampe J, Schreiber S, Döring F, Schrezenmeir J. Putative association between a new polymorphism in exon 3 (Arg109Cys) of the pancreatic colipase gene and type 2 diabetes mellitus in two independent Caucasian study populations. Mol Nutr Food Res. 2005 Oct;49(10):972-6. PubMed PMID: 16189801.

Selection of dynamic ensembles to achieve maximum correspondence to experimental NMR data

Daniel DUDOLA
(Supervisor: Zoltán GÁSPÁRI)
Pázmány Péter Catholic University, Faculty of Information Technology and Bionics
50/a Práter street, 1083 Budapest, Hungary
dudola.daniel@itk.ppke.hu

***Abstract*—Besides their structure, the internal dynamics of proteins plays an important role in governing their function like protein-protein and protein-ligand interactions. Conventional models protein structures based on experimental data only yield structural information as they are composed of a single conformer or a limited number of similar conformers.**

NMR-spectroscopy allows atomic motions to be measured on a wide range of time scales from nanoseconds to minutes. Dynamics-related information can be incorporated in ensemble-based structural models of proteins, either by restrained molecular dynamics simulations or by selection-based approaches. It is self-evident, that dynamics can only be represented in structural ensembles, since a single structure can not hold dynamic information. The resulting dynamical models need to be carefully evaluated in relation to geometry and correspondence to experimental data. As ensembles fulfill experimental data more easily than single structures, the issue of potential overfitting has to be considered. I have performed a number of exploratory molecular dynamics simulations with the use of order parameter data as restraining parameters to determine the best possible parametrization for such a simulation. The output of these simulations were analyzed with the current version of the CoNSEnsX server to back-calculate the experimental parameters from the created ensemble. [1]

***Keywords*-protein dynamics; protein ensembles; ubiquitin ensembles**

I. Introduction

Proteins – as well as many other biological macromolecules – are present in various conformers at the same time. These conformational states are separated by energy barriers and are responsible for the diverse and specific functionality of the proteins. Their motions cover 14 magnitudes of time scales and there is no experimental method with which all of these motions could be studied simultaneously. [2] Due to structural differences, these conformations show different affinity towards various ligands, so the presence of a specific ligand can shift the dynamic equilibrium of the system. This scenario of ligand binding is called conformational selection and can be contrasted with the classical lock-and-key model of molecular recognition.

NMR spectroscopy can yield information on the structure and dynamics of a protein at various time scales. A number of experimental parameters can be measured, each of which reports on motions on different time scales. For globular proteins with a well-defined fold it can be assumed that structural fluctuations can be described as deviations from the average structure. in such cases, molecular dynamics simulations with experiment.derived restraints can be used to generate ensembles that reflect their internal dynamics. Such restraints include nuclear Overhauser effect-based distance restraints, averaged over two replicas at a time to avoid overfitting (MUMO paper), S^2 order parameter restraints (Best and Vendruscolo 2004) that report on the ps-ns time scale dynamics and residual dipolar couplings (RDCs) which, if sufficient independent data sets are available, can be used to estimate the dynamics of the protein up to the μs time scale (Lange et al). During the simulation, the restraints are applied at each step on the replicas simulated in parallel. However, if a structural drift occurs during the simulation, the final set of conformers captured at regular intervals during the simulation, might not correspond to all the restraints used. Especially S^2 order parameters are sensitive to structural transitions occurring during such simulations, as e.g. conformational changes in a loop region relative to the other parts of the molecule can result in low order parameters for that region even when the restraining worked well for each simulation step. Moreover, it was pointed out in the literature that amide bond planarity might not be maintained in simulations employing a large number of restraints that act on the amide N-H bond like backbone S^2 parameters and N-H RDCs. In such cases, additional restraining of the geometry of the amide bonds might be necessary.

I have performed exploratory molecular dynamics calculations on the protein ubiquitin with a modified version of the GROMACS 4.5.5. free molecular dynamics package by applying different sets of experimental restraints and varying the parameter settings. The resulting ensembles were evaluated for their correspondence to experimental parameters, both those applied for the simulations and independent ones. In addition, amide bond geometry was carefully checked for each ensemble.

Ubiquitin plays an important role in cellular signaling networks and its crystal structure is well determined. Additionally, ubiquitin is widely studied with NMR spectroscopy and there are many experimental data sets available, as well es structural ensembles calculated from experimental NMR data. Because of the amount of experimental data available, ubiquitin often servers as a test molecule for various molecular dynamic calculations. Because its structural features, the molecule is suitable of examining various interface adaption dynamics, which is responsible for conformational selection features. [3]

These restraints prevent the molecules from movements which were not measured during the NMR experiments the experimental parameters come from. To assess the compliance of the experimental and the from simulations back-

D. DUDOLA, "Selection of dynamic ensembles to achieve maximum correspondence to experimental NMR data" in *PhD Proceedings Annual Issues of the Doctoral School, Faculty of Information Technology and Bionics, Pázmány Péter Catholic University – 2016.* G. Prószéky, P. Szolgay Eds. Budapest: Pázmány University ePress, 2016, pp 29– 31.

calculated parameters, we back-calculated the parameters from the simulations output ensemble. To ensure the correctness of the used methods, we carried out several Leave-One-Out experiments, in which we excluded an RDC data set from the restraining data sets during the molecular dynamic simulation. These parameter sets were back-calculated as well and the compliance of the not included data set is highly correlated with the correspondence of the data sets used for restraining. This proves that the applied parameters, force-field and restraining parameters are configured properly and the simulation yields a dynamical structural ensemble, in which the back-calculated dynamical parameters correspond to the experimentally determined data sets.

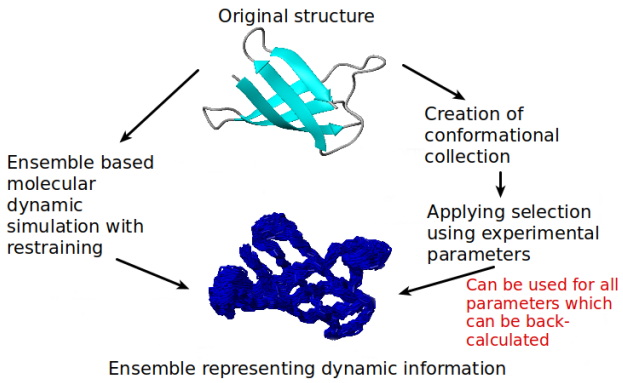

Fig. 1. Creation of dynamical structural ensembles

To simplify the experiments with various parameters and force constants of the force field and restraints, we created a protocol, with which we can carry out molecular dynamic simulations in a highly automatized manner. A new server was set up and configured as well, suitable to run many simulations parallel. With this opportunity, we can run more simulations with slightly different configurations to find the best parametrization for the given task. For the initial simulations, our objective was to maximize the correspondence of the back-calculated residual dipolar coupling parameter sets and the back-calculated order parameters with the experimental data. Besides, several molecular dynamic simulations were carried out to find the optimal ensemble size for a given molecule, in which the dynamical parameters are well represented, but not due to overfitting the restraining parameters during the simulation.

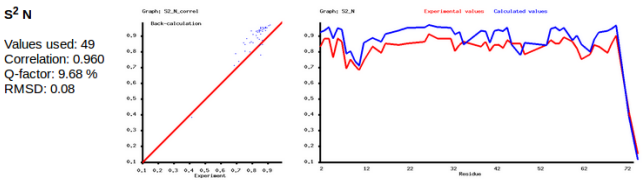

Fig. 2. Correspondance of back-calculated N-H order parameters - 2NR2

The output ensembles of the simulations are analyzed with the CoNSEnsX server [4], with which we can assess the correspondence of the back-calculated and the experimental parameters. The server yields three measures: correlation, q-factor and rmsd, as shown in the figures (Fig.1., Fig.2.).

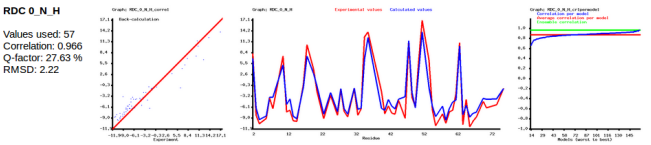

Fig. 3. Correspondance of back-calculated N-H RDC parameter set - 2NR2

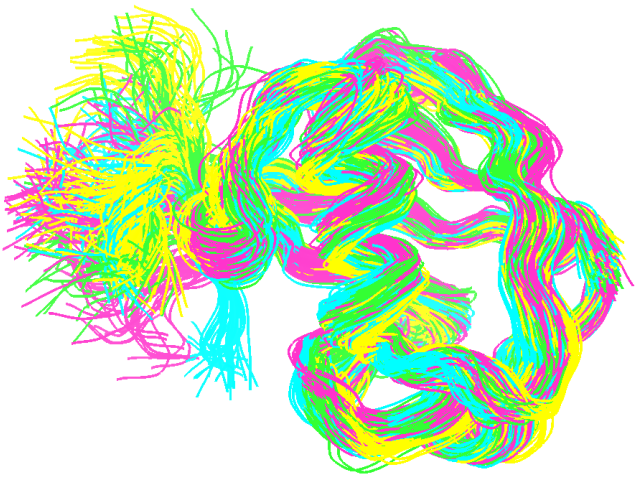

Fig. 4. Ubiquitin ensemble - molecular dynamic simulation output

II. Further plans

During the analysis processes of the newly created ensembles, we became aware of the fact, that the current CoNSEnsX implementation lacks some features, which would be relevant and/or helpful during the process of back-calculations. Work has been begun on the new implementation of the server using modern web technologies.

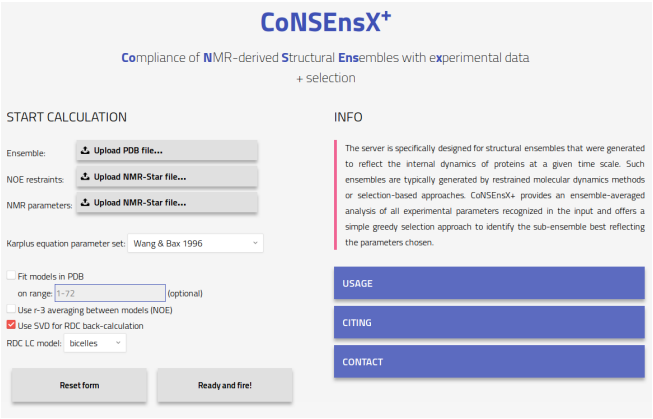

Fig. 5. User interface of the new CoNSEnsX server (work in progress)

To simplify and speed up the analysis, the following features has to be implemented in the upcoming CoNSEnsX version:

- complete server reimplementation in Python (Django)
- store data in database for future use
- handling RDC sets from different experiments separately
- support for accepting NOE distance data in STAR-NMR format using Prody [5] and NMRPyStar (https://github.com/mattfenwick/NMRPyStar)

- redesigned client-side
- vector graphic output of graphs

Additionally, we plan to implement a selection feature, with which the user can filter the input ensemble to achieve maximum correspondence to experimental data.

REFERENCES

[1] B. Richter, J. Gsponer, P. Várnai, X. Salvatella, and M. Vendruscolo, "The mumo (minimal under-restraining minimal over-restraining) method for the determination of native state ensembles of proteins," *J Biomol NMR*, vol. 37, p. 117–135, 2007.

[2] Z. Gáspári and A. Perczel, "Protein dynamics as reported by nmr," *Annual Reports on NMR Spectroscopy*, vol. 71, pp. 35–76, 2010.

[3] e. a. Oliver F. Lange, "Recognition dynamics up to microseconds revealed from an rdc-derived ubiquitin ensemble in solution," *Science*, vol. 320, p. 1471, 2008.

[4] A. F. Ángyán, B. Szappanos, A. Perczel, and Z. Gáspári, "Consensx: an ensemble view of protein structures and nmr-derived experimental data," *BMC Structural Biology*, vol. 10:39, 2010.

[5] B. I. Bakan A, Meireles LM, "Protein dynamics inferred from theory and experiments," *Bioinformatics*, vol. 27(11), pp. 1575–1577, 2011.

Age-related changes of the representative modular structure in the brain

Bálint File
(Supervisor: Dr. Dániel Fabó, Dr. István Ulbert)
Pázmány Péter Catholic University, Faculty of Information Technology and Bionics
50/a Práter street, 1083 Budapest, Hungary
file.balint@itk.ppke.hu

***Abstract*—Modularity maximization algorithms are generally used for identifying functional subnetworks. Comparison of the community assignment of certain brain regions between two subpopulations is not a straightforward methodological issue. An exact comparison has to deal with the differences of the module assignment, the uncertainty of the non-overlapping clustering and the degenerative property of modularity. The current study aimed to propose a permutation framework for modelling the changes between the representative partitions of two groups. The technique is based on constraining the natural partition of a homogenous group toward an unfamiliar modular organization by changing the modular assignment of the nodes. The distance between the native and constrained partitions can be measured by the modularity change as a cost function. Certain node shifts between communities perturb more the modular organization than others. The question, whether the modularity drop of a given transformation is typical for a group was investigated. The level of significance of a transformation was determined by the distribution provided by mixed groups. The method was tested on resting-state fMRI data of 20 young and 20 elderly subjects. Increased segregation of the occipital module was found in the young, while the importance of the default mode network in the maintenance of the modular organization was slightly affected by aging. These findings were in line with, and partly complete the results of previous studies indicating the validity of the method.**

***Keywords*-functional connectivity; community detection; representative network; modularity; aging**

I. Introduction

Graph theoretical analyses have demonstrated that brain functional networks have a modular structure. A module is defined as a highly integrated sub-network consisting of regions with much denser connectivity within themselves than the rest of the brain. In general, integration within a module allows efficient local processing, while segregation between modules may be necessary to avoid internal or external noise. Therefore, studies of brain modules enable to identify groups of brain regions that may serve common functions of neural activity [1].

Although there is not a unique way for detecting the community structure in complex networks, the modularity (Q) value optimizing algorithms [2] became the gold standard for identifying the functional brain modules. The modular partition of a network with the highest Q value comprises many within-module links and as few as possible between-module links.

During the recent years graph theoretical measurements were developed to define the differences in community assignments of brain regions between the two subpopulations[3][4]. The consistency of the modular structure across subjects is measured by the scaled inclusivity [3], and the modular classification of a particular brain region can be detected by Pearson's phi [4]. These methods work with the labels of the modular assignment corresponding to the maximal modularity partitioning. The label assignment is a binary process: a node is included or excluded from a community, however it is clear, that changes of the partition label of certain brain regions influence the modular organization more, than other do.

The current study aimed to present a method to statistically evaluate the differences between representative modular structures. The technique is based on warping the native partition of a subgroup to an unfamiliar modular organization. The distance between the native and warped partitions can be measured by the modularity change as a cost function. Measuring the extent of the modularity change of a network between different partitioning, can distinguish the degenerative partitions of the modularity maximization [5] and the negligible, minor effects between the groups from the relevant changes in the modular assignment of certain brain regions.

We tested the method on resting-state fMRI data of young and elderly subjects. The elderly functional network was characterized by altered community structure [6][7], reduced modularity [8] and generally more between module connectivity than the young network [7]. We expected that our method can detect the prominent regions, which modular memberships are crucial for the formation in the elderly brain network.

II. Methods

A. Participants

Healthy young (19-21 years; N =20; SD= ± 1; 9 women) and elderly (67-85 years; N = 20; SD=± 6; 10 women) individuals took part in this study. fMRI data was obtained from the 'INDI NKI/Rockland Sample'. fMRI time series from each participants were acquired in eyes open resting state condition during a 11 minutes period.

B. fMRI recording, preprocessing and functional connectivity assessment

All subjects were scanned with the same scanner (MRC35390 SIEMENS TrioTim 3T, TR=2500=ms, TE=30 ms, FA=80°, $3x3x3$ mm voxels, 260 frames). Preprocessing steps were carried out using SPM12 and Conn 15d toolboxes. Default preprocessing steps were applied with default parameters in Conn: (1) realignment, (2) slice-timing correction, (3) segmentation and normalization, (4) ART-based scrubbing, (5) smoothing using a 8 mm full-width half-maximum (FWHM) Gaussian kernel. After the preprocessing steps fMRI time series were band-pass filtered ([0.008 0.09] Hz), white matter and cerebrospinal fluid time series were regressed out. 95 ROIs (cortical areas and the hippocampus) were determined applying the FSL Harvard-Oxford Atlas parcellation scheme [9]. Regional average time courses of the ROIs were extracted

B. FILE, "Age-related changes of the representative modular structure in the brain" in *PhD Proceedings Annual Issues of the Doctoral School, Faculty of Information Technology and Bionics, Pázmány Péter Catholic University – 2016.* G. Prószéky, P. Szolgay Eds. Budapest: Pázmány University ePress, 2016, pp 33– 36.

for each individual. Cross-correlations between all pairwise ROIs' time series were calculated. Correlation coefficients were converted into z-values using Fisher's equation. Because of the ambiguity regarding the meaning of negative correlations [10], negative z-values were set to zero in the connectivity matrix. The connectivity strength of every subject was normalized between 0 and 1 avoiding the possible bias of the inter-subject connectivity strength variance. Every subject was characterized by a weighted, undirected network, where the ROIs represented the nodes and the connectivity strength defined as the weight of edges. The representative modular structures were derived from the average connectivity network [6].

C. Modularity and partition distance

In order to determine the modular structure, smaller functional subgraphs or modules were decomposed from the entire resting state network. The modularity (Q) of a graph describes the possible formation of communities in the network:

$$Q = \sum_{i=1}^{N} \left[\frac{l_s}{L} - \left(\frac{d_s}{2L} \right)^2 \right] \quad (1)$$

where N is the number of modules, L is the total sum of all edge weight in the network, l_s is the sum of all weight in module s, and d_s is the sum of the strength of nodes (the sum of edge weight of a certain node) in module s [2]. The Louvain algorithm [11] was applied to identify modular partition with high modularity. The representative modular structure was determined by applying the modularity algorithm on the young and elderly subjects' average connectivity matrices respectively. For providing evidence of the highly modular organization of the averaged functional networks, the maximal modularity value of the biological functional network was compared to the value of the corresponding random networks. Degree-, weight-, and strength-preserving randomization [12] were applied to generate 5000 independent null model for both age groups. The distance between different partition representations of networks with identical nodes can be determined by the normalized mutual information (MIn):

$$MIn = 2 * \frac{(H(Y) + H(E) - H(Y,E))}{(H(Y) + H(E))} \quad (2)$$

where H(X) and H(Y) is the entropy of the two partitions separately and H(Y,E) is the joint entropy of the two partitions [13]. We determined the level of similarity between the young and elderly representative modules.

D. Local modularity and warping of the partitions

It is important to emphasize, that the presented analysis is not symmetric, thus it is necessary to perform it on the calculated networks both in the young and the elderly separately. The following steps were described by choosing the young group as the reference partition. The relative importance of each region in the maintenance of the modular organization was measured by forcing each brain region to an extraneous module. Moving a node with an unstable community membership has less effect on the changing of the modularity value than transfer a node from its unique group [12]. Every node was moved to all possible clusters. Each transformation can be characterized by the change of the modularity value:

$$dQ_i = Q\left(before\ shift\ of\ node_i\right) - \\ - Q\left(after\ shift\ of\ node_i\right) \quad (3)$$

The average of the modularity drop (local modularity) of each node can define how strongly a node is assigned to its own module. The local modularity value can also be interpreted as the correspondence of a given node to the modular organization of a network. The local modularity is positively related to the within module connectivity and negatively to the between module connectivity [14]. Beside the calculation of the local modularity we can mark certain node shifts between modules, which warp the young partition towards the elderly. The changes of the MIn can assign these node shifts:

$$dMIn = MIn\left(young, elderly\right) - MIn\left(young', elderly\right) \quad (4)$$

dMIn values with negative sign denote node transformations, which warp the young partition towards the elderly.

E. Statistical evaluation

The modularity values of the representative partitions were compared to the null models and to each other. The MIn of the young and elderly representative networks were related to the MIn value of the representative modules. We also defined the level of significance of the node shifts. Alpha level was set to 0.05 in every test. Nonparametric statistics (one-sided) were applied to test whether the modularity value of the young and elderly representative networks were higher than the 5% of the null models' modularity value. The modularity value of the two age groups were compared using a permutation procedure. By randomly exchanging the membership of young and elderly subjects an average network of mixed group was created. The maximal modularity value for the mixed group was calculated. Repeating the procedure 5000 times, we can fit the original young and elderly modularity value to the distribution of the mixed groups' maximal modularity value. A similar procedure was applied to test, whether the effect of aging, or the individual variance of the modular organization is more prominent. The MIn value of the mixed groups partitions were compared to the MIn of the representative partitions. We expected a lower MIn in case of the representative partitions, reflecting the more pronounced effect of aging than individual variance. The level of significance of a node shift was also determined with a distribution provided by mixed groups. The young and elderly modular partitions show a different pattern of node assignment to modules, thus we tested them separately. The mixed group average network was constrained to the modular organization of the young, or elderly representative partition (reference group). The same node shifts were applied on the mixed group as in the reference group. The null hypothesis was rejected, if the dQ value of a particular node shift of the reference group was lower than 95% of the same node shift of the mixed group. In case of the local modularity the mean dQ value of every node in the original group was compared with the mixed groups' mean dQ values.

III. Results

A. Modularity and partition distance

The modularity value of the young ($Q_{young} = 0.25$) and elderly ($Q_{elderly} = 0.21$) representative networks were

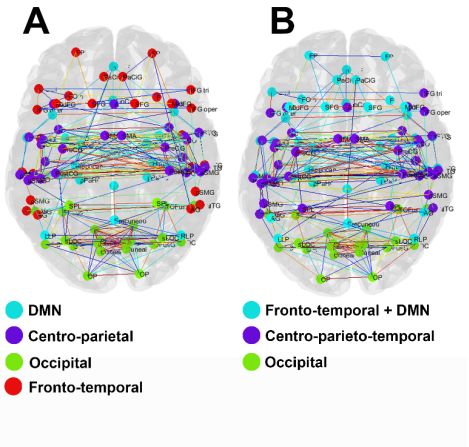

Fig. 1. Representative modular organization of young (A) and elderly (B) groups. Different node colors denote different modules. The coloring of the modules was optimized by the Hungarian algorithm [15] using Jaccard-similarity between the modules as a cost.

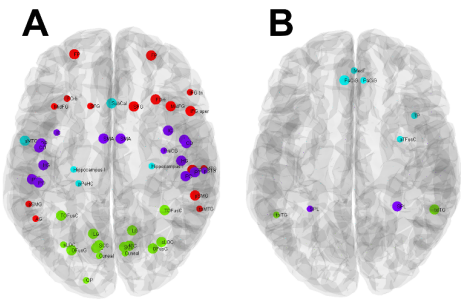

Fig. 2. . Age-related differences in the local modularity value. The local modularity determines the correspondence of a given node to the modular organization of a network. The spheres denote the brain regions which show a significantly higher local modularity (segregation) in the young (A) and elderly (B) representative community structure. Spheres with larger radius mark p¡0.01 level of significance. Color marks the modules.

significantly higher, than the corresponding random networks (p¡.001 for both age groups).

The modularity value of the young representative network was significantly higher than that of the mixed group (p=0.0036, 5000 permutations), while the modularity value of the elderly representative network was significantly lower than that of the mixed group (p=0.016, 5000 permutations). A tendency of lower MIn between the two representative partitions compared to the mixed groups was observed (p=0.08, 5000 permutations). The modularity algorithm detected 4 functional modules in the young and 3 modules in the elderly group (Fig 1.). The occipital module shows the higher overlap between the two age group, while the fronto-temporal and the default mode network (DMN) were merged to one single cluster.

B. Age-related local modularity of brain networks

The local modularity determines the correspondence of a given node to the modular organization of a network. As the young group is characterized by a significantly higher modularity than the elderly group, the higher local modularity values also appear in this group (Figure 2.). The most prominent age-related segregation in the young representative modular structure was observed in the occipital regions (15 from the 18 occipital regions showed an increased local modularity). On the contrary, the segregations of the structures of the default mode network were slightly affected by aging. Increased local modularity was measured only for 4 (right/left hippocampus, left parahippocampal gyrus, left angular gyrus) of the 13 regions of the DMN. A few regions with increased local modularity were observed in the elderly group. The medial frontal cortex (p=0.03), paracingulate gyri (pright=0.03; pleft=0.001), Superior Parietal Lobules (pright=0.009; pleft=0.01) and inferior temporal gyri (pright=0.004; pleft=0.05) were identified as brain regions serving an increased importance in the maintenance of the elderly modular structure.

C. Node shifts with negative dMIn sign

dMIn values with negative sign denote node transformations, which warp one partition toward the other. In case of the young node transformations with negative dMIn sign indicated shift mainly from the fronto-temporal module, since this module was absorbed to other modules in the elderly group. The majority of node shifts caused a significant modularity decrease compared to the mixed group, validating the age-related segregation of the fronto-temporal module. Transformation of the bilateral middle temporal gyri (pright=0.05; pleft=0.05) and the right supramarginal gyrus (p=0.045) from the ‘Centro-parieto-temporal’ module to the ‘Fronto-temporal + DMN’ module resulted in a significant modularity decrease compared to the mixed age group. Changing of the modular assignment of the bilateral superior parietal lobules (pright=0.02; pleft=0.04) from the elderly ‘Centro-parieto-temporal’ to the young ‘Occipital’ module also resulted ina significant modularity decreasecompared to the mixed age group.

IV. Conclusion

This work introduced a method for the comparison representative partitions of two subpopulations. The method allows the quantification of the modularity decrease caused by constraining the native partition of a subgroup to an unfamiliar modular organization.

We tested the method on resting state fMRI data of young and elderly subjects. As far as we know, this is the first attempt to describe the elderly functional modular organization by examining the capability of adaptation to the young modular configuration.

Similarly to other findings [8][7] we found an increased modularity in the young group. The highest correspondence of the increased modularity was observed in the occipital module in the young group. This observation is in line with the increased segregation of the visual cortex in the young [8]. Increased local modularity in the elderly was mainly observed within the regions of the dorsal attention network (prefrontal cortex, anterior cingulate, posterior parietal lobule). The long range connections within this system showed an age-related decrease [16]. Probably the disconnection of the networks resulted in the increase of local modularity. Similarly to other findings [8], we have found the merging of the DMN to the ‘fronto-temporal’ module in the elderly group. Our method demonstrated that the changes of the community assignment of these regions have a significant impact on the modularity. In the elderly, the middle temporal gyri and the

superior parietal lobules participated in an altered module compared to the young group. These regions belong to the DMN [17]. The results suggest that the age-related alteration of the community membership of these brain regions preserve the modular structure.

As a limitation of this study we have to refer to the thresholding problem of functional brain networks. We used a biologically relevant cut-off [10][18], but we have to acknowledge that choosing a threshold is always an arbitrary choice [19]. Changing the community memberships of a partition was limited to individual node shifts between communities. Applying more sophisticated transformation rules (e.g: merging, splitting partitions) can improve the sensitivity of the method.

ACKNOWLEDGEMENTS

The present work was supervised by Dr. Márk Molnár, Dr. Zoltán Somogyvári, Dr. István Ulbert and Dr. Lajos R. Kozák. The fMRI data processing was carried out by Zoltán Klimaj.

REFERENCES

[1] O. Sporns and R. F. Betzel, *Modular Brain Networks*, Annu. Rev. Psychol., vol. 67, no. 1, pp. 613–640, 2016.

[2] M. Newman and M. Girvan, *Finding and evaluating community structure in networks*, Phys. Rev. E, pp. 1–16, 2004.

[3] M. N. Moussa, M. R. Steen, P. J. Laurienti, and S. Hayasaka, *Consistency of network modules in resting-state FMRI connectome data*, PLoS One, vol. 7, no. 8, p. e44428, Jan. 2012.

[4] A. Alexander-Bloch, R. Lambiotte, B. Roberts, J. Giedd, N. Gogtay, and E. Bullmore, *The discovery of population differences in network community structure: New methods and applications to brain functional networks in schizophrenia*, NeuroImage, vol. 59, no. 4. pp. 3889–3900, Feb-2012.

[5] B. H. Good, Y. A. De Montjoye, and A. Clauset, *Performance of modularity maximization in practical contexts*, Phys. Rev. E - Stat. Nonlinear, Soft Matter Phys., vol. 81, no. 4, pp. 1–20, 2010.

[6] D. Meunier, S. Achard, A. Morcom, and E. Bullmore, *Age-related changes in modular organization of human brain functional networks.*, Neuroimage, vol. 44, no. 3, pp. 715–23, Feb. 2009.

[7] M. Y. Chan, D. C. Park, N. K. Savalia, S. E. Petersen, and G. S. Wig, *Decreased segregation of brain systems across the healthy adult lifespan*, Proc. Natl. Acad. Sci., vol. 111, no. 46, pp. E4997–E5006, 2014.

[8] L. Geerligs, R. J. Renken, E. Saliasi, N. M. Maurits, and M. M. Lorist, *A brain-wide study of age-related changes in functional connectivity*, Cereb. Cortex, vol. 25, no. 7, pp. 1987–1999, 2015.

[9] N. Tzourio-Mazoyer, B. Landeau, D. Papathanassiou, F. Crivello, O. Etard, N. Delcroix, B. Mazoyer, and M. Joliot, *Automated anatomical labeling of activations in SPM using a macroscopic anatomical parcellation of the MNI MRI single-subject brain*, Neuroimage, vol. 15, no. 1, pp. 273–289, 2002.

[10] M. L. Schölvinck, A. Maier, Q. Y. Frank, J. H. Duyn, and D. A. Leopold, *Neural basis of global resting-state fMRI activity*, Proc. Natl. Acad. Sci., vol. 107, no. 22, pp. 10238–10243, 2010.

[11] V. D. Blondel, J.-L. Guillaume, R. Lambiotte, and E. Lefebvre, *Fast unfolding of communities in large networks*, J. Stat. Mech. Theory Exp., vol. 2008, no. 10, p. P10008, 2008.

[12] M. Rubinov and O. Sporns, *Weight-conserving characterization of complex functional brain networks*, Neuroimage, vol. 56, no. 4, pp. 2068–2079, 2011.

[13] M. Meilă, *Comparing clusterings-an information based distance*, J. Multivar. Anal., vol. 98, no. 5, pp. 873–895, 2007.

[14] R. Guimera and L. Amaral, *Functional cartography of complex metabolic networks*, Nature, vol. 433, no. February, pp. 895–900, 2005.

[15] H. W. Kuhn, *The Hungarian method for the assignment problem*, Nav. Res. Logist. Q., vol. 2, no. 1-2, pp. 83–97, 1955.

[16] D. Tomasi and N. D. Volkow, *Aging and functional brain networks*, Mol. Psychiatry, vol. 17, no. 5, pp. 549–558, 2012.

[17] J. S. Damoiseaux, C. F. Beckmann, E. J. S. Arigita, F. Barkhof, P. Scheltens, C. J. Stam, S. M. Smith, and S. a R. B. Rombouts, *Reduced resting-state brain activity in the 'default network' in normal aging*, Cereb. Cortex, vol. 18, no. 8, pp. 1856–1864, 2008.

[18] X. J. Chai, A. N. Castañón, D. Öngür, and S. Whitfield-Gabrieli, *Anticorrelations in resting state networks without global signal regression*, Neuroimage, vol. 59, no. 2, pp. 1420–1428, 2012.

[19] B. C. M. Van Wijk, C. J. Stam, and A. Daffertshofer, *Comparing brain networks of different size and connectivity density using graph theory*, PLoS One, vol. 5, no. 10, p. e13701, 2010.

Connection between a nested oscillation system and the interictal-epileptic discharges

Edit Lelle GYŐRI
(Supervisor: Dániel FABÓ, István ULBERT)
Pázmány Péter Catholic University, Faculty of Information Technology and Bionics
50./a Práter street, 1083 Budapest, Hungary
National Institute of Clinical Neurosciences
57. Amerikai street, 1145 Budapest, Hungary
Institute of Cognitive Neuroscience and Psychology, Research Centre for Natural Sciences, Hungarian Academy of Sciences
2. Magyar Tudósok körútja, 1117 Budapest, Hungary
gyori.edit@itk.ppke.hu

***Abstract*—Epilepsy is the most common primary neurological disorder that affects people of all ages and all social classes. Many people with this syndrome have more than one type of recurrent, unprovoked seizures and may have complex negative effects on a psychological function and a social situation. The exact neurobiological mechanism underlying epilepsy is still unknown. Our research group has set the goal to characterize this underlying mechanisms by recording electrical properties of multi-phase electrophysiological events in vivo and in vitro techniques in epilepsy patients undergoing presurgical evaluation. With the aid of the cortico-cortical evoked potentials (CCEP) [1] [6] [7] we attempt to identify the location and boundaries of the epileptogenic area, in addition this type of stimulation is suitable for mapping effective brain connectivity. In order to characterize the brain activity. We analyzed the sweep to sweep amplitude variance of CCEP response in epilepsy patients implanted with subdural electrodes. Based on the change in the spatial extension of the significantly evoked responses, we found nested oscillations including infraslow components below 0.1Hz and we hypothesized this nested oscillation system and related these results to the occurrence of interictal epileptiform discharges (IEDs).**

***Keywords*-activated grid points, amplitude, CCEP, epilepsy, IEDs, nested oscillation**

I. Introduction

Approximately 65 million people suffer from epilepsy around worldwide. This neurological disorder can affect different areas of the brain, so it can generate different symptoms/epilepsy types as well. During a seizure, the conscious control of behavior can disappear, automatic series of actions can occur, and memory processes may be severed.

About 30 % of people with epilepsy do not respond to antiepileptic drug treatment. Surgical resection of the seizures generating brain area can be an alternative treatment in these case. The complete resection of the seizure-onset zone (SOZ) is mandatory for the positive surgical outcome, to be seizure free. The involved patients underwent standard pre-and intraoperative epilepsy surgery evaluation to locate the SOZ and to guide the extent of resection. Beside various preoperative, non-invasive neuroimaging modalities (PET, MRI, CT), video-EEG was performed to record spontaneous seizures and interictal activity. The spontaneous interictal and ictal discharges, low and high frequency electrical stimulation induced activities were recorded from the cortex with electrocorticography (ECoG) [9] [11]. Epilepsy can be diagnosed by detecting ictal and interictal epileptiform discharges (IEDs) on the electrophysiological recordings. IEDs are brief (<250 millisecond), morphologically defined events, which are widely accepted diagnostic sign of epilepsy. The reasons for the presence of this activity in the epileptic brain are still unknown. Vanhatalo showed from human electroencephalography (EEG) research, that the interictal events are strongly synchronized to the infraslow oscillations (<0.1 Hz ISO). Large degree of phase-amplitude coupling was found between the ISO and a wide frequency range activity (theta – 4-8 Hz, gamma-30-100 Hz) [2] [3] [4] [5] [10]. This nested oscillation occurred when the amplitude of a faster rhythm was coupled to the phase of a slower rhythm [5] [8].

II. Methods

A. Electrical stimulation and recording

We involved nine focal epilepsy patients (3 females and 6 males) undergoing standard phase 2 (including implanted intracranial electrodes) pre-and intraoperative epilepsy surgery evaluation to locate the SOZ and to guide the extent of resection. During the invasive video-EEG monitoring (5–10 days) single pulse electrical stimulation was performed with bipolar stimulation on adjacent electrode contact (0.5 Hz, 10 mA, 0.2 ms, 80-450 trials per electrode pair) of the grid or the strip. The signal was recorded with 500 or 1024 Hz sampling rate and >0.16 Hz hardware filter. The 3D positions of subdural electrode arrays were reconstructed based on preoperative MRI and postoperative CT scans.

B. Data analysis

Electrophysiological data analyses were performed using the Edit modul of Neuroscan (Neuroscan Inc.) and Matlab scripts (Mathlabworks Inc.). We used automated methods for the analysis of mCCEP induced by single pulse electrical stimulation. The method was described previously [11]. Briefly, the local field potential data was filtered between 0.3-30 Hz around every stimulation in a -500 ms -1500 ms window. The evoked response consist of an early sharp wave between 10–50 ms (N1) and a later slow-wave between 50–500 ms (N2) after stimulation. The significantly activated electrode contacts were determined for every single epoch for both N1 and N2 components using an amplitude threshold of 3 or 6 standard deviation relative to the -450 - -50 ms baseline. The number of the activated electrodes were plotted against time, resulting multiple time-series of the activated brain areas sampled at 0.5 Hz and measured in electrode contact

E. GYŐRI, "Connection between a nested oscillation system and the interictal-epileptic discharges" in *PhD Proceedings Annual Issues of the Doctoral School, Faculty of Information Technology and Bionics, Pázmány Péter Catholic University – 2016.* G. Prószéky, P. Szolgay Eds. Budapest: Pázmány University ePress, 2016, pp 37– 39.

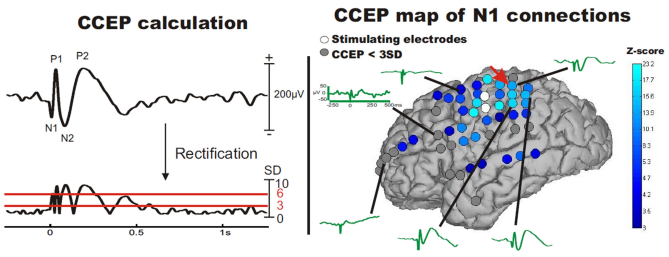

Fig. 1. The time course of the number of the activated electrode contacts (peak amplitude exceeding 3 or 6 SD relative to the -450–50ms prestimulus baseline) was determined in the times of 10-50 ms (N1) and 50-500 ms (N2) for every stimulation epochs. CCEPs were elicited (parameters: 2sec, 10mA, 0.5Hz, 80-450 stimuli) and analyzed in sleeping and awake grid implanted epilepsy patients undergoing presurgical evaluation. The 3D positions of subdural electrode arrays were reconstructed based on preoperative MRI.

numbers. The number of simultaneously activated electrodes through the stimulations resulted in an oscillation-like signal (simultaneously activated brain area oscillation - SABAO) with 2 s sampling rate. On this derived electrophysiological signal, Fast Fourier Transform, wavelet analysis were applied to characterize the frequency and Hilbert transformation was calculated on the 10 point moving averaged SABAO signal to extract the phase information. To control the method these analysis were repeated on stimulation free data. IEDs were detected manually between stimuli (500-1500 ms after each stimulus) on the unfiltered raw data.

III. Results

The SABAO signal shows how many number of grid points activated from stimulation to stimulation. It showed significant variance in time (in the highest varying case: 2-50/52 contacts). The time-frequency analysis resulted 0.01-0.035 Hz modulation both in sleep and awake states (Fig.2 /. A. and B.). Similar modulation was found in the stimulation-free activity with lower amplitude. IEDs were increased at the troughs of the 0.01-0.035 Hz oscillations (Fig.5.). Oscillation of the power of 0.01-0.035 Hz range generates ultraslow (<0.003 Hz) frequency was found in the stimulation free and long stimulation (450 epoch) data.

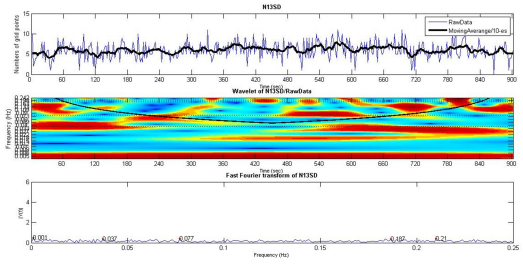

Fig. 2. Wavelet analysis. Illustration of the wavelet transformation for one case with the cone of influence (black curve). Dotted lines indicate the main peaks in the FFT derived from the same data. The maximal amplitude value curves were calculated across the frequency ranges.

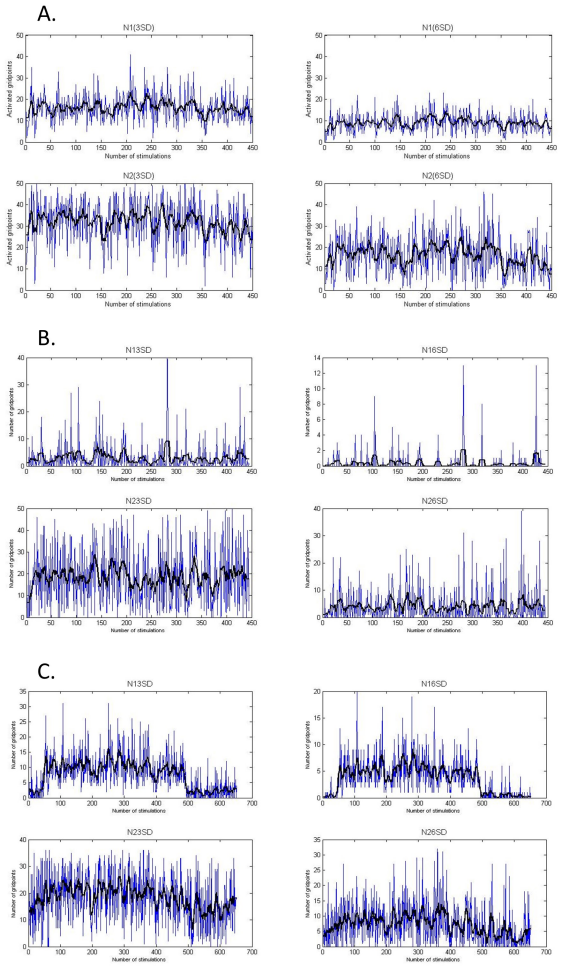

Fig. 3. Activation of grid points. A. Stimulated sample (450 events). Four representative traces on the quantity of the activated grid points at the two previously mentioned timepoints (N1, N2) with the two different standard deviation values showes significant variance in time (in highest varying case: 2-50/52 contacts) (blue lines). Black line represents the moving average (n=10). B. We could recognise activated grid points in stimulation-free data with lower tendency. C. Stimulated and the continuing, not-stimulated brain recordings. The electrode points activation increased during early sharp response (N1) of CCEP. This effect was not present during the later slow-wave (N2).

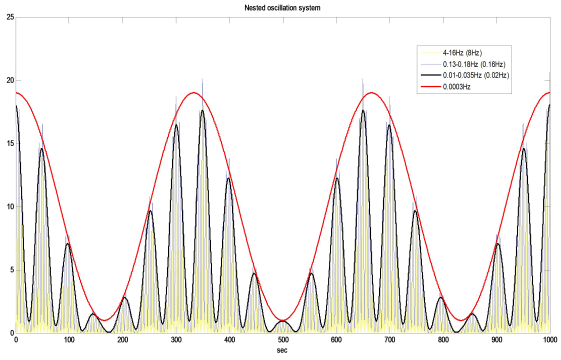

Fig. 4. Simulation results. Schematic drawing of nested oscillations illustrates the theoretical connections between four frequency bands 4-16 Hz (yellow), 0.13-0.16 Hz (blue), 0.01-0.035 Hz (black) and ultraslow (<0.003 Hz) ranges (red).

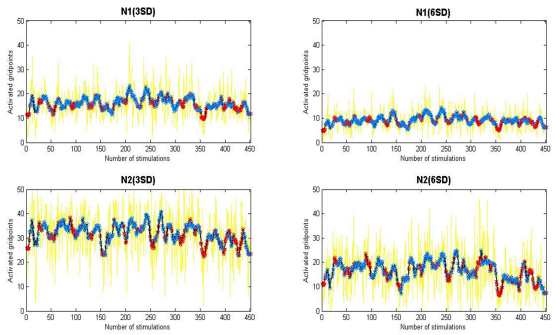

Fig. 5. Nested oscillation and interictal spikes. IEDs were detected manually between stimuli (500-1500 ms after each stimulus epoch) on the unfiltered raw data (in sleep). IEDs (red stars) were increased at the troughs of the 0.01-0.035 Hz oscillations (blue line). 0.13-0.16 Hz (yellow line) is SABAO.

IV. Conclusion

The size of the CCEP area showed 0.01 - 0.035 Hz infraslow oscillation which correlated with the appearance of IEDs. This result questions the usage of averaging method measuring brain connectivity. Further investigation is needed to find the connection between the members of nested oscillations and the occurrence of IEDs.

Statement of originality

This report describes the work of the doctoral student during the academic year 2015/2016. Parts of this work might be under submission to scientific conferences and journals.

Acknowledgements

This work was funded Hungarian Brain Research Program - Grant No. KTIA_13_NAP-A-IV/1,2,3,4,6 EU FP7 Grant No. 600925 NeuroSeeker. We thank Loránd Erőss and László Entz for surgery. We are grateful to Emília Tóth and Zoltán Somogyvári for their comments.

References

[1] Corey J. Keller, Christopher J. Honey, Laszlo Entz, Stephan Bickel, David M. Groppe, Emilia Toth, Istvan Ulbert, Fred A. Lado, and Ashesh D. Mehta, *Corticocortical Evoked Potentials Reveal Projectors and Integrators in Human Brain Networks*, doi: 10.1523/JNEUROSCI.4289-13.2014.

[2] Simo Monto, Satu Palva, Juha Voipio and J. Matias Palva, *Very Slow EEG Fluctuations Predict the Dynamics of Stimulus Detection and Oscillation Amplitudes in Humans*, doi: 10.1523/JNEUROSCI.1910-08.2008.

[3] Stuart W. Hughes, Magor L. Lőrincz, sör, H. Rheinallt Parri and Vincenzo Crunelli, *Infra-slow (<0.1 Hz) oscillations in thalamic relay nuclei: basic mechanisms and significance to health and disease states*, doi: 10.1016/B978-0-444-53839-0.00010-7.

[4] Vanhatalo S, Palva JM, Holmes MD, Miller JW, Voipio J and Kaila K., *Infraslow oscillations modulate excitability and interictal epileptic activity in the human cortex during sleep*, doi: 10.1073/pnas.0305375101.

[5] B. Schack, W. Klimesch and P. Sauseng, *Phase synchronization between theta and upper alpha oscillations in a working memory task*, doi:10.1016/j.ijpsycho.2005.03.016.

[6] A. Valentín, M. Anderson, G. Alarcón, J. J. García Seoane, R. Selway, C. D. Binnie and C. E. Polkey, *Responses to single pulse electrical stimulation identify epileptogenesis in the human brain in vivo*, doi: 10.1093/brain/awf187.

[7] Riki Matsumoto, Dileep R. Nair, Eric LaPresto, Imad Najm, William Bingaman, Hiroshi Shibasaki and Hans O. Lüders, *Functional connectivity in the human language system: a cortico-cortical evoked potential study*, doi: 10.1093/brain/awh246.

[8] P. Lakatos, C.M. Chen, M.N O'Connell, A. Mills, and C.E. Schroeder, *Neuronal Oscillations and Multisensory Interaction in Primary Auditory Cortex*, doi: 10.1016/j.neuron.2006.12.011.

[9] Groppe DM, Bickel S, Keller CJ, Jain SK, Hwang ST, Harden C and Mehta AD, *Dominant frequencies of resting human brain activity as measured by the electrocorticogram*, doi: 10.1016/j.neuroimage.2013.04.044.

[10] Canolty RT, Edwards E, Dalal SS, Soltani M, Nagarajan SS, Kirsch HE, Berger MS, Barbaro NM and Knight RT, *High gamma power is phase-locked to theta oscillations in human neocortex*, doi: 10.1126/science.1128115.

[11] Entz, László and Tóth, Emília and Keller, Corey J. and Bickel, Stephan and Groppe, David M. and Fabó, Dániel and Kozák, Lajos R. and Erőss, Loránd and Ulbert, István and Mehta, Ashesh D., *Evoked effective connectivity of the human neocortex*, doi: 10.1002/hbm.22581.

YOUR NOTES:

Implementation of sample preparation methods for DNA amplification technologies in microfluidic environment

Márton HARTDÉGEN
(Supervisor: Kristóf IVÁN PhD)
Faculty of Information Technology and Bionics, Pázmány Péter Catholic University
50/a Práter street, 1083 Budapest, Hungary
hartdegen.marton@itk.ppke.hu

***Abstract*—In the last decades the miniaturization of bioanalytical processes into microfluidic devices received an increasingly important role in the world. At the Biomicrofluidics Laboratory of Pázmány Péter Catholic University we develop different kind of biological and clinical measurements to Lab-on-a-Chip (LoC) devices. One of the most important research areas is food safety diagnostic rapid test to detect pathogenes on chip.**

The aim of this paper is to demonstrate the implementation of the above mentioned basic sample preparation methods for DNA amplification technologies like Polymerase Chain Reaction (PCR) and Loop-mediated isothermal amplification (LAMP) in microfluidic environment.

At first we summarize the different kinds of food sampling and cell growing methods then the cell lysation and isolation protocols. We present standard purification protocols, fabrication methods, especially laser cutting and soft lithography methods. Furthermore, the basic PCR and LAMP methods in laboratory and microfluidic environment are presented. We summarize the required reagents for LAMP method and we provide an overview of the sample storage technologies in LoC devices.

Finally the validation technologies are highlighted i.e. gel electrophoresis and spectrophotometry.

***Keywords*-Microfluidics; Lab-on-a-Chip; Food-safety; Polymerase Chain Reaction; Loop-mediated isothermal amplification; Gel electrophoresis; Spectrophotometry**

I. Introduction

Pathogen infections are among the leading causes of infirmity and mortality among humans and other animals in the world [**?**]. We are focusing on food-borne illnesses caused by pathogens and one of the most widely known illnesses of these is listeriosis, which is a bacterial infection caused by *Listeria monocytogenes*. *Listeria monocytogenes* is a food-borne pathogen that is widely distributed in both natural and human-made environments. [**?**] Another important bacterium is the enteroinvasive *Escherichia coli* (EIEC) which is an important human pathogen, responsible for the majority of cases of endemic bacillary dysentery prevalent in developing nations [**?**].

Nowadays the detection of these pathogens became an increasingly important role in the world and one possible solution could be the point of care testing LoC devices. [**?**]

In laboratories the basic detection methods are PCR based methods after a some days cell growing procedure therefore to reduce the necessary investigation time, microfluidic devices and point-of-care devices are planned.

Unfortunately the PCR methods have a disadvantage in LoC: the thermal cycling and control system is hard to implement and the process has a very big energy consumption. Notomi et al. developed the loop-mediated isothermal amplification (LAMP) [**?**] what is an isotherm reaction, i.e. in LAMP reaction no thermal cycling control system is needed. Because of the high specificity of the LAMP reaction it is ideal to detect pathogens from food or environmental samples.

Nowadays polydimethylsiloxane (PDMS) and poly(methyl methacrylate) (PMMA) based microfluidic devices are used to make chips for DNA amplification. The PDMS is an excellent material for designing microfluidic devices: optically transparent down to $280\ nm$ so it can be used for a number of detection schemes, nontoxic, can be implanted *in vivo*, it can be deformed reversibly, it can seal reversibly to itself (van der Waals forces), it can seal irreversibly (after exposure to an air plasma by formation of covalent bonds), it is elastometric and it has a high gas solubility. [**?**],[**?**] PMMA has a number of significant advantages: chemical inertness in neutral aqueous solutions, resistance to hydrolysis, non-porous solid, suppresses the contamination effect caused by bimolecular adsorption at the microchannel walls. Another important advantage is that the evaporation rate of PMMA is incomparably smaller than PDMS, [**?**] therefore we can take the advantage of it in sample storage.

The commonly used manufacturing methods for these materials are CO_2 laser micromachining [**?**] and soft lithography. [**?**] Laser cutting technologies are cheaper and faster but compared to the $5-10\ \mu m$ accuracy of the soft lithography procedure the accuracy of laser cutting technology is $100-150\ \mu m$.

In summary the aim of this article is to overview cell growing, lysation and isolation, PCR based and the isothermal amplification methods and validation methods both in laboratory and microfludic environment.

II. Cell growing methods

A. Standard methods

In the case of *Listeria monocytogenes* the bacterium samples were stored under oil in agar slant at $-20°C$. The bacterial culture was inoculated on Tryptone Soya Agar then incubated for 24 hours at $37°C$. After that the culture placed on a new Petri dish for another 24 hours at $37°C$.

Escherichia coli strains are stored in Eppendorf tube at $-80°C$ then inoculated on Luria broth (LB), nutrient-rich and antibiotic free media in petri dish. The plates are incubated at $37°C$ for 15 hours. Next fluid LB media inoculated by the grown bacteria for another 15 hours at $37°C$. After these

M. HARTDÉGEN, "Implementation of sample preparation methods for DNA amplification technologies in microfluidic environment" in *PhD Proceedings Annual Issues of the Doctoral School, Faculty of Information Technology and Bionics, Pázmány Péter Catholic University – 2016.* G. Prószéky, P. Szolgay Eds. Budapest: Pázmány University ePress, 2016, pp 41– 44.

steps the bacterial cultures are ready for lysation and isolation protocols.

B. Selective mediums for Listeria monocytogenes and Escherichia coli

The Fraser broth can selectively and differentially enrich *Listeria* from foods. The standard incubation time is $18-24$ hours at $33-37°C$. After the incubation the broth will turn black because of the released esculetin. [**?**]

Another widely used selective chromogenic medium is the ALOA agar. It is utilized for the detection of *Listeria spp.* in food and environmental samples. The incubation time is 24 hours at 37 $°C$ and the *Listeria* form a blue-green plant with a turbid white zone. [**?**]

The BBL CHROM agar is a selective medium for the isolation, differentiation and identification of *Listeria monocytogenes*, *ivanovii* from food and environmental samples. [**?**] The incubation time is 24 hours at $33-37°C$ and the *Listeria* is blue-green surrounded by a white halo.

The Palcam agar is a selective differential medium for the isolation and detection of *Listeria monocytogenes* and other *Listeria* species from foods and clinical specimens. [**?**] After 18 to 48 hours at $35-37°C$ aerobic incubation the colonies of *Listeria* appear gray-green with a black halo.

In 1989 Curtis et al. described the the Oxford agar, a selective medium for *Listeria monocytogenes*. [**?**] After 18 to 24 hours at $33-37°C$ incubation the colonies of *Listeria spp.* are round in shape, black in color and surrounded by a black zone.

III. Cell lysation and isolation technologies

Generally the nucleic acid sample preparation process consist of two main steps: cell or tissue lysis and nucleic acid extraction or separation. In 2009 Kim et al. reviewed the general sample preparation methods in microfluidic environment. [**?**] Based on this article cell lysis mechanisms in microfluidic environment can be grouped into the following categories: thermal, electrical, mechanical and chemical.

At high temperatures proteins within the cell membrane are denatured, irreparably damaging the cell and releasing the cytoplasmic contents. [**?**] The most common used thermal cell lysis method is the boiling water bath for a predetermined time.[**?**] Be on hand solution can be to take the advantage of the existing PCR heater: Liu et al. used an integrated PCR heating device to implement lysis [**?**]

Another lysation technology is the electrical lysis: depending on the applied electric field the cell can be lysed by dielectric breakdown of the cell membrane. [**?**] Carlo et al. presented a method for on-chip cell lysis based on local hydroxide electro-generation by direct current.[**?**]

Mechanical lysis uses a mechanical force to tear or puncture the cell membrane. Typical physical contact based lysis method is to form microtips in microfluidic channel with soft lithography then force the cells through in this microfluidic channel. [**?**]

Taylor et al. integrate sonication into a microfluidic system and show that increasing the fluid pressure enhances the coupling between the ultrasonic horn tip and the liquid region, which leads to more efficient cell lysis. [**?**]

In chemical lysis buffers or other lytic agents are employed to break down the cell wall and membrane. [**?**] Sethu et al. described a streamline modified process of plasmid extraction based on boiling lysis in case of *Escherichia coli* cultures. [**?**]

After the lysation steps DNA isolation methods are needed. With silicon microfilter chambers cell filtration system were fabricated by Wilding et al. [**?**] This device isolate the white blood cells from whole blood in silicon-glass based microchips with a series of weir-type filters.

IV. DNA Amplification methods in microfluidic environment

A. PCR and isothermal nucleic acid amplifications

The PCR method first presented by R. Saiki et al. in 1985 [**?**] and since then different kind of version was implemented: digital PCR (dPCR) [**?**], in silico PCR [**?**], inverse PCR [**?**], nested PCR [**?**], assembly PCR [**?**], etc.

Further different kind of PCR on microfluidic device were implemented: Chang et al. for an integrated microfluidic chip for PCR [**?**], Hua et al. for multiplexed real-time PCR [**?**] and Beyor et al. for pathogen detection [**?**].

Park et al. summarized the recent advances in microfluidic PCR technologies and showed the practical issues and perspectives related to implementing them into infectious disease diagnostic. [**?**] Furthermore this article showed and summarized the necessary technologies to PCR on LoC: device materials and fabrication, chip design technologies, detection systems, sample preparation, automation and different lysation technologies.

Nucleic acid sequence-based amplification (NASBA) is a primer-dependent isothermal amplification reaction mimicking retrovial RNA replication. [**?**] NASBA has large amplification factor and because of the isothermal property it has a wide range of applications. In 2004 Gulliksen et al. were made a LoC device to detect human papillomavirus (HPV) in $41°C$ heated silicon-glass microchambers. [**?**] In 2008 Dimov et al. published an integrated microfluidic system to isolate, amplificate and real-time detect E. coli RNA with NASBA. [**?**]

Another isothermal amplification method the strand displacement amplification (SDA) that uses the activity of a restriction endonuclease and a strand displacing DNA polymerase to generate copies of a target DNA sequence. [**?**] In 1998 M. A. Burns et al. developed a SDA based LoC device with heaters, temperature sensors and fluorescence detectors to analyze nanoliter-size DNA samples. [**?**] J. M. Yang et al. published an integrated, stacked microlaboratory for performing automated electric-field-driven immunoassays and DNA hybridization assays. The microlaboraty detect *Escherichia coli* bacteria and Alexa-labeled protein toxin staphylococcal enterotoxin B by electric-field-driven immunoassays. [**?**] In 2000 Westin et al. described a simultaneous amplification and discrimination of six gene sequences on a microelectronic chip. The chip can detect both plasmid and transposon gens of *Escherichia coli gyrA, Salmonella gyrA, Campylobacter gyrA, E. coli parC, Staphylococcus mecA* and *Chlamydia cryptic*. [**?**]

The Helicase-Dependent Amplification (HDA) utilizes a NDA helicase to generate single-stranded templates for primer hybridization and subsequent primer extension by a DNA polymerase. This method was described by M. Vincent et al. in 2004. [**?**] and D. Andersen et al. gave an overview on the HDA and OnChip-HDA technology and its potential for point-of-care diagnostics. [**?**]

In 1996 Dongyu Liu et al. described the Rolling Circle Amplification (RCA) what uses strand displacing DNA polymerase to continuously amplify a circular DNA template at a constant low temperature producing a long DNA molecule with tandem repeats of the circular template [**?**]. L. Mahmoudian and N. Kaji developed an integrated platform for RCA and subsequent microchip electrophoretic detection of a specific gene on a PMMA microchip. The device capable to detect $25\ ng$ bacterial genomic DNA in less than $65\ min$. [**?**]

Recombinase polymerase amplification (RPA) was developed by O. Pipenburg et al. which is couples isothermal recombinase-driven primer targeting of template material with strand-displacement DNA synthesis. The developed amplification method is very sensitive, specific, rapid and operate at constant and low ($37°C$) temperature. Further the developed method tested by the pathogen methicillin-resistant *Staphylococcus aureus*. [**?**]

B. Loop-mediated isothermal amplification

In 2000 Notomi et al. developed a novel method, termed LAMP that amplifies DNA with high specificity, efficiency and rapidity under isothermal conditions. Due to the two inner and two outer primers this method amplify the target sequence with high selectivity and the LAMP reaction is easily detectable with naked eye because of a formation of magnesium pyrophosphate. [**?**] Based on this article different kind of pathogen detection method were developed: J. Hill et al. for *Escherichia coli* [**?**], M. Miks-Krajnik et al. and M. Tang et al. for *Listeria monocytogenes* [**?**][**?**] and K. Dhama et al. for the most of the pathogens. [**?**]

X. Fang et al. take the advantages of the LAMP method and designed an integrated microfluidic chip the so called microLAMP (μLAMP). The LAMP reaction can be detect by the naked eye or the designed absorbance based optic sensor and $10\ fg$ of DNA sample could be detected under isothermal conditions ($63°C$).

V. Validation technologies

A. Gel electrophoresis

The gel electrophoresis is a separation and analysis method for DNA, RNA and proteins and their fragments, based on their size and charge. [**?**] The most typically used gels are agarose, polyacrylamide and starch gels. The agarose have a greater range of separation but it has lower resolving power for DNA while the polyacrylamide used for proteins. [**?**] To provide ions that carry a current and to maintain the pH at a relatively constant value buffers are used. The basic buffers for nucleic acids Tris/Acetate/EDTA (TAE) and Tris/Borate/EDTA (TBE). [**?**] The DNA can be visualized using ethidium bromide, silver stain or different types of dyes. The DNA ladder serve as feedback and positive and negative control are used to observe and avoid contamination. To validate the successfulness of the LAMP reaction typically gel electrophoresis is used. [**?**]

B. Spectrophotometry

Spectrophotometry is the quantitative measurement of the reflection or transmission properties of a material as a function of wavelength. [**?**] In standard laboratory environment the validation of pathogen lysation working as follows: The relative absorbance are measured between inoculated fluid LB media and sterile fluid LB media then the lysis puffer were added to the inoculated LB media. After $15\ min$ relative absorbance measured between the sterile fluid LB media and the lysed fluid LB media. The *Listeria monocytogenes* and *Escherichia coli* bacteriums give a signal about $600\ nm$ and after the lysation the proteins, DNA and cell components give signal about $280 - 350\ nm$.

VI. Conclusions

In this paper we showed sample preparation methods for DNA amplification technologies in microfluidic environment. We described the selective cell growing methods and selective mediums for *Listeria monocytogenes* and *Escherichia coli* then the different cell lysis and isolation technologies (thermal, electrical, mechanical and chemical lysation) in microfluidic environment are presented.

We collected and showed DNA amplification methods in microfluidic environment like PCR, NASBA, SDA, HDA, RCA and RPA then the application of LAMP on LoC devices are presented. Finally the necessary and standard laboratory and microfluidic validation methods (gel electrophoresis, spectrophotometry) have been summarized.

Acknowledgements

I would like to thank to my supervisor Kristóf Iván PhD for his continuous help and support further I also want to thank the guidance to András József Laki PhD.

References

[1] Demuth, A., Aharonowitz, Y., Bachmann, T. T., *Pathogenomics: an updated European Research Agenda* Infection, Genetics and Evolution 8.3 386-393 2008.

[2] Farber JM., Peterkin PI., *Listeria monocytogenes, a foodborne pathogen* Microbiol Rev 55:476-511 1991.

[3] Tianyan Song, Caludia Toma, Noboru Nakasone, Masaaki Iwanaga, *Sensitive and rapid detection of Shigella and enteroinvasive Escherichia coli by a loop-mediated isothermal amplification method* FEMS Microbiology Letters 243.1 259-263 2005.

[4] Sista, Ramakrishna, et al. *Development of a digital microfluidic platform for point of care testing* Lab on a chip 8.12 2091-2104 2008.

[5] Notomi, Tsugunori, et al. *Loop-mediated isothermal amplification of DNA* Nucleic acids research 28.12 e63-e63 2000.

[6] Anderson, Janelle R. et al., *Fabrication of microfluidic systems in poly(dimethylsiloxane)* Electrophoresis 21.1 27-40 2000.

[7] Liang, David Y. et al, *Systematic characterization of degas-driven flow for poly(dimethylsiloxane) microfluidic devices* Biomicrofluidics 5.2 024108 2011.

[8] Houaria Bourbaba, Chellali Ben achaiba, Bouanini Mohamed, *Mechanical behavior of polymeric membrane: comparison between PDMS and PMMA for microfluidic application* Energy Procedia 36 231-237 2013.

[9] Klank, Henning, Jörg P. Kutter and Oliver Geschke *CO_2 laser micromachining and back-end processing for rapid production of PMMA-based microfluidic systems* Lab on a Chip 2(4) 242-246 2002.

[10] Whitesides, George M., et al. *Soft lithography in biology and biochemistry* Annual review of biomedical engineering 3.1 335-373 2001.

[11] Ágnes Belák, Gabriella Kiskó, Mónika Kovács, Anna Maráz *Gyors és molekuláris biológiai módszerek alkalmazása élelmiszerek mikrobiológiai vizsgálatára* Nemzeti Tankönyvkiadó 2011.

[12] Vlaemynck, G., V. Lafarge and S. Scotter *Improvement of the detection of Listeria monocytogenes by the application of ALOA, a diagnostic, chromogenic isolation medium* Journal of Applied Microbiology 88.3 430-441 2000.

[13] Odumeru, Joseph A., Veena Hedge, and C.G. Velarde *Evaluation of New BBL CHROM agar Listeria for Isolation of Listeria monocytogenes in Foods* Annual International Association for Food Prot. Meeting, Baltimore Vol. 92. 2005.

[14] Van Netten, P., Perales I., et al. *Liquid and solid selective differential media for the detection and enumeration of L. monocytogenes and other Listeria spp.* International journal of food microbiology 8.4 299-316 1989.

[15] Curtis, G. D. W., Mitchell R.G., et al. *A selective differential medium for the isolation of Listeria monocytogenes* Letters in applied microbiology 8.3 95-98 1989.

[16] J. Kim, M. Johson, P. Hill and B. K. Gale *Microfluidic sample preparation: cell lysis and nucleic acid purification* Integrative Biology vol. 1, no. 10, 574-586 2009.

[17] K. Zhu, H. Jin, Y. Ma, Z. Ren, C. Xiao et al. *A continuous thermal lysis procedure for the large-scale preparation of plasmid DNA* Journal of biotechnology vol. 118, no. 3 257-264 2005.

[18] R. H. Liu, J. Yang, R. Lenigk, J. Bonanno and P. Grodzinski *Self-contained, fully integrated biochip for sample preparation, polymerase chain reaction amplification, and DNA microarray detection* Analytical chemisry 76.7 1824-1831 2004.

[19] S. W. Lee and Y. C. Tai *A micro cell lysis device* Sensors and Actuators vol. 73, no. 1 74-79 1999.

[20] D. Di Carlo, C. Ionescu-Zanetti, Y. Zhang, P. Hung and L. P. Lee *On-chip cell lysis by local hydroxide generation* Lab on a Chip vol. 5, no. 2 171-178 2005.

[21] D. Di Carlo, K. H. Jeong and L. P. Lee *Reagentless mechanical cell lysis by nanoscale barbs in microchannels for sample preparation* Lab on a Chip vol. 3, no. 4 287-291 2003.

[22] M. T. Taylor, P. Belgrader, B. J. Furman, F. Pourahmadi, g. T. Kovacs and M. A. Northrup *Lysing bacterial spores by sonication through a flexible interface in a microfluidic system* Analytical chemistry vol. 73, no. 3 492-496 2001.

[23] P. Sethu, M. Anahtar, L. L. Moldawer, R. G. Tompkins and M. Toner *Continuous flow microfluidic device for rapid erythrocyte lysis* Analytical chemistry vol. 76, no. 21 6247-6253 2004.

[24] Wilding, Peter, et al. *Integrated cell isolation and polymerase chain reaction analysis using silicon microfilter chambers* Analytical biochemistry 257.2 95-100 1998.

[25] Saiki, Randall K., et al. *Enzymatic amplification of beta-globin genomic sequences and restriction site analysis for diagnosis of sickle cell anemia* Science 230.4732 1350-1354 1985.

[26] Fan, H. Christina, and Stephen R. Quake *Detection of aneuploidy with digital polymerase chain reaction* Analytical chemistry 79.19 7576-7579 2007.

[27] San Millán, Rosario M., et al. *Online exercise for the design and simulation of PCR and PCR-RFLP experiments* BMC research notes 6.1 513 2013.

[28] Ochman, Howard, Anne S. Gerber, and Daniel L. Hartl. *Genetic applications of an inverse polymerase chain reaction* Genetics 120.3 621-623 1988.

[29] Garson, J. A., et al. *Detection of hepatitis C viral sequences in blood donations by "nested" polymerase chain reaction and prediction on infectivity* The Lancet 335.8703 1419-1422 1990.

[30] Stemmer, Willem PC, et al. *Single-step assembly of a gene and entire plasmid from large numbers of oligodeoxyribonucleotides* Gene 164.1 49-53 1995.

[31] Chang, Yi-Hsien, et al. *Integrated polymerase chain reaction chips utilizing digital microfluidics* Biomedical microdevices 8.3 215-225 2006.

[32] Hua, Zhishan, et al. *Multiplexed real-time polymerase chain reaction on a digital microfluidic platform* Analytical chemistry 82.6 2310-2316 2010.

[33] Beyor, Nathaniel, et al. *Integrated capture, concentration, polymerase chain reaction, and capillary electrophoretic analysis of pathogens on a chip* Analytical chemistry 81.9 3523-3528 2009.

[34] Park, Seungkyung, et al. *Advances in microfluidic PCR for point-of-care infectious disease diagnostics* Biotechnology advances 29.6 830-839 2011.

[35] Compton, Jean *Nucleic acid sequence-based amplification* Nature 350.6313 91-92 1991.

[36] Gulliksen, Anja, et al. *Real-time nucleic acid sequence-based amplification in nanoliter volumes* Analytical chemistry 76.1 9-14 2004.

[37] Dimov, Ivan K., et al. *Integrated microfluidic tmRNA purification and real-time NASBA device for molecular diagnostics* Lab on a Chip 8.12 2071-2078 2008.

[38] Walker, G. Terrance, et al. *Isothermal in vitro amplification of DNA by a restriction enzyme/DNA polymerase system* Proceedings of the National Academy of Sciences 89.1 392-396 1992.

[39] Burns, Mark A., et al. *An integrated nanoliter DNA analysis device* Science 282.5388 484-487 1998.

[40] Yang, Joon Mo, et al. *An integrated, stacked microlaboratory for biological agent detection with DNA and immunoassays* Biosensors and Bioelectronics 17.6 605-618. 2002.

[41] L. Westin, C. Miller, et al. *Antimicrobial resistance and bacterial identification utilizing a microelectronic chip array* Journal of clinical microbiology 39.3 1097-1104 2001.

[42] Vincent, Myriam, Yan Xu and Huimin Kong *Helicase-dependent isothermal DNA amplification* EMBO reports 5.8 795-800 2004.

[43] Andresen, Dennie, Markus von Nickisch-Rosenegk, and Frank F. Bier *Helicase-dependent amplification: use in OnChip amplification and potential for point-of-care diagnostics* Expert review of molecular diagnostics 9.7 645-650 2009.

[44] Liu, Dongyu, et al. *Rolling circle DNA synthesis: small circular oligonucleotides as efficient templates for DNA polymerases* Journal of the American Chemical Society 118.7 1587-1594 1996.

[45] Mahmoudian, Laili, et al. *Rolling circle amplification and circle-to-circle amplification of a specific gene integrated with electrophoretic analysis on a single chip* Analytical chemistry 80.7 2483-2490 2008.

[46] Piepenburg, Olaf, et al. *DNA detection using recombination proteins* PLoS Biol 4.7 e204 2006.

[47] Hill, Joshua, et al. *Loop-mediated isothermal amplification assay for rapid detection of common strains of Escherichia coli* Journal of Clinical Microbiology 46.8 2800-2804 2008.

[48] Miks-Krajnik, Marta, et al. *Loop-mediated isothermal amplification (LAMP) coupled with bioluminescence for the detection of Listeria monocytogenes at low levels on food contact surfaces* Food Control 60 237-240 2016.

[49] Tang, Meng-Jun, et al. *Rapid and sensitive detection of Listeria monocytogenes by loop-mediated isothermal amplification* Current microbiology 63.6 511-516 2011.

[50] Dhama, Kuldeep, et al. *Loop-mediated isothermal amplification of DNA (LAMP): A new diagnostic tool lights the world of diagnosis of animal and human pathogens: A review* Pakistan Journal of Biological Sciences 17.2 151 2014.

[51] Fang, Xueen, et al. *Loop-mediated isothermal amplification integrated on microfluidic chips for point-of-care quantitative detection of pathogenes* Analytical chemistry 82.7 3002-3006 2010.

[52] Kryndushkin, Dmitry S., et al. *Yeast [PSI+] prion aggregates are formed by small sup35 polymers fragmented by Hsp104* Journal of Biological Chemistry 278.49 49636-49643 2003.

[53] Weber, Klaus, and Mary Osborn *The reliability of molecular weight determinations by dodecyl sulfate-polyacrylamide gel electrophoresis* Journal of Biological Chemistry 244.16 4406-4412 1969.

[54] Brody, Jonathan R., and Scott E. Kern *History and principles of conductive media for standard DNA electrophoresis* Analytical biochemistry 333.1 1-13 2004.

[55] Allen, D., C. Cooksey and B. Tsai *Spectrophotometry* The National Institute of Standards and Technology (NIST) 2010.

Dynamic simulation of the third PDZ domain of PSD-95

Anett HINSENKAMP
(Supervisor: Dr. Zoltán GÁSPÁRI)
Pázmány Péter Catholic University, Faculty of Information Technology and Bionics
50/a Práter street, 1083 Budapest, Hungary
hinsenkamp.anett@itk.ppke.hu

***Abstract*—The PDZ domain containing PSD-95 is a key protein in organizing in the postsynaptic density. The third PDZ domain of PSD-95 has an additional alpha helix, which affects its binding affinity to the CRIPT peptide, believed to result from an intermolecular allosteric mechanism. Detailed description of internal dynamics of proteins is essential for understanding the mechanistic details of partner molecule binding and allostery. Ensemble-based models incorporating experimental data can be used for atomic-level representation of the observed conformational dynamics. I performed ensemble-restrained molecular dynamics simulations with mobility parameters derived from relaxation data to create protein ensembles of the third PDZ domain of PSD-95. Exploratory calculations on selected PDZ3 variants and their complexes with different restraining schemes were applied and analyzed. The results can be used to generate ensembles that give insights into the role of residue-residue interactions and conformational entropy in ligand binding and selectivity.**

***Keywords*-PSD-95; structural ensemble; molecular dynamics**

I. Introduction

The underlying molecular mechanisms of synaptic plasticity are not yet fully understood. The generation of long term potentiation (LTP) is thought to be a major step in the formation of memory. The precise steps leading to LTP are known to involve the reorganization of the postsynaptic density (PSD), an elaborate protein network characteristic of exctitatory synapses. Exactly how the PSD is organized and reorganized is subject to intensive research. Novel findings continue to challenge accepted models, for example, the requirement for the GluA1 subunit has been refuted as other subunit types available can take over its supposed role.[1] Therefore, detailed study of PSD proteins and their interactions are of crucial importance.

The PSD contains a number of proteins harboring a so-called PDZ domain (the name comes from those of three proteins where it was first identified: PSD95,DLG1,ZO-1) 1. PDZ domains are though to be key organizers of the PSD network as they mediate protein-protein interactions [2], [3], [4]. Their most prominent role is to bind C-terminal residues of partner proteins but a number of other interaction modes have also been identified [5], [6]. PDZ domains are approximately 90 amino acid long, adopt a globular structure of 5-6 beta sheets forming a half barrel and 2 helices on each side 2.[2], [3], [4], [7]

PSD-95 (Postsynaptic protein 95, also DLG4) is one of the most intensively studied PDZ domain containing protein in the PSD. It consists of 3 PDZ domains as wel as, a SH3 and a GK domain. It organizes signaling complexes at the postsynaptic membrane and it is thought to have a major role in many other processes of the PSD, like regulating the activity of the

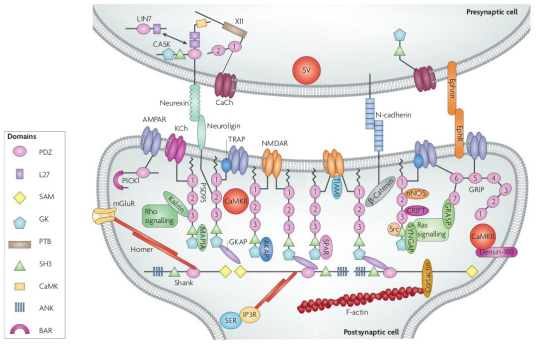

Fig. 1. Regulating complexes of the postsynaptic density, with focus on the PDZ containing proteins.[2]

interacting membrane proteins.[3] PSD-95 has been proposed to form a flexible matrix which confers stability to the PSD while allowing its dynamic reorganization [8]. The number of PSD-95 molecules correlates with the size of the PSD, consistent with a model based on fixed-distance packing of these molecules in mature PSDs, although PSD enlargement upon stimulation seems to be governed by other proteins and PSD-95 molecules appear to be included only at a later stage [9]. There have been multiple models proposed for the di- and multimerization mode of PSD95, most recently, by the means of PDZ domain-mediated interactions with partner molecules [10], which might be the only one reconcilable with the in vivo observed spacing of PSD-95 molecules [8], reasonably coinciding with but not necessarily governed by their size.

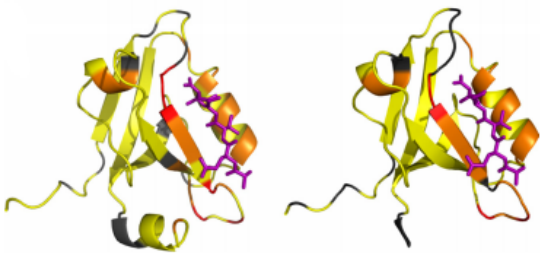

Fig. 2. The full PDZ3 domain of PSD-95 in complex with CRIPT peptide (left). PDZ3's C-terminally truncated form (PDZ3 d7ct) in complex with CRIPT peptide. Although PDZ3 d7ct does not form a third alpha helix it has the conventional PDZ fold.[7]

The third PDZ domain of PSD-95 (PDZ3, 303-402) has an "extra" alpha helix not commonly found in other PDZ domains at its carboxy terminus. Although this helix does not form direct contacts with the peptide ligand, a C-terminally truncated construct of PDZ3 (PDZ3 d7ct) binds the CRIPT

A. HINSENKAMP, "Dynamic simulation of the third PDZ domain of PSD-95" in *PhD Proceedings Annual Issues of the Doctoral School, Faculty of Information Technology and Bionics, Pázmány Péter Catholic University – 2016.* G. Prószéky, P. Szolgay Eds. Budapest: Pázmány University ePress, 2016, pp 45– 46.

partner peptide with a 21-fold lower affinity than the wild type variant.2 The changes in the binding affinity were attributed to the presence of entropic contributions resulting from an intramolecular allostery involving the extra helix and the ligand binding pocket. In this experiment isothermal titration calorimetry was used to evaluate the thermodynamical changes. Backbone and side-chain order parameters characteristic of picosecond-nanosecond (ps-ns) motions were obtained from NMR spin relaxation experiments.[7] My aim was to generate detailed atomic-level structural models that reflect the experimentally determined mobility of the free and ligand bound-states of PDZ3 variants. These models can help in establishing the mechanistic details behind the allosteric behaviour of the domain.

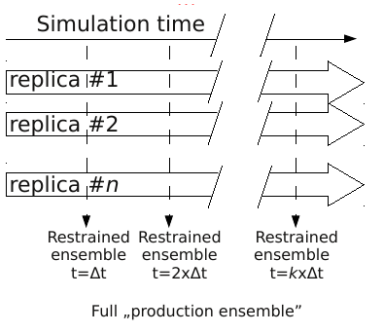

Fig. 3. Procedure of structural ensemble selection from the molecular dynamic simulation.[13]

II. Methods

For the generation of protein structural ensembles I performed ensemble-restrained molecular dynamics simulations using a modified version of the free GROMACS.4.5.5. Package [11]. In this context, the experimental restraints ensure that the ensemble corresponds to the observed dynamics as much as possible and the applied amber99sb-ildn force field is responsible for sampling physically reasonable conformations to achieve this. The initial structures were X-ray structures from the PDB database (ids:1be9,1bfe)[12]. The restrained production run is preceded by a minimization and solvation steps as well as a position restrained equilibration. S2 order parameters were applied in a so-called half-harmonic scheme ensuring that the fluctuations are only allowed to bring the system closer to the experimentally observed parameters.3

I have performed a number of exploratory simulations with different restraining parameters and have evaluated the resulting ensembles using the CoNSEnsX method [14]4.

These calculations will be used to select the parameter sets to be applied for longer production runs. The resulting ensembles will be compared and analyzed in detail.

Acknowledgements

The author would like to thank her supervisor Dr. Gáspári Zoltán for his guidance and support.

References

[1] Adam J. Granger, Yun Shi, Wei Lu, Manuel Cerpas and Roger A.Nicoll, 'LTP requires a reserve pool of glutamate receptors independent of subunit type', *Nature*, Volume 493, Pages 495-500, 2013.

[2] Wei Feng and Mingjie Zhang, 'Organization and dynamics of PDZ domain related supramodules int he postsynaptic density', *Nature Reviews Neuroscience*, Volume 10, Pages 87-99, 2009.

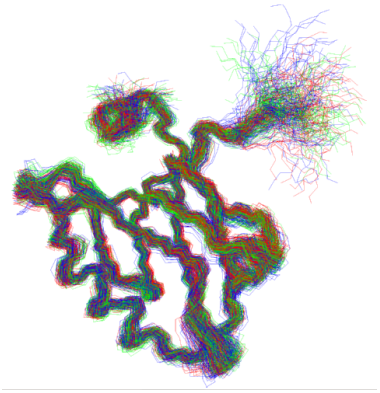

Fig. 4. Generated ensemble of the free, full form of PDZ3

[3] Eunjoon Kim and Morgan Sheng, 'PDZ domain proteins os synapses' *Nature Reviews Neuroscience*, Volume 5, Pages 771-781, 2004.

[4] Alan S. Fanning and James Melvin Anderson, 'Protein-protein interactions: PDZ domain networks', *Current Biology*, Volume 6, Number 11, Pages 1385-1388, 1996.

[5] Ylva Ivarsson, 'Plasticity of PDZ domains in ligand recognition and signaling', *FEBS Letters*, Volume 586, Pages 2638-2647, 2012

[6] Katja Luck, Sebastian Charbonnier and Gilles Travé, 'The emerging contribution of sequence context to the specificity of protein interactions mediated by PDZ domains', *FEBS Letters*, Volume 586, Pages 2648-2661, 2012.

[7] Chad M. Petit, Jun Zhang, Paul J. Sapienza, Ernesto J. Fuentes and Andrew L. Lee, 'Hidden dynamic allostery in a PDZ domain', *PNAS*, Valume 106, Number 43, Pages 18249-18254, 2009.

[8] Thomas A. Blanpied, Justin M. Kerr and Michael D. Ehlers, 'Structural plasticity with preserved topology in the postsynaptic protein network' *PNAS*, Volume 105, Pages 12587-12592, 2008.

[9] Harold D. MacGillavry, Yu Song, Sridhar Raghavachari, Thomas A. Blanpied, 'Nanoscale scaffolding domains within the postsynaptic density concentrate synaptic AMPA receptors', *Neuron*, Volume 78, Pages 615-622, 2013.

[10] Nils Rademacher, Stella-Amrei Kunde, Vera M. Kalscheuer, Sarah A. Shoichet, 'Synaptic MAGUK multimer formation is mediated by PDZ domains and promoted by ligand binding' *Chem Biol* Volume 20, Pages 1044-1054. 2013.

[11] B. Hess, C. Kutzner, D. van der Spoel, and E. Lindahl, 'Gromacs 4: algorithms for highly efficient, load-balanced, and scalable molecular simulation', *Journal of Chemical Theory and Computation*, Volume 4, Pages 435-447, 2008.

[12] Doyle,D.A., Lee,A., Lewis,J., Kim,E., Sheng,M., MacKinnon,R., 'Crystal structures of a complexed and peptide-free membrane protein-bindig domain: molecular basis of peptide recognition by PDZ', *Cell* Volume 85, Pages 1067-1076, 1996.

[13] Annamária F. Ángyán and Zoltán Gáspári, 'Ensemble-Based Interpretations of NMR Structural Data to Describe Protein Internal Dynamics', *Molecules*, Volume 18, Pages 10548-10567, 2013.

[14] A.F.Ángyán, B. Szappanos, A. Perczel and Z. Gáspári, 'Consensx: an ensemble view of protein structures and nmr-derived experimental data', *BMC Structural Biology*, Volume 10 2010.

Modelling the effects of internally produced antibiotics in multispecies bacterial communities

János JUHÁSZ
(Supervisor: Dr. Sándor PONGOR)
Pázmány Péter Catholic University, Faculty of Information Technology and Bionics
50/a Práter street, 1083 Budapest, Hungary
janos.juhasz@itk.ppke.hu

***Abstract*—The composition of multispecies microbial communities can be stable even though the members of these systems use the same environmental resources. Secreted chemical compounds can have an important role in stabilizing complex bacterial communities. The effects of these compounds can be either positive or negative for the neighboring cells. My aim was to study the impact of these negative (so-called antimicrobial) factors on the stability of multispecies communities via *in silico* simulations. The experiments were performed in a hybrid computational model which is able to simulate the quorum sensing mediated swarming behavior of bacteria. The bacterial cells are represented as discrete agents and the chemical signals, factors and nutrients are considered as diffusible gradients in the model. The results show that cell populations sharing at least their factor molecules can form stable multispecies communities, even in case of antimicrobial factors are involved in their interactions. This finding can help to model and better understand the complex dynamics of diverse natural microbial communities.**

***Keywords*-microbiome stability; quorum sensing; multispecies communities; antibiotic production; agent-based model**

I. Introduction

Bacteria are the most widespread life forms on Earth, although they are unicellular and of micrometer size. They populate every habitat, including the surfaces of the human body, which holds more prokaryotes than human cells. In most cases bacterial cells form communities that consist of many species. Most of these bacteria are not pathogenic, and even play an important role in conditioning the immune system, producing important substances for the host (e.g. amino acids or vitamins) and serve as a first barrier against pathogens [1].

Members of complex microbial communities, for example human gut flora, interact with each other, despite competition for resources like nutrients and/or habitats. Cooperative behavior is therefore essential for stable and permanent coexistence between cells. One way of inter-cellular bacterial cooperation is quorum sensing, where bacteria produce and respond to diffusible chemical signal molecules and regulate cellular metabolism in a concentration-based manner [2]. Cells constantly produce signal molecules and if cell density is low, the overall signal concentration that every cell can sense around itself is also low. However, in the event of high cell density, the signal concentration reaches a threshold which induces changes in the regulation and behavior of all cells simultaneously. For example, cells start to produce chemical compounds (so-called factors) that act only in a concentration that can be achieved with the contribution of a given number of cells [2][3].

There are multiple different quorum sensing systems used by different bacterial strains. These strains are often fully or partially able to sense or respond to signal and factor molecules from other species, which could influence the nature of their interactions [4]. This phenomenon can be termed as the sharing of resources or public goods (signals, factors or nutrients) [5]. However, the interactions between microbes are not always beneficial. Many bacteria (and fungi) produce materials that have negative effects on other species. These materials are called antimicrobial factors, they are related to natural antibiotics, but the purpose of their production is not always eliminating others in order to get more nutrient or habitat, sometimes it is only a useful side effect [6].

It is still not completely understood why bacteria respond to different chemical compounds in different manners, and how this phenomenon affects the coexistence of species, as well as the stability of the community under different circumstances. In order to study these I used an *in silico* agent-based computational model of quorum sensing controlled swarming (synchronized movement of group members) implemented in MATLAB programming language.

II. The Model

For studying the effects of self-restraint and sharing of public goods, we used a previously developed model of quorum sensing (QS) mediated swarming [2][7][4]. Bacterial cells are represented in this model as random moving computational agents who produce, release, uptake and respond to diffusible signals (S) and factors (F), and also uptake and consume nutrients (N) from their environment. They are placed on the end of a 2 dimensional half-closed longitudinal track with a periodic boundary condition on its two sides. When the concentration of a signal reaches its threshold, the cells that can sense it modify their metabolism and increase their signal production and start factor production. If the appropriate factor concentration is achieved, the cells enter their swarming state, resulting in increased movement, nutrient consumption, signal and factor production. Swarming cells can extend the colony boundaries and populate fields of the track with high nutrient concentration, while cells that move slower starve and become eliminated in the nutrient depleted environment. This modeling setup is a simplified representation of a dendrite growing from a bacterial colony (e.g. *Pseudomonas aeruginosa*) placed on an agar plate (Figure 1).

I introduced antibiotics (AB) in this model, because in natural communities species can protect themselves by producing chemical compounds against the proliferation of other species to reduce their fitness [8]. In other words, our previous QS models concentrated only cells positively acting on each other (cooperation); here I included negative effects by which cells can down-regulate other cells in their neighborhood. Antibiotics were defined as diffusible materials, like signals

J. JUHÁSZ, "Modelling the effects of internally produced antibiotics in multispecies bacterial communities" in *PhD Proceedings Annual Issues of the Doctoral School, Faculty of Information Technology and Bionics, Pázmány Péter Catholic University – 2016.* G. Prószéky, P. Szolgay Eds. Budapest: Pázmány University ePress, 2016, pp 47– 50.

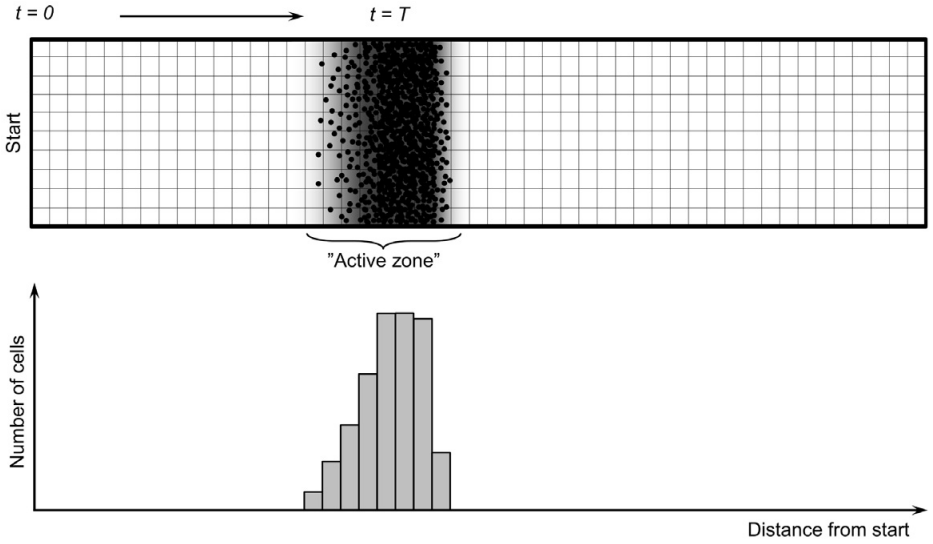

Fig. 1. Principle of the model [2][7]. Bacterial agents (black dots) are placed in a longitudinal two dimensional track, which is covered with nutrients. The cells consume nutrients and can produce diffusible signal and factor compounds around themselves (gray area). The gradients of these materials enable them to switch into their active state and swarm to nutrient rich regions from the starting point. The region where most swarming cells are situated and the concentrations of public goods are high is called the active or swarming zone.

and factors. Cells started AB production when they sensed the presence of bacteria from other species, through their own signals. Two scenarios were considered as the effect of the antibiotics: in the first one the cells that sense the AB above a given threshold could not swarm and "stepped back" to their stationary (baseline) state; while based on the second one living in high AB concentration required extra energy. AB production could also have an energy cost compensating the fitness benefit of these cells. Other ways of compensating the advantage of AB producer cells are increasing their metabolic energy or division threshold. In that simulation setup, each agent could produce or react to this new gradient which has resulted in doubling their internal states from the previous 4 to 8 (Table I), and swarming was not defined as producing a high amount of signals and factors, but as moving with maximal speed. The effects of antibiotics production on community stability were studied with 2 species simulations considering the fitness of species, the compensation of benefits that are due to AB production, and the connection between their quorum sensing systems (common, partially or fully different).

III. Results

In the experiments without self-restraint and AB production the results agreed with observations from a previous study [4], where at least factor sharing was necessary for stable coexistence. If the chemical language of the cells is common, the ones with higher fitness (e.g. lover division energy threshold or lower metabolic energy) extrude the others, but this advantage can be compensated, for example by modifying the signal threshold. In this case stable coexistence can arise between species using the same signals and public goods.

Species that consume the same nutrient source and use different signals and factors cannot live together, and applying antibiotics production does not change this behavior. The species with higher fitness populate the entire swarming zone. Antibiotic molecules do not change the behavior of the system. AB producer cells win the competition and eliminate others if the energy requirement of AB production is not too high. The competition advantage of AB production can be reduced by applying higher metabolic or division energy threshold or higher AB production cost for the AB producers or higher AB sensing threshold for the responders. The fitness of the species can be equalized with these modifications. It can result in temporal coexistence and then stochastic exclusion, which is analogous with previous findings [4].

Same factor usage enables stable coexistence, and it can also be achieved with AB production when the AB producer cells have some "metabolic handicap". The two scenarios for the effect of the antibiotics produce different communities. If living with AB requires extra energy form the AB uptaker cells, these cells will not exceed the concentration when their signal concentration starts to trigger AB production. That AB model results in a stable population, where most of the cells are not affected in antimicrobial factor production or response. If AB concentration "pushes back" the respondent cells to their stationary, ground state when they cannot swarm, many cells produce or respond to AB during the entire simulation (Figure 2). In this case, the fitter (respondent) cells cannot exceed a concentration and extrude less fit AB producers, because the latter ones can end their swarming with the produced chemical compounds. The ground state cells move slower and produce a smaller amount of signals. Their high concentration is situated in the back of the swarming zone, but there are some cells in the front or in the middle part. They divide faster due to their energetic advantage, and reach the AB production threshold again soon.

IV. Discussion

Different bacterial species often use different quorum sensing signaling systems, and also often produce antibiotics (antimicrobial factors) against each other. I introduced these antimicrobial factors in the model, which resulted in more intensive competition between cell types. Antibiotics provide an advantage for the producer cells, but it can be compensated and enables the stable coexistence between species with at least shared factors. The results above showed that we can simulate direct inhibitory microbial interactions with our model, and

TABLE I

THE POSSIBLE STATES OF AB PRODUCER AND AB RESPONDER AGENTS. AB PRODUCER CELLS CAN PRODUCE THEIR OWN SIGNAL (S1), FACTOR (F1) AND ANTIBIOTICS (AB) AND CAN SENSE THEIR OWN SIGNAL, FACTOR AND THE SIGNAL OF THE OTHER SPECIES (S2). AB RESPONDER CELLS CAN PRODUCE THEIR OWN SIGNAL (S2) AND FACTOR (F2) AND CAN SENSE THEIR OWN SIGNAL, FACTOR AND THE AB OF THE OTHER SPECIES.

state	AB producer			AB responder		
	produce	sense	behavior	produce	sense	behavior
1	baseline S1	-	stationary state	baseline S2	-	stationary state
2	S1+F1	S1	stationary state	S2+F2	S2	stationary state
3	S1	F1	stationary state	S2	F2	stationary state
4	S1+F1	S1+F1	swarming	S2+F2	S2+F2	swarming
5	baseline S1 +AB	S2	stationary state	baseline S2	AB	stationary state + AB response
6	S1+F1 +AB	S1+S2	stationary state	S2+F2	S2+AB	stationary state + AB response
7	S1 +AB	F1+S2	stationary state	S2	F2+AB	stationary state + AB response
8	S1+F1 +AB	S1+F1+S2	swarming	S2+F2	S2+F2+AB	swarming + AB response

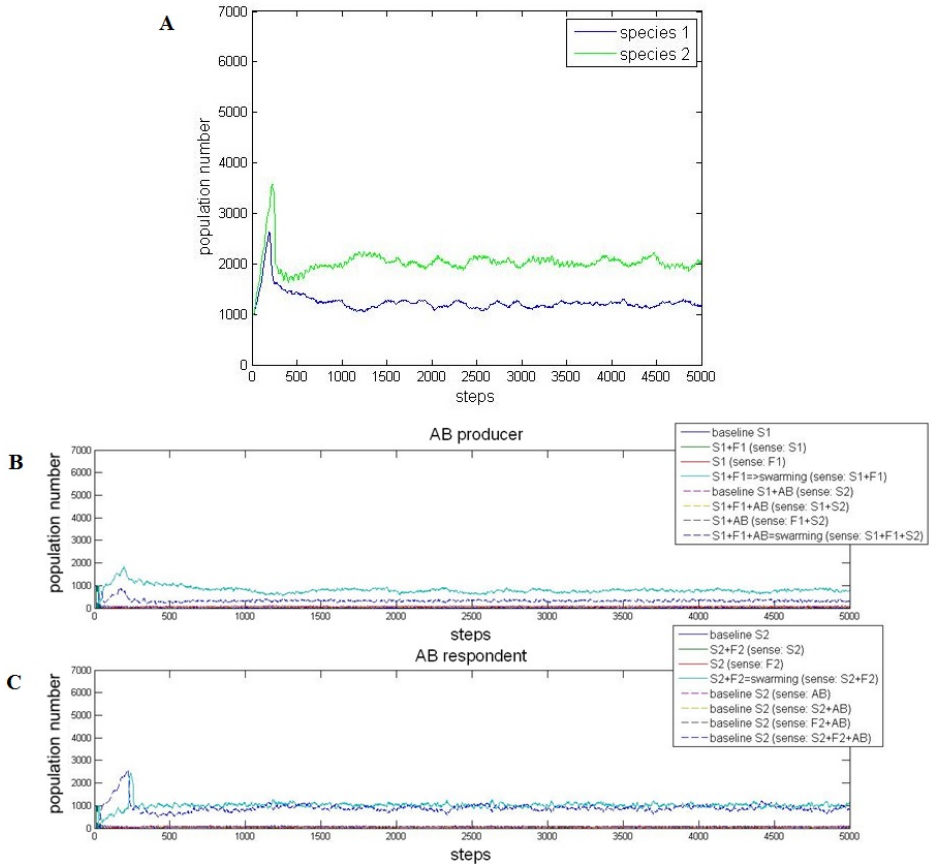

Fig. 2. Stable coexistence in two species community where the species have different signals but same factors, and one species produces AB against the other one (initial cell numbers were 1000-1000 agents for both species, and the simulation time was 5000 steps). The AB producer cells use self-restraint, they have higher metabolic energy (0.15) than the others, and AB production also has an energy cost (0.15). The threshold of AB production is 30, and the cells that respond to the AB step back to their stationary ground state and cannot swarm. A: Numbers of cells in each species during the simulation. B: Distribution of states during the simulation for cells capable of AB production. C: Distribution of states during the simulation for cells capable of responding to AB.

our qualitative results agree with previous findings and basic biological expectations.

As this is an *in silico* study, some limitations of the modeling approach have to be noted. First of all, the used parameters in the agent-based model are symbolic. They are not based on physical measurements. Consequently, the outcomes are qualitative, represent tendencies and possibilities, not exact biological events in case of a given parameter set. Second, the model uses several simplifications which are not capable of describing the complexity of interactions between the members of natural microbial communities. For example, systems were studied with only two species while natural microbiomes contain more kinds of bacteria, viruses, fungi and eukaryotes. The nutrient supply of the cells was also simplified: only one nutrient type was applied, which diffused in the medium uniformly and constantly while in the nature cells can access multiple nutrient types and can uptake and consume them with different metabolic efficiency.

In spite of all these, the implemented methodological development in the quorum sensing model makes it possible to simulate more complex systems, and answer questions that have closer connection with the natural microbial communi-

ties.

ACKNOWLEDGEMENTS

This project was developed in the Faculty of Information Technology and Bionics, Pázmány Péter Catholic University, Budapest. Thanks are due to my supervisor, Prof. Sándor Pongor as well as Dóra Bihary and Ádám Kerényi, who were the previous developers of the quorum sensing model. Furthermore, I would like to thank Dr. Nóra Wenszky and Ms. Hanni Thoma for their remarks about the language and style of this paper.

REFERENCES

[1] F. Guarner and J. R. Malagelada, "Gut flora in health and disease," *Lancet*, vol. 361, no. 9356, pp. 512–519, 2003.

[2] S. Netotea, I. Bertani, L. Steindler, V. Venturi, S. Pongor, and A. Kerenyi, "A simple model for the early events of quorum sensing in Pseudomonas aeruginosa: modeling bacterial swarming as the movement of an "activation zone"," *Biol Direct*, vol. 4, p. 6, 2008.

[3] L. Steindler, I. Bertani, L. De Sordi, S. Schwager, L. Eberl, and V. Venturi, "LasI/R and RhlI/R quorum sensing in an environmental strain of Pseudomonas aeruginosa," *submitted*, vol. 75, pp. 5131–5140, 2009.

[4] Á. Kerényi, D. Bihary, V. Venturi, and S. Pongor, "Stability of Multispecies Bacterial Communities: Signaling Networks May Stabilize Microbiomes," *PLoS ONE*, vol. 8, p. e57947, mar 2013.

[5] A. Ross-Gillespie, A. Gardner, A. Buckling, S. A. West, and A. S. Griffin, "Density Dependence and Cooperation: Theory and a Test With Bacteria," *Evolution*, vol. 63, no. 9, pp. 2315–2325, 2009.

[6] A. Bryskier, ed., *Antimicrobial Agents: Antibacterials and Antifungals*. Washington DC: American Society of Microbiology Press., 2005.

[7] V. Venturi, I. Bertani, A. Kerenyi, S. Netotea, and S. Pongor, "Co-swarming and local collapse: quorum sensing conveys resilience to bacterial communities by localizing cheater mutants in Pseudomonas aeruginosa," *PLoS ONE*, vol. 5, p. e9998, 2010.

[8] K. Todar, *Online Textbook of Bacteriology*. 2008.

The effect of $GABA_A$ receptor antagonist Bicuculline on human neocortex in vitro

Ágnes KANDRÁCS
(Supervisor: István ULBERT)
Pázmány Péter Catholic University, Faculty of Information Technology and Bionics
50/a Práter street, 1083 Budapest, Hungary
kandracs.agnes@itk.ppke.hu

***Abstract*—Background. Epilepsy is a neurological disorder, caused by the abnormal and excessive activity of the brain.**

Aims.The aim of the studies reported here was to observe the cellular properties of the epileptic human neocortex, especially under the effect of the GABAerg receptor antagonist Bicuculline.

Method. Tissue slices were prepared from postoperative human neocortical tissue from patients with epilepsy or tumor. Local field potential gradient (LFPg) recordings were obtained by a 24 channel laminar microelectrode in physiological conditions and during Bicuculline bath. Single cell detection was performed and acquired action potentials were classified by their properties. Postoperative neocortical tissue from patients with tumor, but without epilepsy has been used as control.

Results.Analysis showed that the application of Bicuculline cause increase in the activity of inhibitory neurons, while it decreases the activity of principal cells in the epileptic neocortical tissue. This effect seems to be less conspicuous in tumor tissue. During the blockade of GABAerg interneurons, granular cells showed enhanced activity.

Conclusions. The blockade of GABAergic inhibition by Bicuculline cause changes in postoperative human neocortex at the level of singular cells. The investigation of particular neurons can help to reveal network characteristics.

***Keywords*-human; electrophysiology; epilepsy; inhibtion; bicuculline; local field potential**

I. Introduction

The generally accepted definition of epilepsy has been formed by the International League Against Epilepsy (ILAE) and the International Bureau for Epilepsy (IBE) in 2005. Most importantly, they have specified the chief differences between epileptic seizures and epilepsy, as a disease. The former is a transient sign or symptom. It is the result of excessive or synchronous, but definitely abnormal neuronal activity in the brain. However, epilepsy refers to disorders of the brain. It is characterized by a permanent tendency to epileptic seizures. Furthermore, it may have neurological, cognitive, psychological and social consequences [1].

Neurons of the cortex have two major groups. The principal cells (like pyramidal cells) are responsible for excitability, while interneurons (like basket cells) are responsible for the inhibition. The complex and intricate network of these neurons makes possible the proper functioning of the brain. According to the most common hypothesis, if the proportion of these components shifts to the direction of excitation and reaches a certain level, a seizure will be generated. Distinct intrinsic (e.g. biochemical modification of receptors) and extrinsic (e. g. synaptic reorganisation) factors can be responsible for the abnormal behavior of neurons [1], [2].

The major inhibitory neurotransmitter is the gamma-aminobutyric acid (GABA). The postsynaptic $GABA_A$ receptor regulates the flow of chloride (Cl^-) ions across cell membranes. The inflow of negatively charged ions hyperpolarize the cell, thus inhibiting the generation of action potentials. $GABA_A$ receptor antagonist Bicuculline is widely used to induce epileptiform (interictal-like) activity in animal cortical tissue. By using this agent, we investigate the effect of the blockade of GABAergic inhibition in human neocortical tissue [2], [3], [4], [5].

The estimated number of patients suffering from epilepsy worldwide is about 65 million. 0.3-0.6% of the Hungarian population are affected. If the medical treatment fails, the removal of the epileptogenic zone can provide a solution. Epilepsy surgery is currently at the stage of development. An important element is to enhance the efficiency of the triggering foci's detection. Understanding the pathological neuronal properties and behavior can help in this intention. Our goal is to compare the electrophysiological characteristics of postoperative neocortical slices derived from patients with epilepsy and patients with tumour but without epilepsy in vitro [6], [7], [8].

II. Methods and Materials

A. Patients

Postoperative neocortical tissue was examined, which was resected from patients with focal epilepsy. As a control, we used neocortical tissue obtained from patients with tumor. The sample used in this experiment was not affected by the tumor. Tumor patients with at least one diagnosed epileptic seizure were excluded from the study.

A written consent was given by all the patients. Our study was approved by the Hungarian Ministry of Health and also by the Regional and Institutional Ethics Committee of Science and Research of Scientific Council of Health. The surgery and the experiment were performed at the National Institute of Clinical Neurosciences.

B. Preparation of the tissue

The brain tissue resected during the surgery was transported to the experimental laboratory. It was placed in an ice-cold sucrose solution (composition: 248 mM D-sucrose, 26 mM $NaHCO_3$, 1 mM KCl, 1 mM $CaCl_2$, 10 mM $MgCl_2$, 10 mM glucose, 1mM phenol red), thus preventing the death of the cells. Then the dura mater and major blood vessels were

Á. KANDRÁCS, "The effect of GABAA receptor antagonist Bicuculline on human neocortex in vitro" in *PhD Proceedings Annual Issues of the Doctoral School, Faculty of Information Technology and Bionics, Pázmány Péter Catholic University – 2016.* G. Prószéky, P. Szolgay Eds. Budapest: Pázmány University ePress, 2016, pp 51– 54.

removed, in order to make the processing easier. Keeping the tissue in the icy sucrose solution, slices of 500 μm thickness were made by using vibratome. The cutting was performed perpendicular to the brain surface so that the slices contained all the 5 layers of the cortex. Afterwards, they were placed in an interface chamber. They were reposed for an hour to restore the normal activity of neurons from the shocks caused by the surgery and preparation. During both restoration and recordings physiological artificial cerebro-spinal fluid (ACSF) of 35-37 °C was circulated in the chamber (composition: 124 mM NaCl, 26 mM $NaHCO_3$, 3,5 mM KCl, 1 mM $CaCl_2$, 1 mM $MgCl_2$, 10 mM D-glucose). Both sucrose solution and ACSF were equilibred with carbogen gas (95% O2, 5% CO2). On active slices 20 μM Bicuculline bath was applied [3], [5], [9].

C. Recordings

The recording was performed in an interface chamber. The bottom of the setup was filled with heated and oxygenated distilled water to provide proper conditions to the examined tissue. Two chamber were installed with separated fluid inlet so that experiments with two distinct solutions could be performed. The whole set up was placed in a Faraday cage to eliminate the distraction of the surroundings during the registration [3], [9].

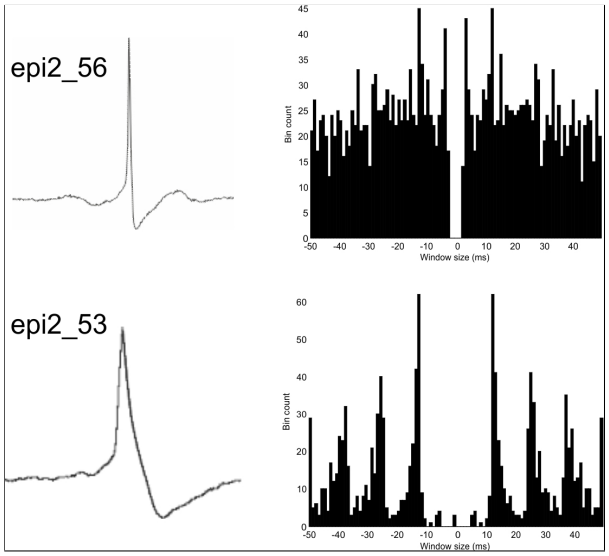

Fig. 1. Typical action potential and autocorrelogram of an interneuron (upper) and a principal cell (lower)

We have performed extracellular recordings applying 24-channel laminar multi-electrode. The contacts were 150 μm away from each other so it could cover the whole cortex along the layers. The end of the electrode was bent, so that the positioning was easier to the slice horizontally. It allows us to obtain local field potential gradient (LFPg), multiple-unit activity (MUA) and single cell action potential (AP) recordings. The end of the electrode pointed to the deeper structures of the cortex. So the lower-numbered channels corresponded to layer I, moving all the way through the cerebral cortex to channel 24, which was located in layer VI. According to bipolar recordings (field potential gradient), the obtained signal is a first order spatial derivative. After a preliminary amplification and filtering we have converted the recordings to digital signal. Fort hat we used a LABView based software, which was made specifically to such experiments [3], [10], [11].

D. Data analysis

For the cell detection preliminary signal procession was required. In the case of recordings in which the brain slices were in ACSF, we used high-pass filter above 80 Hz. This option was inapplicable in the case of experiments Bicuculline bath. Since the inhibition was blocked in the cortex, we experienced higher multiple-unit activity. High-pass filter above 500 Hz was necessary to exclude unexpected signals [3].

			Frequency(Hz)	
		n	avg	std
Epilepsy	Control	57	2,17	4,76
	Bicuculline	60	0,89	1,72
Tumor	Control	23	0,80	1,54
	Bicuculline	59	1,02	2,06

TABLE I
DISTRIBUTION OF DETECTED CELLS AMONG EPILEPTIC/TUMOR AND CONTROL/BICUCULLINE GROUPS

In some cases, artefacts generated during the recordings made the detection more difficult. I cut out the problematic sections and replaced with a sign of baseline. This method did not affect the required results[3].

I detected the action potentials of each cell in the pre-processed recordings channel by channel. I set the threshold of detection manually. Then, i used k-means clustering to separate distinct cells on the same channel. The dimensions of clustering were the amplitudes of the action potential at specified time moments. The ideal number of dimensions was between 3 and 5. I created an error cluster for the detected noise. In case of recordings made during Bicuculline bath required additional check to exclude the ripples detected accidentally as cells[3].

According to the obtained events i cut the original recording to epochs of 50 ms (action potential peak $\pm$25 ms). Then i averaged the epochs for each channel. Thus, it outlined the specific shape of the action potential to each cell. Using this, i divided the neurons into 3 groups: principals cells, interneurons and unspecified. In the case of unspecified neuron the firing pattern of cells were taken into account (figure 1). The high peak at 3-5 ms followed by a fast exponential decay characteristic was to autocorrelogram on the principal cells, whereas the slow decay identified interneurons[3].

For data analysis i used NeuroScan 4.5 and routins written in Matlab (SpikeSolution, WaveSolutin, cell_typing)[3].

III. Results

I could detect a total of 80 cells in the slices with physiological ACSF (table 1). 57 of them occurred in the epileptic tissue (with average firing frequency of 2.17 $\pm$4.76 Hz), while 23 of them occurred in tumor tissue (with average firing frequency of 0.8 $\pm$1.54 Hz). Then, leaving the electrode in the same position, we applied Bicuculline bath on the slices and registered 119 cells. 60 cells were detected in epileptic tissue (with average firing frequency of 0.89 $\pm$1.72 Hz) and 59 cells patients in tumor tissue (with average firing frequency of 1.02 $\pm$2.06 Hz). While the average firing frequency was 0.41 (=0.89/2.17) times lower during the application of Bicuculline in epileptic patients, in tumor patients the same ratio was 1.27 (=1.02/0.8) times higher.

		Epilepsy			Tumor		
		n	frequency (Hz)	AP duration (ms)	n	frequency (Hz)	AP duration (ms)
principal cell	control	32	2,19	1,07	10	0,65	0,71
	Bicuculline	10	0,4	0,79	21	0,85	0,97
interneuron	control	19	1,69	0,5	9	1,3	0,32
	Bicuculline	33	1,08	0,47	25	1,07	0,65
unspecified	control	6	3,55	1,1	4	0,04	0,78
	Bicuculline	17	0,84	0,72	13	1,35	0,97

TABLE II
DISTRIBUTION OF DIFFERENT KIND NEURONS AMONG EPILEPTIC/TUMOR AND CONTROL/BICUCULLINE GROUPS

I have investigated the distribution of principal cells (PC), interneurons (IN) and unknown neurons (UK) in epileptic and tumor tissue during the use of physiological ACSF and Bicuculline bath (for details have a look at table 2). Briefly, the PC/IN ratio is higher during the application of physiological ACSF in both epileptic (32/19) and tumor (10/9) tissue. During Bicuculline bath the these values turns around (10/33 and 21/25, respectively). There are also significant changes in the firing frequency. Both principal cells and interneurons (even unspecified cells) became slower after the application of Bicuculline. In contrast to that, in tumor tissue principal and unspecified cells increased their firing frequency, while interneurons became a bit slower.

I had a look at the distribution of neurons through the different layers of the neocortex (table 3). I classified the cells into 3 groups: supragranular (layer I-III), granular (layer IV) and infragranular (layer V-VI) cells. In epileptic tissue, during use of physiological ACSF, the number of supragranular and infragranular cells were similar, but the firing frequency was higher in the lower layers. There were less neurons in the third group but they were also more active. After the blocade of GABAergic inhibition, they showed similar activity, but the firing frequency decreased in all layers.

In tumor tissue at physiological conditions the infragranular layer showed the highest cellular activity. After the application of Bicuculline, there were no significant changes in the number of cells, but both granular and supragranular neurons increased their firing frequency. While in the infragranular layer the firing frequency remained more-less the same.

		Epilepsy		Tumor	
		n	frequency (Hz)	n	frequency (Hz)
supra	control	25	1,11	3	0,55
	Bicuculline	27	0,5	16	1,01
gran	control	8	3,52	6	0,19
	Bicuculline	10	1,85	12	1,76
infra	control	24	2,81	6	0,87
	Bicuculline	23	0,92	31	0,81

TABLE III
DISTRIBUTION OF NEURONS BY THEIR LOCATION IN THE NEOCORTEX

IV. Conclusions

Our preliminary data showed that the blockade of GABAergic inhibition by Bicuculline cause changes in the network properties of the neurons in postoperative human neocortex . The recent study show that these changes start at the level of singular cells.

An interesting result is that the ratio of the active principal cells and interneurons turns around by the application of Bicuculline. It's a paradox situation, that at physiological conditions, the epileptic neocortex seems to have less inhibition. After the blockade of GABAerg receptors, interneurons become more active, while the excitatory pyramidal cells tend to be more silent. This effect seems to be less conspicuous in tumor tissue.

Recent studies suggested the importance of the supragranular layer in the generation of syncronous activity in the human neocortex. Also the infragranular layer showed an enhanced participation in the activation of single cells. The blockade of inhibition seems highlight the role of the granular layer.

Acknowledgements

The author would like to thank Lucia Wittner and István Ulbert for supervision as well as Kinga Tóth and Katharina Hofer for collaboration and advice.

References

[1] R. S. Fisher et al., "Epileptic seizures and epilepsy: definitions proposed by the International League Against Epilepsy (ILAE) and the International Bureau for Epilepsy (IBE)," *Epilepsia*, vol. 46, pp. 470–472, 2005.
[2] E. B. Bromfield et al. (2006). *An Introduction to Epilepsy* [Online]. Available: http://www.ncbi.nlm.nih.gov/books/NBK2510/
[3] Á. Kandrács, "Az operáció során eltávolított humán epilepsziás neocortex elektrofiziológiai jeleinek szoftveres analízise, " M. S. thesis, Pázmány Péter Catholic University Faculty of Information Technology and Bionics, Budapest, Hungary, 2014
[4] A. Bragin et al., "Local Generation of Fast Ripples in Epileptic Brain, " *The Journal of Neuroscience*, vol. 22, no. 5, pp. 2012-2021, March 2002
[5] Á. Kandrács, "Investigation of the role of GABAergic inhibition in epileptic human neocortex" in PhD Proceedings Annual Issues of the Doctoral School, Faculty of Information Technology and Bionics, Pázmány Péter Catholic University, 2015, pp. 57–60.
[6] J. Janszky and A. Szűcs, "Az epilepsziás rohamok diagnózisa és kezelése, " *Hippocrate: Neurológia*, pp.104-109, March-April, 2002.
[7] A. T. B. David et al., "Standards for epidemiologic studies and surveillance of epilepsy," *Epilepsia*, vol. 52, pp. 2–26, 2011

[8] B. Mikudina et al., “Epilepszia betegségteher felmérés Magyarországon,” *Gondolatok közös javainkról. Válság az oktatásban? Oktatás a válságban!*, Budapest, 2010, pp. 179–188.
[9] R. Köhling, A. Lücke, H. Straub, E. J. Speckmann, I. Tuxhorn, P. Wolf, H. Pannek, and F. Oppel, ”Spontaneous sharp waves in human neocortical slices excised from epileptic patients,” *Brain*, vol. 121, pp. 1073-1087, 1998.
[10] I. Ulbert, Z. Maglóczky, L. Eross, S. Czirják, J. Vajda, L. Bognár, S. Tóth, Z. Szabó, P. Halász, D. Fabó, E. Halgren, T. F. Freund, and G. Karmos, “In vivo laminar electrophysiology co-registered with histology in the hippocampus of patients with temporal lobe epilepsy.,” Exp. Neurol., vol. 187, pp. 310–318, 2004.
[11] I. Ulbert, E. Halgren, G. Heit, and G. Karmos, “Multiple microelectrode-recording system for human intracortical applications.,” J. Neurosci. Methods, vol. 106, pp. 69–79, 2001.

Comparative analysis of intrinsic disorder in proteins of the central nervous system

Annamária Kiss-Tóth
(Supervisor: Zoltán Gáspári)
Pázmány Péter Catholic University, Faculty of Information Technology and Bionics
50/a Práter street, 1083 Budapest, Hungary
kiss-toth.annamaria@itk.ppke.hu

***Abstract*—Predicting a protein's structure and function is a big challenge in proteomics. Analyzing a protein's structural preferences, such as secondary structure and intrinsic disorder tendency is an important step towards determining its function.**

The aim of this paper is to take a closer look at the structured organization of a set of proteins located in the synapses. Proteins were collected from the Synaptome Database. GO term filtering was applied, and only proteins participating in synaptic transmission were further investigated. Orthologous proteins in great apes were obtained from multiple ortholog databases. A comprehensive bioinformatical analysis was performed to determine intrinsic disorder tendency and search for coiled-coil structures. Preliminary results show that the majority of the analyzed sequences contain only short disordered regions if any. The majority of these proteins contain no coiled-coil structures at all. Only a handful of proteins are predicted to be mostly disordered. A few of these sequences will be selected in the future for experimental analysis.

***Keywords*-synaptic protein, synaptic transmission, coiled-coil prediction, disorder prediction**

I. Introduction

Proteins in the central nervous system have a wide range of functions. They can serve as signal transducers, structural building blocks or take part in ion conduction.

The human brain consists of more than a 100 billion neurons, which process and transmit information in the form of electrical signals. Communication between neurons occurs at specialized junctions called synapses. Many of the proteins in the central nervous system are located in synapses. They are essential to the function of the brain and may be an important source of dysfunction underlying many neuropsychiatric disorders [1]. Consequently, a synapse is an excellent candidate for large-scale genomic and proteomic study. Determining the secondary and tertiary structures of synaptic proteins is the first step towards determining their function in the human body.

SynaptomeDB is a database which contains genes encoding the components of the synapse including neurotransmitters and their receptors, adhesion/cytoskeletal proteins, scaffold proteins, and transporters [2]. The content of this database is constantly expanded manually, it currently holds more than 1800 sequences (as of May 24th, 2016).

A pair of proteins are considered homolog if a shared ancestry exists between them. Homolog sequences are divided into two subsets. Orthologous sequences are descended from the same ancestral sequence by speciation. Generally, orthologs retain the same function in the course of evolution. Identification of orthologs is crucial for reliable prediction of protein function. Paralog sequences are created by gene duplication. Paralogs may have new functions, even if these are connected to the original one (**Figure 1.**) [3].

EggNOG is a hierarchical system of orthology classification with function annotation. It can be updated without manual curation, consists of more genes and genomes than other existing databases, contains a hierarchy of orthologous groups to balance phylogenetic coverage and resolution and provides automatic function annotation of similar quality to that obtained through manual inspection [4].

OMA ("Orthologous MAtrix") is a database for the inference of orthologs among complete genomes. Key aspects include broad scope and size, high quality of inferences, feature-rich web interface, availability of data in a wide range of formats and interfaces, and an update twice a year [5].

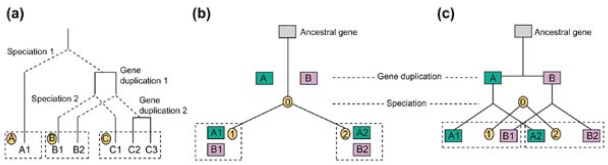

Fig. 1. (a) Simplified diagram of homology subtypes (showing orthologs and paralogs). Speciation events produce the species A, B and C. A1, B1, B2, C1, C2, and C3 have descended from the ancestral sequence following evolutionary events of speciation and gene duplication. (b,c) Evolutionary descent of an ancestral sequence to paralogs and orthologs following duplication in species 0, and then speciation to yield species 1 and 2.

II. Methods

A. Synaptic proteins

The gene IDs of the genes comprising the synaptome and the Uniprot IDs of the corresponding proteins were obtained from the Synaptome database. This way a list of 1872 synaptic proteins was created. The entire content of Uniprot was downloaded and the FASTA sequences of these proteins were extracted with the help of a program written in Perl. Many of these proteins are not limited to synapses. Using functional considerations, a restricted list of 161 proteins was created, and various computational tools for sequence analysis, structure- and function prediction were applied. One of these proteins is the guanylate kinase-associated protein (**Figure 2.**) [6].

First, intrinsic disorder tendency was predicted with 3 different disorder predictors: IUPred, RONN and VSL2B (**Figure 3.**) [7-10]. Applying the online servers would be too time-consuming for this many proteins, the predictors'outputs were processed with Perl. The minimum disordered sequence length was set to 30, shorter regions were discarded. The consensus of the predictors was also calculated.

A. KISS-TÓTH, "Comparative analysis of intrinsic disorder in proteins of the central nervous system" in *PhD Proceedings Annual Issues of the Doctoral School, Faculty of Information Technology and Bionics, Pázmány Péter Catholic University – 2016.* G. Prószéky, P. Szolgay Eds. Budapest: Pázmány University ePress, 2016, pp 55– 57.

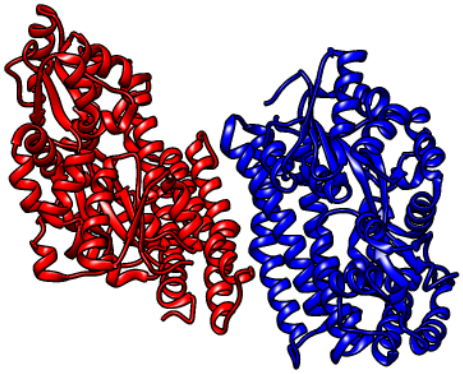

Fig. 2. Structure of maltose-binding protein fusion with the C-terminal GH1 domain of guanylate kinase-associated protein from *Rattus norvegicus* viewed in UCSF Chimera.

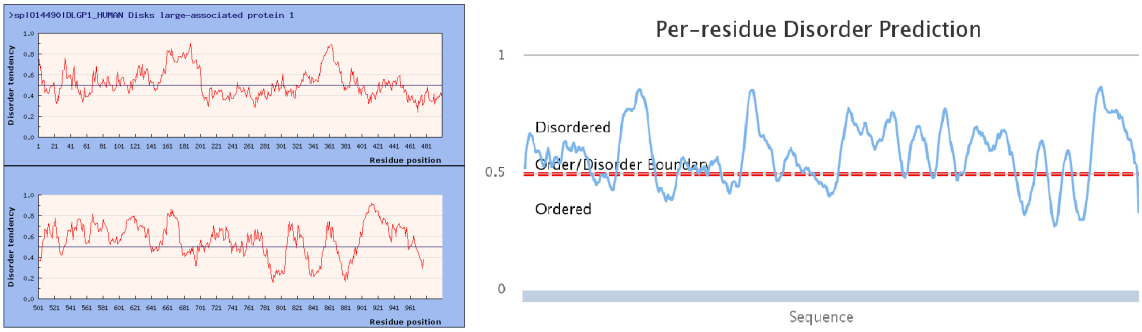

Fig. 3. Results of disorder prediction for GKAP protein (O14490) with IUPred (left) and RONN (right). The regions above the 0.5 line are considered disordered.

Coiled-coil structures are frequently disordered, which can be explained by their obligate multimeric nature. Reverse cross-prediction is rare, but disordered sequences might take up coiled-coil conformation fairly easily during evolution [11].

Second, coiled-coil structures were identified in the sequences with 2 different predictors, Coils and Paircoil, using Perl (**Figure 4.**) [12,13]. The window size (minimum length of a coiled-coil structure) was set to 21. The consensus of the predictors was also calculated.

B. *Orthologous proteins*

The orthologs of synaptic proteins were identified in 3 different species: Western lowland gorilla (*Gorilla gorilla gorilla*), Sumatran orangutan (*Pongo abelii*) and common chimpanzee (*Pan troglodytes*). Two different ortholog databases were used: OMA and eggNOG. Comparing the two databases, it was found that the eggNOG database yields slightly better results. EggNOG uses ENSEMBL IDs for proteins which were converted into Uniprot IDs. Most proteins have orthologs in all 3 species, a few of them have none.

Then, once again various sequence analysis tools were applied. First, disorder tendency was determined with the same 3 disorder predictors. Second, coiled-coil regions were found with the same 2 coiled-coil predictors. The consensus of the prediction results was also calculated.

III. Results

A. *Synaptic proteins*

Using multiple prediction methods in both intrinsic disorder prediction and coiled-coil prediction leads to better, more reliable results.

Disorder prediction shows that the majority of these proteins display little to no intrinsic disorder tendencies, which means they have a well-defined three-dimensional structure. A few of the proteins are (almost) completely disordered. The longer the protein the likelier it contains at least one disordered region. Thus, according to our preliminary survey, the synaptome largely consists of globular proteins.

The results of the coiled-coil search were similar. In the vast majority of cases no such structures were found, and most of the remaining sequences only contain relatively short coiled-coils. In a handful of cases, the coiled-coil structures take up approximately half of the sequence.

At first glance, there is no obvious connection between a protein's predicted disorder tendency and willingness to form coiled-coil structures. In some cases, a completely ordered protein contains several coiled-coils, or a partially disordered one has no coiled-coils at all. A possible correlation between the two requires further research.

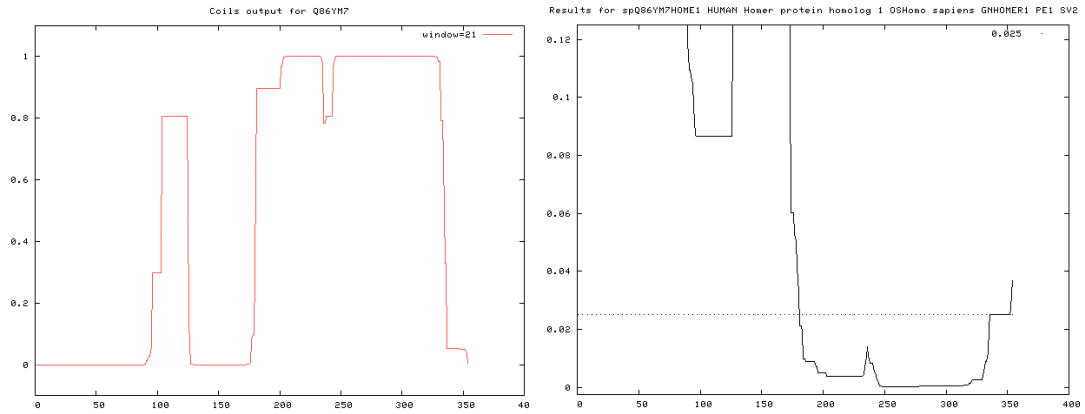

Fig. 4. Results of coiled-coil prediction for HOMER1 (Q86YM7) with Coils (left) and Paircoil2 (right). The regions above the 0.5 line (left) and below the 0.25 line (right) are considered part of a coiled-coil form.

B. Orthologous proteins

The prediction results in the orthologs are expectedly similar. It can be observed that the length of the disordered sequences and coiled-coil structures in the great ape proteins generally corresponds to their human counterparts.

IV. Conclusion and future plans

In case of the synaptic proteins, the relationship between the disorder prediction results and the coiled-coil prediction results will be further examined. The overlap between disordered and coiled-coil regions will be calculated.

The synaptic proteins' corresponding orthologs generally have disordered- and coiled-coil regions of similar length.

The synaptic protein sequences will also be compared to sets of proteins participating in other biological processes.

Acknowledgment

The kind help of Zoltán Gáspári and my fellow PhD researchers is acknowledged for their expertise and helpful insights into my research and the creation of this manuscript.

References

[1] Van Spronsen M, Hoogenraad CC. Synapse pathology in psychiatric and neurologic disease. Current Neurology and Neuroscience Reports 10(3):207-214 (2010).

[2] Pirooznia M, Wang T, Avramopoulos D, Valle D, Thomas G, Huganir RL, Goes FS, Potash JB, Zandi PP. SynaptomeDB: an ontology-based knowledgebase for synaptic genes. Bioinformatics (2012).

[3] Jensen, Roy A. "Orthologs and paralogs - We need to get it right." Genome Biology 2.8 (2001).

[4] Jensen LJ, Julien P, Kuhn M, et al. eggNOG: automated construction and annotation of orthologous groups of genes. Nucleic Acids Research 36(Database issue):D250-D254 (2008).

[5] Schneider A, Dessimoz C, Gonnet GH. OMA Browser - Exploring orthologous relations across 352 complete genomes. Bioinformatics 23:16 pp. 2180-2182 (2007).

[6] Tong J, Yang H, Eom SH, Chun C, Im YJ. Structure of the GH1 domain of guanylate kinase-associated protein from Rattus norvegicus. Biochemical and Biophysical Research Communications 452(1):130-5 (2014).

[7] Zsuzsanna Dosztányi, Veronika Csizmók, Péter Tompa and István Simon. IUPred: web server for the prediction of intrinsically unstructured regions of proteins based on estimated energy content. Bioinformatics 21, 3433-3434 (2005).

[8] Yang, ZR, Thomson, R, McNeil, P, and Esnouf. RONN: the bio-basis function neural network technique applied to the detection of natively disordered regions in proteins. RM (2005).

[9] Peng K., Radivojac P., Vucetic S., Dunker A.K., and Obradovic Z. Length-dependent prediction of protein intrinsic disorder. BMC Bioinformatics 7:208 (2006).

[10] Obradovic Z., Peng K., Vucetic S., Radivojac P., and Dunker A.K., Exploiting heterogeneous sequence properties improves prediction of protein disorder. Proteins 61(S7):176-182 (2005).

[11] Balázs Szappanos, Dániel Süveges, László Nyitray, András Perczel, Zoltán Gáspári. Folded-unfolded cross-predictions and protein evolution: The case study of coiled coils. FEBS Letters (2010).

[12] Lupas, A., Van Dyke, M., and Stock, J. Predicting coiled-coils from protein sequences. Science 252:1162-1164 (1991).

[13] Bonnie Berger, David B. Wilson, Ethan Wolf, Theodore Tonchev, Mari Milla, and Peter S. Kim. Predicting coiled-coils by use of pairwise residue correlations. Proceedings of the National Academy of Science USA, vol 92, pp. 8259-8263 (1995).

Functional investigation of non-canonical pathways originating from the auditory thalamus

Kinga KOCSIS
(Supervisor: István ULBERT, MD, DSc)
Pázmány Péter Catholic University, Faculty of Information Technology and Bionics
50/a Práter street, 1083 Budapest, Hungary
kocsis.kinga@itk.ppke.hu

Increasing number of studies are dedicated to show that the thalamus is not simply a messenger for the cerebral cortex. It is instead an active and dynamic modulator of the sensory information flow. Thus, the thalamus has a predominant role in cognitive functions, including auditory fear learning. The purpose of my study is the optogenetic dissection of the thalamo-amygdala pathways and the investigation of their contribution to emotional processes as well as their electrophysiological properties.

Anatomical lesion and tracing studies have revealed diverse and distinct cell populations in the posterior region of the medial geniculate body (MGB), one of the subcortical stations of auditory processing. In this area, amygdala-connected thalamic cells are considered to mediate classical Pavlovian conditioning of fear responses to tones in rodents [1]. These neurons compose a so-called extrageniculate or non-lemniscal sensory pathway [2] receiving multimodal sensory information and projecting to higher-order cortical areas as well as to the fear memory related amygdala (lateral amygdala (LA) and amygdalostriatal transition zone (AStr)) [3]. These cells can be potentially distinguished by their neurochemical properties as well. Calcium-binding proteins such as calbindin (CB) and calretinin (CR) are predominant in the medial nucleus of the MGB (MGM), the suprageniculate nucleus (SG), and the posterior intralaminar nucleus (PIN) [4], the so-called 'posterior group'. These results point to straightforward optogenetic potential of these cell populations. Anatomical evidence suggests that the CR-Cre mouse strain is a valuable tool to investigate the connections of non-lemniscal auditory nuclei in the thalamus, as well as their role in auditory plasticity.

Wild-type and transgenic CR-Cre mice were examined in a classical fear-conditioning behavioral paradigm. In the latter animal group, CR+ cells were retrogradely labelled with channelrhodopsin from the amygdala by adenoassociated virus vector two months before conditioning. Mice were habituated to Gaussian white noise (not conditioned stimulus, CS-). Cue-dependent fear-conditioning was achieved by delivering a 7.5 kHz pure tone (conditioned stimulus, CS+,) paired with a mild footshock. The magnitude of fear responses was quantified by immobility (freezing) percentages during fear retrieval. Our behavioural paradigm is proven to be functional in terms of proper sound discrimination and association.

Acute extracellular electrophysiological recordings were performed in the CR-Cre mice under urethane anesthesia. To trial the optogenetic resposes of channelrhodopsin-expressing CR+ cells, 1 Hz trains of 0.5 ms long light pulses (10 mW, 473 nm) were applied. Auditory signals were composed of the CS+ and CS-. According to my preliminary results, LA/AStria-projecting CR+ cells of the SG are not shown to possess predominant auditory responses, which raises important questions about their putative integrative function. In lower thalamic regions (PIN) both optogenetic and auditory responses were present. It is paramount to further elucidate how and to what extent posterior auditory thalamic cells carry information about behavior relevance to the LA.

Although the computational capacities of the aforementioned system is limited, it may act as filter for emotionally significant events. Investigation of the subcortical components of fear-learning can potentially improve our understanding on behavioural plasticity, debilitating mental disorders and their potential new therapies.

My main purpose is to further elucidate at which point of the subcortical auditory pathways multimodal integration and plasticity can emerge. To achieve this, I aim to investigate how different periods of learning affects the receptive field (frequency tuning) and electrophysiological response characteritics of the non-lemniscal pathways in freely-moving or head-restrained mice.

References

[1] E. Lanuza, J. Moncho-Bogani, and J. E. LeDoux, "Unconditioned stimulus pathways to the amygdala: effects of lesions of the posterior intralaminar thalamus on foot-shock-induced c-fos expression in the subdivisions of the lateral amygdala," *Neuroscience*, vol. 155, no. 3, pp. 959–968, 2008.

[2] R. Linke and H. Schwegler, "Convergent and complementary projections of the caudal paralaminar thalamic nuclei to rat temporal and insular cortex.," *Cerebral cortex (New York, N.Y. : 1991)*, vol. 10, no. 8, pp. 753–771, 2000.

[3] E. L. Bartlett, "The organization and physiology of the auditory thalamus and its role in processing acoustic features important for speech perception," *Brain and language*, vol. 126, no. 1, pp. 29–48, 2013.

[4] E. Lu, D. Llano, and S. Sherman, "Different distributions of calbindin and calretinin immunostaining across the medial and dorsal divisions of the mouse medial geniculate body," *Hearing research*, vol. 257, no. 1, pp. 16–23, 2009.

K. KOCSIS, "Functional investigation of non-canonical pathways originating from the auditory thalamus" in *PhD Proceedings Annual Issues of the Doctoral School, Faculty of Information Technology and Bionics, Pázmány Péter Catholic University – 2016.* G. Prószéky, P. Szolgay Eds. Budapest: Pázmány University ePress, 2016, pp 59– 59.

Divergent in vivo activity of non-serotonergic and serotonergic VGluT3-neurones in the median raphe region

Tamás LASZLOVSZKY
(Supervisor: Balázs HANGYA, former: Viktor VARGA, István ULBERT)
Pázmány Péter Catholic University, Faculty of Information Technology and Bionics
50/a Práter street, 1083 Budapest, Hungary
laszlovszky.tamas@itk.ppke.hu

***Abstract*—The median raphe is a key subcortical modulatory center involved in several brain functions [1], such as regulation of the sleep–wake cycle, emotions and memory storage. In the median raphe, a pure glutamatergic neurone population projecting to limbic areas was also discovered with a possibly novel, yet undetermined function. In the present study, we report the first functional description of the vesicular glutamate transporter type 3 (VGluT3)-expressing median raphe neurones. Furthermore we reconstructed the recorded cells and found a morphological difference between the different raphe cell populations which can influence the cell's firing properties [2].**

***Keywords*-Subcortical modulation; vGluT3; 5-HT; morphology; electroporation**

I. Introduction

The ascending projection from the median raphe region (MRR; median raphe nucleus and paramedian raphe nucleus) is essential for a multitude of brain functions, such as the regulation of the sleep–wake cycle or the modulation of oscillations [3]. The MRR consists of a heterogeneous collection of serotonergic, GABAergic and later identified glutamatergic neurones. The discovery of the third isoform of the vesicular glutamate transporter (VGluT3) in 5-HT+ neurones, amongst others, raised the possibility of a novel, uncharacterized form of modulation by co-released glutamate. Glutamate from MRR axons, in contrast to 5-HT, selectively and powerfully recruits certain interneurone types in the hippocampus via synapses that contain both 5-HT and VGluT3 or only VGluT3. In parallel with the identification of fast glutamatergic modulation, a large fraction of MRR projection neurones was reported to be purely glutamatergic in addition to serotonergic and dual-transmitter subpopulations [4]. However, the functional characteristics of VGluT3+ MRR neurones (i.e. whether they resemble the classic slow firing phenotype of 5-HT+ neurones or belong to fast spiking subgroups or form a mixed population) remain to be determined. The relationship of their discharge pattern to forebrain activity states, as well as to oscillations, is unknown. In the present study, we characterized the in vivo activity of VGluT3-expressing (5-HT+ and 5-HT–) MRR neurones and compared them with VGluT3– subgroups (5-HT+ and 5-HT–). We juxtacellularly recorded their activity followed by labelling and identification utilizing post hoc immunohistochemistry. We did morphological analysis of the labeled cells to discover their anatomical properties. Our future aim is to get stronger labeling's for the morphological analysis so we implemented a novel electroporation based labeling technique.

II. Methods

Animals

A total of 301 male Wistar rats, weighing 200–500 g, were used in the present study. All experiments were performed in accordance with the Institutional Ethical Codex, Hungarian Act of Animal Care and Experimentation (1998, XXVIII, section 243/1998) and the European Union guidelines (directive 2010/63/EU), and with the approval of the Institutional Animal Care and Use Committee of the Institute of Experimental Medicine of the Hungarian Academy of Sciences. All efforts were made to minimize pain and suffering and to reduce the number of animals used.

Juxtacellular recording in the MRR

The rats were anaesthetized by I.P. injection of 20 percent urethane (Sigma-Aldrich, St Louis, MO, USA; dose: 0.007 ml g–1 body weight). During the experiments, the temperature of animals was held constant by a homeothermic heating pad. A cranial window was drilled to access the MRR either from lateral [stereotactic co-ordinates: anteroposterior (AP) +1.0 mm, mediolateral (ML) –1.4 to –2.0 mm from lambda and 15 percent angle] or from posterior (stereotactic co-ordinates: AP –2.6 mm, ML 0 mm from lambda and 30 percent angle). For juxtacellular recording, filamented borosilicate micropipettes were filled with 0.5 M NaCl containing 2 percent Neurobiotin (Vector Laboratories, Inc., Burlingame, CA, USA; impedance of micropipettes: 20–45 M). After reaching the target zone (6900–8500 um from brain surface), the recording pipette was slowly (0.8–1 um s–1) advanced using a micropositioner (EXFO, Quebec, Canada). The juxtacellular MRR unit signal was filtered between 0.1 and 5 kHz and amplified (gain: 500 or 1000) using an AxoClamp 2B amplifier (Axon Instruments, Foster City, CA, USA) and a LinearAmp signal conditioner (Supertech, Pecs, Hungary).

Histological processing

After successful labelling, animals were transcardially perfused with saline followed by Zamboni's fixative or 4 percent paraformaldehyde (survival time after labelling varied between 10 and 150 min). Brains were cut to 40–80 um thick coronal slices on a vibrotome (Leica Microsystems, Wetzlar, Germany). After extensive washing in 0.1 M phosphate buffer (pH 7.4), the sections were transferred into Tris-buffered saline (Sigma-Aldrich) (pH 7.4). Subsequent to this step,

T. LASZLOVSZKY, "Divergent in vivo activity of non-serotonergic and serotonergic VGluT3-neurones in the median raphe region" in *PhD Proceedings Annual Issues of the Doctoral School, Faculty of Information Technology and Bionics, Pázmány Péter Catholic University – 2016.* G. Prószéky, P. Szolgay Eds. Budapest: Pázmány University ePress, 2016, pp 61– 63.

all the washes and serum dilutions were performed in Tris-buffered saline. Neurobiotin-filled neurones were identified by Alexa488-conjugated Streptavidin staining (Life Technologies, Grand Island, NY, USA, catalogue no.: S-32354, dilution 1:2000), neurochemical content (5-HT and VGluT3) was screened by immunofluorescence [primaries: rabbit anti-5-HT (ImmunoStar Inc., Hudson, WI, USA, catalogue no.: 20080, dilution 1:10000) and guinea pig anti-VGluT3 (Merck, Darmstadt, Germany, catalogue no.: AB5421, dilution 1:2000); secondaries: Dylight405-conjugated donkey anti-rabbit (Jackson ImmunoResearch, West Grove, PA, USA, catalogue no.: 711-475-152, dilution 1:400) and Cy3-conjugated donkey anti-guinea-pig (Jackson Immunoresearch, catalogue no.: 706-166-148, dilution 1:200)]. Fluorescence signals were inspected using an Axioplan 2 microscope (Carl Zeiss, Oberkochen, Germany) with a DP70 CCD-camera (Olympus, Tokyo, Japan) or using an A1R confocal laser scanning microscope (Nikon, Tokyo, Japan).

Reconstruction of the cells and the recording positions

Neurobiotin signal was intensified using Nickel-DAB (2,3 - diaminobenzidine, Sigma-Aldrich) chromogen developed by avidin-biotinylated horseradish peroxidase complex (Elite ABC; Vector Laboratories, Inc., Burlingame, CA, USA). Dendritic arborization of neuro- nes with good labelling quality was three-dimensionally reconstructed using Neurolucida software (MBF Bioscience, Williston, VT, USA) and an Axioplan 2 microscope. The maximal diameter of the coronal projection of dendritic arborization was measured. The position of recovered neurones, as well as the position of LFP recording wires was determined based on the Paxinos stereotaxic atlas of the rat brain.

Recording protocol

Spontaneous and sensory stimulation-evoked activity of MRR neurones simultaneous with hippocampal and occasionally prefrontal cortical LFP was registered. Tail pinch served as the sensory stimulation. The recording duration of spontaneous activity was 2–10 min (except for one case in which 1 min spontaneous activity was saved). In all experiments, the tail pinch was applied by the same small crocodile clip (the serrated surface was covered by thin plastic tape) for 30 s. In five cases, the tail pinch duration was 60 s. If the first stimulation had not evoked brain state change after at least 1 min, a second tail pinch was applied using a stronger clip. Only the first effective tail pinch was considered when the data were analysed. In the case of one neurone, no tail pinch was executed, and therefore the data from this recording were used only in spike half-width analysis and phase preference calculation.

Labelling of recorded neurones

In 166 animals (from a total of 301 rats), successful recordings were followed by Neurobiotin-labelling of the neurones: 1–10 nA current (gradually increased until current-modulated neuronal firing was detected) was applied via the recording pipette, in parallel with a cathodal DC current of 0.5–0.9 nA amplitude. The duration of labelling was 2–10 min.

Plasmid electroporation

pAAV-hSyn-EGFP (addgene) plasmid was injected to the gyrus dentatus and to the thalamus (23, 50, or 100 ml). TTL pulses were 50 ms longs, 1 Hz, -90V, and delivered with a CED driven stimulus isolator (Iso-Flex, Ampi). Glass pipette end diameter varied between 35 and 50 um. Two tungsten electrodes were used for electroporation.

Data analysis

Spikes in unit recordings were detected using Spike2 software, controlled by visual inspection to remove artefacts, and time stamps corresponding to the spike peaks were exported to the MATLAB (MathWorks Inc., Natick, MA, USA) environment, where custom-written routines and scripts were run for further analysis. To calculate the spike waveform average, data in +/- 5 ms time windows around spike peaks were interpolated linearly to obtain a waveform oversampled at 1 MHz. Spike half-width was determined as the duration of the action potential halfway between the baseline and the peak of the waveform average. For calculation of spike averages, all data from pre-labelling recordings (i.e. including spontaneous and sensory stimulation periods) were used.

Statistical analysis

Individual values and medians are presented. In some cases, medians and interquartile range are plotted. Group differences were tested by Kruskal–Wallis ANOVA and the two-sided Wilcoxon rank sum test. Divergence between theta and non-theta, as well as between spontaneous and stimulated conditions, was assessed using a sign test. In the case of maximal dendritic diameter analysis, data are only presented in the text.

III. Results

Comparison of the action potential half-width from both spontaneous and stimulated conditions revealed that the 5-HT– population had narrower spikes (group median of VGluT3+/5-HT–: 223.5 us and VGluT3–/5-HT–: 257.1 us) compared to their 5-HT+ counterparts (group median of VGluT3–/5-HT+: 319.9 us and VGluT3+/5-HT+: 349.3 us). We demonstrate that VGluT3+/5-HT– neurones fundamentally diverged from VGluT3+/5-HT+ cells in several aspects. VGluT3+/5-HT– neurones, resembling VGluT3–/5-HT– cells, had narrow action potentials and fired faster and more variably compared to their VGluT3+/5-HT+ counterparts, whereas the latter population emitted broad action potentials at lower frequency in a regular fashion and, as such, overlapped with the VGluT3–/5-HT+ subgroup. The activity of 5-HT– populations was characteristically higher during hippocampal theta compared to non-theta state, as opposed to the lack of group-level state-preference in the 5-HT-containing subgroups. In the case of some VGluT3+/5-HT– and VGluT3+/5-HT+ cells, weak modulation by forebrain oscillations was also detected.

The temporal relationship between the firing of MRR neurones and the phase of hippocampal and pre- frontal oscillations was analysed. 5-HT– (both VGluT3+ and VGluT3–) cells were weakly phase-coupled to hippocampal and/or prefrontal slow oscillation, which disappeared during sensory stimulation. Although 5-HT– neurones were characteristically modulated by forebrain slow oscillation, the mean vector length corresponding to the strength of phase coupling was low in most cases. Phase coupling to hippocampal theta was

observed for one VGluT3+/5-HT+ neurone. VGluT3–/5-HT+ cells showed weak coupling to hippocampal or prefrontal activity.

The dendritic arborization of 15 neurones was three-dimensionally reconstructed. The dendritic tree of VGluT3+/5-HT– neurones span a larger distance as a result of long, relatively branchless dendrites (group median diameter of dendritic arbor: 752.9 um, interquartile range: 594.9–859.9 um) compared to the two 5-HT+ (VGluT3+ and VGluT3–, group medians: 536.2 and 510.1 um, interquartile ranges: 488.0–713.8 um and 325.5–694.6 um, respectively) and the VGluT3–/5-HT– (group median: 522.1 um, interquartile range: 272.6–841.5 um) populations (number of reconstructed cells: VGluT3+/5-HT–, n = 5; VGluT3+/5-HT+, n = 4; VGluT3–/5-HT+, n = 2; VGluT3–/5-HT–, n = 4). The pure glutamatergic cells showed longer dendritic tree which spread out to the paramedian raphe where they can get a distinct input as compared to the locally projecting pure 5-HT+ cells in the MR.

For testing this hypothesis we implemented an electroporation based technique which was tested in the hippocampus and in the thalamus. The preliminary data showed strong single cell labeling which can be used to characterize the MR populations.

IV. Figures

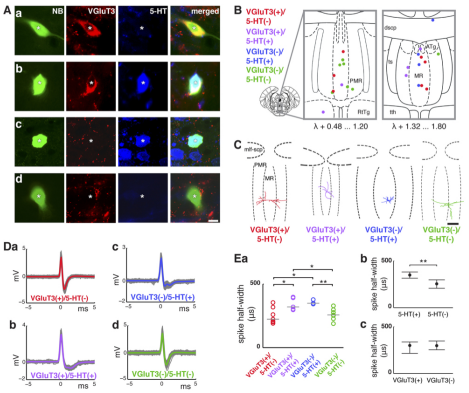

Fig. 1. Functionally and morphologically characterized Median Raphe Region neurones. Examples and recording positions of all neurochemically identified MRR neurones. Immunofluorescence images of example Neurobiotin (NB)-filled neurones: VGluT3+/5-HT– (Aa), VGluT3+/5-HT+ (Ab), VGluT3–/5-HT+ (Ac) and VGluT3–/5-HT– (Ad) neurones. Asterisks indicate the soma. Scale bar = 10 um. B, coloured dots indicate the position of recorded and neurochemically identified neurones overlaid onto two representative coronal diagrams of MRR (MR + PMR). ATg, anterior tegmental nucleus; dscp, decussation of the superior cerebellar peduncle; MR, median raphe nucleus; PMR, paramedian raphe nucleus; RtTg, reticulotegmental nucleus of the pons; ts, tectospinal tract; tth, trigeminothalamic tract. C, coronal projections of three-dimensionally reconstructed dendritic arborization of four representative neurones. mlf-scp, medial longitudinal fascicle and superior cerebellar peduncle; MR, median raphe nucleus; PMR, paramedian raphe nucleus. Scale bar = 300 um. Da–Dd, spike waveform averages (plotted in colour) of corresponding neurones in (A). Ea, spike half-width (grey lines: group medians). Kruskal–Wallis ANOVA: P = 0.0146. Wilcoxon rank sum test: P ¡ 0.05; P ¡ 0.01. Data grouped on the basis of 5-HT (Eb) and VGluT3 (Ec) content (median + interquartile range).

V. Conclusions

VGluT3+/5-HT– neurones fundamentally diverged from VGluT3+/5-HT+ cells based on their firing properties. Their morphological characteristics showed a tendency that they exhibit distinct dendritic properties between the groups which can have functional relevance. Also a new electroporating technique was implemented to answer this question.

Acknowledgements

The author wishes to acknowledge Dr. Viktor Varga, Dr. Andor Domonkos and all the co-authors who contributed with their excellent work in our paper, and Dr. István Ulbert for the supervision.

References

[1] Baudry A, Mouillet-Richard S, Schneider B, Launay JM, Kellermann O *MiR-16 targets the serotonin transporter: a new facet for adaptive responses to antidepressants.*, Science 329, 1537–1541, 2010

[2] Domonkos A, Nikitidou Ledri L, Laszlovszky T, Cserép Cs, Borhegyi Zs, Papp E, Nyiri G, Freund TF , Varga V. *Divergent in vivo activity of non-serotonergic and serotonergic VGluT3–neurones in the median raphe region.*, J Physiol, DOI: 10.1113/JP272036, 2016

[3] Allers KA, Sharp T, *Neurochemical and anatomical identification of fast- and slow-firing neurones in the rat dorsal raphe nucleus using juxtacellular labelling methods in vivo.*, Neuroscience 122, 193–204., 2003

[4] Varga V, Losonczy A, Zemelman BV, Borhegyi Z, Nyiri G, Domonkos A, Hangya B, Holderith N, Magee JC, Freund TF *Fast synaptic subcortical control of hippocampal circuits.*, Science 326, 449–453, 2009

Lateral migration based particle sorting in microfluidic systems

Eszter Leelőssyné Tóth
(Supervisor: Kirstóf Iván, Péter Fürjes)
Pázmány Péter Catholic University, Faculty of Information Technology and Bionics
50/a Práter street, 1083 Budapest, Hungary
toth.eszter@itk.ppke.hu

***Abstract*—Microfluidic system was designed and fabricated for particle separation and sorting by their hydrodynamic parameters such as cell size or density to be applied for sample preparation in optical scattering based pollution monitoring device. The microfluidic device was tested with two type of fluorescent particles with 10 and 16 μm diameters using fluorescent multichannel imaging. The device was modelled in COMSOL Multiphysics simulating the fluid dynamics and calculating particle trajectories. Modelled and measured results were in good agreement and showed the successful sorting of the two particles.**

***Keywords*-Lab-On-a-Chip; microfluidics; sample preparation; particle separation; Computational Fluid Dynamics**

I. Introduction

The rapid development of microscale medical diagnostic devices has underlined the importance of microfluidics enabling fast and effective preparation and analysis of liquid samples. On microscale, classical sample preparation methods might become challenging, such as the effective mixing of fluids as well as the size-dependent separation of corpuscles and their filtering from blood. Macroscale tools cannot be scaled down to resolve these issues, this leads to the development of new structures as separators based on the physical laws of microfluidics. [1] In our previous studies we examined blood plasma separation enhancing Zweifach-Fung bifurcation effect utilizing geometric singularities [2]. For optical scattering based pollution monitoring separation of particle by their size is often required [3].

II. Materials and Methods

A. Microfabrication

The microfluidic channels were realized in Polydimethilsiloxane (PDMS) with rapid prototyping. SU-8 negative photoresist [4] was patterned by spin-coating (Brewer Science Cee 200CBX spin-coater [5]), litographic exposure (Süss MicroTech MA6 mask aligner [6]) and a final development step, as illustrated in Figure 1. PDMS prepolymer was poured onto the developed replica and polymerized in two days in room conditions. At the final step of the fabrication process, PDMS was sealed to glass by low temperature bonding after oxygen plasma treatment applying 200 W plasma power, 100 kPa chamber pressure and 1400–1900 sccm oxygen flow (Terra Universal Plasma Preen Cleaner/Etcher [7]).

B. Measurement

Low Reynolds regime[8] laminar flow was generated by syringe pumps. The measurement of particle trajectories is a challenging task. Observation of particle separation by microscope requires optically distinguishable particles. High intensity fluorescent polystyrene microparticles were used as

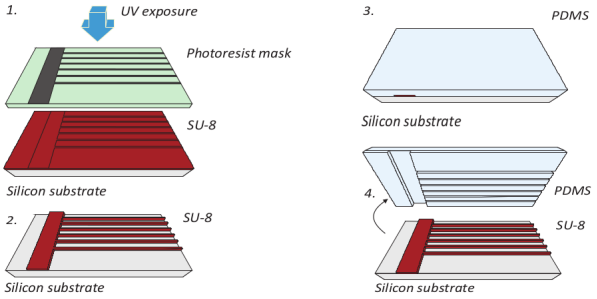

Fig. 1. Schematic view of PDMS rapid prototyping. UV light passes the photoresist mask exposing the SU-8. The developed photoresist then serves as a moulding replica for PDMS moulding.

analyte and recorded by Zeiss AxioVert A1 [9] inverted fluorescent microscope. The analyte components were the following: 100 μL 1% w/v 10 μm diameter bead solution (Spherotech Inc. FP-10052-2 [10]), 200 μL 1% w/v 16 μm diameter bead solution (Spherotech Inc. FP-15040-2 [10]) and 2 ml distilled water. The two particle size (10 μm and 16 μm diameter) had two different excitation and emission spectra (Figure 2. Trajectory images were recorded with FITC and DAPI filter sets and combined to multichannel images in ImageJ [11]. The non-overlapping excitation ranges (Figure 2) of filters ensured minimal crosstalk between the signal of the two fluorescent bead types. Fluorescent intensity distributions were recorded from the source (grayscale) images and post-processed by ImageJ [11]. The original .czi file format of the microscope [12] [13] was used to preserve lossless pixel information and metadata.

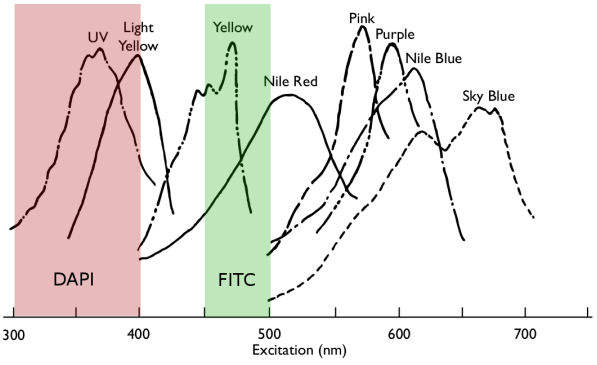

Fig. 2. Excitation spectra of high intensity fluorescent polystyrene microparticles. UV particles (16μm) and Yellow particles (16μm) can be excited well with the DAPI (red color) and FITC (green color) fluorescent microscope filters without considerable crosstalk. [10]

E. LEELŐSSYNÉ TÓTH, "Lateral migration based particle sorting in microfluidic systems" in *PhD Proceedings Annual Issues of the Doctoral School, Faculty of Information Technology and Bionics, Pázmány Péter Catholic University – 2016.* G. Prószéky, P. Szolgay Eds. Budapest: Pázmány University ePress, 2016, pp 65– 67.

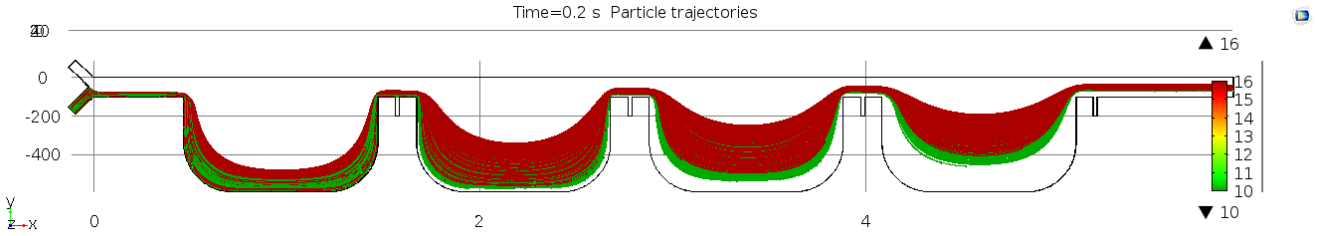

Fig. 3. Calculated trajectory of 1000 particles. Green color denotes 10 μm and red color denotes 16 μm particle diameters. Particle separation by size is well observable

C. Numerical modeling

COMSOL Multiphysics was used to calculate a laminar and stationary velocity field by solving the Navier-Stokes equation [14]. The pre-calculated velocity field then was used for the calculation of particle trajectories. The particle tracing based model calculates, follows and depicts the individual particle trajectories according to the hydrodynamic drag force described by Stokes' law [15]:

$$F_d = \frac{1}{\tau_p} m_p(\mathbf{u}\text{-}\mathbf{v}) \tag{1}$$

where

$$\tau_p = \frac{\rho_p d_p^2}{18\mu}, \tag{2}$$

ρ_p is particle density, d_p is particle diameter, μ is dynamic viscosity of the fluid, m_p is the particle mass, **u** is the velocity of the fluid, **v** is the particle velocity. The lift force was not considered due to the low Reynolds number and the small difference between the particle and water density. Laminar inflow boundary condition was applied on the inlet with different average velocities and zero pressure was set at the outlet. On the channel walls, no slip boundary conditions were defined for the laminar flow model and bounce boundary was used for the trajectory model as summarized in Table I. The properties of room temperature water (density: 1000 kg/m^3, kinematic viscosity: 10^{-6} m^2/s) were applied as material parameters. Properties of the model particles were set to be in correspondence with the fluorescent particles (density: 1040 kg/m^3, diameter: 10 μm and 16 μm [10]). Spherical particle geometry was used as high intensity fluorescent beads have spherical shape [10].

Boundary	**Model**	**Boundary condition/ Initial condition**	**Value**
Inlet	CFD	Laminar inflow with average flow velocity	0.01-5 $\mu L/s$
Inlet	Trajectory	Particle inlet	1000 particles with uniform density
Channel wall	CFD	No slip	-
Channel wall	Trajectory	Bounce	-
Outlet	CFD	Pressure	0 Pa
Outlet	Trajectory	Freeze	-

TABLE I
SUMMARY OF BOUNDARY CONDITIONS FOR THE NUMERICAL MODEL

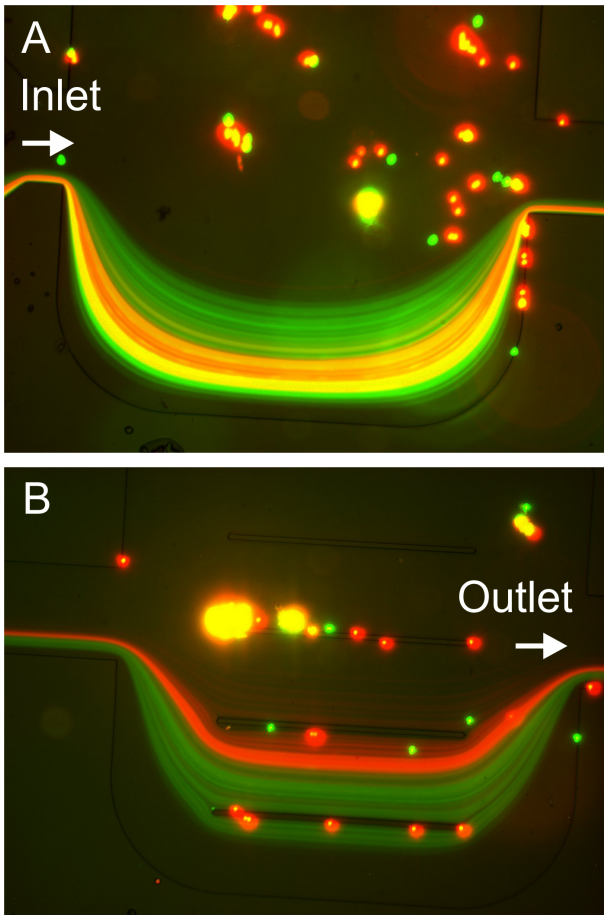

Fig. 4. 10 μm (green) and 16 μm (red) diameter high intensity fluorescent particles were mixed and introduced to the microchannel (A) The overlapping of these colors results in yellow. At the outlet (B) separation of the two sizes are clearly visible. Yellow color is only present at the adherent particles, the green and red colored trajectories (hence the two particle sizes) are visibly separated

III. RESULTS

A. Particle trajectory model

1000 particles with two different diameters (10 μm and 16 μm) were uniformly distributed at the inlet of the microchannel. The particle trajectory model predicted separation of particles by size, however separation is not complete. Figure 3 shows overlapping between the two particle sizes. The cell-free layer generated by the geometry [2] is also observable.

B. Multichannel fluorescent measurement

Fluorescent multichannel images were recorded with DAPI and FITC filter sets of the inverted microscope. The images were combined and their intensity profile was analysed. At

the inlet of the channel mixed particles were introduced (Figure 4 A). Green color denotes 10 μm particles while red color indicates 16 μm diameter. The overlapping of these colors results in yellow color. At the outlet measuring window separation of the two particle size is clearly visible (Figure 4 B) Yellow color is only present at the adherent particles, the green and red colored trajectories (hence the two particle sizes) are visibly separated.

Intensity measurement of the two multichannel records (inlet and outlet) gave quantitative information about the particle distribution. At the inlet (Figre 5 A) the two particle sizes (10 μm (green) and 16 μm (red)) are overlapping. At the outlet (Figure 5 B) the two intensity peaks are well separated, altough a small overlapping is observable.

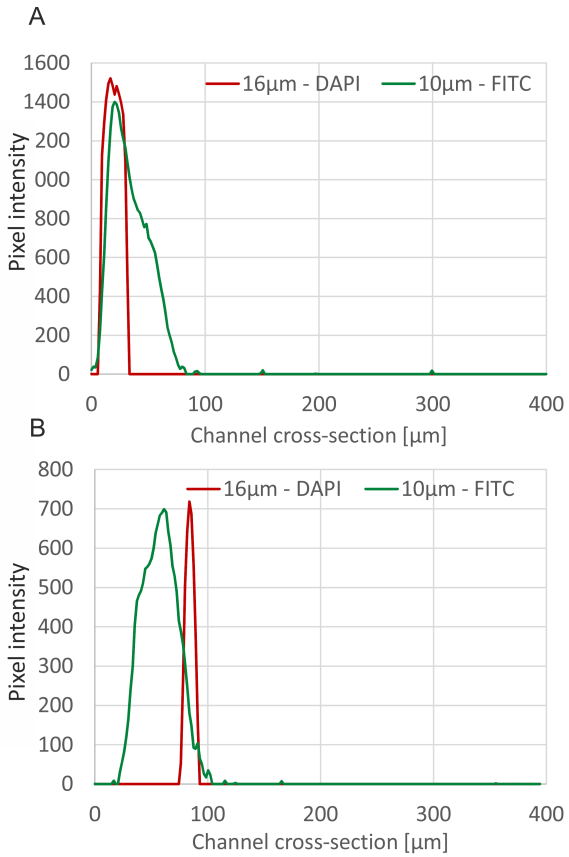

Fig. 5. Fluorescent intensity profliles were recorded at the inlet (A) and at the outlet (B) of the microchannel. Separation of the two types of particles 10 μm (green) and 16 μm (red) is well observable.

IV. Discussion

In this work, computational fluid dynamics (CFD) simulations, trajectory modeling and its experimental validation were carried out to characterise in details the performance of lateral migration based microfluidic separator structures. The selected separation structures were characterised by using numerical modeling and measurements. Comparison of theoretical and experimental results highlighted the strengths and weaknesses of the finite element modeling of fluids with significant amount of formed elements. Based on the simulation outputs and measurement results, the main characteristics of the selected structures were described in details. Particle trajectory model predicted the separation of the two particle size with small overlapping. Fluorescent multichannel records of inlet and outlet of the microfluidi channel showed the separation of the two trajectories. Intensity analysis revealed a small overlapping region at the outlet, wich was in a good agreement with the numerical modeling.

Acknowledgements

The author would like to thank to Kristóf Iván and Péter Fürjes for their patient guidance, enthusiastic encouragement and useful critiques of the research work. The help of the technicians of the laboratory of the Centre for Energy Research Institute of Technical Physics and Materials Science Microtechnology department is greatly appriciated.Supported by the National Research, Development and Innovation Office (NKFIH) EUREKA_HU_13-1-2013-0016 grant.

References

[1] P. Sajeesh and A. K. Sen, "Particle separation and sorting in microfluidic devices: a review," *Microfluidics and Nanofluidics*, vol. 17, pp. 1–52, Nov. 2013.
[2] E. L. Tóth, E. Holczer, K. Iván, and P. Fürjes, "Effect of Geometric Singularities on Plasma Separation Performance in Cascade Zweifach-Fung Bifurcations," *Procedia Engineering*, vol. 120, pp. 1083–1086, 2015.
[3] P. Kulkarni, P. A. Baron, and K. Willeke, *Aerosol Measurement: Principles, Techniques, and Applications*. John Wiley & Sons, Sept. 2011.
[4] "MicroChem: Innovative Chemical Solutions for MEMS and Microelectronics." http://www.microchem.com/.
[5] "Brewer Science, Inc.." http://www.brewerscience.com/.
[6] "Semiconductor Equipment Manufacturing - SUSS MicroTec." http://www.suss.com/.
[7] "Cleanrooms, Glove Boxes, Pass-Throughs, Hoods, Desiccators." https://www.terrauniversal.com/.
[8] J. Happel and H. Brenner, *Low Reynolds number hydrodynamics: with special applications to particulate media*. Springer Science & Business Media, Dec. 2012.
[9] "ZEISS International." http://www.zeiss.com/corporate/en_de/global/home.html.
[10] "Spherotech Inc.." http://www.spherotech.com/.
[11] "ImageJ." https://imagej.nih.gov/ij/index.html.
[12] "CZI The File Format for the Microscope." http://www.zeiss.com/microscopy/en_de/products/microscope-software/zen/czi.html.
[13] Y. Sucaet and W. Waelput, "Hardware and Software," in *Digital Pathology*, SpringerBriefs in Computer Science, pp. 15–29, Springer International Publishing, 2014.
[14] P. Fürjes, E. G. Holczer, E. Tóth, K. Iván, Z. Fekete, D. Bernier, F. Dortu, and D. Giannone, "PDMS microfluidics developed for polymer based photonic biosensors," *Microsystem Technologies*, vol. 21, pp. 581–590, Apr. 2014.
[15] C. BV and C. OY, "COMSOL Multiphysics Reference Guide," 1998.

Targeted simultaneous recordings on rat hippocampal CA1 cells, in vitro

Domokos MESZÉNA
(Supervisor: István ULBERT, MD, D.Sc.)
Pázmány Péter Catholic University, Faculty of Information Technology and Bionics
50/a Práter street, 1083 Budapest, Hungary
meszena.domokos@itk.ppke.hu

***Abstract*—This study aims to investigate several questions related to extracellularly recorded potentials of the underlying neural activity. We design an experimental method for analysing extracellular data focusing particularly on the patterns of transmembrane currents (CSD - Current Source Densities). The extracellular potential pattern can be easily re-calculated from the CSD distribution, but the inverse problem is not solvable (so called ill-posed problem). Our task is to assemble a new measurement tool to generate more reliable experimental data and thus to improve the CSD estimation and the parameter fitting in single cell level. This complex set-up has been already tested on pre-experiments. We are able to record intra- and extracellular single cell activity (Patch-Clamp technique) and population activity (LFP) at the same time, in vitro on rat hippocampal slices. To achieve this, we have developed a novel, arrowhead like 24-channel laminar multi-electrode for better accessibility. We integrate the electrophysiological measurements with a two-photon laser scanning microscopy for imaging the cellular structure and calcium signals. The experimental method we describe here can determine crucial unknown parameters for CSD analysis such as the exact electrode-cell distance. Using the two-photon imaging technique during the recordings has a widespread impact, because we can uniquely specify the solution space of the CSD calculations. This complex experiment can provide an important additional information for the further investigations of single cell dynamics.**

***Keywords*-Extracellular Recordings; Patch-Clamp; Electrode development; two-photon microscopy; Current sources and sinks;**

I. Introduction

It has long been known, that neurons communicate via bioelectric signals, which are systematic alterations of the membrane potential (both positive and negative directions are allowed). There are numerous ways for studying these bioelectric phenomena. In the case of single-unit recordings, sharp microelectrodes or glass micropipettes are positioned close to the neural cell body (or even inside the cell). In contrast to this, during extracellular recordings, the contact points collect signals of a group of neighbouring neurons from the extracellular space. Clustering methods have become available to distinguish different spike shapes (which are the extracellular signatures of intracellular action potentials). In spite of these advanced spike sorting algorithms, complications may arise when more neurons are involved in extracellular potential generation. For example, if two firing neurons have the same electrode-cell distance, it can be very difficult to differentiate the occurring spikes without knowing any further information about the neural structures [1]. Recently, multi-electrode arrays were developed (from 16 up to 512 channels) and automatic spike sorting algorithms were implemented to separate hundreds of neurons simultaneously in one experiment [2]. Despite the technological advances, several aspects of extracellular potential generation remain poorly understood. The main, currently unsolved questions are the following:

- What is the origin of the great amplitude variability among extracellular potential patterns, while intracellular action potentials are so conserved? Can we calculate back the original governing currents from its produced potentials?
- Which are the most important parameters of the neural signal integration and output formation? Can we define an exact input-output function for the recorded neurons?
- How likely is that different neurons produce similar spike amplitude and thus they produce clustering problems and biased source localizations?

Our study attempts to assemble a panoramic view of the neural signal integration using intra- and extracellular recordings, Ca^{2+} dynamics and morphological information. These investigations can significantly help us to understand single-cell dynamics better.

II. Background and Methods

A. Current source density analysis

The electrostatic background of the extracellular potentials has been quite well understood for decades. [8], [9] Due to the laws of electromagnetism, extracellular potentials are generated as result of ionic currents through the cell membrane. The equation, which describes how potentials are generated by electrical charges, is known as the Poisson-equation in electrostatics (by replacing the conductivity σ with the dielectric constant ϵ). The extracellular potential is generated by a discretized line source, parallel to the electrode. In a discrete case, the averaged current source density is equal to the second spatial derivative of the potential [7].

The potential is ignored along the direction of the orthogonal z-y plane. Smaller dendritic branches are neglected as well, we consider the neuron as a line source. The crucial and very non-linearly depending model parameter is the cell-electrode distance, usually denoted by d. Note that d is an Euclidean distance and it is not identical to the so called inter-electrode distance (between the contact points of the electrode shaft, which is mainly marked as d_x). To narrow down the possible solution space, we have to introduce more assumptions. The position of the neuron to the electrode has to be parallel, as it would be in the optimal case. In general, the model has a main active current *sink* (meaning depolarization or positive ion influx from the point of view of the neuron), and a set of smaller *sources* (meaning hiperpolarizations, or positive ion outflow across the membrane). And there are still more

D. MESZÉNA, "Targeted simultaneous recordings on rat hippocampal CA1 cells, in vitro" in *PhD Proceedings Annual Issues of the Doctoral School, Faculty of Information Technology and Bionics, Pázmány Péter Catholic University – 2016.* G. Prószéky, P. Szolgay Eds. Budapest: Pázmány University ePress, 2016, pp 69– 71.

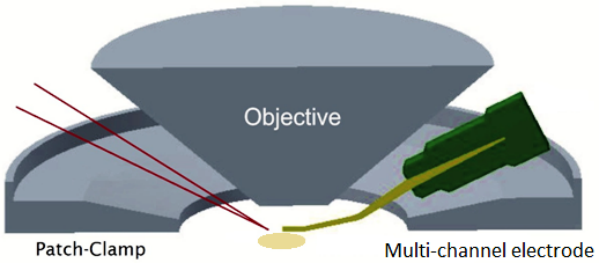

Fig. 1. Schematic layout of the recording instruments. *Left*: Glass micropipette for Patch-Clamp recording. *Right:* self-developed, custom made 24-channel laminar microelectrode for extracellular recording. *Top:* objective of the two-photon microscope. *Bottom:* 500 μm thick hippocampal slice from *Wistar* rat within a dual-perfusion microfluidic chamber. *(Our group's unpublished picture)*

assumptions regarding the isotropy of the extracellular field, the ohmic medium, frequency independent conductivities, etc. And there are more details described in Pettersen's works: [10].

B. Two-photon laser scanning microscopy

Two-photon Ca^{2+} microscopy is a fluorescence imaging technique that allows for imaging of living tissue under specific conditions (both *in vivo* and *in vitro* methods are possible). In rat and mice experiments, such imaging studies have been focused mainly to Ca^{2+} measurements from neurons that were individually dye-loaded through a Patch-pipette (glass microelectrode). The advantage of Ca^{2+} imaging is that it allows for real-time analysis of individual cells and even subcellular compartments, such as tiny dendritic spines.

The concept of two-photon excitation is based on the idea that two photons of lower energy than needed for one photon excitation can also excite a fluorophore in one quantum event [5]. The excitation results in the emission of a fluorescence photon, typically at a higher energy than either of the two excitatory photons. Therefore a high flux of excitation photons is required, which is usually generated by a *femtosecond laser* [4]. We use the Femto2D-uncage system (Femtonics Ltd., Budapest, Hungary) in our experimental set-up. The imaging laser wavelength is set to 900 nm (infrared spectrum). The excitation is delivered to the sample, and the fluorescent signal is collected using lenses and separated from the incoming signal using dichroic mirrors. The experiment was conducted following the protocol suggested by G. Katona et al. [4] and B. Kerekes et al. [3]. It is worth to note, that two-photon excitation can be a superior alternative to confocal microscopy due to its deeper tissue penetration, efficient light detection, and reduced phototoxicity.

C. Targeted simultaneous electrophysiology

Patch-clamp recordings are made by glass microelectrodes (5-9 $M\Omega$) filled with special intracellular solution. The measurement set-up consists a MultiClamp 700B Amplifier and a data acquisition software, pClamp8 as well (both were provided by the Axon Instruments Company, Foster City, California). Cells are held at $-65mV$ in current clamp recordings.

Extracellular recordings are carried out with a self-developed, custom made, spiky 24-channel linear multi-electrode. Because of its arrow-like electrode endings, it is able to slightly penetrate into the tissue (for the electrode design, please see the Fig. 2). This new spiky arrangement allows us to approach even individually selected cells and to record extracellular potentials from the close vicinity of the Patch-Clamp. The spiky multi-electrode has 100 μm inter-contact distance (d_x, as mentioned before). We also plan to design a new electrode with 25 μm to achieve better extracellular resolution. We used the INTAN RHD2000 FPGA-based acquisition system for processing the raw signal recordings (Intan Technologies, Los Angeles, California). Filtered and digitized signals can be analysed using LabVIEW or MATLAB programs (written in our lab). The linear multi-electrode is placed on the surface of the brain slice (transverse 500 μm thick hippocampal slices of male *Wistar* rats were prepared). This way, the whole extent of the examined sample is covered and we are able to record simultaneously from different regions of interest.

To summarise, the use of electrophysiology combined with two-photon imaging is very promising especially to achieve good temporal and spatial resolutions. And it has new application possibilities, such as cell-fulfilment and 3-D reconstruction or local glutamatergic excitation. During the off-line processing, slices could be investigated using light or electron microscopy or with other histological techniques (Please see B. Kerekes et al. for more details [3]).

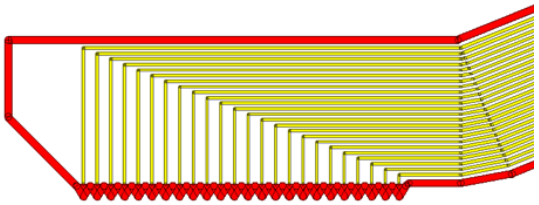

Fig. 2. Scheme of the 'SPIKY' multi-electrode: This arrowhead like contact design allows us to target even individual cells and to record from the close vicinity of the Patch-Clamp. (*Our group's unpublished picture.*)

III. Results

Fig. 3, 4 and Fig. 5 are the results from one of our experiments. On the Fig. 3 we can see the complete arrangement of the electrode positioning and the cell morphology. Extracellular recordings (on the left) and intracellular Patch-Clamp (on the right) were executed simultaneously, under the two-photon microscope. The picture shows the so called Z-stack projection of the selected CA1 layer pyramidal cell. During the Z-stack projection, numerous surface scans are merged together into one 3-D like picture. The approximated cell-electrode distances from the first and the second contact points are indicated. Please note that Patch-Clamp method is capable of filling the neuron with *neurobiotin* tracer dye, thus reconstructing the complete cell morphology. Now we show a fulfilled neuron by using *OGB-1* (green) and *Alexa594* (red) fluorescent dyes. The yellow colour appears as an overlapping between the two different dyes. Please also note the phenomenon of light diffraction on the spiky electrode contact points.

IV. Conclusion

This study addresses several questions related to extracellularly recorded potentials of the underlying neural activity. We have designed a new, integrative method for multi-modal

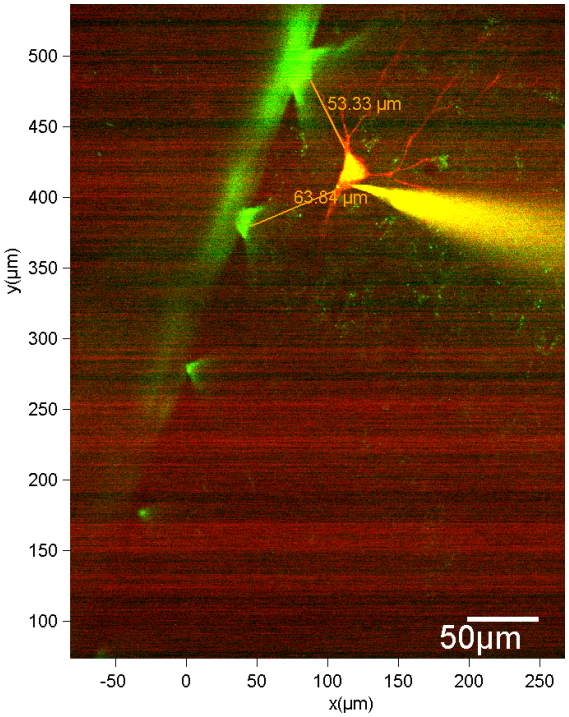

Fig. 3. Simultaneous intra- and extracellular recordings executed under the two-photon microscope. The picture shows the so called Z-stack projection of the selected CA1 layer pyramidal cell. The approximated cell-electrode distances from the first and the second contact points are indicated. *(Our group's unpublished picture)*

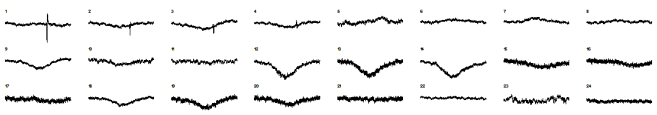

Fig. 4. Spike-triggered averages on the 24-channel extracellular signal. The firing of the Patch-Clamped cell is clearly recognisable on the first 4 channels. This indicates that we were able to record extracellular signals along the apical dendritic axis up to 400 μm, which is a very promising experimental finding. Please note that the big negative waves on the lower channel represents the Sharp Wave population activity, which is almost in phase with the firing of our cell. *(Our group's unpublished picture)*

investigation of in vitro slices. We had already tested the complex methodology on pre-experiments. We have acceptable Patch-Clamp, multi-electrode, and two-photon Ca^{2+} signals with high signal-to-noise ratio. It is also worth to note that this targeted measurement can determine the exact inter-electrode distance (using the two-photon imaging information), which is a crucial, and non-linearly depending unknown parameter during the CSD calculations. So the preliminary results are very promising, we are currently waiting for the new spiky electrode with more dense inter-contact distance. We plan to present our results at the FENS Forum in Copenhagen, Denmark (in July). An article manuscript is also to be started until the end of this summer.

Finally, we can conclude that these investigations can help us to understand neural communication dynamics better. Thus in the future, they would have a good contribution even for the therapy of neural diseases.

Statement of originality

This report describes the work of the doctoral student during the academic year 2015/2016. Parts of this work might be under submission to scientific conferences and journals.

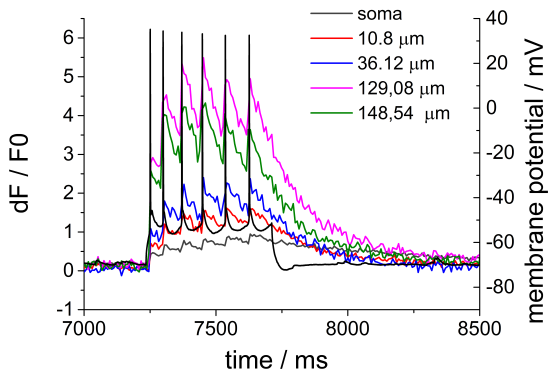

Fig. 5. Combined figure of the Patch-Clamp and triggered Ca^{2+} signals. The fluorescence intensity, $dF/F0$ is on the left axis, and the intracellular membrane potential is on the right axis. The different colour coding shows Ca^{2+} responses from increasing distances compared to the soma. Black lines are the somatic action potentials recorded in current clamp mode. *(Our group's unpublished picture)*

Acknowledgement

The author would express deep gratitude to his supervisor, István Ulbert, MD, DSc for the promotion of the doctoral research work. In addition, the author wish to express thanks to Zoltán Somogyvári, PhD, "Soma", for his excellent advices, to Gergely Márton for developing the novel electrode, and to Viktor Oláh, Bálint Kerekes and Ildikó Pál, for their technical assistances and their encouragements. This research has been funded by the EU FP7 Grant No. 600925 NeuroSeeker and the Hungarian Brain Research Program - Grant No. KTIA-13-NAP-A-IV/1,2,3,4,6.

References

[1] Pettersen, K. H., Lindén, H., Dale, A. M., and Einevoll, G. T. (2012). Extracellular spikes and CSD. *Handbook of Neural Activity Measurement*, 92-135.

[2] Gold, C., Henze, D. A., Koch, C., and Buzsáki, G. (2006). On the origin of the extracellular action potential waveform: a modeling study. *Journal of neurophysiology*, 95(5), 3113-3128.

[3] Kerekes, B. P., Tóth, K., Kaszás, A., Chiovini, B., Szadai, Z., Szalay, G., ... and Wittner, L. (2014). Combined two-photon imaging, electrophysiological, and anatomical investigation of the human neocortex in vitro. *Neurophotonics*, 1(1), 011013-011013.

[4] Katona, G., Szalay, G., Maák, P., Kaszás, A., Veress, M., Hillier, D., ... and Rózsa, B. (2012). Fast two-photon in vivo imaging with three-dimensional random-access scanning in large tissue volumes. *Nature methods*, 9(2), 201-208.

[5] Denk, W., Strickler, J. H., and Webb, W. W. (1990). Two-photon laser scanning fluorescence microscopy. *Science*, 248(4951), 73-76.

[6] Somogyvári, Z., Zalányi, L., Ulbert, I., and Érdi, P. (2005). Model-based source localization of extracellular action potentials. *Journal of neuroscience methods*, 147(2), 126-137.

[7] Somogyvári, Z., Cserpán, D., Ulbert, I., and Érdi, P. (2012). Localization of single cell current sources based on extracellular potential patterns: the spike CSD method. *European Journal of Neuroscience*, 36(10), 3299-3313.

[8] Nicholson, C., and Freeman, J. A. (1975). Theory of current source-density analysis and determination of conductivity tensor for anuran cerebellum. *Journal of Neurophysiology*, 38(2), 356-368.

[9] Mitzdorf, U. (1985). Current source-density method and application in cat cerebral cortex: investigation of evoked potentials and EEG phenomena. *Physiological reviews*, 65(1), 37-100.

[10] Pettersen, K. H., Devor, A., Ulbert, I., Dale, A. M., and Einevoll, G. T. (2006). Current-source density estimation based on inversion of electrostatic forward solution: effects of finite extent of neuronal activity and conductivity discontinuities. *Journal of neuroscience methods*, 154(1), 116-133.

VividSTORM: a new software for the correlated visualization and analysis of pixel intensity-based and localization microscopy data

Vivien MICZÁN
(Supervisors: Dr. István KATONA, Dr. András HORVÁTH)
Pázmány Péter Catholic University, Faculty of Information Technology and Bionics
50/a Práter utca, 1083 Budapest, Hungary,
Magyar Tudományos Akadémia Kísérleti Orvostudományi Kutatóintézet
43 Szigony utca, 1083 Budapest, Hungary
miczan.vivien@itk.ppke.hu

***Abstract*—Determining the nanoscale targeting and distribution of proteins within cells or cellular compartments is necessary to delineate the molecular mechanisms underlying physiological and pathophysiological processes of the nervous system. Single-Molecule Localization Microscopy (SMLM) offers a flexible and efficient way to obtain precise molecule localization data. However, its capability to visualize the respective cellular and subcellular context of molecular information is rather limited. To circumvent this obstacle, we recently developed a new approach, which combines SMLM with confocal microscopy for cell-type- and subcellular-compartment-specific nanoscale molecular imaging, and thereby facilitates functional interpretation of quantitative molecular observations. The correlated use of these two imaging modalities also require adequate software tools for the simultaneous visualization and handling of the different image types, e.g. for the filtering of respective SMLM coordinates belonging to the selected cell and subcellular compartment on the confocal image. Although the localization-based data are amenable for a wide variety of analysis approaches that are impossible to perform on conventional images, to date, these features have not been included in available software packages. Therefore, we developed VividSTORM, a unique tool for the correlated visualization and analysis of pixel intensity-based and localization microscopy data. By using VividSTORM, the custom subpopulations of SMLM localization points can be selected based on the cellular and subcellular environment with manual selection or by an automatic image segmentation method called Morphological Active Contours Without Edges (MACWE). As the next step, one can rapidly measure molecular abundance, clustering, internalization, receptor surface density, and inter-molecular distances on the selected localization points. The software is freely accessible with an easy-to-handle graphical user interface and the source code written in Python is also available for custom modifications *(www.katonalab.hu/vividstorm2)*. To demonstrate its usefulness, we employed VividSTORM and determined the nanoscale localization and abundance of molecular components of the endocannabinoid system at subcellular domains of specific cell types.**

***Keywords*-super-resolution; confocal microscopy; SMLM; VividSTORM**

I. Introduction

The mammalian brain is a rather complex organ, it is exceptionally hard to study. One of the major dimensions of this complexity is that there are about 100 billion neurons in 1000 cell types forming approximately 10^{14} synapses [1]. Thousands of different proteins are the building blocks of these synapses, and their quantity can differ in specific diseases even in a cell-type specific manner. For example in epilepsy the number of CB_1 receptors, which is the main player of the endocannabinoid system and controls synaptic communication, decreases in excitatory but increases in inhibitory axon terminals [2]. Another factor that adds to this complexity is that the proper targeting of molecules into specific nanodomains and multimolecular complexes is essential for the functioning synapses. For instance a 100 nm shift in the endocannabinoid synthesizing enzyme DGL-α underlies the Fragile-X syndrome and mental retardation [3]. So it is also necessary to monitor protein positions at the nanoscale. Taking these factors into consideration cell type-specific nanoscale molecular imaging is needed to bring us closer to understanding the physiological and pathophysiological functions of the brain.

So far electron microscopy with immunogold labelling has been the most used method for visualizing anatomical localization of synaptic proteins at nanometer-scale resolution. It also provides labelling of cellular membranes, but due to the highly complex nature of sample preparation high-throughput analysis, cell-type specific or multiple staining is limited and anisotropic shrinking of the sample may introduce artefacts [4]. In the case of classical fluorescent microscopy we can get higher experimental flexibility but orders of magnitude weaker resolution (2-300 nm of lateral and 5-600 nm of axial resolution) due to the longer wavelength of light. Recently several methods emerged to break the limitation of light diffraction, one of the main branches is single molecule imaging. The main concept behind it that the position of only one fluorophore can be determinded with arbitrary precision, and it is possible using special imaging medium that only a sparse subset of the fluorophores are emitting light at once. This way their images can be distinguished and their centroids determined with nm precision. If we iterate this stochastic process we can reconstruct the whole structure. Our method of choice, Stochastic Optical Reconstruction Microscopy (STORM) uses the stochastic photoswitching of organic dyes in thyiole-containing imaging buffer. It is a highly flexible method, capable of 3D and multi-channel imaging as well [4].
Considering the complex nature of brain circuits and the lacking investigation tools our aim was to develop an efficient approach for cell and cell-type specific nanoscale molecular imaging in the brain. Recently, we have developed an immunostaining and imaging protocol optimized for correlated confocal and super-resolution microscopy and since the analysis of the coordinate-based SMLM data needs special tools we

V. MICZÁN, "VividSTORM: a new software for the correlated visualization and analysis of pixel intensity-based and localization microscopy data" in *PhD Proceedings Annual Issues of the Doctoral School, Faculty of Information Technology and Bionics, Pázmány Péter Catholic University – 2016.* G. Prószéky, P. Szolgay Eds. Budapest: Pázmány University ePress, 2016, pp 73– 76.

developed an open-source visualization and analysis software named VividSTORM [5].

To demonstrate the utility of our approach we show the subcellular distribution of CB_1 receptors in axon terminals of individually filled interneurons. It is one of the most ubiquitously expressed a G-protein-coupled receptors in the brain and controls synaptic transmission. We study its distribution in the hippocampus where it is localized in huge quantity on GABAergic and at a much smaller extent on glutamatergic axon terminals [6], [7].

II. Materials and Methods

A. Preparation of tissue sections

All animal experiments were approved by the Hungarian Committee of the Scientific Ethics of Animal Research, and were performed according to the Hungarian Act of Animal Care and Experimentation. Minimal number of mice were sacrificed and all efforts were made to minimise pain. Adult wild type C57BL/6 mice were deeply anesthetised by 70 μL isoflurane and decapitated. Brains were removed from the skull and sliced to 300 μm in ice-cold ACSF using a Leica (Nussloch, Germany) VT-1000S vibratome and single-cell electrophysiological recording was performed with biocytin filling. Then slices were fixed overnight in a 4% paraformaldehyde (PFA) solution (dissolved in 0.1 M Phosphate buffer, PB, pH 7.4). After several washing steps in PB and TBS buffers the membranes were permeabilized by 2x30 minutes incubation in 0.5% Triton X-100 dissolved in TBS. Sections were then incubated in 1:1000 Alexa Fluor 488:streptavidin in TBS for 3 hours to visualize the biocytin filling. After washing steps in TBS and PB sections were mounted to glass slide, covered with Vectashield, coverslipped and sealed with nail polish. For morphological analysis imaging of the filled cells were performed by a NIKON C2 confocal scan head. After imaging, the sections were returned to PB and were embedded in 2% agarose and resliced in PB to achieve ideal section thickness (20 μm) for STORM imaging.

B. Immunostaining

Immunostaining was performed in BSA-treated 24-well plates in a free-floating manner. After washing in TBS buffer, nonspecific binding of antibodies was prevented by using 1% albumin from bovine serum (Sigma) dissolved in TBS. The following primary antibodies were used in TBS for overnight incubation on orbital shaker: guinea pig anti-CB_1 [8] 1:1000, mouse anti-Bassoon (ab82958, Abcam) 1:2000 and rabbit anti-TOM20 (Santa Cruz Biotechnology, cat. no. s-11415) 1:500. After several washing steps in TBS, slices were exposed to secondary antibodies for 4 hours in the following concentrations in TBS: anti-guinea pig Alexa-488-conjugated secondary antibody (Jackson) 1:400, anti-rabbit Alexa-647-conjugated secondary antibody (Jackson) 1:400 and anti-mouse CF-568-conjugated secondary antibody 1:1000 (Biotium). After washing in TBS and PB, slices were mounted and dried on #1.5 borosilicate coverslips which were previously cleaned with acetone. Coverslips with the samples were stored at $4\,^{\circ}\mathrm{C}$ until imaging. Right before STORM imaging slices were covered in imaging buffer optimized for STORM microscopy [9] and were placed on glass slides. The freshly prepared imaging medium contained the following ingredients: 5% glucose, 0.1 M mercaptoethylamine, 1 mg/ml glucose oxidase and catalase (2.5 μl/ml water-based solution from Sigma) dissolved in Dulbecco's PBS (Sigma). Coverslips were sealed with nail polish and imaged not more than 3 hours per sample.

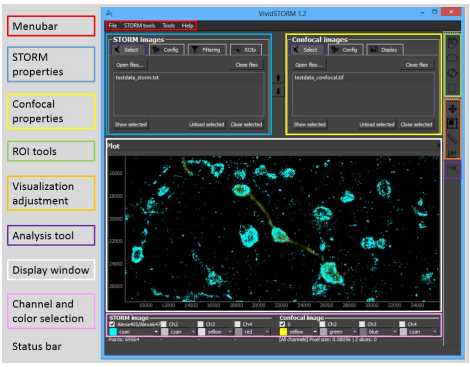

Fig. 1. Graphical user interface of VividSTORM

C. Correlated confocal and STORM imaging

The following equipment was used for STORM and confocal imaging: CFI Apo TIRF 100x objective (NA: 1.49) and Nikon Ti-E inverted microscope equipped with Nikon N-STORM system, C2 confocal scanner and Andor iXon Ultra 897 EMCCD camera. 3D STORM experiment was possible by using a cylindrical lense [10]. Imaging was controlled with Nikon NIS-Elements AR software equipped with N-STORM module. A 300 mW laser (VFL-P-300-647, MPB Communications, Montreal, Canada) was used for STORM imaging. Region of interests were selected based on an image acquired by 488 nm illumination. 488 nm, 561 nm 647 nm illumination was used for the confocal z-stack imaging (512x512x15 pixels, 78x78x150 nm resolution). STORM or DUAL filter cube (Nikon) and an EMCCD were used for STORM image acquisition. Low-intensity 405 nm activator (in order to achieve sparse activation of fluorophores) and high intensity 647 nm reporter illumination were used in 3000 cycles. A TIRF illuminator was utilized to prevent out-of-focus background. A Perfect Focus System was used to stabilise the focal plane. In order to minimize errors due to differences in antibody penetration, samples were collected from similar depths and only those localization points were counted that fell into a -300 to +300 nm range from the center plane to prevent errors caused by light scattering.

D. Correlated confocal and STORM analysis

Confocal stacks were deconvolved by using a classical maximum likelihood estimator algorithm with 40 iterations and theoretical point spread function with the Huygens software (SVI, Netherlands). STORM images were analysed with the STORM module of the NIS-Elements software to determine the coordinates of the localization points (LPs). Finding localization points and overlapping peaks was improved by a 3D-DAOSTORM algorithm [11]. Each image was analysed with the help of VividSTORM.

III. Results

A. Correlated visualization of confocal and STORM data

In contrast to electron microscopy, where the membranes and synapses are always visible, a STORM image does not have inherent benchmarks of the subcellular compartments, so we need additional tools to visualize the boundaries of the studied objects. We performed correlated confocal and

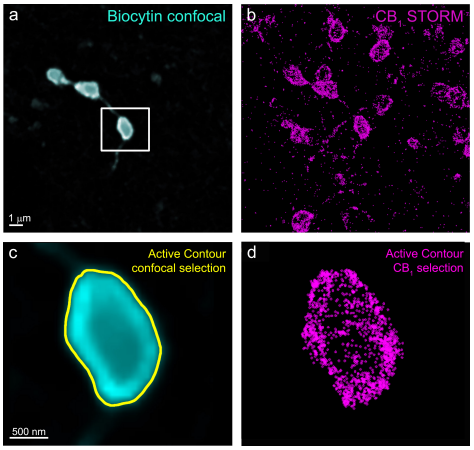

Fig. 2. Correlated visualization of confocal and STORM data and ROI selection with MACWE algorithm a) Deconvolved confocal image of an axon of an identified, biocytin-filled hippocampal interneuron. b) STORM image of anti-CB_1 immunostaining in the same field of view. c) Automatic axon terminal outline delineation performed by MACWE algorithm. d) Active contour selection allows for the unbiased and easy detection of CB_1 STORM localization points belonging to the same axon terminal based on the correlated confocal image of the bouton. The coordinates of the selected LPs can be shown and saved for the purpose of subsequent analysis.

STORM imaging to put the STORM coordinates to a cellular context namely to visualize the STORM localization points belonging to an individually selected cell. Handling the pixel-intensity image and molecule list together is not a trivial task, no available software tool existed previously for correlated confocal and STORM visualization. In many STORM studies localization data is discarded by rendering a pixelated image so the coordinate based STORM data analysis remained unexploited. Therefore we have developed a new stand-alone software with an easy-to-use graphical user interface (Figure 1.) to overcome the limitations of the correlated analysis of the two imaging approaches and published it along with a detailed sample preparation and imaging protocol for correlated confocal and STORM data acquisition [5]. The program can be used to open molecule lists and confocal images and display them together. Since the two images were taken with different cameras it is also essential to overlay them with mouse dragging or an automatic image registration method. Visualization properties can be adjusted for both modalities, and STORM data can be filtered for various attributes eg. local density, localization accuracy and z position.

B. ROI selection

An average workflow of correlated data analysis continues with the selection of the region of interest (ROI) (Figure 2.). It is also not trivial to decide which STORM coordinates belong to the ROI determined by the confocal image. In VividSTORM subsets of LPs can be specified using multiple ROI tools. Moreover, to facilitate the unbiased selection of labeled cellular profiles, we have implemented an automatic ROI selection tool Morphological Active Contours Without Edges (MACWE) [12] , which differs from the conventional threshold-based segmentation methods as it takes the shape of the selected area into consideration as well and can select object boundaries with varying pixel intensities. So we can separate the localization points belonging to our ROI easily and we can use them for further coordinate-based analysis.

C. Analysis of STORM data

To be able to analyze the extra information present in the molecule list data, we need tools that are different from the usual measurement functions in existing imaging softwares. We implemented the following ones in VividSTORM:

- We can measure **molecular abundance** in a region of interest so differences in protein number for example in different cell types or in response to a treatment can be uncovered.
- With 2D and 3D convex hulls **area and volume** of selected structures can be estimated.
- Also we can define **clusters** (Figure 3.) in the selected localization points based on their distance by using the DBSCAN algorithm [13], [14].

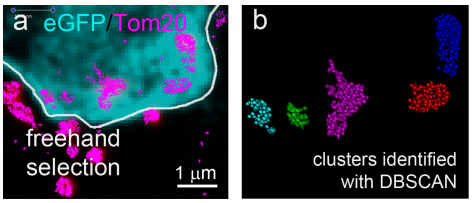

Fig. 3. Cluster analysis by VividSTORM a) Confocal images of EGFP fluorescence (cyan) and immunostaining against the mitochondrial protein Tom20 (red) were taken from transfected neuroblast cells. Tom20-immunostaining was also imaged in 3D-dSTORM mode (magenta). The corresponding confocal and STORM images were overlaid in VividSTORM, and a local density filter was applied on the STORM data. To analyze the number and size of individual mitochondria in transfected neuroblast cells, a freehand ROI containing the cell body of the EGFP-expressing cell was selected. The LPs located within the ROI were passed for cluster analysis. b) The resulting clusters, each representing individual mitochondria, are displayed in different colors.

- The relative position of localization points can be determined from the surface of the structure, and for example receptor **internalization indices** can be calculated (Figure 4.) [14].

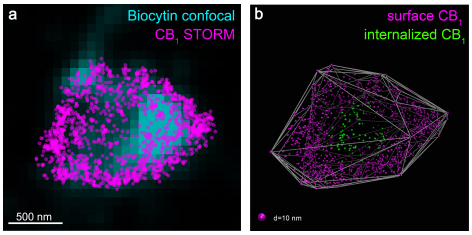

Fig. 4. Internalization analysis by VividSTORM a) Overlaid confocal and CB_1-STORM image of an axon terminal of a biocytin-filled hippocampal CA1 interneuron. b) Internalization index (d/r) for each CB_1-LP was calculated, where d is the distance from the center of mass of all the LPs in the channel, and r is the estimated radius of the signal (radius of a circle with the area of the 2D convex hull fitted on the data). This measure is sensitive to a shift of the localizations towards the center of the structure thus capable of discriminating between internalized (green) and surface (magenta) receptors. The output is visualized in the VMD software.

- **Surface density** of the receptors can be measured based on the number of LPs that are in a predefined vicinity of random sampling points on the hull surface (Figure 5.) [14].
- **Intermolecular distance distributions** can be calculated based on Euclidean distance and surface distance (Figure 6.) [14].

Our correlated imaging approach is not only useful in brain samples but it can be used for cell-type specific investigation

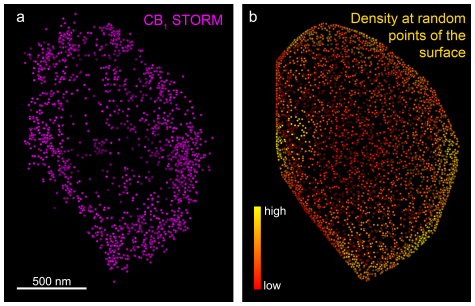

Fig. 5. Surface density analyis by VividSTORM a) CB_1 staining of an axon terminal of a hippocampal interneuron visualized in 3D by VividSTORM. b) Random sampling points were placed on the surface of the 3D convex hull of the bouton and were colored according to the local surface density of CB_1 receptors.

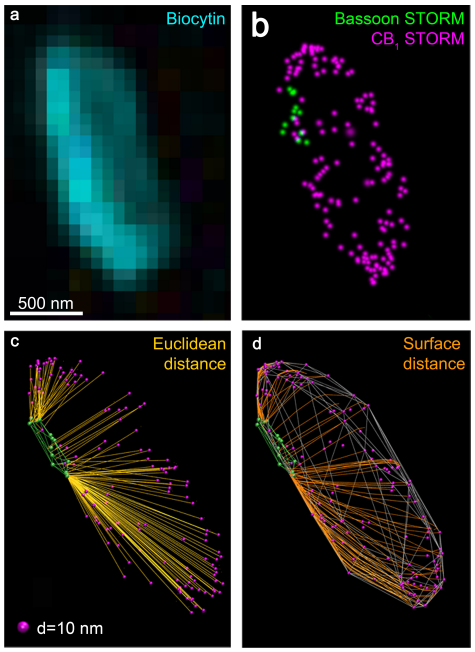

Fig. 6. Analysis of inter-molecular distances by VividSTORM a) Deconvolved confocal image of an axon terminal of an identified, biocytin-filled hippocampal interneuron. b) A dual channel 3D-STORM image of immunostaining against CB_1 receptors (magenta) and the presynaptic active zone protein bassoon (green). c) Euclidean distances between CB_1 and bassoon LPs are shown. d) To allow intermolecular distance measurements along the structure surface, the shortest paths between CB_1 and bassoon LPs on the bouton surface were determined after fitting a 3D-convex hull on the CB_1 localization points. The coordinates of CB_1 LPs (magenta), convex hull edges (silver), and minimal distance trajectories (orange) were saved in pdb file format and then rendered in a separate software, Visual Molecular Dynamics (VMD).

of protein distribution in heart and kidney samples as well [5]. With the help of the presented measurements we answered biological questions like cell type specific differences between synapse organization and molecular redistribution of CB_1 receptors in chronic cannabis consumption model [14]. We studied the molecular anatomical effect of acute pharmacological manipulations, and the internalizaion of CB_1 receptors due to external agonist [15].

IV. Conclusion

We have developed an open-source software called VividSTORM with an easy-to-use graphical user interface for correlated confocal and STORM super-resolution image analysis. The software facilitates cell-type-specific nanoscale molecular imaging in various tissue samples and allows quantitative analysis of protein distributions in a compartment-specific manner.

Acknowledgements

I would like to thank my supervisors Dr. István Katona and Dr. András Horváth and Barna Dudok, László Barna, Judit Glavinics, Zsófia László, Balázs Pintér, Erika Tischler, Sándor Turbucz and all members of the Laboratory of Molecular Neurobiology of the IEM-HAS for help and support. Anti-CB_1 antibody was a gift from Masahiko Watanabe.

References

[1] R. W. Williams and K. Herrup, "The control of neuron number," *Annual Review of Neuroscience*, vol. 11, no. 1, pp. 423–453, 1988. PMID: 3284447.

[2] A. Ludanyi, L. Eross, S. Czirjak, J. Vajda, P. Halasz, M. Watanabe, M. Palkovits, Z. Magloczky, T. F. Freund, and I. Katona, "Downregulation of the cb1 cannabinoid receptor and related molecular elements of the endocannabinoid system in epileptic human hippocampus," *J Neurosci*, vol. 28, no. 12, pp. 2976–90, 2008.

[3] K.-M. Jung, M. Sepers, C. M. Henstridge, O. Lassalle, D. Neuhofer, H. Martin, M. Ginger, A. Frick, N. V. DiPatrizio, K. Mackie, I. Katona, D. Piomelli, and O. J. Manzoni, "Uncoupling of the endocannabinoid signalling complex in a mouse model of fragile x syndrome," *Nature Communications*, vol. 3, p. 1080, sep 2012.

[4] L. Schermelleh, R. Heintzmann, and H. Leonhardt, "A guide to super-resolution fluorescence microscopy," *J Cell Biol*, vol. 190, pp. 165–175, jul 2010.

[5] L. Barna, B. Dudok, V. Miczán, A. Horváth, Z. I. László, and I. Katona, "Correlated confocal and super-resolution imaging by VividSTORM," *Nat Protoc*, vol. 11, pp. 163–183, dec 2015.

[6] R. I. Wilson and R. A. Nicoll *Nature*, vol. 410, pp. 588–592, mar 2001.

[7] T. Ohno-Shosaku, T. Maejima, and M. Kano, "Endogenous cannabinoids mediate retrograde signals from depolarized postsynaptic neurons to presynaptic terminals," *Neuron*, vol. 29, pp. 729–738, mar 2001.

[8] Y. Fukudome, T. Ohno-Shosaku, M. Matsui, Y. Omori, M. Fukaya, H. Tsubokawa, M. M. Taketo, M. Watanabe, T. Manabe, and M. Kano, "Two distinct classes of muscarinic action on hippocampal inhibitory synapses: M2-mediated direct suppression and m1/m3-mediated indirect suppression through endocannabinoid signalling," *Eur J Neurosci*, vol. 19, no. 10, pp. 2682–92, 2004.

[9] A. Dani, B. Huang, J. Bergan, C. Dulac, and X. Zhuang, "Superresolution imaging of chemical synapses in the brain," *Neuron*, vol. 68, no. 5, pp. 843–56, 2010.

[10] B. Huang, W. Wang, M. Bates, and X. Zhuang, "Three-dimensional super-resolution imaging by stochastic optical reconstruction microscopy," *Science*, vol. 319, no. 5864, pp. 810–3, 2008.

[11] H. Babcock, Y. M. Sigal, and X. Zhuang, "A high-density 3d localization algorithm for stochastic optical reconstruction microscopy," *Opt Nanoscopy*, vol. 1, no. 6, 2012.

[12] P. Marquez-Neila, L. Baumela, and L. Alvarez, "A morphological approach to curvature-based evolution of curves and surfaces," *IEEE Transactions on Pattern Analysis and Machine Intelligence*, vol. 36, pp. 2–17, jan 2014.

[13] M. Ester, H.-P. Kriegel, J. Sander, and X. Xu, "A density-based algorithm for discovering clusters in large spatial databases with noise," pp. 226–231, 1996.

[14] B. Dudok, L. Barna, M. Ledri, S. I. Szabó, E. Szabadits, B. Pintér, S. G. Woodhams, C. M. Henstridge, G. Y. Balla, R. Nyilas, C. Varga, S.-H. Lee, M. Matolcsi, J. Cervenak, I. Kacskovics, M. Watanabe, C. Sagheddu, M. Melis, M. Pistis, I. Soltesz, and I. Katona, "Cell-specific STORM super-resolution imaging reveals nanoscale organization of cannabinoid signaling," *Nature Neuroscience*, vol. 18, pp. 75–86, dec 2014.

[15] S.-H. Lee, M. Ledri, B. Toth, I. Marchionni, C. M. Henstridge, B. Dudok, K. Kenesei, L. Barna, S. I. Szabo, T. Renkecz, M. Oberoi, M. Watanabe, C. L. Limoli, G. Horvai, I. Soltesz, and I. Katona, "Multiple forms of endocannabinoid and endovanilloid signaling regulate the tonic control of GABA release," *Journal of Neuroscience*, vol. 35, pp. 10039–10057, jul 2015.

Different Brain Computer Interface approaches to detect motor planning and execution

Tamás MOLNÁR
(Supervisors: Loránd ERŐSS, MD, PhD; Kristóf KARACS, PhD)
Pázmány Péter Catholic University, Faculty of Information Technology and Bionics
Práter utca 50/a, Budapest H-1083, HUNGARY
tamas.molnar@itk.ppke.hu

***Abstract*—The last several years have brought a debate among Brain-Computer Interface (BCI) researchers whether to use invasive or non-invasive setups for their experiments. In this paper the experience with three distinctive methods for motor related tasks is reported. Participants performed motor related tasks which were recorded with different BCI systems. The recordings were then analyzed and compared. The study concludes that for very basic tasks the used non-invasive system could give satisfactory results but for more complicated tasks the invasive systems performed better and were more reliable.**

***Keywords*-Brain Computer Interface; Motor cortex; CNS injury**

I. Introduction

A serious car accident or sometimes even just a small injury can alter someone's life depending on the location of the damage in the human body. A crucial part of our nervous system, the motor system may be damaged selectively at the level of the primary motor cortex, the spinal cord, the peripheral nerves or the muscles, resulting in the otherwise intact brain being unable to control body functions and movements. Such a damage can cause a decrease in life quality, especially in terms of communication and mobility [1]. Amyotrophic lateral sclerosis (ALS, Lou Gehrig's disease) is a well-known example of such a selective motor damage. Brain-computer interfaces can help in these cases to replace the missing link between the brain and the environment. The basic idea of a BCI is that intact brain areas are capable of producing signals which can be translated as inputs into a computer that can drive a communication interface [2] or an external prosthetic device [3] to restore the patient's communication or movement abilities.

Two main types of BCI devices can be distinguished: 1) invasive and 2) non-invasive. Invasive BCIs require intracranially implanted electrodes, while non-invasive ones use electric signals recorded from the scalp [4]. Both invasive and non-invasive BCIs then process these signals and translate them into commands for an external device. However, there are certain input signals such as unit activities, used to control very fine movements, which can be detected only invasively. Not only the signal but also the cost, the easiness of the application, or the stability of action differs between the two approaches. Non-invasive systems are easy to install, offer minimal discomfort and are relatively cheap. On the other hand, invasive systems offer superior temporal and spatial resolution [5].

This paper describes three different types of BCI approaches with their advantages and disadvantages when used to detect motor planning and execution. One device is commercially available and is fully non-invasive, the Emotiv Epoc, based on electroencephalography (EEG). The second approach is a semi-invasive one as it is based on implanting electrodes on the surface of the cortex: this is generally known as electrocorticography (ECoG). The third one is a fully invasive system, which relies on an implanted array in the motor cortex, and it not only records Local Field Potentials (LFP) but spike activity as well.

II. Non-invasive technique

Fig. 1. Emotiv Epoc

Three participants were assessed with the Emotiv system (Figure 1) during a 30 minute examination for repetitive, self-paced Finger Tapping (FT, about 200 times each trial, 1 Hz). The electrodes were placed in saline water and then fixed on the surface of the participants' head. Following contact-voltage tests recordings were performed. The system allowed for the monitoring of the whole scalp albeit with low spatial and temporal resolution due to coverage (in space, low electrode density) and sampling rate (in time, 128 Hz).

Following the calculation of FT button press averages, Morlet-wavelet time-frequency analysis (plotted up to 43 Hz only, as the system has a cut-off frequency at that point) revealed event related changes in the power spectrum around the finger tapping (Figure 2, red line is t=0 the FT event) albeit with poor reliability across all three participants.

III. Partially invasive technique

Eight participants with therapy resistant focal epilepsy were implanted with subdural strip or grid electrode arrays over the sensory-motor region (Figure 3) as part of their evaluation for epilepsy surgery in order to determine the exact location of

T. MOLNÁR, "Different Brain Computer Interface approaches to detect motor planning and execution" in *PhD Proceedings Annual Issues of the Doctoral School, Faculty of Information Technology and Bionics, Pázmány Péter Catholic University – 2016.* G. Prószéky, P. Szolgay Eds. Budapest: Pázmány University ePress, 2016, pp 77– 80.

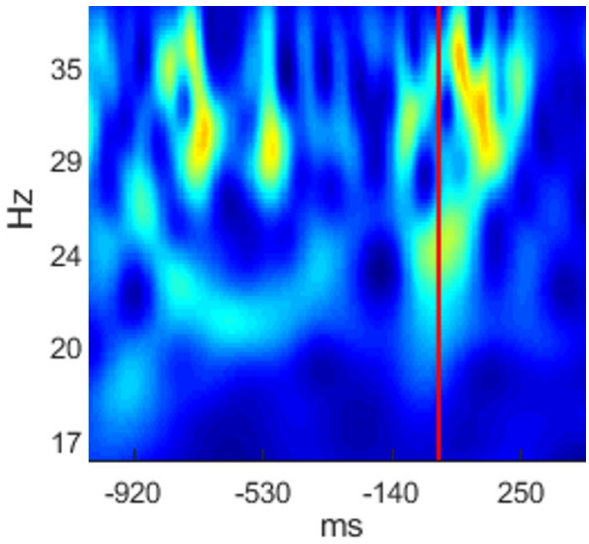

Fig. 2. Power on electrode T7

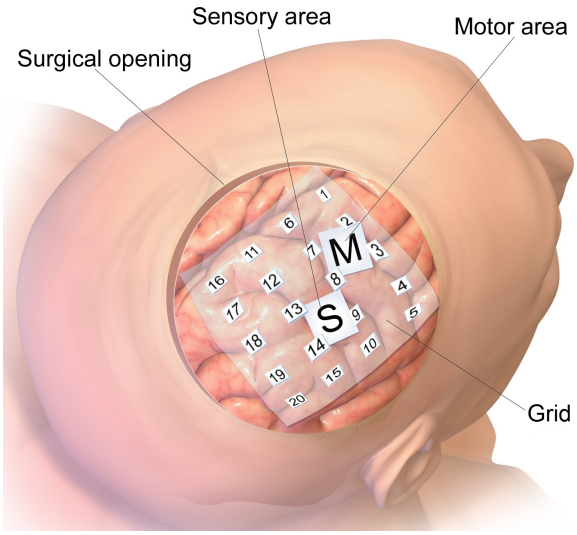

Fig. 3. Electrocorticography

epileptic focus. Motor related potentials were evoked by self-paced (around 1 Hz) finger tapping (about 150 times for each trial) of the contralateral hand relative to the implantation side. Recording was carried out at 1024 Hz.

FT button press averages were calculated and time-frequency analysis was performed using the event related spectral perturbation method. Changes in a low (8-30 Hz, alpha and beta) and in a high (above 30 Hz) frequency band were assessed. Decrease in spectral power was observed in the lower frequency band on the implanted electrodes. This event related desynchronization (ERD) was detected across all examined patients. The ERD typically began slightly before the FT event. Additionally, in a few cases this ERD was associated with an event related synchronization (ERS) in the high frequency band (one of the electrodes recording this phenomena is labeled on Figure 4 and its power shown on Figure 5, t=0 is the FT event).

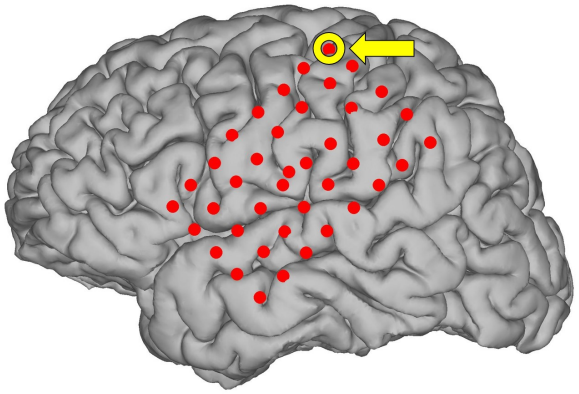

Fig. 4. Implanted grid array

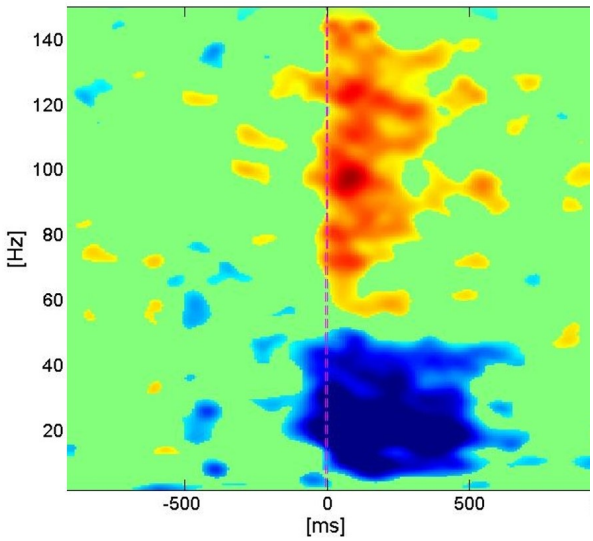

Fig. 5. Power on electrode 8

IV. Fully invasive technique

Two non-human primates (NHP) were implanted with Utah arrays (Figure 6) in their primary motor area (M1). The NHPs participated in tasks where they were instructed to wait for a visual signal coding for to move and grab the object which was presented in front of them. There were about 150-200 completed trials each dataset. Neural activity was recorded at 20 000 Hz.

Following averaging across all trials and electrodes the LFP power spectrum was visualized using the multi-taper spectral estimation method (Figure 7). Changes in the power spectrum were analyzed in two categories: low (beta band) 13-30 Hz, and high (gamma band) 125-140 Hz. Around the start of movement, changes in the power of these bands were detected (decrease or increase, appearing as valleys and peaks) as reported on Figure 8 and Figure 9, shown from one of the datasets. The blue line represents averaged power value, red bars show standard deviation, t=0 is the start of movement.

Using a peak detector algorithm on the LFP dataset, the peaks in the power spectrum as predictors for start of movement can be classified and then evaluated if they were correctly chosen or not. To measure for the accuracy of this prediction, the F1-score (has its best value at 1 and worst at 0) was used as follows:

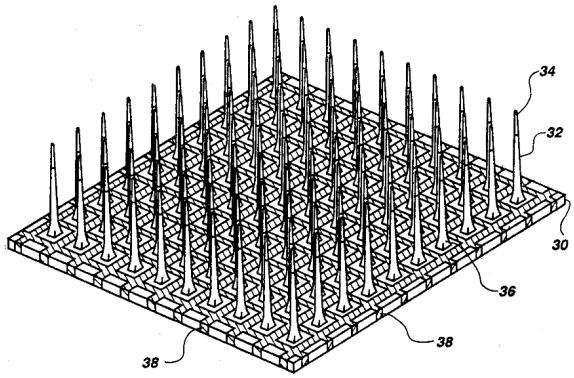

Fig. 6. Utah array

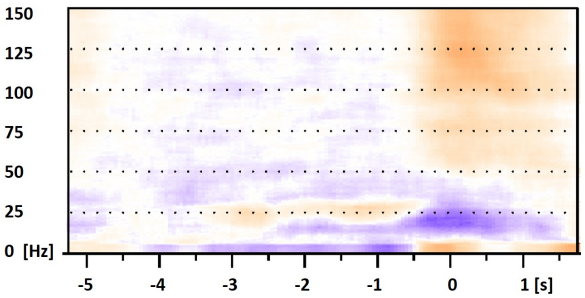

Fig. 7. Power average on all electrodes

$$F_1 = 2 \cdot \frac{precision \cdot recall}{precision + recall} \tag{1}$$

where

$$precision = \frac{tp}{tp + fp} \tag{2}$$

and

$$recall = \frac{tp}{tp + fn} \tag{3}$$

True Positive (tp) represent a correctly classified event, False Positive (fp) stands for an incorrect hit, while False Negative (fn) is a missed prediction. This metric was also used to evaluate predicating using spike rates. Spike activity from the same dataset used for the LFP power spectrum analysis was investigated. Peaks were identified in the spike rates to predict for the onset of movement – this is displayed on Figure 10 showing the change in spike rate over time. Dashed lines represent start of movements.

To compare the efficiency of using peak detection in the LFP and spike rate data for start of movement detection the F1-score is given with also the percentage of True Positives, False Positives and False Negatives relative to the number of all real events. A predicted event is considered True Positive if it falls in the 1 s long time bin placed symmetrically on the real event (0.5 second before and after). Table 1 shows that prediction using power changes in the gamma band or spike rate yields better results compared to using changes in the beta band (based on the comparison of respective F1-scores).

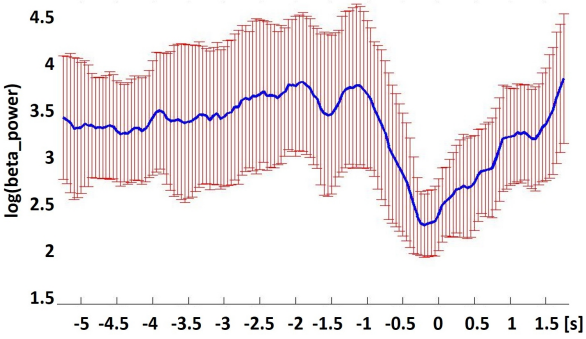

Fig. 8. Beta power

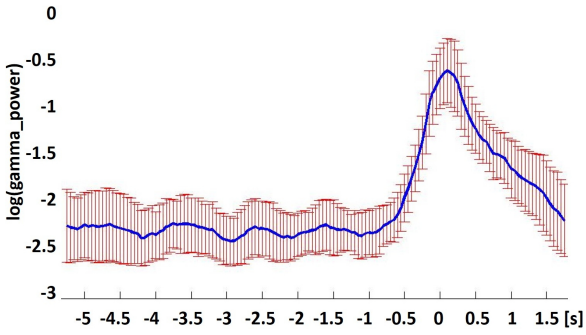

Fig. 9. Gamma power

V. Discussion

The phenomena of changes in power over the cortex was detected with all three methods. Ultimately the invasive systems proved to be offering a much finer way to investigate these changes. For very basic tasks the signal extracted using the Emotiv system could be feasible enough as simple operations are already available using this system [6]. The ease of application is certainly a great benefit of this BCI, however it seems that for effective BCI applications based on changes in the power spectrum, either more sophisticated EEG systems [7], or invasive systems such as the two described in this paper are needed.

The detailed understanding of movement related potentials

TABLE I
Comparison of methods

NHP 1	Method	True Positives	False positives
	Beta band	60%	89%
	Gamma band	97%	20%
	Spike rate	100%	9%
	Method	False Negatives	F1-score
	Beta band	40%	**0.49**
	Gamma band	3%	**0.89**
	Spike rate	0%	**0.96**
NHP 2	Method	True Positives	False Positives
	Beta band	57%	103%
	Gamma band	97%	7%
	Spike rate	100%	5%
	Method	False Negatives	F1-score
	Beta band	43%	**0.45**
	Gamma band	3%	**0.95**
	Spike rate	0%	**0.98**

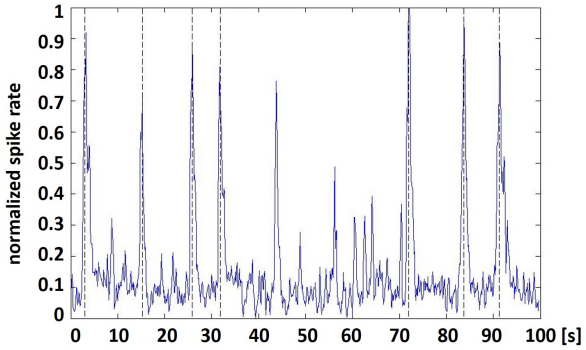

Fig. 10. Normalized spike rate

can lead to better BCI applications. This study only analyzed effective movements but motor imaginary could be enough to create similar electrical responses that have been evaluated in this paper. Patients without the ability to move their limbs can still imagine movements and the electrical responses can be used in a BCI system to e.g. control a wheelchair [8]. Further investigations are required to have a better understanding of motor imagery when contrasting non-invasive and invasive BCI systems.

ACKNOWLEDGEMENTS

For the guidance and support, from my supervisors, Dr. Loránd Erőss and Dr. Kristóf Karacs. For the help received from the VLSI Lab at Pázmány Péter Catholic University, the Erőss Lab at the National Institute of Clinical Neurosciences, the Ulbert Lab at the Hungarian Academy of Sciences, and the Donoghue Lab at Brown University.

REFERENCES

[1] A. B. Jackson, M. Dijkers, M. J. DeVivo, and R. B. Poczatek, *A demographic profile of new traumatic spinal cord injuries: Change and stability over 30 years*, Archives of Physical Medicine and Rehabilitation, vol. 85, no. 11, pp. 1740–1748, November, 2004.

[2] N. G. N. Birbaumer, T. Hinterberger, I. Iversen, B. Kotchoubey, A. Kübler, J. Perelmouter, E. Taub and H. Flor, *A spelling device for the paralysed*, Nature, vol. 398, no. 6725, p. 297, March 25, 1999.

[3] L. R. Hochberg, D. Bacher, B. Jarosiewicz, N. Y. Masse, J. D. Simeral, J. Vogel, S. Haddadin, J. Liu, S. S. Cash, P. van der Smagt, and J. P. Donoghue, *Reach and grasp by people with tetraplegia using a neurally controlled robotic arm*, Nature, vol. 485, no. 7398, pp. 372–375, May 17, 2012.

[4] M. A. Lebedev, and M. A. Nicolelis, *Brain–machine interfaces: past, present and future*, TRENDS in Neurosciences, vol. 29, no. 9, pp. 536–546, September, 2006.

[5] N. Birbaumer, L. G. Cohen, *Brain–computer interfaces: communication and restoration of movement in paralysis*, The Journal of Physiology, vol. 579, Issue 3, pp. 621–636, March, 2007.

[6] L. Mayaud, M. Congedo, A. Van Laghenhove, D. Orlikowski, M. Figère, E. Azabou, F. Cheliout-Heraut, *A comparison of recording modalities of P300 event-related potentials (ERP) for brain-computer interface (BCI) paradigm*, Clinical Neurophysiology, vol. 43, issue 4, pp. 217–227, October, 2013.

[7] Siamac Fazli, Jan Mehnert, Jens Steinbrink, Gabriel Curio, Arno Villringer, Klaus-Robert Müller, Benjamin Blankertz, *Enhanced performance by a hybrid NIRS–EEG brain computer interface*, NeuroImage, vol. 59, issue 1, pp. 519–529, January, 2012.

[8] F. Galán, M. Nuttin , E. Lew, P.W. Ferrez, G. Vanacker, J. Philips, J. del R. Millán, *A brain-actuated wheelchair: Asynchronous and non-invasive Brain–computer interfaces for continuous control of robots*, Clinical Neurophysiology, vol. 119, issue 9, pp. 2159–2169, September, 2008.

Simulation of Hawkes-processes to analyze the self-exciting nature of epilepsy

György PERCZEL
(Supervisor: Loránd ERŐSS, László GERENCSÉR, Zsuzsanna VÁGÓ)
Pázmány Péter Catholic University, Faculty of Information Technology and Bionics
50/a Práter street, 1083 Budapest, Hungary
National Institute of Clinical Neurosciences, Department of Functional Neurosurgery
57. Amerikai street, 1145 Budapest, Hungary
perczel.gyorgy.miklos@itk.ppke.hu

***Abstract*—Epileptic seizure with regard to their dynamics are often paralleled to earthquakes and financial crises where small and seemingly insignificant microscopic events interact and eventually grow into large, macroscopically observable phenomena. Based on these analogies, modeling of epileptic patients' electroencephalographic (EEG) signals with non-linear stochastic systems with a certain feedback effect or self-excitation was previously proposed. Following the practice in seismology, we focus on point processes defined in terms of level crossings or high frequency oscillations (HFO) of the EEG signals. Thus we arrive at the concept of self-exciting point processes introduced by Hawkes in 1971. The validation of this model in the field of neuroscience requires the simulation and statistical analysis of Hawkes processes, such as fitting, classification and real-time change detection. In this work we focus on simulating Hawkes processes in real-time for a wide class of response functions, extending the results given previously by others, in particular by Ozaki. In addition we provide experimental results for fitting a Hawkes process, using an off-line maximum likelihood method to real data, both prior to and during seizure.**

***Keywords*-epilepsy; seizure detection; point process**

Statement of originality:
This report describes the work of the doctoral student during the academic year 2015/2016. Parts of this work might be under submission to scientific conferences and journals.

I. Introduction

Epilepsy is one of the most common neurological disease worldwide with a prevalence of 0.5-1%. It presents in the form of seizures such as, muscle contractions or transient loss of consciousness. Among other causes the disease can be a result of genetic and congenital abnormalities, perinatal brain injury, infections, head trauma, stroke. However, 6 out of 10 cases are idiopathic, i.e. without any identifiable cause. Despite the wide variety of medications, only 70% of patients can be sufficiently treated with drugs. The remaining 30% may benefit from surgical interventions, including the resection of the epileptogenic focus or deep brain stimulation[1].

The patients' quality of life (QoL) is largely dependent of the seizures themselves. It should be stressed that only very modest improvement of QoL can be achieved via the *reduction* of seizure frequency [2]. It is generally accepted that even at low seizure rates patients' interictal time is still determined by the fear of an impending seizure. Thus, an appropriate seizure prediction system would significantly enhance the QoL even without any intervention. This positive effect should be amplified via the application of on-demand therapeutic devices, such as an implantable electrical stimulating or drug delivery system to prevent the onset of seizures.

Prediction of epileptic seizures has a long and extensive history. Regarding the underlying pathophysiology, we may distinguish between sudden onset seizures such as the ones observed in primary generalized epilepsy and the ones in focal epilepsies that evolve as a cascade of changes [3]. Naturally, one would assume, that no matter how abrupt an event in nature is, at some scale of time and size it would be preceded by some kind of presage. This hypothesis of preictal state is supported by the observation of increased blood oxygen-level-dependent signal and changes in heart rate before seizures [3].

However, early and specific phenomena that would indicate a forthcoming seizure with high fidelity is still lacking. The general approach to identify this is to derive a measure from the EEG signal that would have a well observable change-point only before seizures. A variety of static and dynamic mathematical models have been proposed to derive such measures, including linear and non-linear dynamic models, ARMA modeling, or analysis of phase-synchrony of the signals [3]. Nonetheless, only very few methods exceeded above-chance results yet [4].

A difficulty in identifying adequate measures can be described as the problem of coarse-graining [5]. Starting from a solid model based approach where the computational costs are too high, we aim to reduce the degree of freedom to the dimensionality essentially needed to solve the exact problem. However, as we reduce the amount of data, we may lose essential information. Thus, we are looking for a mesoscopic model that is precise enough the answer our question, but which is still computationally manageable. For that reason, we chose to mimic the expert medical analysis of an EEG signal by specifying and identifying points of interest, such as level crossing or HFO-s, and then perform a statistical analysis of the derived point process. searching for an appropriate probabilistic model for these point processes we choose a class reflecting some of the mechanisms that generate electric signals inside the brain, such as interconnection and feedback, or self-excitation.

Hawkes' self-exciting point processes have been previously used to forecast earthquakes, based on the similarities in the mathematical concepts describing the brain and the upper crust of the Earth [5]. In the field of neurosciences this tool has been applied only to model neural interactions regarding spikes as events [6], [7], and our aim was to examine the heuristic findings of the EEG with such a model.

Gy. PERCZEL, "Simulation of Hawkes-processes to analyze the self-exciting nature of epilepsy" in *PhD Proceedings Annual Issues of the Doctoral School, Faculty of Information Technology and Bionics, Pázmány Péter Catholic University – 2016.* G. Prószéky, P. Szolgay Eds. Budapest: Pázmány University ePress, 2016, pp 81– 84.

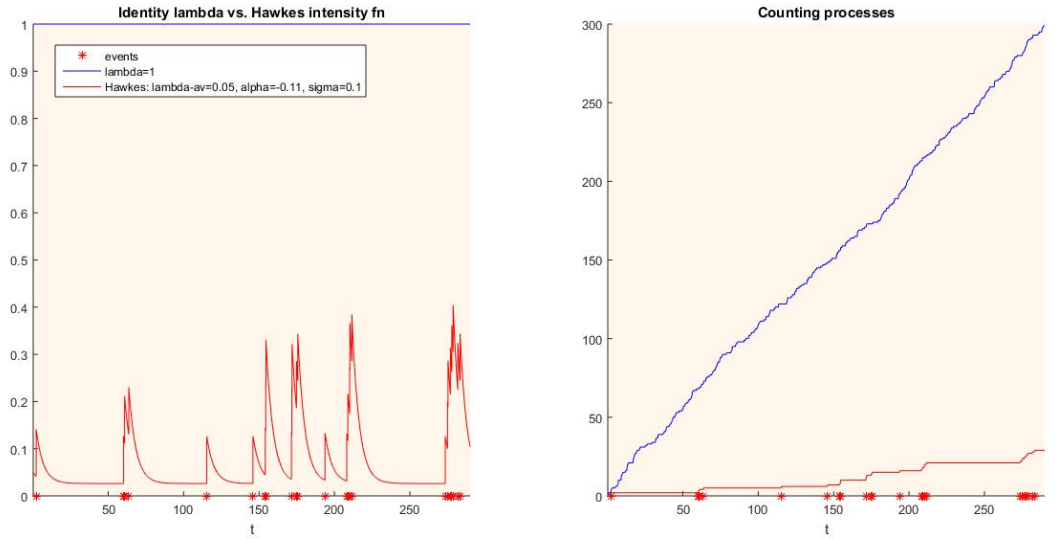

Fig. 1. Observe Hawkes process' (red) increased intensity function after each event (asterisk) resulting in increased probability of events to occur in a small neighboring interval, leading to cluster formation that is represented as rapid increments of the otherwise declivous graph of the counting process. As a reference, unit rate Poisson process is also indicated (blue).

II. Background and Methods

A. Hawkes processes

Let us consider a stationary point process as events given with the time of their occurrence $(T_0 = 0 < T_1 < ... < T_n < ...)$ and its counting process N_t (the cumulative number of events up to time t). According to [8], if the process is self-exciting, then its intensity function can be written as

$$\lambda_t = \mu + \int_{-\infty}^{t} g(t-s)dN_s \tag{1}$$

, where μ represents the baseline intensity, while $g(u)$ is the response function, i.e. the effect of an event on the intensity function of the process. If $\bar{\lambda} = E(\lambda_t)$ then the intensity function can be separated as follows:

$$\lambda_t = \lambda_t^0 + \bar{\lambda} \tag{2}$$

Thus, the following dynamic equation holds:

$$d\lambda_t = \alpha\lambda_t^0 dt + \sigma(dN_t - \lambda_t dt) \tag{3}$$

,with parameter α and σ representing the decaying coefficient and the growth of the intensity at every event, respectively. Solving this inhomogeneous linear differential equation, we receive

$$\lambda_t = \frac{\alpha\bar{\lambda}}{\alpha-\sigma} + \int_{-\infty}^{t} \mathrm{e}^{(\alpha-\sigma)(t-s)}\sigma dN_s \tag{4}$$

Thus, the dynamic form (i.e. eq.(3)) of eq.(1) holds.

B. Simulation

However, as the intensity function is continuous on every $[T_{n-1}, T_n)$ interval, on such a period eq.(4) can be simplified to

$$\lambda_t = \left(\lambda_{T_{n-1}} - \frac{\alpha\bar{\lambda}}{\alpha-\sigma}\right)\mathrm{e}^{(\alpha-\sigma)(t-T_{n-1})} + \frac{\alpha\bar{\lambda}}{\alpha-\sigma} \tag{5}$$

This means that the intensity function on every inter-event interval (IEI) is integrable, thus we can apply the time-rescaling theorem on these intervals. This follows that with the aid of a unit-rate Poisson process we can simulate a Hawkes-process. Below we summaries the steps of such simulation.

1) Define starting point $(T_{n-1}; \lambda_{T_{n-1}})$
   1.1. Solve $I\tilde{E}I_n = \int_{Tn-1}^{T_n} \lambda_t dt$ for T_n, thus generate T_n
   1.2. Update parameters: $\lambda_{T_n} = \lambda_t(T_n) + \sigma$
2) Iterate 1-1.2

Note that $I\tilde{E}I_n$ represents the IEI of a unit rate Poisson-process. We also remark that the solution of 1.1 can be done in a closed form using the *Lamber-W function*.

C. Deriving point processes from the EEG signal

EEG data of an epileptic patient containing about half-an-hour preictal period and a consecutive seizure was retrieved from the database of the Epilepsy Monitoring Unit (National Institute of Clinical Neurosciences, Hungary). The signals were preprocessed using 1-10 Hz 4$^{\text{th}}$ order Butterworth band-pass filter. Amplitude-threshold crossing was then applied to reduce the time series data to a point process.

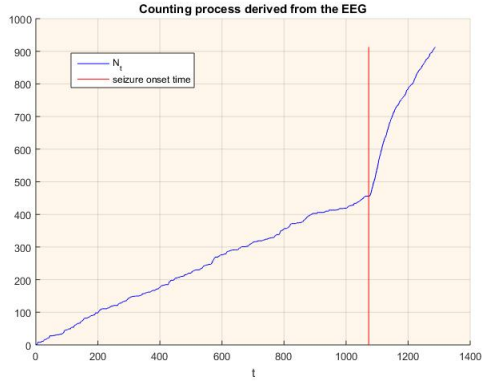

Fig. 2. Counting process (blue) based on thresholding of the band-pass filtered EEG. Seizure onset time is represented by the vertical line (red). Note the abrupt change of intensity at the onset of seizure.

D. Maximum likelihood estimation (MLE)

We computed the negative log-likelihood function (NLL) of Hawkes processes according to [9] and carried out nonlinear optimization in MATLAB (MathWorks, Inc.) to perform MLE on every 60s non-overlapping window.

III. Simulation and Results

In our experiment we simulated Hawkes' self-exciting point processes using the dynamic form in which we rewrote the intensity function. Figure 1 represents the result of our simulation.

We derived a point process from an EEG time series containing both preictal and ictal patterns. Its counting process can be seen on figure 2.

Estimation of the model's parameters was done via MLE however, we received parameter-estimates of the point process that are difficult to interpret(figure 3).

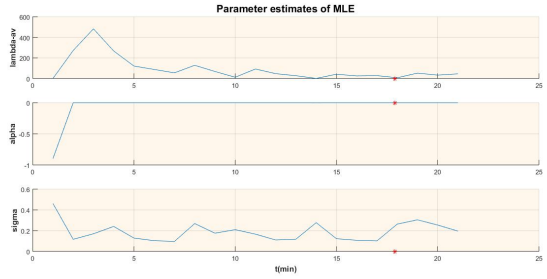

Fig. 3. Parameters of Hawkes process, as the result of MLE for every 60s windows. With red asterisk seizure onset time is labeled.

We performed analysis of the parameter-space $NLL\left(\bar{\lambda}, \alpha, \sigma\right)$ (figure 4) to better understand the task of minimization. All surfaces are presented with their constraints on the $\bar{\lambda}; \alpha; \sigma \in [-1, 1]$.

IV. Conclusion

We successfully simulated Hawkes processes (figure 1) and derived a point process from an EEG that was affected by an epileptic seizure. Though we have yet to quantify the changes of the counting process, abrupt alteration of the process is well observable (figure 2). Despite that ictal onset is clearly visible in the counting process, we received parameter-estimates using MLE of the data that is difficult to interpret (figure 3). Thus, we examined the parameter-space, and multiple local minima can be clearly observed on all three graphs (figure 4). As a preliminary study, our aim was to create a framework for the parameter estimation of a self-exciting point process. However, the next obvious step is to quantify our results and errors and to implement a more robust optimizing method.

Acknowledgment

I would like to express my gratitude for all the help I received from the colleagues in the National Institute of Clinical Neurosciences, especially to Dániel FABÓ and Emília TÓTH.

References

[1] WHO, "Epilepsy," 2016. [Online]. Available: http://www.who.int/mediacentre/factsheets/fs999/en/

[2] B. N. Blond, K. Detyniecki, and L. J. Hirsch, "Assessment of Treatment Side Effects and Quality of Life in People with Epilepsy," *Neurologic Clinics*, vol. 34, no. 2, pp. 395–410, 2016. [Online]. Available: http://dx.doi.org/10.1016/j.ncl.2015.11.002

[3] F. Mormann, R. G. Andrzejak, C. E. Elger, and K. Lehnertz, "Seizure prediction: the long and winding road." *Brain*, vol. 130, no. Pt 2, pp. 314–333, 2007.

[4] M. J. Cook, T. J. O'Brien, S. F. Berkovic, M. Murphy, A. Morokoff, G. Fabinyi, W. D'Souza, R. Yerra, J. Archer, L. Litewka, S. Hosking, P. Lightfoot, V. Ruedebusch, W. D. Sheffield, D. Snyder, K. Leyde, and D. Himes, "Prediction of seizure likelihood with a long-term, implanted seizure advisory system in patients with drug-resistant epilepsy: a first-in-man study." *The Lancet. Neurology*, vol. 12, no. 6, pp. 563–71, jun 2013. [Online]. Available: http://www.thelancet.com/article/S1474442213700759/fulltext

[5] D. Sornette and I. Osorio, "Prediction," in *Epilepsy*. CRC Press, may 2011, pp. 203–237. [Online]. Available: http://dx.doi.org/10.1201/b10866-17 http://arxiv.org/abs/1007.2420

[6] D. H. Johnson, "Point process models of single-neuron discharge," *J. Comp. Neurosci.*, vol. 3, pp. 275–299, 1996.

[7] P. Reynaud-Bouret and S. Schbath, "Adaptive estimation for hawkes processes; Application to genome analysis," *Annals of Statistics*, vol. 38, no. 5, pp. 2781–2822, 2010.

[8] A. G. Hawkes, "Spectra of some self-exciting and mutually exciting point processes," *Biometrika*, vol. 58, no. 1, pp. 83–90, apr 1971. [Online]. Available: http://biomet.oxfordjournals.org/content/58/1/83.abstract

[9] T. Ozaki, "Maximum likelihood estimation of Hawkes' self-exciting point processes," *Annals of the Institute of Statistical Mathematics*, vol. 31, no. 1, pp. 145–155, 1979. [Online]. Available: http://dx.doi.org/10.1007/BF02480272

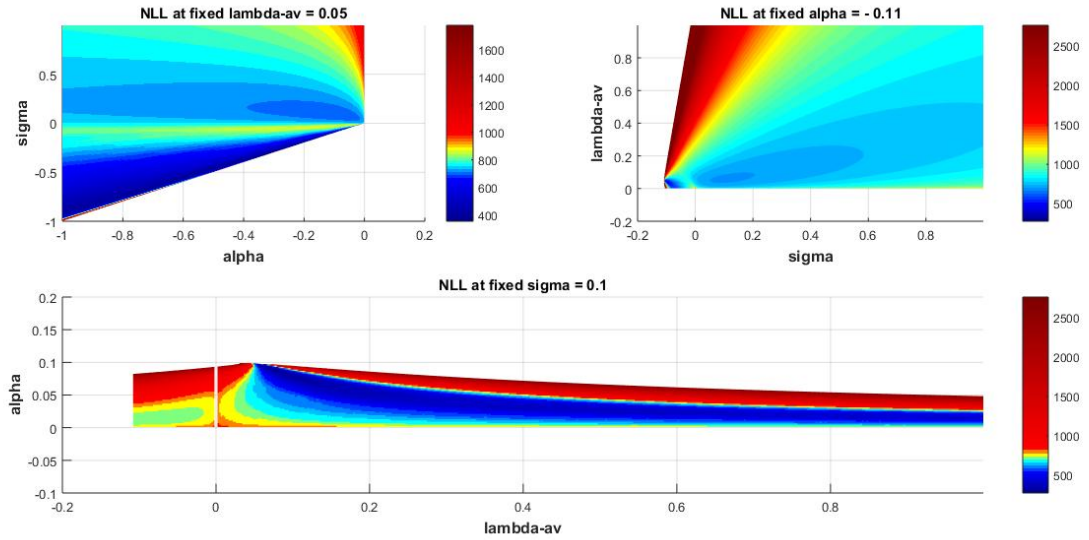

Fig. 4. Distributed representation of the four dimensional space of NLL as a function of the parameters of the Hawkes process.

Developing software tools for parameter fitting and validation of detailed neuronal models

Sára SÁRAY
(Supervisor: Szabolcs KÁLI, Tamás FREUND)
Pázmány Péter Catholic University, Faculty of Information Technology and Bionics
50/a Práter street, 1083 Budapest, Hungary
Institute of Experimental Medicine of the Hungarian Academy of Sciences
43 Szigony street, 1083 Budapest, Hungary
saray.sara@itk.ppke.hu

***Abstract*—Hand-tuning the parameters of a detailed neuronal model is not always effective in the long run, because changing one parameter can alter the previously adjusted behavior of the model, which might not even be realized by the modeler. Models developed this way can often reproduce only the behavior that was adjusted last. To avoid this and in order to make it possible to develop a CA1 pyramidal cell model that shows all the most important characteristics of a real cell of this kind, we develop software tools to automatically fit the parameters of the models and to validate the behavior of them after every iteration of the parameter tuning. Here we describe how we further developed the Optimizer software to make it possible to use it to improve the somatic spiking behavior of the Káli-Freund detailed hippocampal CA1 pyramidal cell model. We show the results of our first optimizations, and suggest ways to improve the performance of our software tools regarding the resultant models and also the computational time.**

***Keywords*-parameter fitting, model validation, CA1 pyramidal cell, feature-based error function, python**

I. Introduction

Multi-compartmental neuronal models can be useful tools in understanding the behavior and function of neurons, but there are still important parameters of which the values are not determined experimentally yet. Neurons have complex behavior that can be examined in many different ways, thus there are a number of different measures to test how the model's behavior corresponds to the behavior of the real cell. According to our experiences, when the parameters of a detailed single cell model is hand-tuned to make the model able to reproduce the desired behavior of the real cell to be modeled, the previously adjusted behaviors can be significantly changed. The changes are often not even realized by the modeler and the model developed this way is usually able to show only a few features of the real cell. To overcome this problem the solution could be to use software tools to automatically fit the model parameters, and to use a test suite to automatically and quantitatively validate the model behavior after every iteration of the parameter tuning [1].

We developed a Python test suite to automatically perform simulations that mimic experimental protocols on detailed hippocampal CA1 pyramidal cell models built in the NEURON simulator [2]. The test suite quantitatively compares the model behavior with experimental results to validate the somatic spiking behavior and the integration properties of the oblique dendrites of CA1 pyramidal cell models [1].

In order to make automatic parameter fitting possible we combine an optimizing software with the python test suite by using the main validation parts of the latter as fitness (cost) functions in the optimization. The optimizing software used is called the Optimizer and was developed in Python. The Optimizer provides a number of different fitness functions and optimization algorithms and also a graphical user interface (GUI) to make it possible for non-expert users to do optimization following some commonly used scenario. The modular design of the software makes it easier to more expert users to extend it with new fitness functions and/or optimizing algorithms. The Optimizer interfaces with NEURON to run the models [3].

At first we would like to use automatic parameter fitting to improve the Káli-Freund anatomically and biophysically detailed hippocampal CA1 pyramidal cell model [4] to make it show appropriate somatic spiking behavior. For this, abstract data (somatic spiking features) extracted by the Blue Brain Project from the results of the measurements made in the lab of Alex Thomson were used, that include values for the inverse of different inter spike intervals (ISI), spike amplitudes, voltage deflection, depth of after hyperpolarization, inverse time to last-, and first spikes at current injections of different amplitudes. Further aim is to reproduce the depolarization block feature of CA1 pyramidal cells. Which means that to prolonged somatic current injections of increasing intensity the cell responds with increasing number of action potentials until the threshold current intensity (I_{th}) is reached. The I_{th} is the current amplitude at which the soma fires the maximum number of spikes. To current intensities higher than this, the cell does not fire over the whole period of the stimulus, but after some action potentials it enters a depolarization block and the membrane potential remains constant. This average equilibrium potential is the V_{eq}. To increasing current intensities above the I_{th} the cell fires decreasing number of action potentials [5].

We use the python test suite to compare the somatic spiking behavior of the hand-tuned model, the model that was optimized using the somatic spiking features, and the model that was optimized to show depolarization block.

II. Methods

The Somatic Features Test of the python test suite is used to compare the somatic spiking behavior of the model with experimental results. In this test the data are read from a file that contains the amplitudes of the current stimulus and the corresponding mean feature values and standard deviation values for each feature. The mean and standard deviation values

S. SÁRAY, "Developing software tools for parameter fitting and validation of detailed neuronal models" in *PhD Proceedings Annual Issues of the Doctoral School, Faculty of Information Technology and Bionics, Pázmány Péter Catholic University – 2016.* G. Prószéky, P. Szolgay Eds. Budapest: Pázmány University ePress, 2016, pp 85– 88.

are from the statistical analysis of the results of experimental measurements on several different cells. Then the NEURON model is run using current injections of the given amplitudes, and the feature values are extracted from the resultant traces using the Electrophys Feature Extraction Library (eFEL) of the Blue Brain Project [6]. The error value of a feature is calculated using a feature-based error function, the difference of the mean experimental result and the model result is divided by the experimental standard deviation, thus the error is given in the units of the experimental SD [7]. The Depolarization Block Test of the python test suite does not extract features from every single trace. It needs a series of traces that are the result of current stimuli of increasing intensity to find the value of the threshold current intensity (I_{th}), and the equilibrium potential (V_{eq}) at the depolarization block. Then the feature-based error function is used to compare the results [1]. These methods are integrated into the Optimizer as fitness functions to make it possible to fit the model parameters using the somatic spiking features and the features of the depolarization block.

The Optimizer software has a modular structure which makes it possible to adapt it to the user's needs. The Optimizer does not use abstract data extracted from traces of the experimental results, but it uses the trace itself, and extracts the features needed to compare the experimental and the model trace within its fitness functions. The traceHandler module reads the input experimental traces and it is responsible for the handling of it. The modelHandler module does the model related tasks, such as handling the stimulation protocol. The optionHandler module stores the settings usually specified in the GUI. The optimizerHandler contains the different optimization algorithms as different classes. The fitnessFunction module contains the fitness functions as class methods and the function (combineFeatures) that creates the combination of the fitness functions and calculates the final fitness value for a pair of experimental and model trace by adding up the weighted results of the given fitness functions. The latter two modules can be expanded by adding new classes that implement new optimizing algorithms, or new class methods to the fitnessFunctions module. The main module of the Optimizer is the Core module. This carries out the steps of the optimization by interacting with the other modules. If the name of the new fitness functions or optimizing algorithm is included in the appropriate lists of the Core module, they will appear in the GUI and can be used in the optimization [3].

The GUI of the Optimizer helps the user to set up the optimization protocol. On the first layer the input trace or traces are loaded and the user has to select the type of the trace(s) (voltage, current) and provide the characteristics of it. The second layer loads the model, and the parameters to be optimized can be chosen or set using a user defined function. On the next layer the simulation protocol can be specified. Here up to 10 amplitude values of the stimuli can be provided by the user. The next layer contains a list of the available fitness functions from which the user can choose and can also set the weights of the chosen ones. After this the optimization algorithm can be chosen and its parameters and the boundary values of the model parameters have to be set. After the optimization is finished a result layer appear. The results are also saved into a HTML file [3].

Among the several available optimizing algorithms in the Optimizer we use the Evolutionary algorithm.

III. Results

A. Further developing the Optimizer software

In order to make it possible to use abstract data that are already extracted from the experimental traces in the Optimizer a new reader function is needed. The abstractDataReader reads the data from a JSON file into a python dictionary. These data include a list of the amplitudes of the current stimuli, the delay and duration of the stimuli, the names of the different spiking features in a form that can be already used by the eFEL, a weight to each of them, and the experimental mean and standard deviation of the given feature for the given current intensities. In the python dictionary the feature names are the keys and the value is another dictionary where the keys are 'mean' and 'std' and their value is a list that contains the experimental mean/std values at indices corresponding to the associated stimuli amplitudes. In the data not every feature has values for every current intensity. In these cases the list contains a None.

The GUI and the optionHandler module also had to be adapted to the usage of abstract data. On the first layer of the GUI the JSON file should be loaded and the *'Features'* option needs to be selected as input data type instead of the *'Current trace'* or *'Voltage trace'*. In this case the other parts of this layer, that in other cases are used to characterize the input trace, can be left empty and the user can go on to the next layer without error messages. On the *'Stimuli & Recording Settings'* layer of the GUI the most important change is that the stimulus amplitudes, duration and delay are already loaded from the input file and appear in the GUI, the user only needs to accept them. The *'Fitness Function Selection'* layer in this case contains only the names of the spiking features that are read from the input file, and does not contain the other fitness functions of the Optimizer that would need input traces to work with. So the features can be selected here and a weight can be assigned to each. Also the *'Spike Detection Threshold'* can be set here that will be used by the eFEL.

The new fitness function (FFun_for_Features) that we added to the Optimizer uses the eFEL to extract the features that were selected by the user on the GUI from the model trace. Its parameters are a model trace, the corresponding stimulus amplitude, one of the chosen features, and the python dictionary created by the abstractDataReader. The fitness value for these data are calculated using a feature-based error function described in the METHODS chapter. The combineFeatures function calls our new fitness function for each selected feature and each stimulus amplitude and sums the results.

During the optimization it happens of course that the model does not have any action potential to the current stimuli for which we would like to extract an action potential related feature. In these cases we detect the absence of an action potential and apply a relatively large penalty. To avoid RuntimeWarnings thrown by eFEL when it cannot find an action potential when needed, we use the *filterwarnings* function of the *warnings* python module.

As described before, the depolarization block is a feature that needs all the traces that are the model's response to increasing current amplitudes, to be evaluated. So we changed the combineFeatures function to make it collect the resultant model traces into a list that can be used by our other new

fitness function (FFun_depol_block). This function uses the feature-based error function (see METHODS) for the extracted I_{th}, V_{eq} values (described in INTRODUCTION) and for the number of action potentials at I_{th}. This fitness function applies a relatively large penalty if the model fires to the smallest current intensity, in order to avoid spontaneous firing, and also when it detects a current intensity (I_{th}) above which the number of action potentials decreases, but the model did not really entered depolarization block, because there are spikes at the end of the trace where the V_{eq} should be calculated.

To optimize for depolarization block features, in the first layer of the GUI the *'Depol. block'* option should be selected, and in this case the (FFun_depol_block) fitness function appears in the *'Fitness Function Selection'* layer.

Among the several smaller modifications in the different modules of the Optimizer that made the use of the new fitness functions possible, one of the most important ones was to adapt the output to the new results and make it possible to write all important data to the resulting HTML file.

B. Applications of the further developed Optimizer software

We used the improved Optimizer to fit the parameters of the Káli-Freund CA1 pyramidal cell model to show proper somatic spiking behavior corresponding to the somatic spiking features described in the INTRODUCTION chapter. The parameters to be fitted are: the density of the sodium and delayed rectifier potassium channels on the soma, axon and dendrites; the density of the M-type potassium channels on the soma and axon; the mid point (V_{half}) of the activation and inactivation curves of the sodium channels on the soma, axon, dendrites; the V_{half} of activation curve of the M-type potassium channels on the soma and the axon, and the V_{half} of activation curve of the delayed rectifier potassium channels on the soma, axon and dendrites. We chose these parameters because when we tried to improve the somatic behavior of the model by hand-tuning the parameters, we found that varying these parameters has the biggest impact on the spiking behavior and the depolarization block [1]. We also chose the boundaries of the parameters according to our previous observations.

The somatic behavior of the resulting model is shown on Figure 1. Although we do not have the experimental traces yet to compare with our results, it can be seen Figure 1 that the model shows an appropriate somatic behavior of a CA1 pyramidal cell. It responds with a huge hyperpolarization followed by a small rebound spike to a large negative current, it is able to fire slowly to small amplitude current stimulus, and it fires an increasing number of action potentials to increasing current intensities while showing some adaptation in amplitude and frequency as well.

We also used the Optimizer to fit the same parameters of the model as described above in order to make its soma enter a depolarization block to prolonged current injection. Figure 2 shows the somatic response at the current intensity to which the model fires the maximum number of action potentials (I_{th}) and also at 0.05 nA above that. It can be seen that the soma enters some kind of depolarization block, but it is not a complete one, because it still exhibits small spikelets. According to our previous observations, these may be the result of spikes generated at the axon and propagating to the soma.

We used the Somatic Features Test of the python test suite to compare the somatic spiking behavior of the hand-tuned

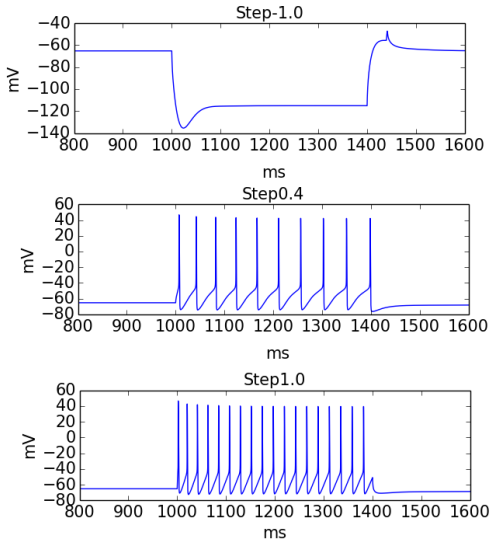

Fig. 1. The somatic spiking behavior of the model of which the parameters were fitted using the somatic spiking features, at different current injection steps.

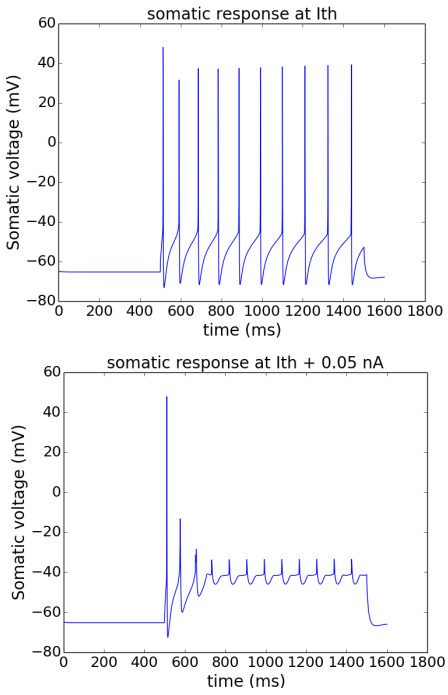

Fig. 2. The somatic spiking behavior of the model of which the parameters were fitted using the depolarization block features, at I_{th} and 0.05 nA above I_{th}.

model and the two differently optimized models (Fig. 3). Adding up the error values for all the features, the hand-tuned model achieves a score of 77.57, the model optimized to show depolarization block gets 81.38, and the model optimized to show proper somatic spiking features gets 75.57 points.

IV. Discussion

A. Ways to improve the results of optimization

We further developed the Optimizer software so that it is able to use abstract data already extracted from the experimental traces and not just the experimental traces themselves during optimization. We added new fitness function to the

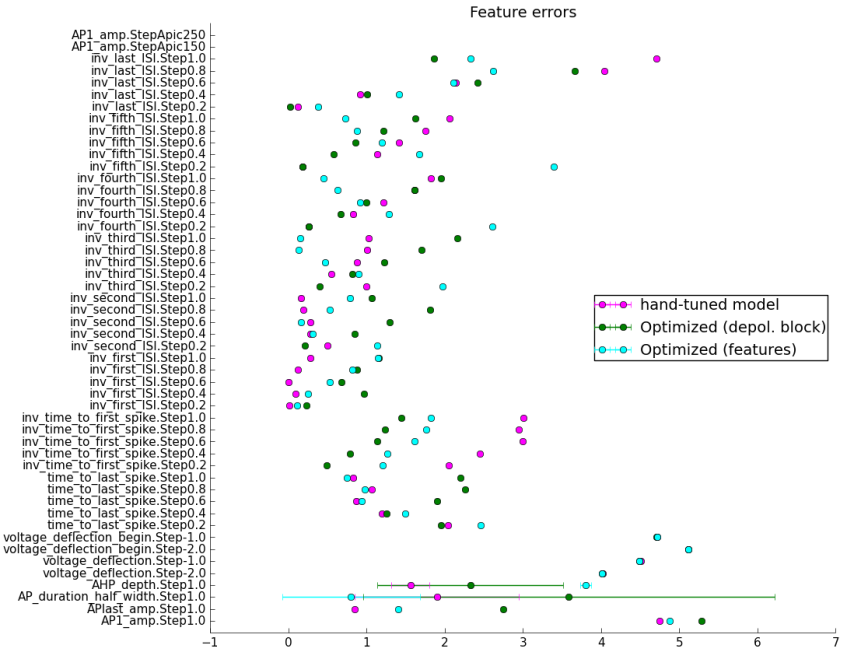

Fig. 3. The errors of the feature values extracted from the somatic response of the different models to current stimuli of different amplitudes in the unit of the experimental standard deviation.

software to make it possible to fit the parameters of CA1 pyramidal cell models to improve its somatic spiking behavior and another fitness function to make the model enter depolarization block in response to prolonged current stimulus. These functions use feature-based error functions to calculate the fitness values.

After running the two different kinds of optimization we used the python test suite to compare the resultant models with each other and with the hand-tuned model (Fig. 3.). When we sum the error values for each feature of every model, the model that was optimized to show depolarization block does not achieves a much higher error score than the others (see RESULTS). However, if we have a closer look at its behavior (Fig. 2, and data that are not shown) we can see that it is not a proper spiking behavior of a CA1 pyramidal cell. From this we can conclude that automatic parameter fitting and model validation without looking at the resultant traces is not always a good solution.

To improve the depolarization block behavior a new feature could be added to the fitness function that determines the standard deviation of the membrane potential at depolarization block, so it would prefer the flat ones and we could avoid the spikelets that can be seen Fig. 2.

To further improve the somatic behavior it would be good to combine the two new fitness functions and fit the parameters of the model so that it shows proper spiking behavior and also enters depolarization block to prolonged stimuli. Calling both fitness functions and adding up their results during the optimization is already possible in the Optimizer; the only obstacle is that the experimental data come from different experimental protocols, so these fitness functions need model responses to current stimuli of different length. Since the Optimizer can currently handle only one kind of stimulus (where only the amplitudes can vary) the fitness function handling and also the GUI, and the option handling have to be adapted to the use of different stimuli.

B. Parallelizing the optimization

The optimization could be improved by parallelizing processes of it. This could be solved in two ways. One of them is to make the evaluation of the candidates in the population of the evolutionary optimizing algorithm parallel, the other is to run the simulations on the model in parallel when stimuli of different amplitudes are used. In both cases it is important to load and run the model independently in each parallel process. Running processes in parallel is possible in Python using the multiprocessing module.

ACKNOWLEDGEMENTS

I would like to thank to my supervisor dr. Szabolcs Káli for his help and support.

REFERENCES

[1] S. Sáray, “Hippokampális piramissejtek dendritikus integrációjának vizsgálata részletes biofizikai modellek segítségével,” Master’s thesis, Pázmány Péter Catholic University, Faculty of Information Technology and Bionics, 50/a Práter street, 1083 Budapest, Hungary, 12 2015.

[2] N. T. Carnevale and M. L. Hines, *The NEURON Book*, 1st ed. New York, NY, USA: Cambridge University Press, 2009.

[3] P. Friedrich, M. Vella, A. I. Gulyás, T. F. Freund, and S. Káli, “A flexible, interactive software tool for fitting the parameters of neuronal models,” *Front. Neuroinform.*, vol. 8, no. 63, 2014.

[4] S. Káli and T. Freund, “Distinct properties of two major excitatory inputs to hippocampal pyramidal cells: a computational study,” *European Journal of Neuroscience*, vol. 22, no. 8, pp. 2027–2048, 2005.

[5] D. Bianchi, A. Marasco, A. Limongiello, C. Marchetti, H. Marie, B. Tirozzi, and M. Migliore, “On the mechanisms underlying the depolarization block in the spiking dynamics of CA1 pyramidal neurons,” *Journal of Computational Neuroscience*, vol. 33, no. 2, pp. 207–225, 2012.

[6] W. V. Geit, R. Moor, R. Ranjan, L. Riquelme, and C. Rössert, “Electrophys feature extraction library v2.10.72,” 2016, last accesed on: 23th March 2016. [Online]. Available: https://github.com/BlueBrain/eFEL

[7] S. Druckmann, Y. Banitt, A. Gidon, F. Schürmann, H. Markram, and I. Segev, “A novel multiple objective optimization framework for constraining conductance-based neuron models by experimental data,” *Frontiers in Neuroscience*, vol. 1, no. 1, p. 7–18, 2007.

Auditory scene analysis - a review of computational models

Beáta Tünde SZABÓ
(Supervisor: István WINKLER, István ULBERT)
Pázmány Péter Catholic University, Faculty of Information Technology and Bionics
50/a Práter street, 1083 Budapest, Hungary
szabo.beata.tunde@itk.ppke.hu

***Abstract*—Auditory scene analysis (ASA) addresses the task of interpreting the acoustic world in terms of an unknown number of auditory objects. So far only a handful of studies offer computational models for this problem. It is important to see that this area of research is not yet mature enough to have a coherent framework, therefore the modelling approaches cover a wide spectrum of ideas. This article reviews how the computational ASA models handle acoustic environments, what aspects they find relevant from a cognitive psychological point of view, and also, what results we can expect from these models at this point.**

***Keywords*-Computational Auditory Scene Analysis; Auditory Streaming; Speech Perception**

I. Introduction

Our acoustic environment is created by multiple acoustic sources, and the sound reaching the ears is a complex mixture of these sources. Given that original signals usually overlap in time and also in frequency, computing source functions from the mixture of acoustic signals is an ill-posed inverse problem. The human auditory system can solve this problem, and in his ground-breaking book, Bregman (1990) termed this function auditory scene analysis (ASA).

Our everyday experience tells us that our auditory system reliably decomposes acoustic scenes, even though the incoming acoustic information usually doesn't fully specify the sources. Under natural circumstances, our auditory perception is rarely chaotic or misleading. Rather, it is populated by sources that are stable over time and sound patterns characterizing actual events in the environment. However, both the computational algorithms and the neural mechanisms by which the human (and animal) brain achieves this feat are largely unknown.

In the past three decades, several theories have been postulated for explaining the processing of complex auditory scenes and the perceptual phenomena deemed to catch some crucial aspect of it. Many of these theories have been expressed or later implemented in the form of computational models. The aim of the current review is to provide a theoretically motivated overview of these computational models.

We will refer to auditory streams (a coherent succession of sounds) as perceptual objects, and we will use the term *proto-object*.

II. Inputs in the computational models

Reviewing the computational models of auditory scene analysis it would be an obvious choice to move from the more simple inputs towards the complex inputs such as speech [9]–[13] or soundscape [14]–[16]. The models that deal with simple, tokenized input [4]–[8] are usually built in order to investigate some specific result of behavioural experiments.

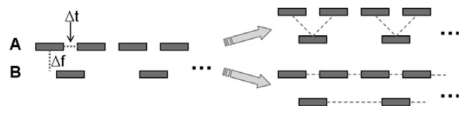

Fig. 1. Visual representation of the ABA- paradigm, as it's showed in [3]. Higher A and lower B tones are presented, and the two most stable perception is showed: segregated (top) and integrated (down)

One of the most widely investigated experiments was conducted by van Noorden (1975). He examined the perception of alternating ABA- tone sequences (A and B stand for pure tones of differing frequencies, "-" stands for a silent interval as long as the duration of the B tone). The subjects' responses showed that the tones are not perceived individually, the most stable percepts were the one where the A and B tones were assigned to the same proto-object (integrated percept), and the one where they were assigned to two different proto-object (segregated percept), see Figure 1. Changing the presentation rate and the frequency difference between the A and B tones the perception of the stimuli changed. The results are shown on Figure 2, demonstrating that stimuli above the temporal coherence boundary are perceived as segregated, stimuli below the fission boundary are perceived as integrated.

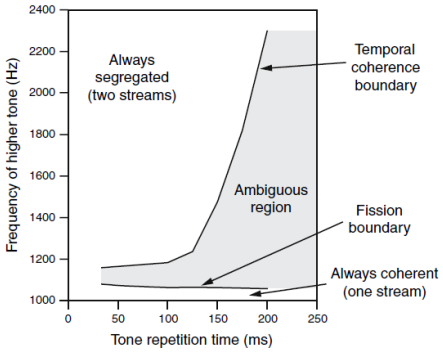

Fig. 2. The results of van Noorden, as it's presented in [7] showing the connection between the segregated/integrated perception and the stimuli's attributes: the presentation rate of the tones and the frequency difference between the two tones.

These findings can be used to compare computational models to the behavioural results, e.g. Wang & Chang (2008) measure the fitness of their model based on the implementation's ability to reproduce the fission boundary and the temporal coherence boundary showed in Figure 2.

In contrast with the models using tokenized input, the models built for complex inputs are rarely compared to

B. SZABÓ, "Auditory scene analysis - a review of computational models" in *PhD Proceedings Annual Issues of the Doctoral School, Faculty of Information Technology and Bionics, Pázmány Péter Catholic University – 2016.* G. Prószéky, P. Szolgay Eds. Budapest: Pázmány University ePress, 2016, pp 89– 92.

behavioural experiments. This suggests that there is a difference between modelling approaches, e.g. the one where the main goal is to reproduce behavioural data and the one where the modelling aims to be as close to the natural sounds as possible. Naturally the measures of the two types of modelling are different. Models in the first type can be measured by closeness to the data they tried to reproduce (as it is the validating metric in [7]), and models in the second group can be measured by the acoustic output's signal to noise ratio or its spectrogram's similarity to the original sounds' spectrogram - e.g. the model of Krishnan et al. (2014) aiming to segregate speech sounds, Figure 3 shows how the output proto-objects' spectrograms look like compared to the inputs' spectrograms.

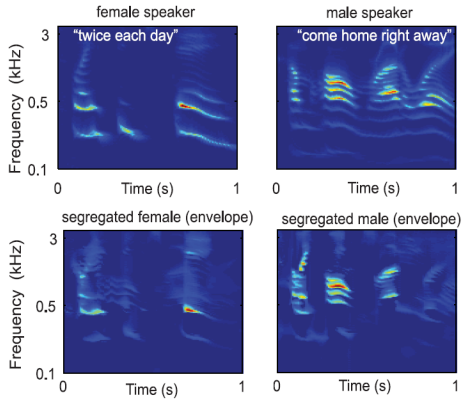

Fig. 3. The results of Krishnan & Elhilali, as it's presented in [12] showing the spectrograms of the input sentences, and the spectrograms of the outputs. Here we only presented their results based on envelope-based segregation.

III. Modelling aspects

In order to understand the motivation behind the unnatural inputs we need to review some theoretical approaches. To investigate the presented issues it is an obvious modelling decision to use tokenized inputs, and move forward with that model adding more and more features to it. Also, the models processing natural complex sounds often implement the approaches presented below.

One of the issues is whether there is any interaction/competition between the proto-objects or the sound organizations they form. The idea is based on Bregman (1990) who broke down ASA into two stages. The first stage is grouping of the incoming sounds, the second stage is the competition between these groupings, and the winning will emerge in perception. The competing entities can be proto-objects, sound organizations, or the foreground and the background.

Another issue that needs to be addressed is whether the auditory processing is a predictive process. If it is, that would mean that we make predictions about what is expected as the next auditory input. There is linking evidence from auditory change detection and ASA that show strong support for the predictive nature of proto-objects (Denham & Winkler 2006).

IV. Models implementing competition

To model the competition between proto-objects Mill et al. (2013) implemented a model that represents each possibly arising cyclic proto-objects called *chains* that can be formed during the grouping period. The competition then depends mainly on the predictive power of a given chain, on the self-excitation, and on the adaptation. Adaptation here means that a chains never completely stabilizes, suppression of the non-dominant chain weakens, therefore new perceptual state can emerge. This model uses tokens as input in order to be able to handle the computationally demanding number of chains (each possible chain can be represented) and the competition between them. Also, the results are compared to behavioural experience findings similar to the presented by van Noorden. The difference is that the settings of the stimuli didn't change, but the perception of it was switching between the two types of percepts.

The Bayesian statistic-based model of Barniv & Nelken (2015) also demonstrates competition between proto-objects. It argues that the switching in multistable auditory situations occurs due to evidence-accumulation, i.e. the more evidence gathered underpinning a proto-objects' presence, with the higher possibility the proto-object will be represented. This modelling approach can explain the correlation between successive integration and segregation phases in behavioural experiments similar to the ones of van Noorden, with constant stimuli. This model also uses tokenized input, as it wants to reproduce the behavioural findings on correlation between successive phases. As the priors in the model change with respect to the input, prediction is represented in the model.

Competition can take place between hypotheses, as it does in the Bayesian statistic-based models of Nix & Hohmann (2007) and Friston & Kiebel (2009). Here the hypotheses gain power if its prediction is correct, which is similar to the model of Mill at al., but here the hypotheses don't necessary belong to the proto-objects as a bijective mapping, they rather represent the sound-organizations. Both of these models segregate complex sounds (speech and bird-songs).

Neural network models

The models based on neural oscillators [6]–[8] use networks of oscillators. They include competition of some kind, given that streams are represented by the oscillators, and the excitation and inhibition of a given oscillator can depend on the other oscillators. Therefore in order to have a dynamic oscillation-based system interaction needs to be modelled. The usage of the oscillators can vary among models, they can represent different frequency channels as in the model of Wrigley & Brown (2004) and Wang & Chang (2008); frequency, spectral stream and pitch in a hierarchical organization in the model of Grossberg et al. All the three models work on tokenized inputs and they are compared to behavioural results.

The goal of the model built by Wrigley & Brown is to capture the role of attention. They used a 1 dimensional LEGION model (locally excitatory globally inhibitory oscillator network) for the dynamics in the network, which ensures that only one block of synchronised oscillators are active at any given time - that will be the proto-object (stream) that the model pays attention to. The implementation models the exogenous and endogenous attention and reproduces behavioural results.

Wang & Chang (2008) used 2 dimensional LEGION neural oscillatory model where the time and frequency is represented. The time dimension is represented by a system of delay-lines which is a novel approach to the time-representation. The model is compared to the behavioural results of van Noorden, the temporal coherence- and fission boundary are investigated by model simulations.

Grossberg et al. (2004) don't use LEGION model for the network-representation, instead, they implemented a hierarchical network. The hierarchy is organized by 3 layers: spectral stream layer, pitch stream layer and pitch summation layer. Each proto-object (stream) is represented in the all the layers, the network is responsible for the activity-dynamics of the proto-objects.

Not all the neural representation models use oscillator networks. In the model of Oldoni et al. (2013) there aren't any oscillator represented, it is built based on the units (neurons) of a self-organizing map computed from feature-vectors. This model also uses the LEGION-type dynamics, and models bottom-up and top-down attention. The output here is the measure of the potential of various soundscape components for attracting attention. The input was street noise, and the modellers measured the duration while the model paid attention to bird chirps.

V. Models not implementing competition

There are models that don't model the competition, the segregation is based on the grouping step, as it is presented in Krishnan et al. (2014) and Thakur et al. (2015). These models exploit the notion that grouping occurs based on temporal coherence between spectral constituents of the complex acoustic input, assuming that the simultaneously recurring parts of the input belong together. As the grouping (clustering) is the final stage after the feature-extraction in both of the implementations, there is no interaction between the outputs of the grouping process. Using spectrotemporal features in the feature-extraction phase, both of the models can segregate the sounds of 2 speakers if the number of the sources is known.

Similarly, the model of Elhilali & Shamma (2008) wants to exploit the specific auditory cortical mechanisms that contribute to the proto-object (perceptual stream) formation. This model also has two steps – feature-extraction and grouping/clustering, but the clustering here is not based on the correlations between temporal features. Instead, it is based on expectations on the next input. This expectation is based on the state of the detected proto-objects. As the prediction is stochastic, there is a possibility in the model to have different outputs for the same stimulus, therefore it is could model multistable perception, as it was tested for the ABA paradigm. The model replicated the results of van Noorden (1975). In the implementation the number of proto-objects is maximized at two. Between them there is no interaction modelled, a new input will be assigned to one of the proto-objects (or to the only proto-object in case there is one) based on the prediction, and there is no additional step in the model.

The early model of Unoki & Akagi (1999) also has the grouping phase as the final step when it tries to segregate complex tone from noise/noise-added complex tones and speech signal from noisy speech. After the pre-processing of the sound, in the grouping phase principles from Bregman (1990) regarding e.g. the harmonicity, common onset and offset are exploited for the sake of stream-segregation. As the grouping is the model's last phase, there is no interaction between proto-object, but the model parameters are updated based on prediction.

Using Bayesian statistics as in [9], [14] doesn't necessary means that interaction between proto-objects or sound organizations is implemented. Boes et al. (2011) used Bayesian statistics, but the prior doesn't change during the sound presentation, and there is no hypotheses testing either. The goal was to model binaural hearing, and for that a feature vector is represented encoding neural sensitivity for interaural time differences and interaural intensity differences. The model could place the source between -90°-90°space, segregating it from the background, using soundscape as the acoustic input.

TABLE I
Model features

Published	Author	Input	Comp.	Pred.
2013	Mill et al.	token	yes	yes
2015	Barniv & Nelken	token	yes	yes
2004	Wrigley & Brown	token	yes	no
2008	Wang & Chang	token	yes	no
2004	Grossberg et al.	token	yes	no
2007	Nix & Hohmann	speech	yes	yes
2008	Unoki & Akagi	speech	no	yes
2008	Elhilali & Shamma	speech	no	yes
2014	Krishnan et al.	speech	no	no
2015	Thakur, C. S., et al.	speech	no	no
2009	Friston & Kiebel	soundscape	yes	yes
2013	Oldoni et al.	soundscape	yes	no
2011	Boes et al.	soundscape	no	no

VI. Conclusion

The computational ASA models presented here show great variety. Their approach towards theoretical issues such as competition between proto-objects, prediction in the models differ, as it is shown in table V. Also, there is no consensus about the measurements of the fitness of any given model. In most of the cases their is no exact comparable metric defined. It would be difficult to define such metrics because of the heterogeneity of the models. This also means that no common framework can be established for the presented implementations, therefore only models in small groups can be compared. As the models are mostly try to implement a conceptual framework rather than an exact replica of a given phenomenon, the parameter- and sensitivity tests are rarely performed.

Further modelling work could be done for non-tokenized inputs, where the sampling time varies based on the natural sound's properties such as surprise/information value at a given point of time. Using the events extracted from natural sounds could be one way for the models built on tokens to work for natural stimuli as well.

Another aspect that is not widely investigated is the model-parameters calibration to the subjects in behavioural experi-

ments. This could give better fittings when reproducing the experiments' results.

The models implemented so far show us the great variety of approaches a modeller can take wanting to model auditory streaming. When a more rigorous framework will be in place based on much wider modelling results, only then will we be able to tell which of the above presented approaches yields to the best outcomes.

ACKNOWLEDGEMENTS

I would like to thank to my supervisors István Winkler and István Ulbert, and Susan Denham for their help with my research.

REFERENCES

[1] Bregman, Albert S., *Auditory scene analysis: The perceptual organization of sound*, MIT press, 1994.

[2] Noorden, Leo Paulus Antonie Servatius van., *Temporal coherence in the perception of tone sequences*, Diss. Eindhoven., 1975.

[3] Denham, S. L., and I. Winkler, *The role of predictive models in the formation of auditory streams*, Journal of Physiology-Paris 100(1), 154-170, 2006.

[4] Mill, Robert W., et al., *Modelling the emergence and dynamics of perceptual organisation in auditory streaming*, PLoS Comput Biol 9(3), e1002925, 2013.

[5] Barniv, Dana, and Israel Nelken, *Auditory Streaming as an Online Classification Process with Evidence Accumulation*, PloS one 10(12), e0144788, 2015.

[6] Wrigley, Stuart N., and Guy J. Brown, *A computational model of auditory selective attention*, Neural Networks, IEEE Transactions on 15(5), 1151-1163, 2004.

[7] Wang, DeLiang, and Peter Chang, *An oscillatory correlation model of auditory streaming*, Cognitive neurodynamics 2(1), 7-19, 2008.

[8] Grossberg, Stephen, et al. *ARTSTREAM: a neural network model of auditory scene analysis and source segregation*, Neural Networks 17(4), 511-536, 2004.

[9] Nix, Johannes, and Volker Hohmann, *Combined estimation of spectral envelopes and sound source direction of concurrent voices by multidimensional statistical filtering*, Audio, Speech, and Language Processing, IEEE Transactions on 15(3), 995-1008, 2007.

[10] Unoki, Masashi, and Masato Akagi, *A method of signal extraction from noisy signal based on auditory scene analysis*, Speech Communication 27(3), 261-279, 1999.

[11] Elhilali, Mounya, and Shihab A. Shamma, *A cocktail party with a cortical twist: how cortical mechanisms contribute to sound segregation*, The Journal of the Acoustical Society of America 124(6), 3751-3771, 2008.

[12] Krishnan, Lakshmi, Mounya Elhilali, and Shihab Shamma, *Segregating complex sound sources through temporal coherence*, PLoS Comput Biol 10(12), e1003985, 2014.

[13] Thakur, Chetan Singh, et al., *Sound stream segregation: a neuromorphic approach to solve the "cocktail party problem" in real-time*, Frontiers in neuroscience 9, 2015.

[14] Friston, Karl, and Stefan Kiebel, *Predictive coding under the free-energy principle*, Philosophical Transactions of the Royal Society of London B: Biological Sciences 364(1521), 1211-1221, 2009.

[15] Oldoni, Damiano, et al., *A computational model of auditory attention for use in soundscape research*, The Journal of the Acoustical Society of America 134(1), 852-861, 2013.

[16] Boes, Michiel, et al., *A biologically inspired model adding binaural aspects to soundscape analysis*, 40th International Congress and Exposition on Noise Control Engineering (Inter-Noise-2011). Vol. 5. Institute of Noise Control Engineering Japan, 2011.

Synchronous population activity in the hippocampal CA3 region and dentate gyrus, in vitro

Csilla SZABÓ
(Supervisor: Lucia WITTNER, István ULBERT)
Pázmány Péter Catholic University, Faculty of Information Technology and Bionics
50/a Práter street, 1083 Budapest, Hungary
szabo.csilla@itk.ppke.hu

***Abstract*—Hippocampal sharp wave-ripples (SPW-Rs) and dentate spikes from the dentate gyrus described for freely moving rats occur during slow wave sleep and behavioral immobility and thought to play an important role in memory formation. We investigated the cellular and network properties of these events with simultaneous laminar multielectrode in a rat hippocampal slice model, using physiological bathing medium. The electrode array was placed on the surface of the hippocampal slice, perpendicularly to the granule and pyramidal cell layer. Spontaneous population activities (SPA) were generated in the dentate gyrus and CA3 region of slices prepared from the temporal hippocampus of young rats, in vitro. These events were characterized by a local field potential gradient (LFPg) transient, increased fast oscillatory activity and increased multiple unit activity (MUA). CSD analysis confirmed that SPW-Rs were locally generated in each of the DG and CA3 region with conserved intrahippocampal connections. Simultaneous recordings indicated that the waves were often synchronized in the DG and CA3, although propagation was observed from the CA3 and DG also. This suggests that the information transmission among the CA3 region and the DG consists of multidirectional processes.**

***Keywords*-rat; linear multielectrode; hippocampus; current source density, multiple unit activity**

I. Introduction

Sharp wave-ripple complexes were observed in the hippocampus of rats during slow wave sleep and behavioral immobility [1]. These bursts have a crucial role in memory consolidation and in conversion into long-term memory trace [2]. In vitro models of SPW-Rs activity show similarities with SPW-Rs occurring in vivo as both kind of events consist of a field potential gradient, high frequency oscillations and increased neuronal firing. In vitro, these events are initiated in the CA3 and spread to the DG [3]. In this study we aimed to reveal the network properties of spontaneous population activity in rat hippocampal slices.

II. Methods

A. Slice preparation

Brain slices were prepared from adult Wistar rats (200-600 g), from both sexes. Animals were anaesthetized intraperitoneally with urethane (1,000 mg/kg) and perfused intracardinally with a solution of 248 mM sucrose, 26 mM $NaHCO_3$, 1 mM KCl, 10 mM $MgCl_2$, 1 mM $CaCl_2$, 10 mM glucose, equilibrated with 5% CO_2– 95% O_2 at 3–5 ^oC. Then animals were decapitated, whole brain dissected and horizontal slices of 500 μm were prepared from ventral hippocampus towards to the dorsal area. Slices were carried to the interface recording chamber and perfused with a soulution of 124 mM NaCl, 26 mM $NaHCO_3$, 4 mM KCl, 2 mM $MgCl_2$, 2 mM $CaCl_2$, 10 mM glucose, equilibrated with 5% CO_2– 95% O_2 at 34–35 ^oC. Slices recuperated in standard oxygenated artificial cerebrospinal fluid (ACSF) for an hour.

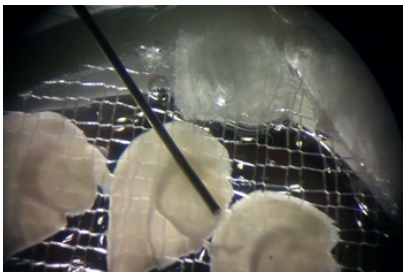

Fig. 1. Simultaneous extracellular recording from CA3 and DG.

B. Recordings

Local field potential gradient (LFPg) was recorded with laminar multielectrode array (Pt/Ir, 24 channels, 150 μm intercontact distance) using a custom made voltage gradient amplifier of pass band 0,01 Hz- 10 kHz). Signals were digitized with an analog-to-digital converter (32 channels, 16 bit resolution) and recorded with LabView7 at 20 kHz sampling rate. The electrode was placed on the surface of the brain slice, perpendicularly to the cell layers of the CA3 region and the dentate gyrus as well. In this way extracellular recordings were made simultaneously from both hippocampal area (Figure 1).

C. Data analysis

Data were analyzed with NeuroScan Edit 4.5 and routines written for MATLAB R2015a (SpikeSolution, WaveSolution). Current source density (CSD) and multiple unit activity (MUA) were derived from the LFPg transient. CSD estimates the population trans-membrane currents, while MUA shows the cell activity. CSD was calculated from LFPg by applying a Hamming-window spatial smoothing and one additional spatial derivation. MUA was obtained by high pass filtering (500 Hz, zero phase shift, 48 dB/octave) and rectification of LFPg. Base line correction (-150 –50 msec) was applied to averaged LFPg, CSD and MUA. In the color maps, CSD sinks and MUA-increases are presented in warm colors, while cold colors show CSD sources and MUA-decreases. Events were detected from LFPg after Hamming-window smoothing and band pass filtering (1–30 Hz) using an amplitude threshold of 3X standard derivation.

III. Results

Spontaneous synchronous population activity (SPA) was generated in the ventral hippocampus of the rat, in vitro.

Cs. SZABÓ, "Synchronous population activity in the hippocampal CA3 region and dentate gyrus, in vitro" in *PhD Proceedings Annual Issues of the Doctoral School, Faculty of Information Technology and Bionics, Pázmány Péter Catholic University – 2016.* G. Prószéky, P. Szolgay Eds. Budapest: Pázmány University ePress, 2016, pp 93– 94.

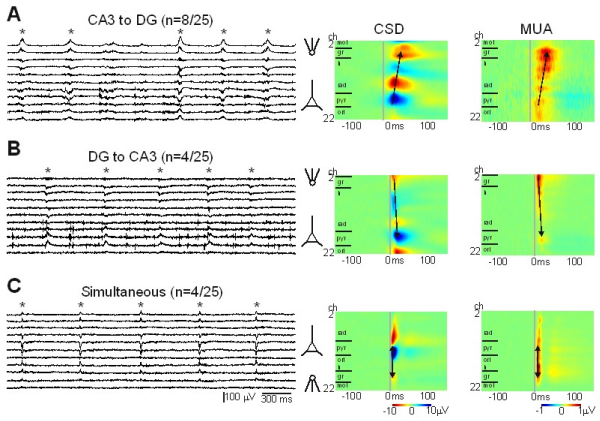

Fig. 2. Different patterns of SPA spreading according to CSD and MUA

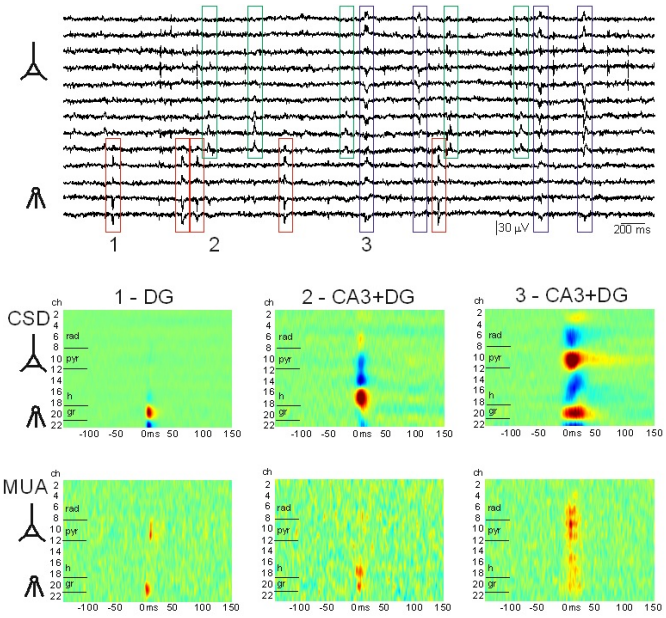

Fig. 3. Multiple population activities derived from the same recording

These events consisted of increased LFPg oscillations and MUA superimposed on an LFPg transient. Because of these attributes they were similar to in vivo sharp wave ripple complexes (SPW-Rs) hence these events can be called SPW-Rs in the CA3 [4], and dentate wave in the DG [5]. CSD analysis confirmed that SPW-Rs were locally generated with intrahippocampal connections in the DG and in the CA3 as well. In several cases (n=12/25) CSD showed delay between DG and CA3 (Figure 2). Multiple population activities were observed in the same recording (Figure 3).

IV. Conclusions

Data showed that hippocampal neuronal network can spontaneously generate population activity. Simultaneous recordings indicated that the waves were often synchronized in the DG and CA3, although propagation was observed from the CA3 and DG also. This suggests that the information transmission among the CA3 region and the DG consists of multidirectional processes.

V. Further plans

In the future we would like to examine the role of glutamatergic signaling in the spreading of SPW-Rs and dentate wave applying the type II. metabotropic glutamate receptor (mGluR2) agonist DCG-IV, as it can be used to block the glutamate release from mossy fibers, the only direct connection between CA3 and DG.

Acknowledgements

The author wish to thank Dr. Lucia Wittner and Dr. István Ulbert for the supervision and all the help.

References

[1] Buzsáki G, Leung LW, Vanderwolf CH. 1983. Cellular bases of hippocampal EEG in the behaving rat. Brain Res 287:139-171

[2] Buzsáki G, 1989. Two-stage model of memory trace formation: A role foor 'noisy' brain states, Neuroscience 31:551-570

[3] Kubota D, Colgin LL, Casale M, BrucherFA, Lynch G. 2003. Endogenous waves in hippocampal slices. J Neurophysiol 89:81-89

[4] Hofer, K. T., Kandrács, Á., Ulbert, I., Pál, I., Szabó, C., Héja, L. and Wittner, L. (2015), The hippocampal CA3 region can generate two distinct types of sharp wave-ripple complexes, in vitro. Hippocampus, 25: 169–186. doi: 10.1002/hipo.22361

[5] Colgin, L. L., Kubota, D., Brucher, F. a, Jia, Y., Branyan, E., Gall, C. M., Lynch, G. (2004). Spontaneous waves in the dentate gyrus of slices from the ventral hippocampus. Journal of Neurophysiology, 92(6), 3385–98. http://doi.org/10.1152/jn.00478.2004

Examination of dermal stem cells in healthy and diseased skin

Balazs Szeky
(Supervisor: Sarolta Karpati, Miklos Gyongy)
Pazmany Peter Catholic University, Faculty of Information Technology and Bionics
50/a Práter street, 1083 Budapest, Hungary
szeba@digitus.itk.ppke.hu

***Abstract*—It is well-known, that the human dermis comprises fibroblast responsible for extracellular matrix production and orchestration of epidermal and follicular homeostasis. Among the heterogeneous fibroblasts, specialized cell populations exist with stem cell properties and enhanced tissue-regenerative potential. Although, little is known about their exact genetic and molecular traits, origin, and interactions with other skin resident cells. Furthermore, their role in tissue repair, or in pathophysiological conditions, such as inflammation and cancer is poorly understood. In this conference paper we set out to give a comprehensive summary of the latest literature on dermal stem cell populations. We focus on stem cell properties and functions of mesenchymal stem cells, skin derived precursors and multilineage differentiating, stress enduring cells. We also give a short summary of our research plan for the selective isolation and analysis of dermal stem cells from healthy and melanoma skin samples.**

***Keywords*-dermal stem cell; molecular phenotype; differentiation potential**

I. Introduction

The outstanding role of stem cells in tissue homeostasis is beyond any question. Besides the maintenance of their undifferentiated state, they differentiate into various cell types through asymmetric cell division to drive embryogenesis or compensate for loss of adult cells in tissues. The balance between the state of stemness and differentiation is tightly regulated by soluble messengers, cell adhesion molecules and extracellular matrix proteins derived from the surrounding micro-environment, i.e., the cellular niche where stem cells reside.

The interactions between stem cells and their niches are indispensable for structural integrity of skin [1]. Skin is a complex tissue encompassing the epidermis, the underlying dermal matrix and fat depots of subcutis. Each layer provides a niche for heterogeneous stem cell populations of different origin and differentiation potentials. The interfollicular epidermis (IFE) and the hair follicles (HF) are easily accessible, well-studied model systems of cellular regeneration [2]. Both the IFE an HF has a specified regulatory network for the generation of their functional constituent cell types. These regulatory mechanisms rely not only on cell-autonomous genetic programs, but also on the molecular signals derived from a mixed population of dermal fibroblasts with variable differentiation potential. Thus, the balanced turnover of keratinocytes, melanocytes and HF cells relies on an intact dermis, and points to the importance of dermal cell populations in the regulation of epidermal and follicle stem cell homeostasis. Although, the gene expression profile, phenotypic heterogeneity and pluripotency of dermal stem cells is far from being completely established. A comprehensive study is required to compare lineage specificity, markers and transcriptomic signature of dermal stem cells and to shed light on their interaction with each other and their neighboring niches. Clarification of their specific stem cell markers and evaluation of the differentiation and tumorigenicity of dermal stem cells in vitro and in vivo could foster the development of dermal stem cell based regenerative therapies.

In this review we provide an overview the current literature on the most relevant dermal stem cell subpopulations for regenerative medicine. We focus on three stem cell subpopulations identified in skin connective tissue; mesenchymal stem cells (MSCs), skin derived precursors (SKPs) and multilineage differentiating, stress enduring (MUSE) cells. We describe their possible origin, proposed dermal micro-environment and phenotypic hallmarks including differentially expressed genes and cell surface markers.Last, but not least, we briefly delineate our research scheme for selective isolation and multilevel comparison of dermal-residing stem cell populations from skin samples of melanoma patients.

II. Skin derived Precursor cells

Skin derived precursor (SKP) cells were identified as the cellular source of both neural and mesodermal progeny [3]. When induced to differentiate in vitro, SKPs gave rise to cells showing the morphological traits and markers of glial, neural and mesodermal lineages. Their discovery underpinned the hypothesis, that adult dermal stem cells can serve as an alternative source for cutaneous nerve regeneration besides glial and fibroblast derived neurotrophic factors.

SKPs have cellular characteristics peculiar to both mesodermal and neural crest derived stem cells (NCSCs). Similarly to fibroblasts, SKPs express fibronectin and vimentin and they can be differentiated into osteoblasts and adipocytes. On the other hand SKPs show profound differences in comparison with mesenchymal stem cells and fibroblasts. Firstly, SKPs are small sized, rounded cells without fibroblast morphology. Secondly, unlike MSCs, SKPs do not adhere to uncoated plastic culture flask, rather they form floating spheres in culture growth medium supplemented by EGF and bFGF. In addition to the lack of melanocyte and hematopoietic markers, SKPs preferentially express NCSC markers, such as nestin, neurofilament M,β III tubulin, and transcription factors involved in epithelial-mesenchymal transition, like snail, slug, Sox9 and Sox2 [4], [5].

To resolve the origin of SKPs, lineage tracing studies were conducted on neural crest (Cre-Wnt1) and somite cell

B. SZÉKY, "Examination of dermal stem cells in healthy and diseased skin" in *PhD Proceedings Annual Issues of the Doctoral School, Faculty of Information Technology and Bionics, Pázmány Péter Catholic University – 2016.* G. Prószéky, P. Szolgay Eds. Budapest: Pázmány University ePress, 2016, pp 95– 98.

(Cre-Myf5) specific reporter lines, and showed, that SKP cells have multiple origins [6]. SKPs residing in facial skin emanate from neural crest, and dorsal trunk resident SKPs arise from the somitic mesoderm, while foreskin SKPs have mesenchymal origin. It has also been demonstrated, that SKPs from dorsal skin and foreskin derived SKPs have quite similar transcriptomic profile to those derived from neural crest with only a few differentially expressed, tissue specific genes. A comprehensive study is required to compare the marker expression and differentiation potential of SKPs from different sources in order to understand their relevance in regenerative medicine.

SKPs are multipotent dermal stem cells capable of differentiating into osteoblasts, chondrocytes, adypocytes, fibroblasts and endothelial cells [7], [8]. Furthermore, in contrast to MSCs, SKP cells can be committed not only to mesenchymal lineages, but they can also undergo neural and Schwann cell differentiation [9]. Schwann cell recruitment and remyelinization are essential for regeneration of injured nerves and to restore their electrophysiological properties. As the isolation of stem cells either from the nervous system and embryonic tissues proposes many technical challenges and ethical concerns, it is extremely desirable to obtain adult neural precursor cells from easily accessible tissues such as skin. As SKPs are skin resident, they could serve as a source for neural precursor cells, thus, the mechanism and extent of their neural differentiation is widely investigated. There is ample experimental evidence, that SKPs can generate cells with neural morphology, moreover, the generation of action potential conducting neurons from SKPs was also observed [10].

SKPs participate in wound healing and promote skin and bone repair.Pharmacologically activated SKPs displayed enhanced regeneration potential when topically applied on punch-wounded mice [11]. They promoted wound closure, epithelial cell proliferation and the increase in the number of $CD31^+$ pericytes around dermal vasculature. The wound healing potential of SKPs through endothelial and neural differentiation was further exemplified by an in vivo study on diabetic mice [12]. Topical application of murine SKPs on full-thickness wounds of diabetic mice led to a significant decrease in wound closure time and increased staining of $CD31^+$ capillary structures and neurofilament M positive cells in wounded cutaneous tissue. These finding suggest, that diabetic foot ulceration, a dramatic consequence of diabetes mellitus could be ameliorated by SKP based cellular therapy.

One of the major impediments of cellular replacement therapy is the emergence of host immune response against transplanted tissues, which is anticipated if they fail to promote a tolerogenic micro-environment and suppress allogeneic activated, inflammatory immune cells. To test the immunogenicity of SKPs, Najar and colleagues cocultured human SKPs with allogenic activated peripheral blood monocytes (PBMCs) in vitro, and cotransfected them into the spleen of immunodeficient (NOD-SCID) mice [13]. Transplanted SKPs engaged to an immunosuppressive phenotype even in the presence of pro-inflammatory stimuli mediated by Il-1 β, TNF-α, IFN-α and -γ. Besides retaining the characteristic SKP markers, SKP cells did not express HLA-DR and other costimulatory molecules. Moreover, they inhibited T-cell proliferation, secreted immune-suppressive factors (HGF, LIF, PGE2) and rescued immunocompromised mice from lethality caused by graft-versus-host disease.

III. Mesenchymal Stem Cells

The continuously thriving theory of mesenchimal stem cells (MSCs) originates from the pioneering research of Alexander Friedenstein (1924-1998) and Alexander Maximov (1874-1928). While Maximov proposed, that stromal cells create a hematopoietic micro-environment (HME) required for physiological hematopoiesis, Friedenstein discovered MSCs as the HME resident population bearing stem cell properties and the potential to generate a broad range of cell types from mesodermal lineage. Over the past decades MSCs were isolated and expanded in culture not only from bone marrow, but from a variety of tissues including dental pulp, umbilical cord, adipose and dermal tissue based on their adherence to plastic culture dishes.

Given the astounding heterogeneity of cells isolated on the basis of plastic adherence, and that MSCs have a highly similar morphology to fibroblasts the field of stem cell research faced with the challenge of defining uniform criteria for MSCs. To make a consensus, the International Society for Cellular Therapy (ISCT) established the minimal criteria for defining MSCs [14]. Firstly, MSCs regarded as plastic adherent cells with the ability of self-renewal, and to generate mesodermal progeny. Secondly, all MSCs express CD73, CD90, and CD105, but they are negative for HLA-DR, hematopoietic markers, such as CD34,CD44 and leukocyte markers CD45. Despite having these uniform molecular and cellular signatures, MSCs represent a highly heterogeneus stem cell population with many subpopulations differing in their specific markers or their osteogenic, adipogenic and chondrogenic potential. For example, differentially expressed genes and different lineage generation potentials identified between bone marrow and adypose tissue derived MSCs [15]. Furthermore, it is also revealed, that MSCs from subcutaneous adipose tissue have a significantly larger proliferative capacity and adypogenic potential than visceral adypose tissue MSCs [16], and different MSC subpopulations were identified in human dermis with variable capacities for osteo- and adypogenic differentiation [17].

MSCs do not exclusively act as stem cells, but also as master regulators of innate and adaptive immune responses [18]. As such cells, MSCs are sensors of inflammation and modulators of the inflammatory milieu in different tissues. MSCs are activated by inflammatory mediators, like TNF-α and IFN-γ, but their mode of activation depends on the quality and concentration of cytokines and other immune-mediator molecules peresent in their local environment. When the level of proinflammatory messengers is low, MSCs boost inflammation via secretion of mediators, that activate proinflammatory T-cells and stimulate the maturation of monocytes to M1 macrophages. In the presence of an inflammatory environment, activated MSCs exert antiinflammatory effects by the release of inhibitory cytokines (PGE2, TGFβ) and by the polarization of T-cells and Macrophages towards immunosuppressive T-reg and M2 phenotypes, respectively. This could explain why tumour cells recruit bone-marrow MSCs for evasion of antitumour immunity or to create premetastatic niches for cancer propagation.

MSCs are the source of mesodermal cell types as they give

rise to osteoblasts, adypocytes, smooth muscle cells, cardiomyocytes and adypocytes in vitro and in vivo. Furthermore, in vivo differentiation of transplanted MSCs beyond mesodermal lineage was also observed, as they generated cells expressing neural markers or hepatic enzymes [19]. This indicates, that MSCs can gain pluripotency in certain conditions or the existence of otherwise dormant, pluripotent subpopulations among MSCs, (see MUSE cells below).

IV. MUSE CELLS

MUSE cells are reminiscent of MSCs in the expression of MSC-featuring markers, such as CD105, CD29, CD90. Although, unlike MSCs, MUSE cells have a round morphology and they form human embryonic stem cell (hESC)-like spheres, the so called M-clusters in vitro instead of adhering to the surface of a plastic flask. As an adult stem cell population, MUSE cells are ubiquitous; they can be isolated from dermal fibroblasts, stromal vascular fraction and bone marrow. Several studies using immunohistochemistry and immune-fluorescence demonstrated that MUSE cells do not associate to any specified structure, like the dermal papillae, nerve terminals or blood vessels, but they are distributed sparsely in bone-marrow, adipose tissue and dermis [20]. Furthermore, MUSE cells acquire a migratory phenotype during tissue damage, migrate the sites of injury, and they reconstitute the injured tissue with mature cell types.

Besides their MSC-like nature, MUSE cells bear outstanding pluripotency and stress tolerance. They are extremely resistant to harsh physicochemical conditions caused by low temperature (4 ^{o}C), long-term trypsinization, hypoxia or serum-starved medium [21]. Under normal physiological conditions, MUSE cells preserve their quiescent, slow cycling state, which is the assurance of self-renewal for both tissue and cancer stem cells. After the exposure to stress in vitro, or disruption of tissue homeostasis in vivo MUSE cells become activated by enhanced proliferation and migration. MUSE cells express pluripotency genes (OCT 3/4, NANOG, Kfl, Myc) in common with hESCs and induced pluripotent sem cells. Among them the cell-surface glycosphingolipid, stage-specific embrionic antigen 3 (SSEA3) serves as a lineage specific marker, which enables FACS-isolation of MUSE cells, as a $CD105^{+}SSEA3^{+}$ double positive cell fraction from dermal connective tissue, bone marrow aspirates and stromal vascular fractions. Though they differentiate spontaneously on gelatine-coated flask, MUSE cells show increased osteocalcin and oil red staining in osteogenic and adypogenic medium, and express endodermal marker α-fetoprotein and neural markers nestin, MAP2 and neuroD when induced to differentiate into hepatocytes and neurons, respectively [22]. The regenerative capacity of MUSE cells was also proved in vivo. MUSE cells isolated from skin fibroblasts migrated into ischaemic brain tissues and generated progenitor cells positive for neural and oligodendrocytic markers [23]. GFP-labeled, bone marrow derived MUSE cells gave rise to hepathocytes, cholangiocytes Kupfer cells and sinusoidal endothelial cells in partially dissected liver of immunocompromised mice [24].

The application of hESCs and IPSCs interferes with the risk of high immunogenicity and teratoma formation. Unlike embrionic stem cells, MUSE cells failed to form teratomas when transplanted into testes of mice despite having similar morphology and pluripotency markers to ESCs [20]. The low teratogenic potential of MUSE cells could be explained by their low expression levels of pluripotency genes, the so called "Yamanaka factors" and their low telomerase activities. On the other hand, MUSE cells can be reprogrammed to IPSCs by overexpression of NANOG, Myc, OCt 3/4 by the delivery of Yamanaka factors in a lentiviral vector [25]. These MUSE IPSCs were able to differentiate towards all the three germ lines, and formed teratomas in mouse testes. The generation of IPSCs from MUSE cells points towards the elite model of IPSC theory, namely, that there is only a small subset of cells with the ability and appropriate set of transcription factors to generate IPSCs. Thus, MUSE cells could be the source of pluripotent, non-tumorigenic cells, as well as IPSCs among heterogeneous fibroblasts.

V. RESEARCH PLAN FOR ISOLATION AND CHARACTERIZATION OF HUMAN DERMIS-DERIVED STEM CELLS

Although a vast amount of study emerged focusing on the efficiency of dermal cell populations in tissue regeneration, comprehensive characterization of their transcriptomics and surface proteome remains elusive. On the other hand, it is still unresolved whether transplanted cells alone have the ability to restore tissue disruptions, or other tissue resident cells are also required for complete regeneration. Another pressing issue is the identification of stem cell subpopulations, which are responsible for generation of the tumor-associated stroma in different pathophysiological conditions and in different types of cancers. Tumor-infiltrating immune cells and protumorigenic cancer-associated fibroblasts are essential stromal components for cancer growth and evasion of antitumor immunity, although the mechanism of their development from normal cells is still poorly understood. Elucidation of the stem cell source of cancer associated stroma could enable the inhibition of tumor growth by deprivation of the tumor from its stromal supplement.

To address these questions, we set out our goal to isolate and analyze dermal stem cells derived from healthy and melanoma

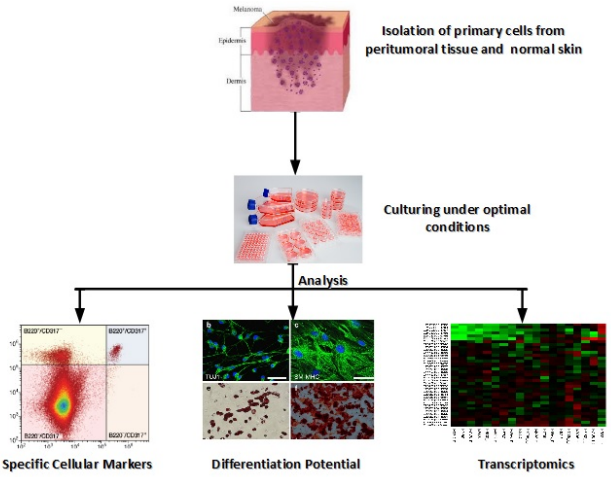

Fig. 1. Proposed scheme for analysis of dermal stem cells from melanoma skin samples. With the informed consent of patients, tumors are cut out bordered by healthy skin tissue. The dermal and subcutan layers are separated from epidermis by enzymatic digestion, and isolated cells are delivered under optimal culture conditions regarding the culture medium, temperature and serum concentrations. Lineage specific genes are identified via transcriptomic analysis (microarray, Q-PCR) and flow cytometry. The differentiation potential of selected cells is evaluated by differentiation assays carried out in vitro or in vivo.

skin patient samples (Fig.1.). We would like to optimize the cultivation of SKPs, MSC and MUSE cells in vitro to enable characterization of their transcriptomic profile and surface marker expression by microarray analysis, quantitative PCR and flow cytometry. Next, we would asses the differentiation potential of these cells by utilizing differentiation assays in vitro and in vivo, via trasplantation of magnetic separated, labeled cells into immunocompromised mice. Last, but not least, we would like to compare the stem cell composition of healthy and melanoma bearing dermal tissues to shed light on the way how melanomas influence stem cell homeostasis in the dermis. We believe, that identification of stem cells residing in skin connective tissue and elucidation of their interactions with their niche cells provides more efficient therapies for the treatment of cutaneous diseases and a better understanding of how skin cancers grow and propagate.

Acknowledgements

The research project aimed in this study is supported by the National Research Fund, OTKA, (OTKA number: OTKA NN 11446).

References

[1] Y. Hsu, L. Li, E. Fuchs, "Emerging interactions between skin stem cells and their niches", Nature Medicine, vol. 20, no. 8, pp. 847-856, 2014.

[2] G. Solanas and S. Benitah, "Regenerating the skin: a task for the heterogeneous stem cell pool and surrounding niche", Nature Reviews Molecular Cell Biology, vol. 14, no. 11, pp. 737-748, 2013.

[3] J. Toma, M. Akhavan et al, "Isolation of multipotent adult stem cells from the dermis of mammalian skin", Nature Cell Biology, vol. 3, no. 9, pp. 778-784, 2001.

[4] K. Fernandes, J. Toma, F. Miller, "Multipotent skin-derived precursors: adult neural crest-related precursors with therapeutic potential", Philosophical Transactions of the Royal Society B: Biological Sciences, vol. 363, no. 1489, pp. 185-198, 2008.

[5] K. Fernandes, I. McKenzie, P. Mill et al, "A dermal niche for multipotent adult skin-derived precursor cells", Nature Cell Biology, vol. 6, no. 11, pp. 1082-1093, 2004.

[6] H. Jinno, O. Morozova, K. Jones et al, "Convergent Genesis of an Adult Neural Crest-Like Dermal Stem Cell from Distinct Developmental Origins", STEM CELLS, vol. 28, no. 11, pp. 2027-2040, 2010.

[7] J. Lavoie, J. Biernaskie, Y. Chen et al, "Skin-Derived Precursors Differentiate Into Skeletogenic Cell Types and Contribute to Bone Repair", Stem Cells and Development, vol. 18, no. 6, pp. 893-906, 2009.

[8] D. Shih, D. Lee, S. Chen et al, "Isolation and Characterization of Neurogenic Mesenchymal Stem Cells in Human Scalp Tissue", Stem Cells, vol. 23, no. 7, pp. 1012-1020, 2005.

[9] M. Krause, S. Dworski, K. Feinberg et al, "Direct Genesis of Functional Rodent and Human Schwann Cells from Skin Mesenchymal Precursors", Stem Cell Reports, vol. 3, no. 1, pp. 85-100, 2014.

[10] L. L., B. C. et al, "Morphological and electrophysiological features of mature neurons in differentiated skin-derived precursor cells.", J Stem Cells Regen Med, vol. 8, no. 1, pp. 35-6, 2012.

[11] S. Naska, S. Yuzwa, A.et al, "Identification of Drugs that Regulate Dermal Stem Cells and Enhance Skin Repair", Stem Cell Reports, vol. 6, no. 1, pp. 74-84, 2016.

[12] H. Sato, K. Ebisawa, K. Takanari et al, "Skin-Derived Precursor Cells Promote Wound Healing in Diabetic Mice", Annals of Plastic Surgery, vol. 74, no. 1, pp. 114-120, 2015.

[13] J. De Kock, P. Meuleman, G. Raicevic et al,"Human Skin-Derived Precursor Cells Are Poorly Immunogenic and Modulate the Allogeneic Immune Response", STEM CELLS, vol. 32, no. 8, pp. 2215-2228, 2014.

[14] M. Dominici, K. Le Blanc, I. Mueller et al, "Minimal criteria for defining multipotent mesenchymal stromal cells. The International Society for Cellular Therapy position statement", Cytotherapy, vol. 8, no. 4, pp. 315-317, 2006.

[15] M. Al-Nbaheen, R. vishnubalaji, D. Ali et al, "Human Stromal (Mesenchymal) Stem Cells from Bone Marrow, Adipose Tissue and Skin Exhibit Differences in Molecular Phenotype and Differentiation Potential", Stem Cell Rev and Rep, vol. 9, no. 1, pp. 32-43, 2012.

[16] W. Ong, C. Tan, K. Chan et al, "Identification of Specific Cell-Surface Markers of Adipose-Derived Stem Cells from Subcutaneous and Visceral Fat Depots", Stem Cell Reports, vol. 2, no. 2, pp. 171-179, 2014.

[17] C. Vaculik, C. Schuster, W. Bauer et al, "Human Dermis Harbors Distinct Mesenchymal Stromal Cell Subsets", Journal of Investigative Dermatology, vol. 132, no. 3, pp. 563-574, 2012.

[18] M. Bernardo and W. Fibbe, "Mesenchymal Stromal Cells: Sensors and Switchers of Inflammation", Cell Stem Cell, vol. 13, no. 4, pp. 392-402, 2013.

[19] Y. Jiang, B. Jahagirdar, R. Reinhardt, R. et al, "Pluripotency of mesenchymal stem cells derived from adult marrow", Nature, vol. 447, no. 7146, pp. 880-881, 2007.

[20] F. Ogura, S. Wakao, Y. Kuroda et al, "Human Adipose Tissue Possesses a Unique Population of Pluripotent Stem Cells with Nontumorigenic and Low Telomerase Activities: Potential Implications in Regenerative Medicine", Stem Cells and Development, vol. 23, no. 7, pp. 717-728, 2014.

[21] S. Heneidi, A. Simerman, E. Keller et al, "Awakened by Cellular Stress: Isolation and Characterization of a Novel Population of Pluripotent Stem Cells Derived from Human Adipose Tissue", PLoS ONE, vol. 8, no. 6, p. e64752, 2013.

[22] S. Wakao, Y. Kuroda, F. Ogura, T. et al, "Regenerative Effects of Mesenchymal Stem Cells: Contribution of Muse Cells, a Novel Pluripotent Stem Cell Type that Resides in Mesenchymal Cells", Cells, vol. 1, no. 4, pp. 1045-1060, 2012.

[23] H. Uchida, T. Morita, K. Niizuma et al, "Transplantation of Unique Subpopulation of Fibroblasts, Muse Cells, Ameliorates Experimental Stroke Possibly via Robust Neuronal Differentiation", STEM CELLS, vol. 34, no. 1, pp. 160-173, 2015.

[24] H. Katagiri, Y. Kushida, M. Nojima et al, "A Distinct Subpopulation of Bone Marrow Mesenchymal Stem Cells, Muse Cells, Directly Commit to the Replacement of Liver Components", American Journal of Transplantation, vol. 16, no. 2, pp. 468-483, 2015.

[25] S. Wakao, M. Kitada, Y. Kuroda et al, "Multilineage-differentiating stress-enduring (Muse) cells are a primary source of induced pluripotent stem cells in human fibroblasts", Proceedings of the National Academy of Sciences, vol. 108, no. 24, pp. 9875-9880, 2011.

Filtration of foodborne parasites using microfluidic devices

Ádám György Szélig
(Supervisor: Kristóf Iván Ph.D.)
Pázmány Péter Catholic University, Faculty of Information Technology and Bionics
50/a Práter street, 1083 Budapest, Hungary
szelig.adam.gyorgy@itk.ppke.hu

***Abstract*—There is a growing need for an efficient, fast diagnostic tool for foodborne pathogen detection. For many parasite infections the cure is not known and can cause chronic diseases or death if not treated thus prevention gets a bigger role. The difficulties encountered in the standard detection methods are false negative tests due to the low concentration of parasites, the small volume of the observed serological samples, and nematodes can also clog flow cytometry devices. Microfluidic technologies for serological separation applications are an efficient alternative due to the numerous advantages such as reduced contamination issues, portability and its small scale. As in classical separation procedures, the size-fractionation of particles or cells could be realized in passive or active methods. In case of active methods the requirement of external forces increases the complexity of the device and may limit the application for some specific reagents such as biological samples. Consequently, researchers have been paying attention to the development of novel physical methods, which are based on varying only the geometry of microchannels, modifying the flow profile and influencing local flow properties. So far a few physical filtering devices have been made which are suitable for efficient parasite detection.**

I. Introduction

Food safety is an extensive scientific discipline that describes handling, preparation and storage of food in ways that prevent foodborne illnesses. Food is able to transmit diseases from person to person, or it can serve as a growth medium of bacteria that might cause food poisoning. The main goals of laboratories related to the field of food safety are the development of novel methods to detect foodborne pathogens and to provide help to medical doctors, veterinarians and laboratory attendants. Foodborne pathogen testing and detection is a major concern for food industries. Each year more than 600 million food-borne sickness is reported worldwide, with 40% of hit in children younger than 5 years. In 2010, according to World Health Organization (WHO), more than 23 million get illness from foodborne parasites. Due to the effects of globalisation today the breaking out of epidemics is not only in the backward areas, but in the advanced countries too. In Europe the number of the observed cases is increasing. This shows, the infections caused by parasites mean increasing threat in the modern world. For many diseases the cure is not known and can cause chronic diseases and death if not treated. In general we can say that prevention is more efficient in protection againts diseases than curing [1]. There are three main classes of parasites that can cause disease in humans: protozoa, helminths, and ectoparasites. Foodborne parasites can be transmitted by ingesting fresh or processed foods that have been contaminated with the transmission stages (spores, cysts, oocysts, ova, larval and encysted stages) via the environment, animals (often from their faeces), or people. Foodborne parasites can also be transmitted through the consumption of raw and undercooked or poorly processed meat and offal from domesticated animals, wild game, and fish [2]. The Food and Agriculture Organization of the United Nations (FAO)/WHO in 2014 ranked the foodborne parasites (Table I). The ranking parameters were: Number of global foodborne illnesses (manifesting disease), Global distribution (number of regions), Acute morbidity severity (disability weight), Chronic morbidity severity (disability weight), Fraction of illness that is chronic (%), Case-fatality ratio (%), Likelihood of increased human burden (%), How relevant is this parasite/food pathway for international trade?, and What is the scope of impact to economically vulnerable communities? [3].

The detection of the foodborne infections and the filtration of the parasites may be based on different procedures. The gold standard in diagnosis depends upon microscopical detection of parasites in blood but classical microbiological test is also used. This is very difficult in some cases where the parasitemia is below 100 nematodes per milliliter of blood. Given the low abundance of parasites in the blood, methods have been developed to raise the efficiency of detection rising the cost and the required time of diagnosis. Currently used diagnostic methods [6]: serologic methods (fresh blood smear and histochemical stain based tests), concentration methods (Knott's test, hematocrit method, filter test), enzyme-linked immunosorbent assays (ELISAs), multiplex real-time PCR amplification. The evaluation of serological methods and the concentration procedures are based on optical detection while the ELISAs and RT-PCR amplification requires further costs (instruments, higher skilled labor). Each diagnostic technique is multiplexable and combinable with other methods. The most widespread technique is the smear test and starts with pipetting serological sample onto a glass slide after the hemolysis the nematodes are counted. The modified Knott's test, which concentrates nematodes by centrifugation and mark specific species by Giemsa stain. The advantage of the concentration method versus the basic serologic methods is the raised detection limit from a bigger sample volume [7]. Table II summarize the currently used standard diagnostic methods.

The difficulties encountered in these methods are false negative tests due to the low concentration of parasites in early diagnostics, the small volume of the observed serological samples and nematodes can also clog flow cytometry devices. Microfluidic technologies for serological separation applications are an efficient alternative due to numerous advantages such as reduced contamination issues, portability and its small scale, which allows better control of the microenvironment during these approaches [8], [9], [10]. The microfluidic designs can fit for one dedicated species increasing the counting and

Á. SZÉLIG, "Filtration of foodborne parasites using microfluidic devices" in *PhD Proceedings Annual Issues of the Doctoral School, Faculty of Information Technology and Bionics, Pázmány Péter Catholic University – 2016.* G. Prószéky, P. Szolgay Eds. Budapest: Pázmány University ePress, 2016, pp 99–103.

	Name	Size	Transmission route	Presence	Symptoms	Detection
1.	*Taenia solium*	larva: 31-34μm, adult: 3-5m	Infected meat	America, Asia, Africa	abdominal irritation with diarrhea, constipation or indigestion, epilepsy	Stool microscopy, Serological Techniques, Isolation Techniques, Antigen detection, PCR
2.	*Echinococcus granulosus*	adult: 3-8mm	Dog feces contaminated food, oralis-fecalis	Cosmopolitan	liver problems, vomiting, abdominal pain, biliary tract obstruction, chest pain, cough, sanguineous, anaphylatic shock, heart disorder	Removed cyst microscopy, Serological Techniques, ELISA, PCR
3.	*Echinococcus multilocularis*	adult: 1,2-3,7mm	Sylvatic animal (mainly foxes) feces contaminated food, oralis-fecalis	North America, Europe, Alaska, North Russia	liver problems, vomitting, abdominal pain, biliary tract obstruction, chest pain, cough, sanguineous, anaphylatic shock, heart disorder	Removed cyst microscopy, Serological Techniques, ELISA, PCR
4.	*Toxoplasma gondii*	5-50μm, adult: 3-5m	tachyzoites and bradyzoites contaminated meat Cat feces contaminated fresh products, oralis-fecalis	Cosmopolitan	flu-like symptoms, myalgia, headache, hepatitis, pneumonia, myocarditis, meningitis	Serological Techniques, Isolation Techniques, Antigen detection, Stool microscopy, PCR
5.	*Cryptosporidium spp.*	5μm oocyst	contaminated fresh products, oralis-fecalis	Cosmopolitan	Gastroenteritis, watery diarrhea, abdominal pain, nausea, vomitting, fever, spleen	Antigen detection, Stool microscopy, PCR

TABLE I
TOP FIVE RANKED FOODBORNE PARASITES [1], [3], [4], [5].

separation efficiency. In this work, a brief overview of recent microfluidic separation techniques is provided focusing on parasite filtration.

Method	Limit of detection	Volume requirement	Duration
Serologic methods (fresh blood smear, histochemical stain based tests)	1-2 nematodes	0,5-1ml	10-30min
Concentration methods (Knott's test, hematocrit method, filter test)	1-2 nematodes	2-3ml	20-40min
Enzyme-linked immunosorbent assays (ELISAs)	22-43kDa antigens	200-400μl	2-4h
PCR amplication	2-3 DNS	10-100μl	3-5h

TABLE II
LABORATORY DIAGNOSTICS OF BLOOD-BORNE PARASITIC DISEASES [7].

II. DEVICE FABRICATION

Microfluidics concerns design, fabrication, and experiments of miniaturized fluidic systems, which has undergone rapid developments during the last two decades. As an interdisciplinary area, this rapidly growing field of technology has numerous applications in biomedical diagnostics, chemical analysis, automotive, and electronic industries [11]. One of the pivotal applications of microfluidics is the development of lab-on-a-chip (LOC) devices as point-of-care (POC) diagnostic tools. A typical LOC device includes various functional modules: sample transport, sample preparation, separation, detection, and analysis module [12]. The label-free size separation of particles or cells is vital to many of the analytical and preparative techniques used in the fields of chemical, biochemical, and clinical analysis, which led to ground breaking advances in terms of speed of analyses, resolution of separations, and automation of procedures [13]. The miniaturization of reactions and assays confers many advantages over "macro" scale techniques beyond the obvious reduction in quantities of reagents and materials required per test. The scaling down of volumes results in higher surface to volume ratio. Thus, miniaturization results in higher reactivities, shorter diffusion distances, smaller heat capacities, faster heat exchange, shorter assay times, and better overall process control, as well as the capability to integrate multiple steps and to achieve massive parallelization on-chip [7].

Microfluidic devices can be fabricated using a standard microfabrication soft-lithographic technique. Microfabrication enables the deposition and etching of thin layers (angstrom to micrometer) of different materials on silicon or glass substrates. These layers can be patterned with accuracy and high resolution, down to the nanometer level using lithography. Lithography is the technique used to transfer a pattern from a mask to the substrate to control the location of the deposition of the next layer or the etching of an existing layer on the substrate. After making the master for replica molding, polydimethylsiloxane (PDMS) pre-polymer can be poured on it. The liquid PDMS pre-polymer conforms to the shape of the master and replicates the features of the master. After the polymerization the solid PDMS replica can be pulled off from the mold surface and access holes can be punched through the patterned PDMS slab. Then the patterned PDMS slab can be bonded to microscope glass slide following surface treatment. The main microfabrication steps are shown in Fig. 1.

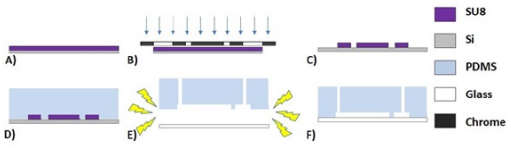

Fig. 1. Fabrication steps of the microfluidic devices. A) SU-8 photoresist was spin coated onto silicon wafer. B) The shape of the microfluidic channels were patterned by UV light through a chrome mask. C) The unpolarized photoresist was washed away from the surface. D) The liquid PDMS pre-polymer conformed to the shape of the master. E) The patterned PDMS slab was bonded to microscope glass slide following surface treatment. F) The final device. (adapted from Ref. [7])

III. Separation techniques

A. Classification methods

The isolation of pure populations of cells is critical in diverse biological applications such as biological research, diagnostics, pathogen detection, and therapeutics. Microfluidic separation techniques can be divided into two main fields: active which requires external forces and passive techniques which does not. The active separation can be categorized into acoustophoresis, chemophoresis, electrophoresis, magnetophoresis, application of mechanical forces and optophoresis. Without external active forces the particle separation which is mostly effected by changing the geometry of the channels is called hydrophoresis. This is classified into subclasses: Batch Separation Procedures (BSP) such as Hydrodynamic Chromatography (HC) and Continuous-Flow Separation Procedures (CFSP). The sample loading method is the main difference between these two passive procedures. The BSP works with quantized inlet volumes, meanwhile the CFSP loads sample continuously. The CFSP procedure can be further subcategorized: using centrifugal extraction, Dean flow in cylindric channels [14], Determinisitc Cell Rolling (DCR) [15], Deterministic Lateral Displacement (DLD) [16], using the elasto-inertial effect, flow through separators [17], hydrocyclones, using membrane [18], Pinched-Flow Fractionation (PFF) [19] or using the Zweifach-Fung effect.

Separation techniques can also be categorized on the basis of what kind of labeling technique is used. There are three principal categories based on its primary cell recognition modality: (i) fluorescent label-based, (ii) bead-based, and (iii) label-free cell sorting [20].

B. Filtration parameters

The values of the characteristic parameters of the filters are an accurate reflection on the filtering efficiency. The important parameters are the throughput, the purity and the filtration efficiency. Retention is one of the best unit describing filtration. It shows that how many of the particles was filtered out. In general, it is given in a percentage form. The separation size is an essential feature of the filtration, which determines the cut off for separation. This will be the value in case of size based filtration where the retention value is more than 90%. In most cases this value is different from the particle size. The filtration efficiency (η), is calculated by taking the amount of the trapped parasites ($\sigma_{captured}$) and the initial number of parasites (σ_{pre}) in the native serological sample. The number of trapped nematodes ($\sigma_{captured}$) can be counted optically within the active zone. Assuming a homogenous sample the following relationship describe the parasite numbers:

$$\sigma_{pre} = \sigma_{captured} + \sigma_{post} \tag{1}$$

If the sample volume is fixed (for example 1ml) the efficiency can be defined as:

$$\eta = \frac{\sigma_{captured}}{\sigma_{post} + \sigma_{captured}} \tag{2}$$

C. Physical filters

The requirement of external forces increases the complexity of the device and may limit the application for some specific reagents such as biological samples. Consequently, researchers have been paying attention to the development of novel physical methods, which are based on varying only the geometry of microchannels, modifying the flow profile and influencing local flow properties. The size of a cell is the cellular phenotype observed most easily. Thus, cell size is a common criterion used for cell separation. Cells can be separated based on their size most simply by using physical filters. Four types of filtration have been reported in microfluidic systems: weir-type, pillar, cross-flow, and membrane (Fig. 2) [21]. Table III shows the comparison of the mentioned physical filters.

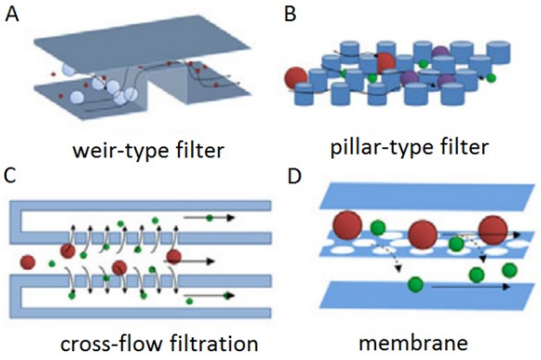

Fig. 2. Schematic representation of four types of filters for size-based cell sorting. (A) Weir-type filter. (B) Pillar-type filter. (C) Cross-flow filtration. (D) Membrane. [21]

In weir-type filtration, a barrier is fabricated to constrict the height of the channel, with a space maintained between the barrier and the ceiling of the channel that allows fluids and small particles to pass through while retaining large particles [21]. Continuously decreasing the space between the barrier and the ceiling along the device makes fractionation of varied sizes available. In pillar-type filtration, micro-pillars are spaced apart in an array along the micro-channel to filter out particles [21]. The distance between the pillars, the pillars diameter, the shape of the pillars and the disposition of the pillar columns will determine the cut off parameter. By dinamically changing the pillar's physical parameter multi-stage filtration is also available. Cross-flow filtration is based on the same principle, but the flow is perpendicular to the micro-pillar array. This system has the advantage of being less prone to fouling than the aforementioned systems because the filtered particles will flow perpendicular to the direction of the flow, while the undesired particles along with the waste will flow parallel to the flow direction. It is also capable of mechanical lysis of cellular components. Membrane filters contain well-defined pores that separate larger cells from the fluid and from smaller particles. This system is robust and widely used in industrial ares but in case of many particles it can be easily clogged. Ultrasound-enhanced membrane-cleaning processes can be used to clean the clogged membranes but it is cumbersome to adapt in a complex microfluidic system.

Size-based filtrations face challenges such as clogging and fouling. However, designing micro-pillars or using cross-flow systems can prevent cells from obstructing flow. The clogging particles locally alter the flow properties, so that the biological samples may be damaged and easily deformable particles will squeeze through the pores. This can also result in the damage of the filtration device. Thus it is essential to select the device appropriately for each application.

Basicly the most separation techniques presume spheroidal particles, respectively when carrying out calculations regarding

	pillar-type filter	weir-type filter	cross-flow filtration	membrane
minimum separation value	2,5μm	1-2μm	2,5μm	2,5μm
typical application	cellular components	cell-free plasma production	purified plasma production	separation of the cellular components of blood
retention value	70-90%	~70%	70-90%	72-85%

TABLE III
COMPARISON OF THE FOUR PHYSICAL FILTERS [21], [22].

the device approximate calculations are often used, which trace back the configuration to a well known geometric shape. This could be difficult in that case when the model organism is a nematode because it is narrow, long-shaped and it can take many different sizes and forms even in the same sample [23], [24]. In the passive or combined nematode filtering procedures described so far the researchers tipically used pillar-type structures. This may be justified by that the weir-type filters can clog from the long-shaped models and that the membrane-type filters can clog from the smaller particles and from the contamination beside the nematodes. In the clogged filter the streaming properties may change, which can affect the separation parameters. The cross-flow, the pillar type and the DLD systems are proven to be suitable for nematode filtration [23]. S. Holm et al. accomplished nematode filtering from red blood cells with more than 95% efficiency in a DLD system, where the model was *Trypanosoma cyclops* [23], [24]. It is possible that properties, such as surface charge and flagellum waveform, for example, differ between different parasite species. However, the Deterministic Lateral Displacement technique depends primarily on cell shape and size. Because of the parasites own sinusoid movement and the streaming phenomena the separation isn't perfect, furthermore capturing the parasites is also not possible due to the structure of the DLD systems. In case of the various hydrodynamic separators like the PFF the unpredictable movement of the animal can affect the result. Parasite filtering with Flow Trough Nematode Filter (FTNF) can also be found in the literature [7]. It was successfully used to filter out *Dirofilaria repens* from blood sample. This is a pillar-type filter, which is capable of capturing the nematodes. This pillar-type filter can clog as well, but it is less significant than in the case of the weir-type or the membrane filters. In addition the pillar structures can be deformed by the nematode movement, thus changing the cut off value [25].

IV. Flow Trough Nematode Filter

A. Device design

The mechanism of separation by FTNF designed by A. Laki is based on the interaction of nematodes suspended in whole blood with an ordered array of microcapillaries and micropillars that the fluid is forced to flow through under low Reynolds number conditions, while the detectable larvae are trapped. The required filtration range of the designed device for nematode filtration comes from parasitology. The examined nematodes are ovoviviparous and the evolving unsheathed embryo (microfilariae) live in the bloodstream. The length of *D. immitis* is 330-380μm and their width is 5-7μm [26]. The microfilariae of *D. repens* is bigger, 300-360μm long and 6-8μm wide [26]. In this matter the developed structure has to be robust, efficient to filter out the desired nematodes and to reduce the risk of coagulation. Figure 3 demonstrates the geometry of the microfluidic filter. Each microfluidic structure has a 400μm wide and 20μm high inlet and an outlet. The widths of microcapillaries ($W_{capillary}$) on the different devices varies from 6,1μm up to 15,4μm. The active zone, where parasites remain trapped is surrounded by these rectangular cross-section microcapillaries, which are on a radius (r) of 1mm from the center and its repetition angle (α) is from 3,38° up to 3,91°. The width of obstacles/pillars (W_{pillar} = 52,8μm) and the angle without capillary connection (β = 75°) are the same in each structure. The capillaries are positioned in a circular manner to increase filtration efficiency by providing an isobaric pressure distribution along the entire filter system.

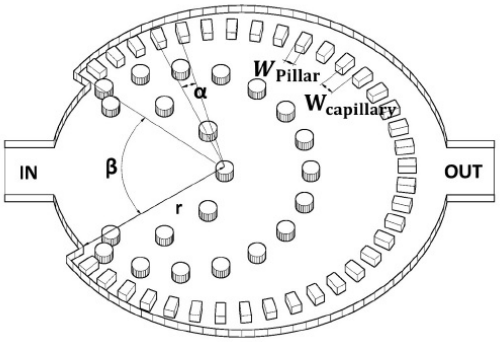

Fig. 3. Schematic of the flow-through nematode filter.

Particles which have greater diameter than $W_{capillary}$, will be filtered out from the liquid flow.

B. Measurements

Figure 4 illustrates the schematic diagram of the nematode filtration platform. Pressure-driven flow can be created using syringe pumps. Typical flow rates were between 0,1ml/h and 2ml/h. Imaging was performed on an inverted Olympus IX71 microscope, while image recording was made by an CCD camera. For parasitological experiments, blood-borne infected, anticoagulant, canine blood has been used.

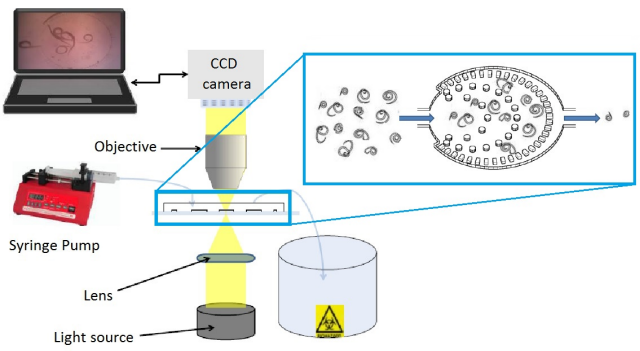

Fig. 4. Schematic image of the parasite filtration platform.

This device was successfully used to filter out nematodes with almost 60% efficiency at 0,5ml/h in case of small capillary widths. The device can be further optimalized by

using different pillar shapes, testing the device at higher flow rates to redound faster sample processing, and using other nematode species.

V. Conclusion

In this paper we have reviewed foodborne parasitosis and the currently used standard detection methods. Microfluidic separators were also introduced and physical filtering methods were further analized. DLD and FTNF devices were shown as so far the best parasite filtration devices. Further developments may include better geometric structures to capture the target parasites and to provide better flow profile. Channel height is also a relevant parameter in case of it's value is comparable to the size of the parasite. Microfluidic devices are useful in a wide range of medical procedures and diagnostics.

Acknowledgements

I would like to acknowledge my supervisors Kristóf Iván and András J. Laki for their kind help and their knowledge on this complex multidisciplinary field. Also I would like to thank Róbert Kovács for his kind help.

References

[1] Michael J. Cuomo, Lawrence B. Noel, Daryl B. White: *Diagnosing Medical Parasites: A Public Health Officers Guide to Assisting Laboratory and Medical Officers"*

[2] T. Slifko, H. Smith and J. Rose, "Emerging parasite zoonoses associated with water and food", *International Journal for Parasitology*, vol. 30, no. 12-13, pp. 1379-1393, 2000.

[3] FAO: *Multicriteria-based ranking for risk management of food-borne parasites*, WHO Press, Switzerland, 2014

[4] L. Garcia, "DIAGNOSTIC MEDICAL PARASITOLOGY, 5TH EDITION", *Shock*, vol. 27, no. 6, pp. 707-708, 2007.

[5] B. Gottstein, E. Pozio and K. Nockler, *"Epidemiology, Diagnosis, Treatment, and Control of Trichinellosis", Clinical Microbiology Reviews*, vol. 22, no. 1, pp. 127-145, 2009.

[6] C. Genchi, L. Venco, and M. Genchi, "Guideline for the laboratory diagnosis of canine and feline dirofilaria infections," *Mappe Parassitologiche*, pp. 139-144,Feb. 2007.

[7] A. Laki, *"Microfluidic Particle Separation Techniques for Biomedical Use"*, Ph.D, Pázmány Péter Catholic University, 2015.

[8] E. D. Pratt, C. Huang, B. G. Hawkins, J. P. Gleghorn and B. J. Kirby, *Chemical engineering science*, 2011, 66, 1508–1522.

[9] A. A. S. Bhagat, H. Bow, H. W. Hou, S. J. Tan, J. Han and C. T. Lim, *Medical & biological engineering & computing*, 2010, 48, 999–1014.

[10] Y. Gao, W. Li and D. Pappas, *Analyst*, 2013, 138, 4714–4721.

[11] S. Haeberle and R. Zengerle, "Microfluidic platforms for lab-on-a-chip applications", *Lab on a Chip*, vol. 7, no. 9, p. 1094, 2007.

[12] P. Auroux, D. Iossifidis, D. Reyes and A. Manz, "Micro Total Analysis Systems. 2. Analytical Standard Operations and Applications", *Analytical Chemistry*, vol. 74, no. 12, pp. 2637-2652, 2002.

[13] T. Squires and S. Quake, "Microfluidics: Fluid physics at the nanoliter scale", *Reviews of Modern Physics*, vol. 77, no. 3, pp. 977-1026, 2005.

[14] A. Bhagat, S. Kuntaegowdanahalli and I. Papautsky, "Continuous particle separation in spiral microchannels using dean flows and differential migration", *Lab on a Chip*, vol. 8, no. 11, p. 1906, 2008.

[15] S. Choi, J. Karp and R. Karnik, "Cell sorting by deterministic cell rolling", *Lab on a Chip*, vol. 12, no. 8, p. 1427, 2012.

[16] H. Joensson, M. Uhlén and H. Svahn, "Droplet size based separation by deterministic lateral displacement—separating droplets by cell-induced shrinking", *Lab on a Chip*, vol. 11, no. 7, p. 1305, 2011.

[17] J. Shim and C. Ahn, "An on-chip whole blood/plasma separator using hetero-packed beads at the inlet of a microchannel", *Lab on a Chip*, vol. 12, no. 5, p. 863, 2012.

[18] H. Wei, B. Chueh, H. Wu, E. Hall, C. Li, R. Schirhagl, J. Lin and R. Zare, "Particle sorting using a porous membrane in a microfluidic device", *Lab Chip*, vol. 11, no. 2, pp. 238-245, 2011.

[19] A. Bhagat, H. Hou, L. Li, C. Lim and J. Han, "Pinched flow coupled shear-modulated inertial microfluidics for high-throughput rare blood cell separation", *Lab on a Chip*, vol. 11, no. 11, p. 1870, 2011.

[20] C. Wyatt Shields IV, C. Reyes and G. López, "Microfluidic cell sorting: a review of the advances in the separation of cells from debulking to rare cell isolation", *Lab Chip*, vol. 15, no. 5, pp. 1230-1249, 2015.

[21] M. Hamon and J. Hong, "New tools and new biology: Recent miniaturized systems for molecular and cellular biology", *Mol Cells*, vol. 36, no. 6, pp. 485-506, 2013.

[22] N. Pamme, "Continuous flow separations in microfluidic devices", *Lab on a Chip*, vol. 7, no. 12, p. 1644, 2007.

[23] S. Holm, J. Beech, M. Barrett and J. Tegenfeldt, "Separation of parasites from human blood using deterministic lateral displacement", *Lab on a Chip*, vol. 11, no. 7, p. 1326, 2011.

[24] S. Lockery, K. Lawton, J. Doll, S. Faumont, S. Coulthard, T. Thiele, N. Chronis, K. McCormick, M. Goodman and B. Pruitt, *"Artificial Dirt: Microfluidic Substrates for Nematode Neurobiology and Behavior"*, Journal of Neurophysiology, vol. 99, no. 6, pp. 3136-3143, 2008.

[25] A. Ghanbari, V. Nock, R. Blaikie, J. Chase, X. Chen, C. Hann and W. Wang, "Force pattern characterisation of Caenorhabditis elegans in motion", *IJCAT*, vol. 39, no. 123, p. 137, 2010.

[26] M. T. Manfredi, A. d. Cerbo, and M. Genchi, "Biology of filarial worms parasitizing dogs and cats." *Mappe Parassitologiche*, vol. 8, pp. 39-45, 2007.

Feature extraction algorithms for brain-computer interfaces

Dóra SZEPES
(Supervisor: István ULBERT)
Pázmány Péter Catholic University, Faculty of Information Technology and Bionics
50/a Práter street, 1083 Budapest, Hungary
szepes.dora@itk.ppke.hu

***Abstract*—Brain computer interfaces (BCIs) are capable of connecting the human brain with different devices or software. Nowadays their main use is making disabled people's lives easier by providing a way of communication or restoration of movement. Feature extraction is part of the signal processing step, where the task is obtaining the most important characteristics of the recorded signal that can indicate the user's intentions. For this step to be successful, the modalities used in the experiment must be carefully selected. Our goal was to put together a BCI system that is capable of producing four different control signals, which can be used for game control. In this article I will provide a basic review on brain computer interfaces, the most common feature extraction algorithms and modalities used, and the results of an offline system that we created.**

***Keywords*-brain-computer interface; EEG; feature extraction; modality; movement imagery; power spectral density, common spatial patterns**

I. Introduction

A brain-computer interface (BCI) records brain signals, then transforms them into control signals, which can be used for various applications. A BCI system consists of three main parts, namely the recording device, the signal processing algorithm and the effector. There are many different approaches for recording brain signals, but the ones that are mainly used in BCI research are electroencephalography (EEG) and electrocorticogram (ECoG). EEG is preferred because its non-invasive nature makes recording from a wide range of people possible, including healthy subjects. ECoG provides higher spatial resolution, but it is an invasive method, so it can only be rarely used on humans.

The signal processing algorithm is responsible for translating the incoming brain signals into control signals. This step consists of filtering, feature extraction and classification. The purpose of feature extraction is obtaining signal characteristics that are specific to the user's intention. To make this possible, carefully selected modalities must be used, which ultimately means that different mental tasks must be performed by the user. The most commonly used task is motor imagery (MI), where the user has to imagine moving one of their body parts (usually legs, hands or tongue), but word association and simple calculations are used too [1]. When the control signals are generated after classification, they can be used as an input to different devices or software. Common applications include letter selection, cursor movement, wheelchair navigation and prosthesis movement.

Since today's BCI systems are still lacking in accuracy and speed, they are mostly used in case of disabled people. The most famous application is providing a way of communication for people suffering in locked-in syndrome because of amyotrophic lateral sclerosis, or other reasons [2]. These people cannot make voluntary movements (except for eye movement in most cases), so BCIs make communication possible that could not be achieved otherwise. Other uses are navigation of a wheelchair for tetraplegic people, or moving a prosthesis or exoskeleton in case of someone who lost their limbs or have them paralyzed. Further applications exist too, but most of them are at the experimental stage and not widely used, since they can be replaced with faster and more accurate solutions. Commercial BCI systems available to the public also exist. These are mostly used for game control, but are usually very inaccurate. In the future with the improvement of BCI systems there will be more applications available for both disabled and healthy people.

II. Methods

A. Subjects and experimental setup

Four healthy and one disabled volunteer participated in the experiment. The healthy subjects had one session, while the disabled subject had two. EEG signals were recorded using 32 Ag/AgCl electrodes in case of the healthy subjects, and 64 Ag/AgCl electrodes in case of the disabled subject. Sampling rate varied between 300, 500 and 1000 Hz.

B. Modalities and execution of the experiment

In case of the healthy subjects the modalities used were tongue, both legs, right hand, and left hand MI. In case of the disabled subject we also added new mental tasks, namely concentrating on a familiar melody, thinking of words starting with a given letter, rotating an imagery 3D body, and navigation in the mind at a familiar place. The subject was sitting in front of a computer screen, where the current task that needed to be performed was written on the screen. Each trial began with resting, then the different mental tasks were repeated multiple times. The length of one type of task varied between 2, 5 and 10 seconds in the case where there was only MI, and it was 9 seconds in case of the expanded task list. One trial consisted of 20 tasks. There was also an other type of trial, where the subject had to maintain one kind of continuous MI for 180 seconds.

C. Software and toolboxes

The offline BCI system was implemented in MATLAB. The EEGLAB toolbox [3] was used for the different signal processing operations such as epoching the data, and also for the power spectral density analysis. The common spatial patterns algorithms were implemented with the help of the Regularized Common Spatial Patterns (RCSP) toolbox [6].

D. SZEPES, "Feature extraction algorithms for brain-computer interfaces" in *PhD Proceedings Annual Issues of the Doctoral School, Faculty of Information Technology and Bionics, Pázmány Péter Catholic University – 2016.* G. Prószéky, P. Szolgay Eds. Budapest: Pázmány University ePress, 2016, pp 105–107.

D. Preprocessing

The recorded signals were either filtered with a 4th order Butterworth filter between 4 and 40 Hz, or passed through the FORCe algorithm, which is an artifact removal algorithm that was designed especially for brain-computer interfaces [4]. Before the feature extraction step, in case the recording contained alternating modalities, the signal was split into sections based on the timing of the different mental tasks. After the separated data was available, 0.5-0.5 seconds were cut off from the beginning and the end of the segments. This was necessary because it takes some time for the subject to switch to a new task. Next, these segments were epoched with an epoch length varying between 0.5 and 2 seconds without overlaps, and in some cases 0.5 seconds with a 50% overlap. Then the epochs of the same tasks were gathered, and the data was ready for classification. In case of the continuous MI recordings, 5-5 seconds were cut from the whole signal, then epoching was performed with 0.5, 2 and 4 seconds long epochs without any overlapping.

E. Feature extraction algorithms

1) Power spectral density analysis: Power spectral density (PSD) is commonly used for feature extraction in BCIs. Its main advantage is that it is easily implementable, and it is robust across different sessions [5]. Its disadvantage is the slower speed, and usually worse accuracy compared to other methods. The power spectra can be calculated for the whole frequency range of the band-pass filtered signal, or for multiple narrow bands within this range. In our experiments the PSD was calculated on the whole preprocessed signal, which means from 4 to 40 Hz, using the built-in PSD algorithm of the EEGLAB toolbox.

2) Common spatial patterns: Another popular choice for feature extraction in BCIs is the common spatial patterns (CSP) algorithm. This algorithm can only be applied to two classes of data, by learning a spatial filter that maximizes the discriminability of these classes. This can be written formally with the following function:

$$J(w) = \frac{w^T X_1^T X_1 w}{w^T X_2^T X_2 w} = \frac{w^T C_1 w}{w^T C_2 w}$$

where w stands for the filters, X is a matrix that contains the data for a given class, and C is the spatial covariance matrix for the given class [6]. An important parameter of the CSP algorithms is the number of filter pairs used. This number varied between 3, 8 and 32 when 64 channels were available, and was either 3 or 8 when the recording consisted of 32 channels, since it cannot be larger than half of the number of channels.

The main disadvantage of this algorithm is that it is sensitive to noise, and tends to overfit the data. To compensate for these problems, different regularized versions of the CSP algorithm had been developed [6]. In our BCI system only the best performing ones were considered, based on the paper that the creators of the RCSP toolbox provided. According to this, the most promising RCSP algorithms are the CSP with Weighted Tikhonov Regularization (WTRCSP) and the CSP with Tikhonov Regularization (TRCSP), both with a mean accuracy around 79%.

TRCSP introduces a quadratic penalty term to the previous function, which ultimately leads to mitigating the effect of artifacts [6]. In the case of this algorithm, an alpha value must be given as an input parameter, which is responsible for the attenuation of the effect of the penalty term. The value of alpha can be selected manually, or the best performing value can be calculated by a script included in the toolbox. Since the latter uses cross validation, it increases the runtime significantly, but also makes the result more accurate.

WTRCSP is a variant of the TRCSP algorithm. It performed slightly better, however it requires not only the data of the given subject, but also recordings from other subjects. This complicates the feature extraction process, so this algorithm was rejected. Ultimately the simple CSP and the TRCSP algorithms were tested in our offline BCI system.

Subject	0.5 s	2 s	4 s
Subject 1	81.62%	98.35%	98.33%
Subject 2	-	93.33%	92.54%
Subject 3	-	71.18%	73.75%
Subject 4	-	73.03%	64.64%
Subject 5	-	90.72%	91.61%

Subject	0.5 s FORCe	2 s FORCe	4 s FORCe
Subject 1	89.44%	95.98%	98.39%

TABLE I
PSD RESULTS FOR CONTINUOUS MODALITIES

III. RESULTS

The classification was performed by other members of the team using support vector machines (SVMs). A more comprehensive analysis of the results only happened in case of the disabled subject, because in his case recordings from two sessions were available. There were different parameters that were investigated during this stage. The first was epoch length, which could be 0.5, 2 or 4 seconds with no overlap, or 0.5 seconds with 50% overlap. Another important task was testing if the use of the FORCe algorithm produced higher accuracy. In case of the different CSPs, the effect of the number of filter pairs was examined too, which was either 3, 8 or 32.

A. PSD results

First the continuous MI task with PSD as the feature extraction algorithm was investigated, the results of this can be seen in Table I. It should be noted that 0.5 seconds epoch lengths and the FORCe algorithm were not tested in case of the healthy subjects.

We can see from the results that Subject 1 performed the best, and it is apparent that there are big differences in accuracy across the subjects. It is possible that the nearly perfect results could be achieved because the system learned artifacts, not the real underlying signal characteristics. In general, longer epochs produced more accurate result. While the difference between using 2 and 4 seconds long epochs was not significant, in case of 0.5 seconds the accuracy noticeably dropped. This does not necessarily mean that longer epochs should be used in the final implementation, since in case of an online system the decision should be made in a short amount of time, so the faster decision making might be worth the drop in accuracy.

Next, the alternating modality recordings were investigated, the results of this can be found in Table II. Note that this type of data was not analyzed in case of Subject 5.

It is clear that the results are a lot more inaccurate than in case of the continuous MI, only being slightly better than

Subject	0.5 s	2 s	4 s
Subject 1	30.47%	36.11%	33.89%
Subject 2	-	35.48%	38.46%
Subject 3	-	25.92%	27.78%
Subject 4	-	30.61%	24.44%

Subject	0.5 s FORCe	2 s FORCe	4 s FORCe
Subject 1	28.71%	30.00%	32.78%

TABLE II
PSD RESULTS FOR ALTERNATING MODALITIES

chance. This supports the suspicion that the previous BCI only learned artifacts. It can be observed that the FORCe algorithm only made the results worse, and unlike previously the drop in accuracy is not that significant when 0.5 seconds epoch length was used.

B. CSP results

The two CSP algorithms were applied to all of the available recordings, but the classification has only been partially done for the data of the disabled subject, so only early results will be discussed here. These recordings are especially of interest because they contain modalities other than MIs. Since the FORCe algorithm did not result in better accuracy in the early tests, only the band-pass filter was applied in the preprocessing stage. Also, 4 seconds long epochs were no longer used, since these would be too long for an online decision making, and they do not produce significantly better results than the 2 seconds long epochs, as previously seen. 0.5 seconds epoch length with a 50% overlap was also examined besides the one without overlapping.

In case of the continuous MI recordings, the accuracy obtained were similar to the PSD result. Both the CSP and TRCSP algorithms produced results with higher than 85% accuracy, with the TRCSP being slightly better. When the recordings with alternating modalities were analyzed it became apparent that in this case the CSP algorithms are performing significantly better than the PSD. Another trend observed was that the accuracy of the classification was higher when more filter pairs were used. Since the larger number of filter pairs does not significantly increase runtime, this will not cause a problem in the online system.

Our goal was to produce four different control signals that can be used in the future online BCI system. For achieving this it is important to choose four modalities that are well separable. Figure 1 contains the classification accuracy for each pair of modalities tested on the disabled subject in case of a TRCSP algorithm with 3 filter pairs and 2 seconds epoch length. We can see that most of the fields are red, which means good accuracy. The early results show that an even more promising feature extraction algorithm is the TRCSP with 32 filter pairs and 0.5 seconds overlapping epochs, and the best mental tasks are tongue MI, right hand MI, thinking of a familiar melody and subtraction. These parameters result in an 87.98% accuracy, and because of the short epoch length this would be suitable for fast online decision making.

IV. CONCLUSIONS

I implemented the feature extraction algorithm of a BCI system that is capable of producing PSD, CSP and TRCSP features from a preprocessed or raw EEG signal. We managed to put together an offline BCI that can mainly be used for

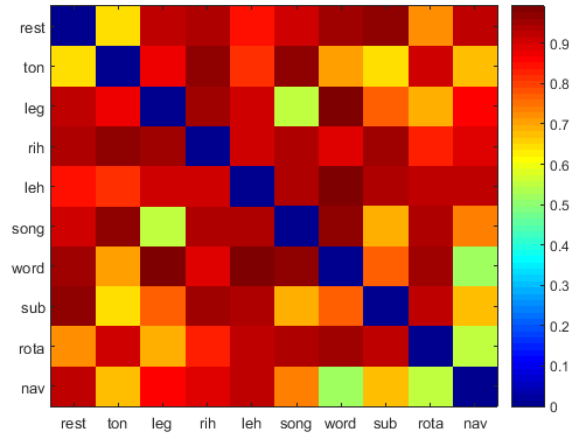

Fig. 1. Classification accuracy for each pair of modalities. A TRCSP algorithm was used with 3 filter pairs, and 2 seconds epoch length. The modalities are the following in order: resting state, tongue MI, leg MI, right hand MI, left hand MI, thinking of a song, thinking of words starting with a given letter, subtracting, rotating a 3D body, and navigation.

deciding which parameters would be the best for an online system. Our early results show that the most promising approach is the use of 0.5 seconds long epochs that are 50% overlapped, and the TRCSP algorithm with 32 filter pairs. Using the FORCe algorithm does not affect the results significantly in a positive way, so it is advisable to discard this preprocessing step, since it increases runtime. We found that the best mental tasks for producing the four control signals are tongue MI, right hand MI, thinking of a familiar melody and subtraction. Based on these findings, our future plan is recording more data, finalizing the parameters, and the implementation of the online BCI system.

ACKNOWLEDGEMENTS

I would like to thank my supervisor, István Ulbert for providing the opportunity to work on this project. I would also like to say thanks to Zoltán Kárász, Tibor Nánási, Csaba Köllőd, György Perczel, László Nikházy and Tamás Molnár for their contribution to the project.

REFERENCES

[1] E. Friedrich, C. Neuper and R. Scherer, *Whatever Works: A Systematic User-Centered Training Protocol to Optimize Brain-Computer Interfacing Individually*, PLoS ONE, vol. 8, no. 9, p. e76214, 2013.

[2] N. Birbaumer, A. Murguialday and L. Cohen, *Brain–computer interface in paralysis*, Current Opinion in Neurology, vol. 21, no. 6, pp. 634-638, 2008.

[3] A. Delorme and S. Makeig, *EEGLAB: an open source toolbox for analysis of single-trial EEG dynamics including independent component analysis*, Journal of Neuroscience Methods, vol. 134, no. 1, pp. 9-21, 2004.

[4] I. Daly, R. Scherer, M. Billinger and G. Muller-Putz, *FORCe: Fully Online and Automated Artifact Removal for Brain-Computer Interfacing*, IEEE Trans. Neural Syst. Rehabil. Eng., vol. 23, no. 5, pp. 725-736, 2015.

[5] P. Herman, G. Prasad, T. McGinnity and D. Coyle, *Comparative Analysis of Spectral Approaches to Feature Extraction for EEG-Based Motor Imagery Classification*, IEEE Trans. Neural Syst. Rehabil. Eng., vol. 16, no. 4, pp. 317-326, 2008.

[6] F. Lotte and Cuntai Guan, *Regularizing Common Spatial Patterns to Improve BCI Designs: Unified Theory and New Algorithms*, IEEE Transactions on Biomedical Engineering, vol. 58, no. 2, pp. 355-362, 2011.

Bioactive properties of nanostructured surfaces

Zsófia SZTYÉHLIKNÉ BÉRCES
(Supervisor: Anita PONGRÁCZ PhD, Kristóf IVÁN PhD)
Pázmány Péter Catholic University, Faculty of Information Technology and Bionics
50/a Práter street, 1083 Budapest, Hungary
berces.zsofia@itk.ppke.hu

***Abstract*—Surface quality of implantable biosensors for recording electrical signals in the central nervous system is of great importance with respect to long-term use in chronic implantations. In our work the interaction of neural stem-cell cultures and nanostructured surfaces was investigated as a model of implanted device surface and living tissue interaction. We have developed a robust, maskless nanostructuring method, which can be integrated into our neural biosensor fabrication process. Morphology of the fabricated nanograss has been characterised using scanning electron microscopy. The nanopillars are between 520-800 nm in height and their density is 18-70/μm^2. GFP-NE-4C cells are cultured on the nanostructured and platinized surfaces and their viability and differentiation are investigated by MTT assay and fluorescent microscopy.**

***Keywords*-neural implant; nanostructuring; biocompatibility**

I. Introduction

CNS implantable devices not only help understanding the neural information processing but also has a potential for clinical treatment on neurological disorders such as Parkinson's desease [1], essential tramor [2] and locked-in sydrome [3]. But the foreign body response (FBR) alters the function of the tissue surround the implanted device. Glial scar formation and neural cell loss takes place [4], [5] which leads to to the faliure of device functionality. Cells in their natural environment interact with nanoscale structures like the extracellular matrix and its proteins [6]. In case of fibroblasts and osteoblasts it is already demonstrated that surfaces with specific surface roughness parameters show better cell adhesive properties [7]. On the other hand, there are only a few results in the case of neural and glial cells.

By modulating the specific surface area, wetting properties and nano-pattern regularity of the nanostructured samples, several groups published better neural cell adhesion and viability on nanostructured surfaces compared to the smooth references in the past few years [8]–[13]. In 5-day long experiments, neural cells showed surface preference. Thely were observed to migrated to nanostructured parts of the sample [14].

In the case of neuroprosthesis in living tissue, the reaction of the surrounding glial cells is as important as the adhesion of the neurons. The astrocytes and microglias are key factors in neuron metabolism and function. They play an emphatic role as the protectors of the central nervous system against diseases and injuries. In case of physical injury such as the microelectrode implantation they generate an aggressive neuroprotective reaction called gliosis [16]. As a result, the so-called glial scar remains around the injury and the foreign body which hinders electrical recordings. As a consequence in neural implant surface development it is also important to investigate the neuroprotective reaction of the glial cells to the proposed surface. In 1997, Turner et al. showed lower astrocyte adhesion on nanostructured samples compared to smooth ones using immortalized cell line. In the same article, the authors presented that primer neural and glial cells react the other way around [15].

Since these cells work in a close cooperation with neurons and also with each other, it is also important to examine them in tissue-like co-cultures. It was also shown that after brain injury specific cells acquire stem cell properties and take a very important role in the wound healing process [17], [18].

Neural stem cells (NCSs) are non-differentiated cells of neuroectodermal origin. Populations of various NSCs co-exist in the mammalian brain [19]. Under appropriate conditions, NSCs can generate neurons, astrocytes and oligodendroglia cells. The conditions under which NSCs are differentiated into neural or glial cells are still nor clearly kown. But they may include appropriate growth factor/cytokine composition and also the surface material and topography of the implant surface offered for cell attachment.

My work aims to develop bioimplant surfaces with nanoscale patterns using novel combination of micro- and nanomachining techniques. The proposed maskless nanopatterning method can easily be integrated into the fabrication process of neural microelectrodes. The expected results are envisioned to minimize the immune response of the neural tissue to the surface of the implanted microelectrodes and thus enable efficient functionality in long-term experiments. As a model for the tissue-implant interface a cell line with neural stem cell like properties is investigated on the designed implant surface samples. Adhesion and differentiation of the stem cells on the surfaces can be a forecast for the behavior of the stem cells in-vivo upon the injury caused by the implant insertion.

II. Materials and Methods

A. Sample design and fabrication

My investigations are based on standard cell viability assays (MTT assay) and fluorescent microscopic observations of cell adhesion and differentiation. To measure the preferential behaviour of cells on nanostructured and smooth reference surfaces, micropatterned chips are designed. Patterns are in the range of the contact site of a microelectrode array usually used for neural recording.

Figure 1 shows the micro pattern of the designed chips for fluorescent microscopy measurements. Chips for MTT assay were designed to fit into the standard 96 well plate and had the same surface among the whole chip which were either polycrystalline silicon (polySi), nanostructured polySi (also called as black polySi), flat platinum (Pt) or blackSi covered with platinum. During the fabrication process first, 500 nm thick thermal oxide is grown on a 4" (100) oriented Si wafer. Then 1000 nm poly-Si is deposited in a Tempress LPCVD equipment. The micropatterning of the black-Si is performed by photolitography and microstructured in poly-etchant. Nanopattern formation is carried out by deep reactive

Zs. SZTYÉHLIKNÉ BÉRCES, "Bioactive properties of nanostructured surfaces" in *PhD Proceedings Annual Issues of the Doctoral School, Faculty of Information Technology and Bionics, Pázmány Péter Catholic University – 2016.* G. Prószéky, P. Szolgay Eds. Budapest: Pázmány University ePress, 2016, pp 109– 112.

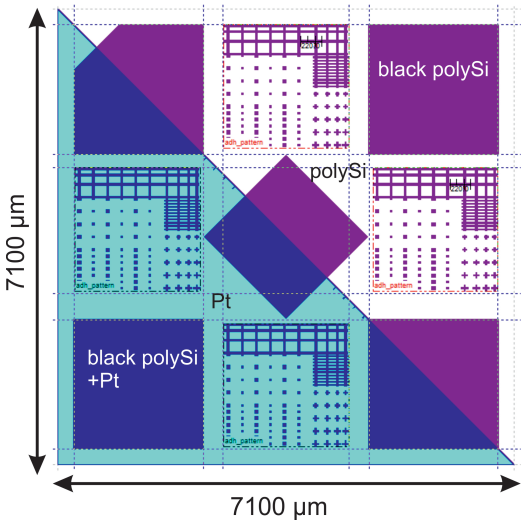

Fig. 1. Sample for fluorescent investigations. Light blue shows platinum, purple represents black silicon covered areas without platinum coating and dark blue areas represent platinum coated black silicon. Different microstructures are designed based on literature or inspired by our microelectrode (contact site sizes and spacing).

ion etching (DRIE) at cryogenic temperature. After black-Si formation platinum deposition is performed and followed by a second patterning step using lift-off process.

Advantages of the process are that the nanostructuring is maskless and it can fully be integrated into an implantable Si microelectrode fabrication process.

B. Surface characterisation

The effect of the different etching parameters and platinum layer thicknesses is investigated using SEM. From the images the pillar height and density parameters of the fabricated samples are also extracted.

C. Cell culturing

1) Sample preparation: The fabricated silicon wafers were diced to fit in the 24 or 96 well plates. Chip size is $7,3x7,3$ mm and $3,2x3,2$ mm respectively. Samples were sterilised by dry heat steriliser and placed into sterile 24 or 96 well plates.

2) Cell line: The GFP-NE-4C cell line is a neuroectodermal cell line derived from embrionic forebrain vesicles of p53 deficient mices [20]. Cells express green fluorescent protein (GFP) in the cell plasm. GFP emits green light upon illumination of approx. 480 nm blue light therefore is capable of fluorescent imaging.

3) Culturing and fixation method for fluorescent imaging: 10^5 GFP-NE-4C cells were seeded in each well. Cultures were grown in minimum essential medium (Sigma, M2279), with 10% fetal calf serum, 2% glutamine and 0,1% gentamicine in 37°C at 5% CO_2. Samples for the investigation of differentiation were treated by all-trans retinoic acid (RA; 10-6 M) after 24 hours of incubation. Than cells were cultured for 9 days during which half of the medium was changed every day.

After the incubation the cultures for fluorescent imaging were fixed on the Si samples. First they were rinsed with PBS than incubated in 4% parafolmadehyde for 20 minutes. To visualise the differentiated neurons III-β-tubuline (with Alexa Fluor ®594, exc. 590nm, em. 619nm)were immunostained on the samples. After 2 subsequent PBS rinsing samples were placed onto microscope slides and coated with Mowiol ®containing DAPI (4',6-diamidino-2-phenylindole) stain and covered with a microscope cover glass. DAPI binds to specific regions of DNA and upon illumination with approx. 350nm wavelength light emits blue light. Therefore nuclei of the cells can be visualised. Some of the samples were fixed after 4 or 24 hours to investigate the adhesion of them. In this cases no III-β-tubuline staining was needed.

Fluorescent images were taken using a Zeiss Axio Vert.A1 microscope both with GFP, DAPI and Cy3 channels. For aquisition, multichannel imaging and basic image enhancement Zeiss Zen Blue edition software was used. A two channel image of the cells on a patterned sample cultured for 24 hours is shown on Figure 2.

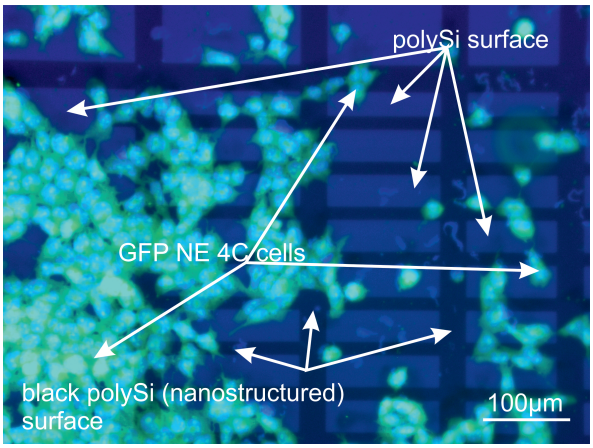

Fig. 2. Fluorescent image of GFP-NE-4C cells on the fabricated samples after 24h adhesion assay. The blue channel corresponds to the DAPI staining which stains the nuclei. Green light is emitted by the GFP which is expressed in the cell plasma. Black stripes are the nanostructured patterns of the sample.

4) Culturing and fixation method for toxicity and adhesion assay: 10^4 GFP-NE-4C cells were seeded in each well. Cultures were grown in minimum essential medium (Sigma, M2279), with 10% fetal calf serum, 2% glutamine and 0,1% gentamicine. The cultures were incubated in 37°C at 5% CO_2 for 4 or 24 hours. Samples for MTT assay were removed from the culturing wells after the 4h or 24h incubation time, gently rinsed with phosphate buffered saline (PBS) and replaced into a clean wells containing 50 μl medium. 10 μl MTT (3-[4,5-dimethylthiazol-2yl]-2-5-diphenyl-tetrazolium bromide [Sigma]) was added and the cells were incubated for 90 min in CO_2 incubator. After the formation of purple formazan crystals, 100 μl acidified isopropanol was added to dissolve the crystals and the cell material. 50 μl of the optically transparent solution was transferred into clean assay-plates and the optical density was determined at double (550 nm measuring, 650 nm reference) wavelengths.

III. Results

The morphological parameters of the samples (pillar density, pillar height) were derived from scanning electron micrographs. The nanopillars are between 520-800 nm in height, and their density is 18-70/μm^2 depending on the fabrication parameters of the DRIE process [21]. A representative scanning electronmicrograph is shown on Figure 3.

Based on the 4h MTT assays there is no significant difference in the surface toxicity of the investigated surfaces and none of them are toxic as measured optical densities are not lower compared to the reference glass surface. However

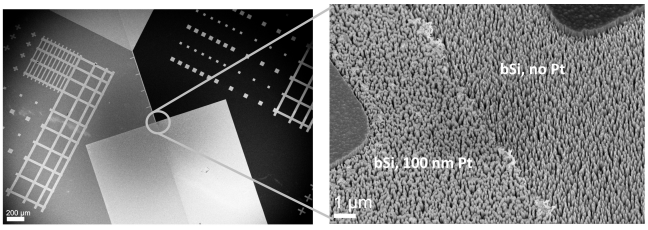

Fig. 3. Scannig electromicrogaphs of the prepared black Si samples. Based ont he SEM images the pillars' height and average density were calculated to characterise the differently etched nanosurfaces.

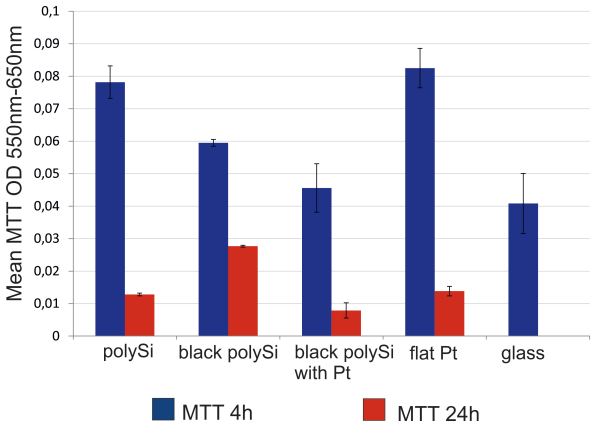

Fig. 4. Results of the MTT assays. Sample means and standars errors are shown (sample counts: 4h: $n_{polySi} = 4, n_{blackpolySi} = 3, n_{blackpolySi+Pt} = 5, n_{Pt} = 4, n_{glass} = 5$; 24h: $n_{polySi} = 4, n_{blackpolySi} = 3, n_{blackpolySi+Pt} = 4, n_{Pt} = 5$). There is no significant difference in surface toxicity and none of the surfaces are toxic. However based on the 24h MTT results these surfaces do not support the adhesion of the GFP-NE-4C cells.

remarkalby less cells could be measured on the black polySi surface compared to the polySi and on the platinum covered blackSi surface compared to the flat platium (Figure 4, blue bars). Based on the 24h MTT assay cell adhesion can be evaluated. No significant difference can be shown between surfaces however it's notable that a very small propotion of the seeded cell were attached to the surfaces which implies that these surfaces not specifically support the adhesion of this cell type (Figure 4, red bars).

Based on the fluorescent imaging after the retinoic acid treatment cells differentiated into neurons on all type of the surfaces. On Figure 5A a single channel (Cy3) fluorescent image shows the developed neurites on a polySi/black polySi surface. In the background the nanostructured grid can be seen. On Figure 5B a three channel fluorescent image is shown. Blue dots are the cell nuclei, cell plasm is visualised in green and the red objects are neural cell components.

IV. Conclusion and Future Plan

Based on our preliminary studies [21], the nanopattern morphology of our chips are tuneable. GFP-NE-4C cells seeded on the surfaces show a remarkable pereference to the flat surface over the nanostructured areas. Stem cell differentiation into neurons took place on all type of surfaces. In our ongoing investigations we develop a quantitative method to evaluate the differences between the surfaces in respect of cell attachment and differentiation more accurately.

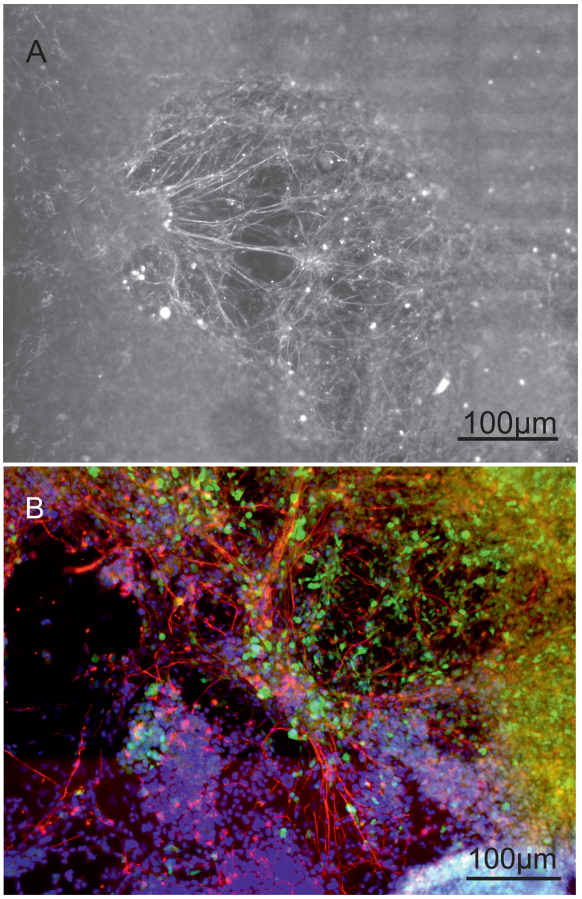

Fig. 5. A) Single channel (Cy3) fluorescent image. Neurites on a polySi/black polySi surface differentiated from GFP-NE-4C neural progenitor cells. B)Three channel fluorescent image. Blue dots (DAPI channel) are the cell nuclei, cell plasm is visualised in green (FITC channel) and the red objects (Cy3 channel) are neural cell components.

Acknowledgment

The author is grateful to the supportive staff of the MEMS Lab in MFA, Centre for Energy Research, HAS and the work of dr. Zoltán Fekete and Mr A. Straszner in deep reactive ion etching is also acknowledged. Thanks are also due to Judit Mercédesz Pomothy for her work with the cellular assays. The authors also would like to thank dr. Emília Madarász and Attila Jády from MTA KOKI for the opportunity of cooperation. Zs. Bérces is thankful for the KTIA-13-NAP-A-IV/6 and KAP15-190- 3.3-ITK grants.

References

[1] The Deep-Brain Stimulation for Parkinson's Disease Study Group, "Deep-Brain Stimulation of the Subthalamic Nucleus or the Pars Interna of the Globus Pallidus in Parkinson's Disease," N Engl J Med, vol. 345, no. 13, pp. 956–963, Sep. 2001.

[2] W. C. Koller, K. E. Lyons, S. B. Wilkinson, A. I. Troster, and R. Pahwa, "Long-term safety and efficacy of unilateral deep brain stimulation of the thalamus in essential tremor," Mov. Disord., vol. 16, no. 3, pp. 464–468, May 2001.

[3] A. Kübler, B. Kotchoubey, J. Kaiser, J. R. Wolpaw, and N. Birbaumer, "Brain-computer communication: unlocking the locked in.," Psychol. Bull., vol. 127, no. 3, pp. 358–375, 2001.

[4] K. A. Moxon, S. Hallman, A. Aslani, N. M. Kalkhoran, and P. I. Lelkes, "Bioactive properties of nanostructured porous silicon for enhancing electrode to neuron interfaces," J. Biomater. Sci. Polym. Ed., vol. 18, no. 10, pp. 1263–1281, 2007.

[5] R. Biran, D. C. Martin, and P. A. Tresco, "Neuronal cell loss accompanies the brain tissue response to chronically implanted silicon microelectrode arrays," Exp. Neurol., vol. 195, no. 1, pp. 115–126, 2005.

[6] D. H. Kim, P. P. Provenzano, C. L. Smith, and A. Levchenko, “Matrix nanotopography as a regulator of cell function,” J. Cell Biol., vol. 197, no. 3, pp. 351–360, 2012.
[7] Dalby, M.J.; Pasqui, D.; Affrossman, S.: ’Cell response to nano-islands produced by polymer demixing: a brief review’, IEE Proceedings - Nanobiotechnology, Volume 151, Issue 2, Pages 53-61, 2004.
[8] Moxon, K.A.; Kalkhoran, Nader M.; Markert, M.; Sambito, M.A.; McKenzie, J.L.; Webster, J.T., ’Nanostructured surface modification of ceramic-based microelectrodes to enhance biocompatibility for a direct brain-machine interface’, Biomedical Engineering, IEEE Transactions on , Volume 51, Issue 6, Pages 881-889, 2004.
[9] Andrei V. Sapelkin, Susan C. Bayliss, Bayram Unal, Amanda Charalambou, ’Interaction of B50 rat hippocampal cells with stain-etched porous silicon’, Biomaterials, Volume 27, Issue 6, Pages 842-846, 2006.
[10] A. M. P. Turner, N. Dowell, S. W. P. Turner, L. Kam, M. Isaacson, J. N. Turner, H. G. Craighead and W. Shain, ’Attachment of astroglial cells to microfabricated pillar arrays of different geometries’, Journal of Biomedical Materials Research Volume 51, Issue 3, Pages 430–441, 2000.
[11] YW Fan, FZ Cui, LN Chen, Y Zhai, QY Xu, IS Lee, Adhesion of neural cells on silicon wafer with nano-topographic surface, Applied surface science Volume 187 Issue 3, Pages 313-318, 2002.
[12] Saida P. Khan, Gregory G. Auner, Golam M. Newaz, Influence of nanoscale surface roughness on neural cell attachment on silicon, Nanomedicine: Nanotechnology, Biology and Medicine, Volume 1, Issue 2, Pages 125-129, 2005.
[13] Gaëlle Piret, Maria-Thereza Perez, Christelle N. Prinz, ’Neurite outgrowth and synaptophysin expression of postnatal CNS neurons on GaP nanowire arrays in long-term retinal cell culture’, Biomaterials, Volume 34, Issue 4, Pages 875-887,2013.
[14] Y.W. Fan, F.Z. Cui, S.P. Hou, Q.Y. Xu, L.N. Chen, I.-S. Lee, Culture of neural cells on silicon wafers with nano-scale surface topography, Journal of Neuroscience Methods, Volume 120, Issue 1, Pages 17-23, 2002.
[15] Turner, S. and Kam, L. and Isaacson, M. and Craighead, H. G. and Shain, W. and Turner, J.,’Cell attachment on silicon nanostructures’ Journal of Vacuum Science and Technology B., 15, Pages 2848-2854, 1997.
[16] Alexei Verkhratsky (Editor), Arthur Morgan Butt (Editor), Glial Physiology and Pathophysiology, Wiley-Blackwell, ISBN: 978-0-470-97853-5, 2013.
[17] Annalisa Buffo, Inmaculada Rite, Pratibha Tripathi, Alexandra Lepier, Dilek Colak, Ana-Paula Horn, Tetsuji Mori, Magdalena Götz, ’Origin and progeny of reactive gliosis: A source of multipotent cells in the injured brain’, PNAS, Volume 105 No. 9, Pages 3581–3586, 2008.
[18] Stefanie Robel, Benedikt Berninger, Magdalena Götz, ’The stem cell potential of glia: lessons from reactive gliosis’, Nature Reviews Neuroscience Volume 12, Pages 88-104, 2011.
[19] E. Madarsz, “Diversity of Neural Stem/Progenitor Populations: Varieties by Age, Regional Origin and Environment,” in Neural Stem Cells - New Perspectives, InTech, 2013.
[20] Katalin Schlett, Emília Madarász, ’Retinoic acid induced neural differentiation in a neuroectodermal cell line immortalized by p53 deficiency’, Journal of Neuroscience Research Volume 47 Issue 4, Pages: 405-415, 1997.
[21] Z Fekete, Á Horváth, Zs Bérces, A Pongrácz ’Black poly-silicon: a nanostructured seed layer for sensor applications’ SENSORS AND ACTUATORS A-PHYSICAL Issue 216, Pages 277-286., 2014.

Program 2

COMPUTER TECHNOLOGY BASED ON MANY-CORE PROCESSOR CHIPS, VIRTUAL CELLULAR COMPUTERS, SENSORY AND MOTORIC ANALOG COMPUTERS

Head: Péter SZOLGAY

Case studies for the structural analysis of biochemically motivated nonlinear systems

Bernadett ÁCS
(Supervisor: Gábor SZEDERKÉNYI)
Pázmány Péter Catholic University, Faculty of Information Technology and Bionics
50/a Práter street, 1083 Budapest, Hungary
acs.bernadett@itk.ppke.hu

***Abstract*—In this paper we demonstrate algorithmic methods for determining realizations of kinetic systems with prescribed properties. The motivation is mainly to explore the structural properties of reaction networks having the same dynamical properties. The proposed computational methods can be applied to compute a special linearly conjugate realization of a kinetic system, or to determine all possible graph structures describing realizations of a kinetic system. The algorithms are proven to return the realizations meeting the descriptions.**

***Keywords*-kinetic system; chemical reaction network; directed graph representation; optimization methods**

I. Introduction and Basic Notions

Kinetic systems with polynomial nonlinearities can be originated from the modelling of dynamical processes in biochemistry [1]. However, these models can be applied to characterize the dynamical behaviour of a much wider range of systems [2].

In general, non-negative polynomial systems are defined in the form:

$$\dot{x} = M \cdot \varphi(x) \tag{1}$$

where $x : \mathbb{R} \to \mathbb{R}^n$ represents a non-negative function, the matrix $M \in \mathbb{R}^{n\times p}$ encodes the coefficients of the monomials defined by the mapping $\varphi : \mathbb{R}^n_+ \to \mathbb{R}^p_+$.

We consider kinetic systems as a special class of non-negative dynamical systems, that are suitable for modelling the dynamical behaviour of chemical reaction networks (CRNs). Reaction networks can be defined by three sets:

- A set of **species**: $\mathcal{S} = \{X_i \mid i \in \{1,\dots,n\}\}$
- A set of **complexes**: $\mathcal{C} = \{C_j \mid j \in \{1,\dots,m\}\}$
  $C_j = \sum_{i=1}^{n} \alpha_{ji} X_i \qquad \forall j \in \{1,\dots,m\}$
  $\alpha_{ji} \in \mathbb{N} \qquad \forall j \in \{1,\dots,m\},\ \forall i \in \{1,\dots,n\}$
- A set of **reactions**: $\mathcal{R} \subseteq \{(C_i, C_j) \mid C_i, C_j \in \mathcal{C}\}$

The reaction $C_i \to C_j$ is referred to as the ordered pair (C_i, C_j), and a non-negative **reaction rate coefficient** $k_{ij} \in \mathbb{R}_+$ corresponds to it, which determines the intensity of the reaction. The reaction $C_i \to C_j$ takes place if and only if the coefficient k_{ij} is positive. Since our interest lies rather in the structure of the reaction network, we are not interested in the actual values of the reaction rates, but distinguish only two cases, when it is zero or positive.

The properties of the reaction networks are encoded by special matrices. The structures of the complexes is characterized by the **complex composition matrix** $Y \in \mathbb{N}^{n\times m}$.

$$[Y]_{ij} = \alpha_{ji} \qquad \forall i \in \{1,\dots,n\},\ \forall j \in \{1,\dots,m\}$$

The presence of reactions in the reaction network is determined trough the reaction rates by the **Kirchhoff matrix** $A_k \in \mathbb{R}^{m\times m}$ of the CRN, which is a Metzler-matrix with zero column sums.

$$\begin{aligned} &[A_k]_{ij} = k_{ji} && \\ &\sum_{i=1}^{m} [A_k]_{ij} = 0 && \forall j \in \{1,\dots,m\} \\ &[A_k]_{ij} \geq 0 && i \neq j \end{aligned}$$

Since the reaction network is uniquely determined by the complex composition matrix and the Kirchhoff matrix, we refer to a CRN by the corresponding matrix pair (Y, A_k).

A. Dynamical description

If the concentrations of the species are characterized by the function $x : \mathbb{R} \to \mathbb{R}^n_+$ and mass action kinetics is assumed, the equations describing the dynamics of the CRN can be written in the form of a polynomial system:

$$\dot{x} = Y \cdot A_k \cdot \psi(x) \tag{2}$$

where $\psi : \mathbb{R}^n_+ \to \mathbb{R}^m_+$ is a monomial function with coordinate functions $\psi_j(x) = \prod_{i=1}^{n} x_i^{[Y]_{ij}},\ j \in \{1,\dots,m\}$.

A non-negative polynomial system (1) is called a **kinetic system** if there exists a reaction network (Y, A_k) so that the two models are governed by the same dynamics.

$$M \cdot \varphi(x) = Y \cdot A_k \cdot \psi(x) \tag{3}$$

Reaction networks with different sets of complexes and reactions can be determined by the same dynamics. If Equation (3) is fulfilled, then the CRN (Y, A_k) is called a **dynamically equivalent realization** of the kinetic system (1).

As it has been described in [3], the kinetic property of polynomial systems (1) can also be characterized by prescribing the sign pattern of the coefficient matrix M:

$$\forall i, j \quad [\ [Y]_{ij} = 0 \implies M_{ij} \geq 0\ ]$$

The definition of dynamical equivalence can be extended to the case when the space of concentrations is subject to a positive definite state transformation defined by the matrix $T \in \mathbb{R}^{n\times n}$ so that $\bar{x} = T^{-1} \cdot x,\ x = T \cdot \bar{x}$.

A reaction network (Y, A_k) is called a **linearly conjugate realization** of the kinetic system (1) if there exists a positive definite diagonal matrix $T \in \mathbb{R}^{n\times n}$ such that the following equation holds:

$$Y \cdot A'_k \cdot \psi(x) = T^{-1} \cdot M \cdot \Phi_T \cdot \varphi(x), \tag{4}$$

B. ÁCS, "Case studies for the structural analysis of biochemically motivated nonlinear systems" in *PhD Proceedings Annual Issues of the Doctoral School, Faculty of Information Technology and Bionics, Pázmány Péter Catholic University – 2016.* G. Prószéky, P. Szolgay Eds. Budapest: Pázmány University ePress, 2016, pp 115– 118.

where $\Phi_T \in \mathbb{R}^{n\times n}$ is a positive definite diagonal matrix, $[\Phi_T]_{ii} = \varphi_i(T \cdot \mathbf{1})$ for all $i \in \{1, \dots n\}$. It can be seen that dynamical equivalence is a special case of linear conjugacy, when the matrices T and Φ_T are identity matrices.

We want to determine realizations on a fixed set of complexes, which defines the matrix Y and the monomial function ψ. The kinetic system (1) can be transformed so that the monomial function φ is equal to ψ (and $p = m$ holds), but the described dynamics remains the same. In this case Equation (3) can be written as:

$$M = Y \cdot A_k \tag{5}$$

and also Equation (4) can be transformed into a more simple form:

$$T^{-1} \cdot M = Y \cdot A_b \tag{6}$$

where A_b is equal to the scaled matrix $A_k \cdot \Phi_T^{-1}$, and therefore A_b is also a Kircchhoff matrix, and it represents the same structure in the reaction network as A_k.

B. Graph representation

A reaction network can also be represented by a weighted directed graph $G(V, E)$ called **Feinberg-Horn-Jackson graph** or reaction graph for brevity. The vertices and edges represent the complexes and reactions, respectively. There is a directed edge from complex C_i to C_j if and only if k_{ij} is positive, which is the weight of the edge.

There are realizations with distinguished properties, a realization of a kinetic system with maximal or minimal number or reactions is called dense or sparse realization, respectively. It is known that there might be several different sparse realizations, however the dense realization is structurally unique. The following example has been first published in [5].

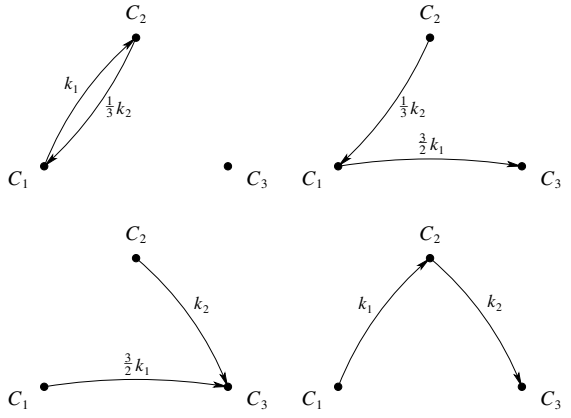

Fig. 1. Structurally different sparse realizations of the kinetic system (7)

$$\begin{aligned} \dot{x}_1 &= 3k_1x_2^3 - k_2x_1^3 \\ \dot{x}_2 &= -3k_1x_2^3 + k_2x_1^3 \end{aligned} \tag{7}$$

$$\mathcal{C} = \{C_1 = 3X_1, C_2 = 3X_2, C_3 = 2X_1 + X_2\}$$

C. Computational model

Realizations of a kinetic system with a fixed set of complexes can be determined by applying linear programming methods. The parameters of the model in case of linearly conjugate realizations are the coefficient matrix M and the complex composition matrix Y. The variables are represented by the off- diagonal entries of the matrix A_b and the diagonal entries of the matrix T. It follows from the definitions that the properties can be written in the form of linear constraints:

$$\begin{aligned} &T^{-1} \cdot M = Y \cdot A_b && \\ &\sum_{i=1}^{m} [A_b]_{ij} = 0 && j \in \{1, \dots, m\} \\ &[A_b]_{ij} \geq 0 && i \neq j \\ &[T]_{ii} > 0 && i \in \{1, \dots, m\} \end{aligned}$$

It is possible to add further linear constraint to de model, for example if it is known that some reactions can not be present in the reaction network, then the corresponding entries of matrix A_k can be prescribed to be zero. The objective function of the optimization model can also be defined according to the properties of the realization in demand.

II. Special properties

If the realizations are represented as points in the Euclidean space $\mathbb{R}^{m^2}$, then according to the model description the set of all realizations corresponds to a convex polyhedron, which implies a very important result, that turned out to be fundamental in the applicability of our algorithms. It has been proposed and proven in [4] as Proposition 5.1

Proposition 1. [4] *Among all the realizations linearly conjugate to a given CRN and fulfilling a finite set of linear constraints there is a realization determining a super-structure.*

The super-structure is the reaction graph representing the dense realization, which contains the reaction graphs of every other realization with the prescribed properties as subgraphs, not considering the edge weights. The superstructure property holds even if only realizations with some prescribed linear property are considered.

From the superstructure property it follows that the structure of the dense realization is unique. If there were two different dense realizations, then the reaction graphs representing them would contain each other as subgraphs, consequently these graphs must be structurally identical.

In Figures 2 and 3 the reaction graphs of the linearly conjugate and dynamically equivalent dense realizations of the kinetic system (8) can be seen. This example has originally been demonstrated in[7] as Example 3.

$$\begin{aligned} \dot{x}_1 &= x_1x_2^2 - 2x_1^2 + x_1x_3^2 \\ \dot{x}_2 &= -x_1^2x_2^2 + x_1x_3^2 \\ \dot{x}_3 &= x_1^2 - 3x_1x_3^2 \end{aligned} \tag{8}$$

$\mathcal{C} = \{C_1 = X_1 + 2X_2, C_2 = 2X_1 + 2X_2, C_3 = 2X_1 + X_2, C_4 = 2X_1, C_5 = X_1, C_6 = 2X_1 + X_3, C_7 = X_1 + 2X_3, C_8 = 2X_1 + 2X_3, C_9 = X_1 + X_2 + 2X_3, C_{10} = X_1 + X_3\}$

It can be seen that the graph in Figure 3 is a subgraph of the other one. This property always holds, since a dynamically equivalent realization is also a linearly conjugate realization, therefore the super-structure property of the dense realization is valid.

III. Computational results

In this section we propose the result of our methods for determining realizations of kinetic systems.

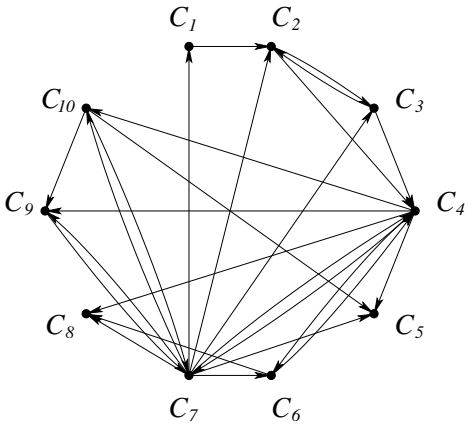

Fig. 2. Reaction graph of the dense linearly conjugate realization of the kinetic system (8)

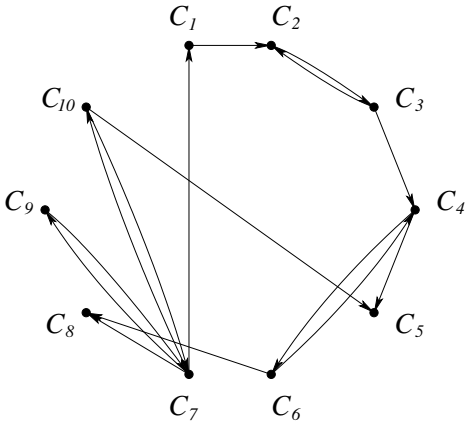

Fig. 3. Reaction graph of the dense dynamically equivalent realization of the kinetic system (8)

A. Algorithm to determine dense realizations

In [4] we have given a polynomial time algorithm for determining (constrained) dense linearly conjugate realizations of kinetic systems. This method also serves as a subroutine in our other algorithms, therefore it is essential to make it effective and accurate.

The basic idea of the algorithm is to generate realizations with predefined properties, and determine a dense realization as the convex combination of points corresponding to the realizations. It is proven that the returned realization is a dense realization, and according to the computational results it is the fastest and most reliable method so far.

B. Algorithm to determine weakly reversible linearly conjugate realizations

A CRN is called a weakly reversible realization of a kinetic system, if the reaction graph corresponding to it is strongly connected. Such realizations are important since in this case the structure has an impact on the dynamical properties as well.

The original version of the algorithm proposed in [6] was developed for computing weakly reversible dynamically equivalent realizations. In [4] we have given an improved version of the method for computing weakly reversible linearly conjugate realizations of kinetic systems. Furthermore, we have given a proof to the correctness of this method.

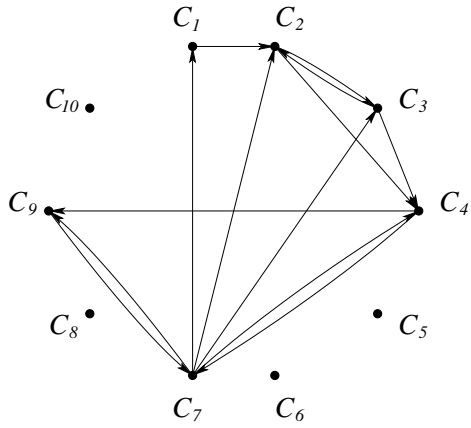

Fig. 4. Weakly reversible linearly conjugate realization of the kinetic system (8)

From the method it follows that the dense weakly reversible realization as well determines a super-structure among the weakly reversible realizations.

C. Algorithm to determine all possible structures

If no structural property only the dynamics of the reaction network is known, then the set of possible structures might give some information about the model. For example only those reactions might be present that are part of the dense realization, and there might be sets of reactions that are present only together.

In [8] we have given an algorithm to determine all possible reaction graph structures representing linearly conjugate realizations of a kinetic system with a fixed set of complexes. The algorithm is the first attempt to solve this problem and is proven to be correct and requiring polynomial computation time among steps. It is not possible to have a polynomial-time algorithm because of the exponential number of the possible structures.

The number of different structures increases rapidly. There are 18 structurally different realizations in case of the kinetic system (7), however during the examination of the kinetic system (9) originally presented in [9] we get 17160 distinct structures.

$$\begin{aligned} \dot{x}_1 &= -x_1 + 0.05x_2 - 0.2x_1^2 + 0.1x_1^2x_2 \\ \dot{x}_2 &= 1 - 0.05x_2 + 0.01x_1^2 - 0.01x_1^2x_2 \end{aligned} \tag{9}$$

$\mathcal{C} = \{C_1 = 0, C_2 = X_1, C_3 = X_2, C_4 = 2X_1, C_5 = 2X_1 + X_2, C_6 = 3X_1\}$

The algorithm is suitable for parallel implementation, the working of this version has also been examined in the paper.

In order to reduce the number of multiple computation we have developed a second algorithm to return all possible structures, which is also proven to return the correct answer, however it runs in a fraction of time required by the first algorithm, and it is also suitable for parallel implementation. The article for publishing this method in under preparation.

IV. Recent results and future plans

If the parameters determining the model are not precisely known, the non-negative system describing the dynamics can be written by the application of uncertain parameters.

We have examined the models describing uncertain kinetic systems, and have developed some new results considering

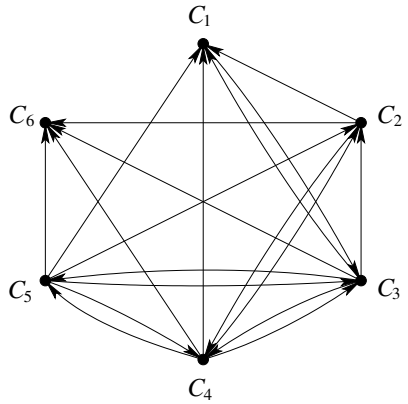

Fig. 5. Dense linearly conjugate realization of the kinetic system (9)

the structural properties of possible realizations. We plan to work more on this topic and publish the achieved results in the future.

ACKNOWLEDGEMENT

This project was developed within the PhD program of the Roska Tamás Doctoral School of Sciences and Technology, Faculty of Information Technology and Bionics, Pázmány Péter Catholic University, Budapest.

I am grateful to my academic advisor, Gábor Szederkényi for the interesting topic and all his help and support.

REFERENCES

[1] P. Érdi, J. Tóth: *Mathematical Models of Chemical Reactions. Theory and Applications of Deterministic and Stochastic Models*, Manchester University Press, Princeton University Press, 1989.

[2] V. Chellaboina, S. P. Bhat, W. M. Haddad, D. S. Bernstein: *Modeling and Analysis of Mass-Action Kinetics – Nonnegativity, Realizability, Reducibility and Semistability*, IEEE Control Systems Magazine, vol. 29, 60–78, 2009.

[3] V. Hárs, J. Tóth: *On the inverse problem of reaction kinetics*, Coll. Math. Soc. J. B. vol. 30, 363–379, 1981.

[4] B. Ács, G. Szederkényi, Z. A. Tuza, Zs. Tuza: *Computing Linearly Conjugate Weakly Reversible Kinetic Structures Using Optimization and Graph Theory*, MATCH Commun. Math. Comput. Chem. vol. 74, 481–504, 2015.

[5] G. Szederkényi, K. M. Hangos, T. Péni: *Maximal and minimal realizations of reaction kinetic systems: computation and properties*, MATCH Commun. Math. Comput. Chem. vol. 65, 309–332, 2011.

[6] G. Szederkényi, K. M. Hangos, Zs. Tuza: *Finding weakly reversible realizations of chemical reaction networks using optimization*, MATCH Commun. Math. Comput. Chem. vol. 67, 193–212, 2012.

[7] M. D. Johnston, D. Siegel, G. Szederkényi: *A linear programming approach to weak reversibility and linear conjugacy of chemical reaction networks*, Journal of Mathematical Chemistry vol. 50, 274–288, 2012.

[8] B. Ács, G. Szederkényi, Zs. Tuza, Z. A. Tuza: *Computing all possible graph structures describing linearly conjugate realizations of kinetic systems*, Comput. Phys. Comm. vol. 204, 11–20, 2016.

[9] A. Császár, L. Jicsinszky, T. Turányi: *Generation of model reactions leading to limit cycle behaviour*, Reaction Kinetics and Catalysis Letters vol. 18, 65–71, 1981.

Application areas of continuous non-invasive blood pressure measurements

Sándor FÖLDI
(Supervisors: Dr. György CSEREY, Dr. Péter SÓTONYI)
Pázmány Péter Catholic University, Faculty of Information Technology and Bionics
50/a Práter street, 1083 Budapest, Hungary
foldi.sandor@itk.ppke.hu

***Abstract*—This paper presents the importance of non-invasive blood pressure measuring and its possible application areas. It is a wide area, with different requirements. Our non-invasive solution can satisfy most of these requirements. Its accuracy, in the sense of blood pressure waveform, is over 90 %. In several test results it can be clearly seen, that different statuses produce different type of blood pressure waveforms, which also indicates our system's usability in diagnostic areas.**

***Keywords*-arterial blood pressure, non-invasive method, pulse diagnosis, arterial pulse waveform**

I. Introduction

Blood pressure was first described by Reverend Stephen Hales in the 18th century by cannulating the femoral artery of a horse [1]. The next breakthrough was made by Scipione Riva-Rocci in 1895. He created a blood pressure measuring method based on inflatable cuff armband. This method was further developed by Korotkoff in 1905, which is used until today. This is called the auscultatory method and it requires a stethoscope in addition to the blood pressure cuff. Current automated technologies use the oscillometric principle.

Oscillometric blood pressure monitors are very popular nowadays. They are based on oscillations in the pressure sensor caused by pulse wave. The cuff of the device is inflated to a point above systolic blood pressure. At this point there are no oscillations. Then, the cuff is slowly deflated. After the systolic pressure reached, oscillations appear in the pressure sensor's signal. These oscillations occure until the cuff reaches the diastolic pressure, then they disappear. The cuff size is an important factor, as using the wrong size cuff can differ the occurrence of oscillations leading to inaccurate measurements [2]. The big advantages of these oscillometric devices are the following, they are cheap, very easy to use, and they have no risks to the patients. But these devices are not very accurate, usually their precision is between 5-10 mmHg [1]. Another issue is the length of the measurement with an automated oscillometric device, which takes at least around 30 seconds.

For continuous blood pressure monitoring the arterial line is the gold standard device. There are several non-invasive solutions too. They based on different measuring methods, like applanation tonometry, Peñáz principle or pulse transit time.

Arterial line is one of the most accurate continuous blood pressure measuring method, only measuring the central aortic pressure can be even more accurate [3]. Arterial line is an invasive method, so it can measure directly the blood pressure by "direct arterial catheterization connected through a fluid column to a pressure transducer" [1]. Although this method is accurate, it has risks to the patient. These risks are the following: injury of the artery, bleeding, haematoma formation, infection at the cannula site and embolism. Embolism can lead to heart attack or stroke. The inserted catheter is very uncomfortable for patients. It requires a trained person to be applied appropriately. Also there must be appropriate hygienic conditions during the catheterization.

One non-invasive continuous blood pressure technique is based on the Peñáz principle. This method could not provide the continuous waveform of arterial blood pressure, but it could give the beat-to-beat systolic and diastolic pressure. This principle applies the volume clamp method that is based on vascular unloading [4]. The device is based on finger cuffs with photoplethysmograph. The signal of the photoplethyshmograph is used in a feedback loop that controls the inflation of the cuff to keep the blood volume constant in the finger arteries. This feedback loop provides the beat-to-beat blood pressure values. To achieve the real blood pressure values a pre-calibration is required with a non-invasive cuff on the upper arm. There are two popular devices based on this method: Nexfin [5]–[7] and CNAP [8], [9]. The Peñáz principle based methods have several limitations mainly due to the plethysmograph. The accuracy of the measurements depends on many factors, like the body and air temperature, skin colour, status of finger arteries, patient sweating, light conditions in the room, etc.

Another non-invasive continuous blood pressure measuring method is the applanation tonometry [10]. It requires a relatively big artery that is close to the skin and could be pressed to a bone. The most commonly chosen artery is the radial artery at the wrist. This method can provide the continuous waveform too. It depends on less factors than the Peñáz based methods, but the measuring itself a bit more complicated. It is very important to place the sensor correctly, which means that the sensor must be exactly over the artery. One solution for this problem is a tonometric array. Another issue is the calibration, which could take several minutes. Patient movement is also a problem, because after a movement the system must be recalibrated. So right now, these devices mostly used on anesthetized patients. The only commercially available applanation tonometry based device is the Tensys T-Line system [11]–[14], which has several good results in the validation trials.

Pulse Transit Time (PTT) is a relatively new method for continuous blood pressure monitoring [1]. It is based on the pulse wave velocity, the speed of the systolic pressure wave propagation. To measure the pulse wave velocity the pulse wave have to be measured at two sites. Another solution includes ECG, in which case the PTT equals the time between the R peak and the arrival of the corresponding systolic wave at the periferial site. Usually the arrival of the systolic wave is measured by a plethysmograph on the finger. The PTT has an

S. FÖLDI, "Application areas of continuous non-invasive blood pressure measurements" in *PhD Proceedings Annual Issues of the Doctoral School, Faculty of Information Technology and Bionics, Pázmány Péter Catholic University – 2016.* G. Prószéky, P. Szolgay Eds. Budapest: Pázmány University ePress, 2016, pp 119– 122.

inverse relationship with the systolic blood pressure, but the mean arterial pressure and the diastolic pressure is difficult to gain accurately. The advantage of this method that it does not requires any cuffs.

Continuous blood pressure monitoring is important for the practitioners to notice sudden changes and be able to immediately react to that change during surgery or intensive care. But that is not the only advantage of continuous monitoring. Having the continuous blood pressure waveform, diagnostic information can be obtained. Analyzing the continuous blood pressure waveform, also called pulse wave, is the topic of pulse diagnosis.

Pulse diagnosis is a non-invasive diagnostic method that can diagnose cardiovascular and several inner organ diseases by analyzing the pulse waveform [15]. The issues with this method that it is done by palpation at this wrist by a trained personal. Thus, it is a very subjective method. Due to this fact, objective automatized solutions have been developed. These automatized methods are based on the continuous arterial blood pressure waveform. This waveform typically consists of three waves, two forward propagating waves and a backward propagating wave. The forward propagating waves are the percussion and the dicrotic wave. Percussion wave reflects the systole. Dicrotic wave is a small blood pressure increase, which is generated when the heart valves are closing. The backward propagating wave is the tidal wave which is a reflection from the periferial arterial site. The tidal wave is usually between the percussion and the dicrotic wave, but it does not always appear distinguishably. A typical single-period pulse signal showed in Fig. 1. The waveform of this pulse signal has the diagnostic information.

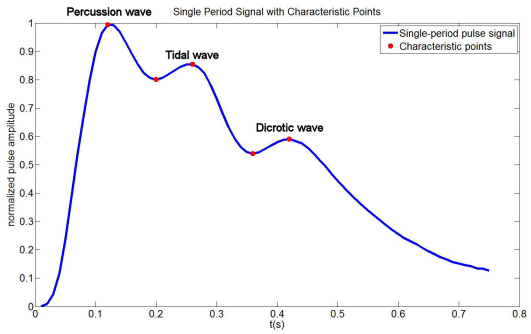

Fig. 1. A healthy single-period pulse signal consisting of three waves: percussion, tidal and dicrotic wave [16].

In the Methods section our solution for the continuous blood pressure monitoring and automatized pulse diagnosis is introduced focusing on the application options. The Results sections shows some primary results achieved by our methods and than a conclusion is made.

II. Methods

Our solution is based on an Optoforce OMD-20-SE-40N force sensor [18]. This sensor can measure the direction of the force that can help in sensor positioning. It is covered by silicone rubber so it is comfortable, easy to clean and disinfect and also durable. It is very sensitive, it can sense 0.01 mm deformation of its dome. The nominal capacity of the sensor is 40 N. The measuring principle is based on light reflection from the deforming dome, so the sensor has no harmful effects on the human body. Fig. 2. shows the measuring environment. The sensor is placed at the wrist. The positioning is crucial for the measurements. The quality of placement could be decided by the 3D vector and a given threshold for signal amplitude. This measuring environment could be used for the continuous blood pressure monitoring and diagnostic purposes too.

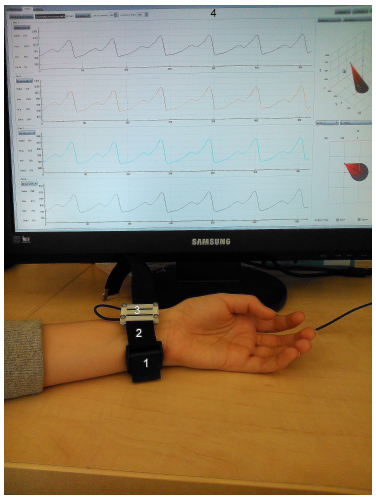

Fig. 2. Continuous non-invasive arterial blood pressure waveform measuring system. 1 - buckle, 2 - band, 3 - sensor holding ”slider” with the Optoforce 3D force sensor, 4 - data visualization and recording software [17].

For continuous blood pressure monitoring, a pre-calibration is required, because the sensor output values depends on several factors, for example: gender, age, weight, placement quality, etc. Another reason for pre-calibration is that the sensor’s output value is a relative value based on the deformation of the silicone dome, so it has to be converted to mmHg units. The pre-calibration could be realized by a cuff based blood pressure measurement, which can provide the baseline blood pressure values. This would not be as accurate as the invasive monitoring, but the sudden changes could be realized immediately and it would also follow the tendencies in the signal, which is important for continuous monitoring.

The calibration method has not yet been fully described it would require more simultaneously recorded measurements with the invasive arterial line. Another issue comes from the sensor itself. In long measurements, a significant amplitude decrease could be seen in the recorded signal. This decrease is continuous, slow, but not linear. The solution for this problem could be a 16th order discrete Meyer wavelet filter. According to my experiences, the 16th order approximation of the recorded signal characterizes this slow decrease noise well, and it does not filter out the diastolic changes.

Validation was made for waveform similarity previously. This validation was made by cross correlation between the simultaneously recorded arterial line and our non-invasive system. Further details could be found in [17].

This non-invasive continuous blood pressure measurement could be used as addition for other hemodynamic experiments. For example it could work well with a CT (Computed Tomography) examination of the vascular system, where hemodynamic parameters that could be calculated from the continuous blood pressure waveform is a great and important additional information for the researchers and practitioners without requirements of invasive arterial line and thus additional permissions.

The diagnostic area requires a bit different signal processing approach. First these signals are much shorter than signals from patient monitoring, typically these are three minutes long. The characteristics of the blood pressure waveform is important in this case. For the noise filtering a cascaded adaptive filter could be applied. The details of this method could be read in [17], [19].

After the filtered signal is acquired, it must be cut into single-period signals according to the onset points. Then comes the feature extraction. Characteristic points of the pulse signal usually can be found as local maximum and minimum points, but there many cases when these points could not be defined as local extremums. This case is frequent for the characteristic points of tidal wave. Moreover there are cases when tidal or dicrotic wave does not appear in the signal. In the feature vector these cases appears as 0 values that equals to '*missing data*'. Our database consists only of our own measurements. Until now, we have made 350 annotated measurements, on 175 people (measuring on each hand). To create a good classificator algorithm a bigger database is required.

The classification of the pulse signals could have another approach. This would based on the wavelet spectrum. By continuous wavelet transformation we could get the time-frequency spectrum of a time series. This time frequency spectrum could be represented as a intensity distribution figure (an example could be seen in Fig. 3.). This figure could be used as an image, and this image can be processed by a regression neural network (deep learning approach). This neural network may be able to detect small differences between different type of single-period signals and thus create a more efficient and accurate classification. But this approach requires much more investigation.

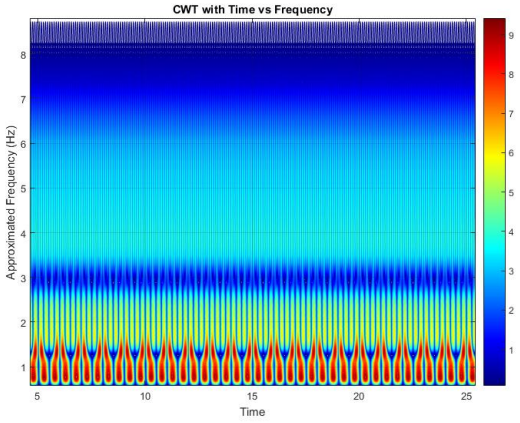

Fig. 3. Continuous wavelet spectrum of a pulse signal segment.

Another application can be the blood pressure measuring itself. One approach is based on cuff, but in stead of oscillometric method the continuous waveform change would detect the systolic and diastolic pressure value. So the measuring environment consists of a cuff at the upper arm and the force sensor at the wrist. The other method could be the pulse transit time. It could be done with two force sensors; one near the elbow the other at the wrist or by one force sensor at the wrist and an ECG. As mentioned above, it is difficult to accurately calculate the diastolic and mean blood pressure value with the current systems which are based on photoplethysmography, because of the limited information. Using our system can deal with this problem due to the continuous waveform, that could make it easier to calculate the diastolic and mean blood pressure values. One of these blood pressure measuring technique would also be advantageous combining with the continuous blood pressure monitoring, because that way our system could calibrate itself without other devices.

Fig. 4. shows a summary of our system's application areas.

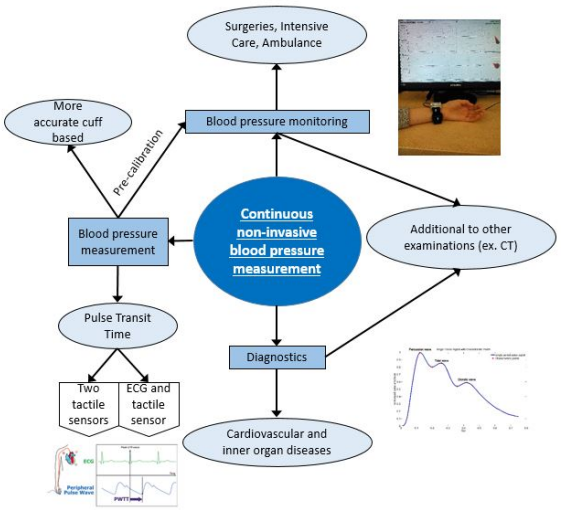

Fig. 4. Summary of the application areas of non-invasive continuous arterial blood pressure measuring system.

III. Results

For the waveform correlation based on 9 measurements the mean correlation value was 0.9527 ± 0.0918.

Fig. 5. shows the comparison of an invasive and a non-invasive simultaneously recorded signal after the noise removal and manual scaling.

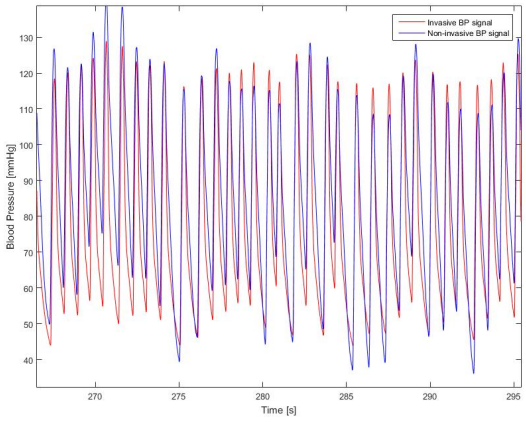

Fig. 5. A noise filtered and manually scaled simultaneously recorded continuous arterial blood pressure segment.

Fig. 6. shows how the single-period signal changes in healthy women due to ageing. Fig. 7. show examples of healthy, hypertension and arteriosclerosis single-period signals recorded by our system.

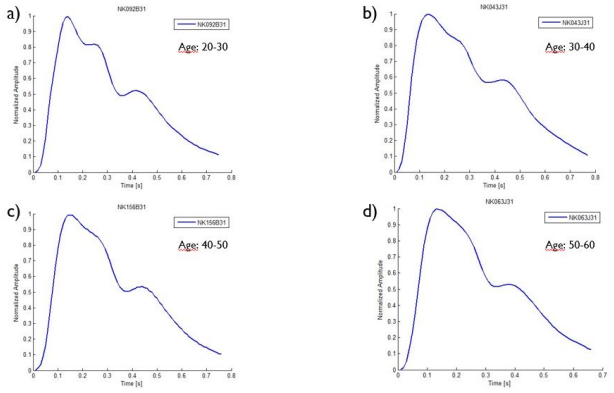

Fig. 6. Changes in pulse signal of healthy women due to ageing measured on healthy women in different age groups: a) 20-30, b) 30-40, c) 40-50, d) 50-60. For older people the arteries become stiffer which leads to faster signal propagation and causes the merge between the tidal and the percussion wave.

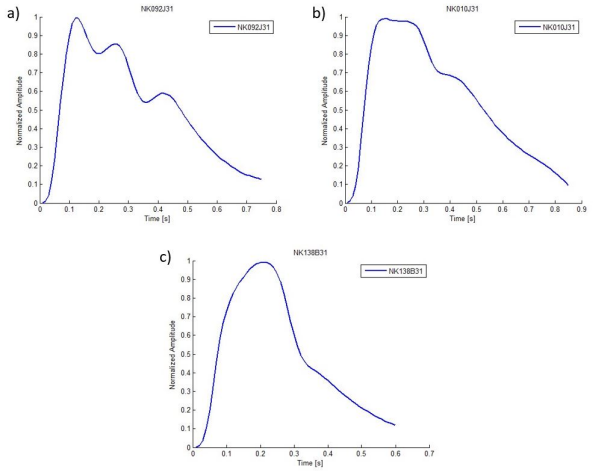

Fig. 7. Different type of pulse signals: a) healthy, b) hypertension and c) arteriosclerosis.

IV. Conclusions

The high correlation value in waveform similarity compared to the invasive continuous blood pressure value, and the good fit between the two blood pressure waveforms after the manual calibration suggest that our system can be a great tool in patient monitoring. The different waveforms for different age groups and diseases proves its usability in diagnostic area. The other described application areas has also great potential based on the advantages of the accurate continuous waveform, and requires further research.

Acknowledgements

The author would like to thank Dr. György Cserey and Dr. Péter Sótonyi for their help and guidance. The support of the Multidisciplinary Doctoral School at the Faculty of Information Technology and Bionics (ITK - Research Faculty) at the Pázmány Péter Catholic University (PPCU - University of National Excellence) and the Semmelweis University Department of Vascular Surgery is also gratefully acknowledged. The author would also like to thank Dr. László Entz, Dr. Dorottya Kiss and Anita Bogdán for their help in the measurements. The technical background is acknowledged to Optoforce Ltd. The author would like to thank Flóra Zieger for the support and help in the project.

References

[1] Chung, Elena and Chen, Guo and Alexander, Brenton and Cannesson, Maxime, *Non-invasive continuous blood pressure monitoring: a review of current applications.* Frontiers of medicine 7.1 (2013): 91-101.

[2] Bur A, Herkner H, Vlcek M, Woisetschläger C, Derhaschnig U, Delle Karth G, Laggner AN, Hirschl MM. *Factors influencing the accuracy of oscillometric blood pressure measurement in critically ill patients.*, Crit Care Med 2003; 31(3): 793–799.

[3] Kroeker EJ, Wood EH. *Comparison of simultaneously recorded central and peripheral arterial pressure pulses during rest, exercise and tilted position in man.*. Circ Res 1955; 3(6): 623–632

[4] Fortin, J., et al. *Continuous non-invasive blood pressure monitoring using concentrically interlocking control loops.* Computers in biology and medicine 36.9 (2006): 941-957.

[5] Martina, Jerson R., et al. *Noninvasive continuous arterial blood pressure monitoring with Nexfin.* Anesthesiology 116.5 (2012): 1092-1103.

[6] Schattenkerk, Daan W. Eeftinck, et al. *Nexfin noninvasive continuous blood pressure validated against Riva-Rocci/Korotkoff.* American journal of hypertension 22.4 (2009): 378-383.

[7] Fischer, M. O., et al. *Non-invasive continuous arterial pressure and cardiac index monitoring with Nexfin after cardiac surgery.* British journal of anaesthesia 109.4 (2012): 514-521.

[8] Hahn, R., et al. *Clinical validation of a continuous non-invasive haemodynamic monitor (CNAP^{TM} 500) during general anaesthesia.* British journal of anaesthesia (2012): aer499.

[9] Ilies, C and Bauer, M and Berg, P and Rosenberg, J and Hedderich, J and Bein, B and Hinz, J and Hanss, R. *Investigation of the agreement of a continuous non-invasive arterial pressure device in comparison with invasive radial artery measurement.* British journal of anaesthesia 108.2 (2012): 202-210.

[10] da Fonseca, Lucas José Sá, Marco Antônio Mota-Gomes, and Luíza A. Rabelo. *Radial Applanation Tonometry as an Adjuvant Tool in the Noninvasive Arterial Stiffness and Blood Pressure Assessment.* World Journal of Cardiovascular Diseases 2014 (2014).

[11] Janelle, Gregory M., and Nikolaus Gravenstein. *An accuracy evaluation of the T-Line Tensymeter (continuous noninvasive blood pressure management device) versus conventional invasive radial artery monitoring in surgical patients.* Anesthesia & Analgesia 102.2 (2006): 484-490.

[12] Meidert, Agnes S and Huber, Wolfgang and Hapfelmeier, Alexander and Schöfthaler, Miriam and Müller, Johannes N and Langwieser, Nicolas and Wagner, Julia Y and Schmid, Roland M and Saugel, Bernd. *Evaluation of the radial artery applanation tonometry technology for continuous noninvasive blood pressure monitoring compared with central aortic blood pressure measurements in patients with multiple organ dysfunction syndrome.* Journal of critical care 28.6 (2013): 908-912.

[13] Saugel, B and Meidert, AS and Hapfelmeier, A and Eyer, F and Schmid, RM and Huber, W. *Non-invasive continuous arterial pressure measurement based on radial artery tonometry in the intensive care unit: a method comparison study using the T-Line TL-200pro device.* British journal of anaesthesia (2013): aet025.

[14] Dueck, Ron, Oliver Goedje, and Paul Clopton. *Noninvasive continuous beat-to-beat radial artery pressure via TL-200 applanation tonometry.* Journal of clinical monitoring and computing 26.2 (2012): 75-83.

[15] Velik, Rosemarie. *An objective review of the technological developments for radial pulse diagnosis in Traditional Chinese Medicine.* European Journal of Integrative Medicine 7.4 (2015): 321-331.

[16] Sándor Földi. *Framework for examination the changes of arterial pulse signal waveform in time and space.* PhD Proceedings Annual Issues of the Doctoral School Faculty of Information Technology and Bionics 2014: (-)

[17] Sándor Földi. *Validation of a non-invasive arterial pressure waveform measuring system.* PhD Proceedings Annual Issues of the Doctoral School Faculty of Information Technology and Bionics 2015: (-)

[18] Optoforce Ltd. *Optoforce web page.* [Online]. Available: http://optoforce.com/index.php, 2016.

[19] Xu, Lisheng, *Baseline wander correction in pulse waveforms using wavelet-based cascaded adaptive filter*, Computers in Biology and Medicine 37.5 (2007): 716-731.

Determination of fetal breathing movement by phonocardiography

Márton Áron GODA
(Supervisor: Ferenc KOVÁCS)
Pázmány Péter Catholic University, Faculty of Information Technology and Bionics
50/a Práter street, 1083 Budapest, Hungary
godamartonaron@itk.ppke.hu

***Abstract*—The principal objective of this study is to determine the fetal breathing movement by phonocardiography. Nowadays, the Doppler-based ultrasonic monitoring is a routine medical examination. While this technique is capable of determining several fetal degenerations, it can offer only a clinical investigation and requires special expertise.**

The assessment of fetal breathing movement can describe fetal well-being. From the third trimester, the fetal breathing movement is well detectable, and it is related to the functionality of autonomic nervous system of the fetus. Phonocardiogram is a commercially available, cheap device, It offers a harmless, easy-to-use, replicable method for 24 hour tele-monitoring fetal breathing. The assessment of breathing motion is based on time-frequency domain analysis. Our findings suggest, that it can offer a reliable real-time data processing, and easy assessment not only for doctors, but also pregnant mothers.

In sum, the fetal phonocardiography is able to determine fetal well-being with the breathing movement detection in tele-monitoring system. Nevertheless, the tool accomplishes real-time data processing. Limitations of the study include its validation on a bigger population. This study contributes to a modern clinical system, which provides further applications to fetal monitoring during the pregnancy.

***Keywords*-keyword; fetal breathing movement, phonocardiography; time-frequency domain analysis**

Statement of originality: This report describes the work of the doctoral student during the academic year 2015/2016. Parts of this work might be under submission to scientific conferences and journals.

I. Introduction

The fetal movement observation has been a popular research topic for more than 30 years. Nevertheless, in 1888 Ahlfred Weber was the first to write about fetal breathing movement (FBM), which he detected using a glass funnel connected to a kymograph [2]. The phonocardiogram can offer a non-invasive, long-term monitoring, which does not have any energy transmission to the fetus [16].

Unfortunately, there could be several complications during the gestational age. For instance it is not evident to define fetal distress [11] and hypoxia [20]. However, the incidence of fetal distress is just 0.2 %, although it is essential to detect because of the fetal health condition. These and other similar cases can help not only for the doctors, but also for the baby's chances of survival.

There are several biological parameters, which help the doctors. For instance, the iron deficiency cause damages of placental insufficiency and hippocampal and striatal abnormalities [4]. Namely, the Fe molecules take big role of hemoglobin synthesis of the red blood cells.

In this study we highlight the importance of fetal breathing movement, introduce the relevant literature and methodology connected to the topic . Finally this study gives some recommendation to the fetal breathing epochs detection of phonocardiography.

II. Fetal Heart Rate Physiology and its control

The human heart and breathing regulation is very complex. But every complex system can be described by a simplified model, which helps us to show the main component of the whole system. In the case of human body, the main elements of the system are the heart and vascular conditions, pulmonary regulation and metabolic processes. These three components working together like interlocking gears. In simple terms, it could be said that the blood is the transport medium, which transmits the fresh oxygen to the cell metabolic processes [1].

The heart is innervated by the vegetative nervous system (ANS) at different points, which is responsible to the sympathetic and parasympathetic regulation. During the fetal development the effect of autonomic nervous system is more and more examinable. The breathing movement is also controlled by the vegetative nervous system, and there is very strong relationship between the fetal sinus arrhythmia and the fetal hart rate [10]. Although the FBM appear already between the 12th and 13th weeks of gestation, it is well detectable from the third trimester. The correlation between fetal body movement and fetal heart rate (FHR) increases with gestation age [6] and is also associated to respiration sinus arrhythmia (RSA) [11]

The fetal heart sound describes the mechanical behavior of heart mitral and tricuspid valves, and also characterizes the physical statement of aorta. The first heart sound depicts the beginning of systolic period, which is followed by second heart sound with the beginning of diastolic period.

There are several cardiorespiratory diseases. As mentioned in the introduction, hypoxia is a serious issue during gestation. Therefore, it is of great interest to be able to detect it. There are three major reasons. The first one is the placental abruption [8]. The second one is abnormal heart rate which can be measured easily by fetal ECG, cardiotocogram or phonocardiography. The third typical reason of hypoxia is smoking.

Maternal health condition has a big effect on fetal development. Therefore the mother has to pay special attention to her health. Research has proved that exercise has many positive maternal effects related to pregnancy [13]. It is also interesting that maternal plasma glucose concentration increases gross fetal body movement [18].

III. Methods

There are several ways to monitor fetal heart. The three mayor approaches for this examination: the fetal ECG, the ultrasonic methods, and the phonocardiography. There are some other methods to data acquisition such as diaphragmatic

M. GODA, "Determination of fetal breathing movement by phonocardiography" in *PhD Proceedings Annual Issues of the Doctoral School, Faculty of Information Technology and Bionics, Pázmány Péter Catholic University – 2016.* G. Prószéky, P. Szolgay Eds. Budapest: Pázmány University ePress, 2016, pp 123– 126.

magnetomyogram (dMMG) [13], or fetal MRI, but they are less popular.

A. Fetal ECG

In the last two decades this method is becoming more popular. Fetal examination has to distinguish the physiological heart operation from the pathological dysfunctionality. The physiological statement of fetal heart can be examined by fetal ECG [6]. It can easily determine the fetal heart rate and its variability (fHRV) with the well-known peak detection algorithms [25].

There are several types of subdivision of frequency regions, but the results are mostly consistent. In one of these studies it was found that the average value of both the VLF/LF and LF/HF [1] ratio decreased significantly with gestation age [6]

B. Ultrasonic methods

Although fetal ECG is very useful, it is not able to characterize pathological cases and other functional heart statements. The ultrasound methods offer two different approaches used in clinics. The first one is cardiotocografia (CTG), which measures only fetal heart rate.

The echocardiogram offers a 2D visualization of the fetus. This way the morphology of the fetal heart can also be observed. The ultrasound imagine is a routine examination, but it requires expertise. The possible risks of this technique are still unknown, and it is not suited for long-term monitoring. Nevertheless, in the end of the 1980s was made several studies with long-term ultrasonic scanner [18].

Thanks to these results [18] we know much more about fetal breathing activity. Research has shown that during the apnea and between each two fetal breaths the chest walls were at rest. The second main thing is venus plasma concentration, which is increased significantly after each meal.

The frequency domain analysis of fetal ECG records and ultrasonic monitoring are consequent. That means, the frequency component of fetal breathing rate is about 0.5-1.5 Hz, but the average value is around 50 breath per minutes [10][12][15][18][23].

C. Phonocardiography

The phonocardiogram (PCG) is a very simple method to examine fetal heart sound. It measures the acoustic propagation on the mother's abdominal wall. The PCG it is totally harmless to the fetus that is why it is appropriate even for 24 hour monitoring. In our research we are using a Fetafon tool, which is provided by the PentaVox Ltd.

There are different types of acoustic sensors e.g.: cantilever type accelerometer [26], piezoelectric elements [27], and inductive-type sensors [5]. Goovaerst was made the fist reliable acoustic sensor in 1989, which was able to record long-term fetal breathing movements on the maternal abdominal wall.

IV. Data acquisition and data processing

In our research there were more than 2500 recorded subjects. Fetafon tool offers a telemonitoring service by the mobile network, but we had to do some hardware modification because of the easier data acquisition. Thus the tool is able to directly record the data on the computer.

[1] 1VLF - very low frequency: 0.01-0.08 Hz; LF - low frequency: 0.08-0.2 Hz; HF - high frequency: 0.4-1.5 Hz. Where HF depicts the breathing rate.

The data processing is separated into three different parts. The first one is time-frequency domain analysis, which helps us in further assessment. That is followed by a fetal breathing segmentation, which is based on fuzzy logic. And finally if various fetal breathing parts are well-defined, it is possible to train a bigger dataset. For this training, one of the best algorithms is deep learning, which is based on the multiple convolution in the time-frequency domain.

Firstly, the input signal must be filtered in the adequate frequency domain. To well define the low–high frequency component, different techniques are to be used. However, at the high frequency (over 20 Hz) component it is enough to calculate the Fourier or Wavelet transform of the signal. Nevertheless, at the low frequency range (under 3 Hz) the Hilbert transform (1) must be used, which is known as the envelope of the signal. The Hilbert transform is a commonly used technique in signal processing; that is why it is also used in adult phonocardiograms [9].

$$H(y(t)) = \frac{1}{\pi} \int_{-\infty}^{\infty} \frac{x(\tau)}{t-\tau} d\tau \tag{1}$$

Fast Fourier Transform (FFT) can represent the dominant frequency component of the input signal. The frequency component of S1 and S2 is from 40-60 Hz, which depicts a crescendo and decrescendo wave form. The fetal low frequency region can be separated into three further frequency components. The beat-to-beat time (T_{bb}) [22] gives the heart rate, with frequencies about 1.5-2.5 Hz. The fetal breathing rate is 0.5-1.5 Hz and the vegetative tone is 0.04-0.4 Hz.

According to the literature, the frequency component of breathing rate is well detectable by ultrasound [10] and fetal ECG [15]. The aim was to determine the fetal breathing movement by phonocardiogram, too. For this purpose firstly the signal was filtered with 2^{nd} order bandpass Butterworth filter between 0.04-3 Hz. After that the Hilbert transform (1) was used. In the frequency domain the Hilbert transformed signal was plotted, which gives the dominant breathing rate. Further visualization was used a time-frequency map, too.

Fuzzy logic is a probabilistic method, which helps to handle the different cases. A typical example is the determination of temperature ranges. Nevertheless, it was already used to separate heart sound signal from Noise [24]. In this study it was discovered that main atoms of heart sound signal congregate in the joint domains. At the fetal breathing movement similar specific atoms were found, which describe a parabolic form in the signal, but it is not yet proved.

V. Results

The dataset was processed in Matlab and a custom program was also created. Matlab helped our work to plot the time-frequency map of the spectrogram and calculate the Wavelet transformation. Matlab was not fast enough to evaluate the more than 2500 subjects, therefore the used time-frequency analysis also had to be implemented in C# program.

At frequency domain analysis a very strong correlation between of the breathing movement (0.5-1 Hz) and the very high frequency (120-130 Hz) was found. The reason for this phenomenon is still not clear, but to clarify that further examinations are needed accompanied by echocardiography. spectrogram

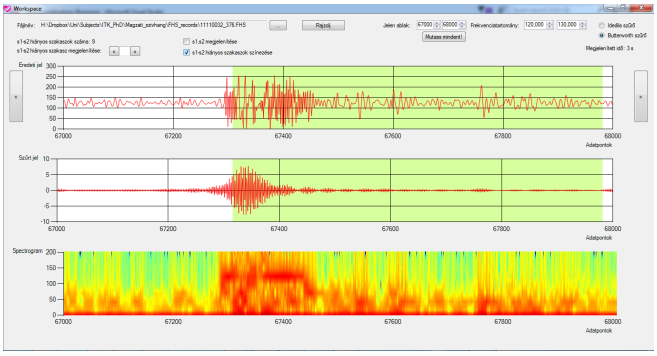

Fig. 1. The first graph depicts the original signal, the second graph is the filtered signal. The green background color marks the supposed fetal breathing regions. The last graph of the signal depicts the spectrogram of the original signal.

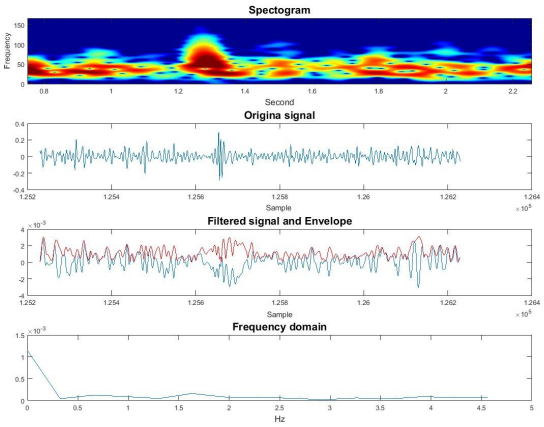

Fig. 2. The spectrogram depicts the time-frequency map of phonocardiogram. The second graph of the figure depicts a breathing region. The third graph depicts the filtered and Hilbert transformed signal. The last graph of the figure depicts spectra of the Hilbert transformed signal. Here the breathing period is visible, furthermore a high frequency (120-130 Hz) component takes part in the signal (the first graph of the picture).

VI. Conclusions

Long -term fetal breathing monitoring is still not in everyday clinical use. Phonocardiography could offer a reliable and easily accessible method to monitor fetal well-being, eventually to prevent complication during pregnancy.

In our examination we recorded 2500 cases with Fetafon tool. In the time-frequency domain analysis of fetal heart sound on the 2500 cases, a very strong correlation was found between the breathing rate (0.5-1.5 Hz) and very high frequency components (120-130 Hz). In order to clarify the clinical relevance of our finding, it is necessary to carry out further complex examinations accompanied by parallel ultrasound measurements.

Acknowledgements

I would like to offer my sincere thanks to my supervisors to Ferenc KOVÁCS - Lecturer of Pázmány Péter Catholic University Faculty of Information Technology and Bionics - for his valuable information and guidance.

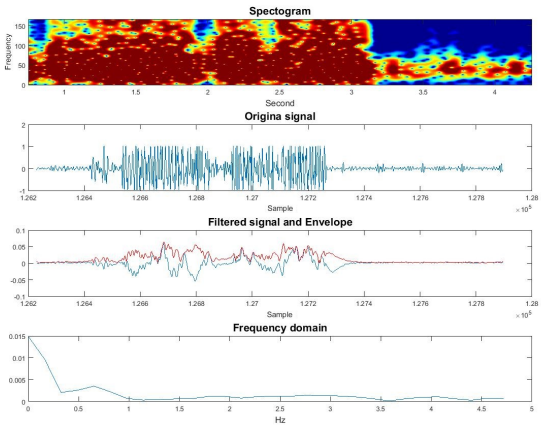

Fig. 3. The spectrogram depicts the time-frequency map of phonocardiogram. The second graph of the figure depicts a breathing region. The third graph depicts the filtered and Hilbert transformed signal. The last graph of the figure depicts spectra of the Hilbert transformed signal. Here the breathing period is visible, furthermore a high frequency (120-130 Hz) component takes part in the signal (the first graph of the picture).

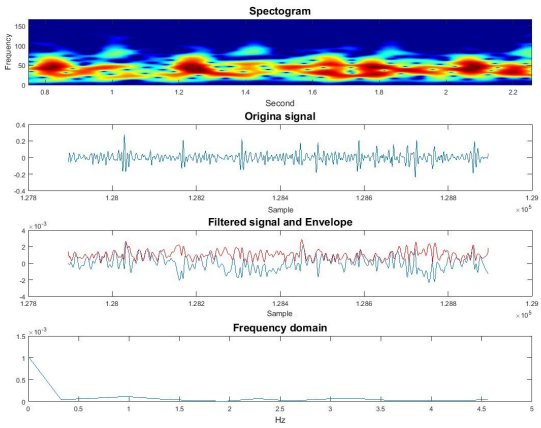

Fig. 4. The spectrogram depicts the time-frequency map of phonocardiogram. The second graph of the figure depicts a breathing absence region after a breathing period. The third graph depicts the filtered and Hilbert transformed signal. The last graph of the figure depicts spectra of the Hilbert transformed signal. The breathing period is not visible.

References

[1] Marton Aron Goda, *Diagnostic tool development on embedded system for heart fitness measurement*, International Conference on Health Informatics and Medical Systems - Las Vegas, 2016.

[2] Ahlfred Weber, *Über bisher noch nicht beschriebene intrauterine Bewegungen des Kindes*, Verhandlungen der Deutschen Gesellschaft für Gynäkologie, pp. 2, 1888.

[3] Michael Y. Divon, *Respiratory sinus arrhythmia in the human fetus*, American Journal of Obstetrics and Gynecology, pp. 425-428, 1985.

[4] Michael K. Georgieff, *The Role of Iron in Neurodevelopment: Fetal Iron Deficiency and the Developing Hippocampus*, Biochem Soc Trans., pp. 1267–1271, 2009.

[5] H. G. Goovaerts, *A transducer for recording fetal movements and sounds based on an inductive principle*, Clinical Physics and Physiological Measurement, pp. 61-65, 1989.

[6] M. David, *Maturation of fetal cardiac autonomic control as expressed by Fetal Heart Rate variability*, Computers in Cardiology, pp. 901-904, 2006.

[7] Michael Y. Divon, *Respiratory sinus arrhythmia in the human fetus*, American Journal of Obstetrics and Gynecology, pp. 425-428, 1985.

[8] Michelle Murray, *Antepartal and Intrapartal Fetal Monitoring: Third Edition*, American Journal of Obstetrics and Gynecology, pp. 1-59, 1993.

[9] Ayush Kumar, *An efficient thresholding technique for segmentation of Phonocardiographic Signals*, IEEE, pp. 154-157, 2013.
[10] Michael Y. Divon, *Respiratory sinus arrhythmia in the human fetus*, IEEE, pp. 425-428, 1985.
[11] M.R. Ortiz, *Analysis of high frequency fetal heart rate variability using empirical mode decomposition*, IEEE Computers in Cardiology, pp. 675-678, 2005.
[12] J. Andrews, *The variability of fetal breathing movements in normal human fetuses at term*, American Journal of Obstetrics and Gynecology, pp. 280-282, 1985.
[13] Kathleen M. Gustafson, *Fetal cardiac autonomic control during breathing and non-breathing epochs: the effect of maternal exercise*, IEEE Early Human Development, pp. 539-546, 2012.
[14] Y. Noguchi, *Breathing modulates fetal heart rate*, IEEE Fifteenth Annual Northeast Bioengineering Conference - Boston, pp. 233-234, 1989.
[15] Foulquiere K., *Using Modified Fetal Monitor and Signal Processing to Detect Fetal Breathing Movement*, IEEE 2000 IEEE Ultrasonics Symposium, pp. 1391-1394, 2000.
[16] Ferenc Kovacs, *A rule-based phonocardiographic method for long-term fetal heart rate monitoring*, IEEE Transactions on Biomedical Engineering, pp. 124-130, 2000.
[17] Kai Yang, *An adaptive real time method for fetal heart rate extraction based on phonocardiography*, IEEE Biomedical Circuits and Systems Conference, pp. 356-359, 2012.
[18] J Patrick, *Patterns of human fetal breathing activity at 34 to 35 weeks' gestational age*, Am J Obstet Gynecol., pp. 507-513, 1978.
[19] M.N. Ansourian, *Autoregressive spectral estimation of fetal breathing movement*, IEEE Transactions on Biomedical Engineering, pp. 1076-1084, 1989.
[20] Patrick Zemb, *Prenatal observation of heart rate sequences presenting entropic analogies with Sudden Infant Death Syndrome: preliminary report*, IEEE 26th International Symposium on Computer-Based Medical Systems, pp. 421-424, 2013.
[21] Maryam Samieinasab, *Fetal phonocardiogram extraction using single channel blind source separation*, IEEE 2015 23rd Iranian Conference on Electrical Engineering, pp. 78-83, 2015.
[22] F. Kovacs, *Fetal breathing transmission in phonocardiographic monitoring telemedicine systems*, Conference of the IEEE Engineering in Medicine and Biology Society, pp. 5226-5229, 2006.
[23] Motokazu Higuchi, *Relationship between the Duration of Fetal Breathing Movements and Gestational Age and the Development ofthe Central Nervous System at 25–32 Weeks of Gestation in Normal Pregnancys*, Gynecologic and Obstetric Investigation, pp. 136-140, 1991.
[24] Hong Tang, *Separation of Heart Sound Signal from Noise in Joint Cycle Frequency–Time–Frequency Domains Based on Fuzzy Detection*, IEEE Transactions on Biomedical Engineering, pp. 2438-2447, 2010.
[25] R. M. Rangayyan, *Biomedical Signal Analysis: A Case Study Approach*, Univeristy of Calgary, Alberta, Canada, pp. 187-190, 2002.
[26] DG Talbert, *Wide bandwidth fetal phonography using a sensor matched to the compliance of the mother's abdominal wall*, IEEE Trans Biomed Eng., pp. 175-181, 1986.
[27] A.J. Zuckerwar, *Development of a piezopolymer pressure sensor for a portable fetal heart rate monitor*, IEEE Trans Biomed Eng., pp. 175-181, 1986.

Sensory Robotics Assisted Dental Applications

Balázs JÁKLI
(Supervisor: György CSEREY)
Pázmány Péter Catholic University, Faculty of Information Technology and Bionics
50/a Práter street, 1083 Budapest, Hungary
jakli.balazs@itk.ppke.hu

***Abstract*—Dental implant installation in the patient's jaw is one of the most challenging procedures in dental medicine. This operation puts high stress on the patient with multiple stages of surgical intervention. On the patient's side, due to the complexity of the surgery the price of medical implant embedding is high, and results a long healing time. On the doctor's side, the process requires high routine and concentration. With the support of modern medical imaging techniques and special instruments, the implant drilling procedure might be refined to 0.01 millimeter positional accuracy and 1° angular accuracy. If so, then the implants can be manufactured before the invasive surgery, and can be installed right after the abutment placement. With this improved process the three-step process could be executed in one surgery, reducing stress, healing time and price of the procedure. the critical step in this proposed method is the automated or semi-automated drilling of the implant's bore in the patient's jaw. This paper introduces the method and the instrument model of this automated drilling process.**

***Keywords*-dental implant, automation, medical imaging, robotics, sensors, sensory robotics, medical robots**

I. Introduction

The most widely practiced method of placing dental implants is a "staged surgery" procedure. The first stage consists of surgically burying the implant (which replaces the tooth root) flush with the bone but underneath the gum. This protects the implant from force while it is healing. At the end of this healing period, the implant needs to be surgically exposed by removing some of the overlying gum.

At this second stage, the surgeon checks the implant his for its successful integration and connects some form of post which penetrates through the gum into the mouth. This post is called the abutment. Abutments come in many forms and can be stock-manufactured or custom-molded by your dentist and a laboratory. The gum is allowed to heal around the abutment and form a cuff or collar through which the dentist has access to the implant when preparing the final restorative stage of placing the prosthetic tooth or teeth.

Research has shown that it is often possible to place a suitable abutment at the same time as the implant. This has certain limitations but can eliminate the need for a second surgery to expose the implant. However, the implant still requires adequate healing time for the bone to osseointegrate.

The abutments must also be protected from chewing forces during this period to assure effective bony integration and successful healing. Once the implants have had a chance to heal and have been tested for successful integration, the final restorative step takes place. This stage consists of fabricating and connecting the prosthetic teeth to the successfully osseointegrated implants.[1]

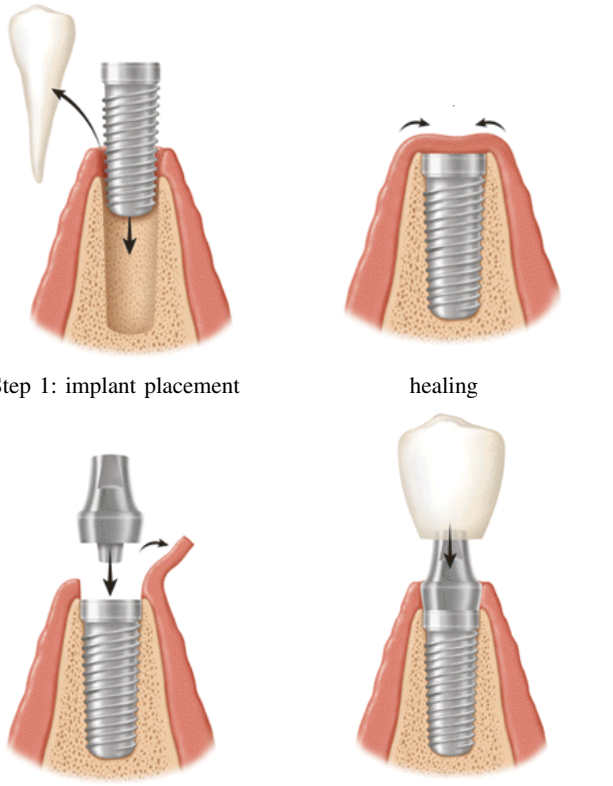

Step 1: implant placement | healing

Step 2: abutment placement | Step 3: prosthetic teeth installation

http://www.osseo.org

During the regular process, The first step is the CT scanning of the patient. On this image the doctor inspects the proposed implant's location in the bone. This is followed by the drilling if the implant's bore with a pneumatic drill guided by hand. This drilling has the accuracy of $<$1mm. After the implant placement, another CT scan is performed to inspect the final location of the implant screw. The prosthetic tooth manufacturing starts based in this data. Mihály Vaszilkó MD DMD Phd., assistant professor of the Department of Oro-Maxillofacial Surgery and Stomatology of the Semmelweis University presented to our workgroup his theory of a new method of a more precise implant placement technique. According to his method, if the proposed and the final locations of the implant screw would be the practically the same, the manufacturing of the abutment and the tooth can be done after the first CT scan, before the drilling. This would give us the opportunity to finish the three-steps procedure in one operation. Reducing the number of surgeries will reduce the chance of infection, shorten healing time and provide the patient an increased comfort.

B. JÁKLI, "Sensory Robotics Assisted Dental Applications" in *PhD Proceedings Annual Issues of the Doctoral School, Faculty of Information Technology and Bionics, Pázmány Péter Catholic University – 2016.* G. Prószéky, P. Szolgay Eds. Budapest: Pázmány University ePress, 2016, pp 127– 130.

Performing this modified operation model on humans is not currently in scope. Doing so would require heavy medical ethical surveys and trials. The requirements of these test are not met yet. Medical approval of robotic systems working alongside humans has a long lead time. The scope of this work is to create a test bed to inspect the possibilities of such an automated method. Further possibilities will be discussed based on the results.

II. Related work

One of the founding articles of automated implant placement systems was *Precision of transfer of preoperative planning for oral implants based on cone-beam CT-scan images through a robotic drilling machine* by Thomas Fortin et. al.[2]. In that study, an image-guided system for oral implant placement was assessed. A specially designed mechanical tool has been elaborated to transfer the preoperative implant axis planned on 3-dimensional imagery into a surgical template by a numerically controlled drilling machine. The main drawback of image-guiding systems is the use of preoperative computed tomography, which is expensive and delivers high radiation doses. Therefore, in that study the image-guiding system was coupled with a cone-beam tomograph that significantly decreased both cost and radiation doses. Three edentulous models were used. To determine the accuracy of the system, the ability of a 1.8-mm diameter drill to enter a 2.0-mm diameter, 10-mm-long titanium tube inserted on the model with no contact was verified. Because the drill entered the tubes with no contact and went beyond the end of the tube, the transfer error was less than 0.2 mm for translation and less than 1.1° for rotation. The method presented there is low cost and high precision compared to other technological solutions such as tracking. That system's capabilities allowed the doctors to perform precise drilling even in thin bone. But this system is not precise enough to allow the pre-drilling prosthesis manufacturing [2].

Another standard and relatively low price tool to assist the drilling is base in the patent "System for preparing the placing of a dental implant" US 6296483 B1 [3]. This is a system of transfer of a simulated position of a dental implant from an X-ray scanner to a robot for drilling a cradle of reproduction, in complementary shape, of a dental casting. The system includes at least one mechanical support and means adapted to removably connecting in a reproducible position the cradle to the support, the cradle containing at least two rectilinear non-concurrent elements visible by X-rays [3].

Robot-assisted placement of prosthetic implants are also common in other areas, such as ear and face implants. "Robot-Assisted Placement of Craniofacial Implants" by M. Kleit et.al. discusses cranofacial (face) implant positioning [4]. The purpose of that study was to improve and accelerate the rehabilitation process for patients with severe ear microtia with an implant-anchored auricular prosthesis. A medically approved robot system was used to place the craniofacial implants and a new process was developed for preoperative fabrication of the prosthesis using a rapid prototyping technique. Materials and Methods: Preoperatively, after computerized tomography, the implant positions were determined in a planning tool according to bone availability and esthetic considerations. Intraoperatively, the robot showed the surgeon the planned implant positions and guided the placement procedure. Results: The accuracy measurements showed that with this robot system, absolute implant position accuracy of approximately -0.5 ± 0.4 mm, a relative accuracy between the implants of approximately 0.2 ± 0.5 mm, and a deviation from the parallel position of approximately 0.6 ± 0.5 degrees were achieved. Thirty implants were placed in 13 patients with robot assistance with no intraoperative injuries. Discussion: This technique made it possible to apply the preoperatively fabricated auricular prosthesis directly after surgery. Conclusion: From this experience it can be concluded that the robot system and the new manufacturing concept for anaplastology can be applied advantageously in other areas of the head as well [4].

Surgical templates are widely used in dental medicine. They help the precise positioning of drill holes and implants. Creating those templates is not easy and requires high experience. Leaving templates would be beneficial, if robotic systems could replace the positioning template adaptively. "Surgical template assembly and method for drilling and installing dental implants" US 5967777 A defines the creation and useage of standard surgical templates [5]. This is a patent defining a surgical template and method for drilling osteotomies (e.g., holes in a jawbone) and installing one or more dental implants using a surgical template assembly. The surgical template assembly is provided with one or more drill guides and one or more dental implant guides. The guides are positioned in the surgical template assembly by a computer-driven milling machine interfaced with a computer-generated image of a patient's jawbone and a computer-generated simulation of at least one dental implant so that when the surgical template is placed in the patient's mouth a trajectory of the guides in the surgical template into the patient's jawbone corresponds to a trajectory of the computer-generated simulation of the dental implant into the computer-generated image of the patient's jawbone. Preferably, three fiducial markers, provide positional coordination between the CT scan data, the computer-generated simulation of the dental implant, and the computer-driven milling machine [5].

Reliability of surgical planning based on 3D imaging software thechnology was investigated in "Reliability of Preoperative Planning of an Image-Guided System for Oral Implant Placement Based on 3-dimensional Images: An In Vivo Study" by T. Fortin et.al. [6] The purpose of that study was to assess the reliability of the planning software of an image-guided implant placement system based on a mechanical device coupled with a template stabilized on soft tissue during surgery. Materials and Methods: Thirty consecutive partially or completely edentulous patients were treated with the image-guided system. For each patient, a study prosthesis was fabricated and duplicated in acrylic resin and served as a scanning template. Axial images were obtained from a computerized tomographic scan and transferred to planning software that provides real 3-dimensional information to plan implant position. Once the final position of the implant was defined, preoperative data such as the size of implants and anatomic complications were recorded using the planning software. The scanning template was then drilled in that exact position by a drilling machine. During surgery, the drilled template was used as a drill guide. After implant placement, intraoperative data were recorded and statistically compared with the preoperative data using the Kendall correlation coefficient for qualitative data and the Kappa concordance coefficient for quantitative data. Results: Agreement between the preoperative and intraoperative data

was high for both implant size and anatomic complications. The Kendall correlation coefficient was 0.8 for the diameter and 0.82 for the length. The Kappa concordance coefficient was 0.87 for both dehiscence and bone graft, 0.88 for osteotomy, and 1.0 for fenestration. Discussion: In the few instances where planning was not perfect, implant placement was completed in a clinically acceptable manner. Conclusion: The results suggest that the image-guided system presented is reliable for the preoperative assessment of implant size and anatomic complications. It may also be reliable for flapless surgery [6].

III. System model

Autonomic – or semi-automatic – drilling of the jawbone depends on the real-time position and orientation detection of the jaw. The drilling system has to know exactly the relative position and orientation of the specified hole and the drilling bit. Recent research work sampled above used optical-based localisation of the jaw and skull. This enabled quite decent automatic drilling, better than human hand drilling, but not precise enough to use pre-manufactured replacement teeth. Our method of localisation is instead of relying on optic principle is based on magnetic hall encoders. With a series of these encoders, we can detect the relative location and orientation between the jaw and the drill.

Mechanical measurement relies on mechanical interconnection between the jaw and the encoder, and also between the encoder and the drilling robot. The encoder-robot connection can be almost any solution that seems reasonable to the engineer. The jaw-encoder interconnection is not so trivial. This solution can be divided into two groups. If the patient has enogh teeth, we can use a mechanical template mounted on the teeth. This solution has some already use principles in daly practice. This can be 3D printed plates based in CBCT scans if the jaw, or something equivalent. The problem gets harder is the patient has not enough teeth to contact the encoder.

If the patient has no useable ”mecahical mounting points”, than one or two small titanium screws will be inserted into the bone. According to the original method of Mihály Vaszilkó MD DMD Phd., we modified the form of a known fixing screw with the help of Mátyás Takács, Promed 2000 Kft. (H-6800 Hódmezővásárhely,Rigó u. 33.). Mr Takács helped us with the manufacturing too. These will have the diameter of 1-1.5mm, and the length of about 5mm. These screws will have a hexagonal head that has dual purpose. The screw will be driven with a screwdriver at this point, and some optical CBCT marker will be located here temporarily as well. The marker is required for CBCT localisation of the screw, because the titanium has a very low contrast ratio at CBCT scans. The dentist will drill a small (0.8mm) hole in the bone, drive the screw in, and fix the marker on the screw.

The marker is manufactured from a softer material with the density around the density of the human bone. This is required, because the CBCT instrument is calibrated to this density. The current prototypes are from POM (polyoximetilene) and from teflon. The dentist scans the patient with attached markers, then removes the markers, because the encoder chain will occupy the same mounting slot. From the CBCT scan, the drilling parameters will be calculated with a custom software. Then the dentist will power on the drilling robot arm, move the drill near the patient’s jaw and attach the robot’s encoder to the patient.

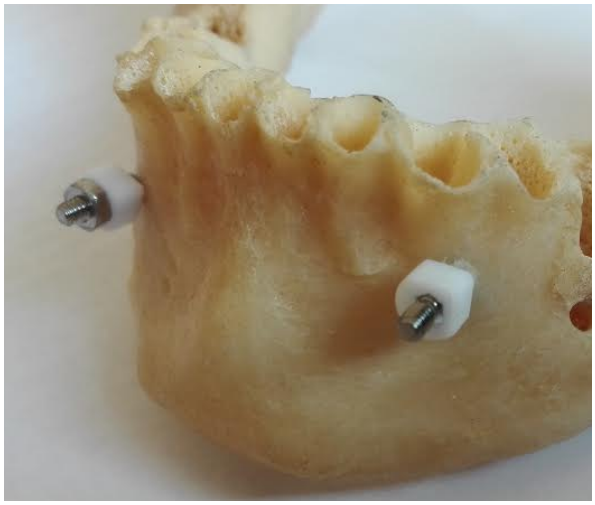

Fig. 1. Markers on the titanium screws in the jaw

From this point, the robot will be attached relatively to the patient. Of the patient will move a bit, the robot will follow. This relative attachment is necessary to safely operate in the mouth. It has to be noted, that the patient’s movement in this state is heavily unrecommended. The patient’s head should be fixed with standard dental equipment to prevent motion of any kind. The relative position following function of the robot still needs to be implemented for safety reasons.

With the robot attached and the drill program prepared, the system could adaptively find the required location to drill and could drill the hole on its own. For safety and comfort reasons the system will be semi-automatic for a while. This means, that the robot will be responsible for the relative placement of the drill to the required position. The dentist will have one degree of freedom to operate the drill in the drilling axis only.

Fig. 2. Double-screw configuration. The screws are interconnected after driven into the bone to prevent rotating motion.

IV. Results

Titanium screws and PFTE markers were designed and manufactured. They were located into a prepared human lower jaw and some CBCT scans were performed on them. The results showed the PFTE marker’s contour with high resolution validating the marker design’s performance. In the current design, the marker is held in place with an aluminum or

Fig. 3. Two-axis rotational encoder based on rotational hall encoders.

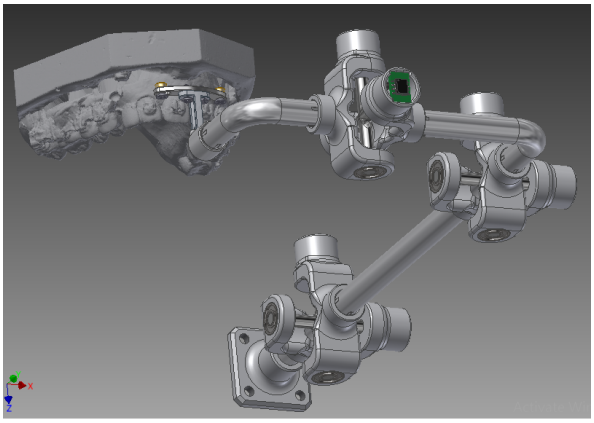

Fig. 4. 6D encoder chain mounted on the jaw.

POM nut, but this had to be removed to achieve the necessary contrast. The marker's inner diameter will have to be modified to fit the screw tightly without further fixtures.

A two-axis rotary encoder was designed and prototyped. Each axis measures the rotation with a TLE5012B 15/16 bit resolution. This gives us 0.01°angular resolution per axis (after calibration). To achieve the maximal positioning accuracy the links between the encoders will need to be shortened.

The current processing software is based on MATLAB. This software reads the CBCT scan data, and visualizes the content. We can manually insert the drilling hole location in the model. The output is the drill hole axis located in the coordinate system of the encoder on the screw.

This data is imported in a ROS (Robot Operating System) application that reads the encoder chain data, localizes the necessary drill hole in the 3D space and controls the UR3/UR5 robot to perform the operation.

V. Conclusions and Future Work

In the following months the drilling test-bed will be completed, and some tests will be performed on 3D printed jaws and probably on some animal heads. The test environment will consist of a UR5 robot, a customized dental chair and dental drill, a custom 7th axis on the UR robot arm and the developed 6-axis encoder chain.

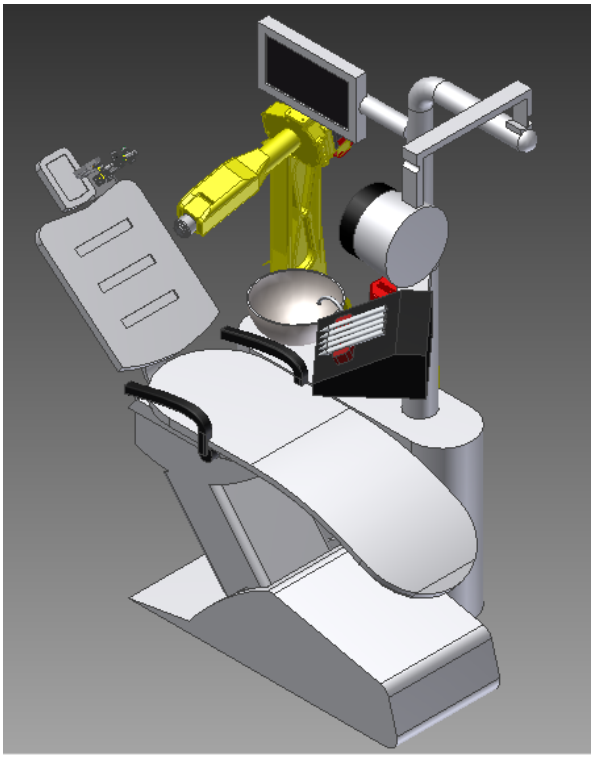

Fig. 5. Proof-of-principle automatic implant drilling system model. Encoder chain is located near the head in the left. The yellow robot beside the patient is responsible for the drilling.

Acknowledgements

The author would like to thank György Cserey PhD for his help and guidance.

This work could not have been possible without the participation and assistance of Mihály Vaszilkó MD DMD Phd., who started this project with his concept ideas.

The support of PROMED 2000 Ltd. is gratefully acknowledged for the manufacturing of the titanium and PTFE marker parts.

The support of the Multidisciplinary Doctoral School of the Faculty of Information Technology and Bionics at the Pázmány Péter Catholic University is also gratefully acknowledged.

References

[1] A. of Osseointegration, "Implant procedure." http://www.osseo.org/NEWhowAreImplantsPlaced.html (Date last accessed May-16-2016).

[2] T. Fortin, G. Champleboux, S. Bianchi, H. Buatois, and J.-L. Coudert, "Precision of transfer of preoperative planning for oral implants based on cone-beam ct-scan images through a robotic drilling machine," *Clinical Oral Implants Research*, vol. 13, no. 6, pp. 651–656, 2002.

[3] G. Champleboux, "System for preparing the placing of a dental implant," Oct. 2 2001. US Patent 6,296,483.

[4] M. Klein, A. Hein, T. Lueth, and J. Bier, "Robot-assisted placement of craniofacial implants.," *International Journal of Oral & Maxillofacial Implants*, vol. 18, no. 5, 2003.

[5] M. Klein, M. Abrams, and R. Manno, "Surgical template assembly and method for drilling and installing dental implants," Oct. 19 1999. US Patent 5,967,777.

[6] T. Fortin, J. L. Bosson, J. L. Coudert, and M. Isidori, "Reliability of preoperative planning of an image-guided system for oral implant placement based on 3-dimensional images: an in vivo study.," *International Journal of Oral & Maxillofacial Implants*, vol. 18, no. 6, 2003.

The open research areas in distributed wireless industrial monitoring and control network

Máté Lőrincz
(Supervisor: András Oláh, Phd)
Pázmány Péter Catholic University, Faculty of Information Technology and Bionics
50/a Práter street, 1083 Budapest, Hungary
lorincz.mate@itk.ppke.hu

***Abstract*—Today, on the threshold of the fourth industrial revolution (or industry 4.0) it became important to rethink the guideline of industrial control systems. Usually, the most widely used control systems contain a centralised CU and some modules controlled by it - like PLC and lots of remote IO modules connected by some sort of wired network. The remote IO modules are responsible for controlling and monitoring the equipments, but they are not capable of making decisions. Their only autonomic error handling capability is to turn on or off an (analog or digital) output in case of network error. In some simple cases this is enough to stop safely a motor or close a valve after a connection loss, but in complicated cases, this behaviour can cause material loss or injuries. To prevent this, the distance between the actuators and the decision-making logic should be minimised. The intelligent remote IO modules could eliminate the risk of network error and reduce the response time, but recently we don't have a good method to ensure the reliable communication between these IO modules neither a good programming method. Our goal is to develop a reliable protocol for these systems which covers the problem of communication and programming. For this, we need an easy-to-use programming toolset, a task distribution method and a communication protocol. Because they are strongly building on each other, we can't separate their designing.**

***Keywords*-industrial; WSAN; Wireless sensor and actuator network; Industry 4.0; parallel programming; heterogeneous network;**

I. Introduction

In the past two centuries there were three industrial revolutions (1. figure). During the first one was the transition from hand production methods to mechanisation[1], during the second one, the emphasis was on the introduction of assembly lines and on mass production and during the third one, the reconfigurable, programmable controllers replaced the hard-wired, relay-based control panels.

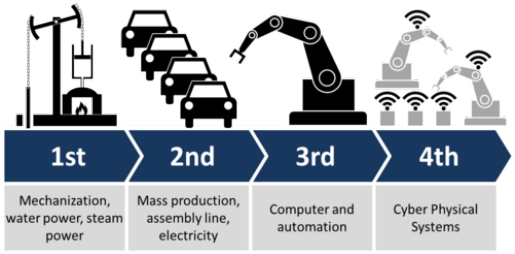

Fig. 1. The four industrial revolutions

Until the first decade of the 21th century, mostly the results of the third industrial revolution gave the guidelines for the industrial controlling. The PLC-s widespread throughout the industry and acquired the 83% of the industrial control market segment[2]. Altough more than 40 years have passed since the first (1968) PLC-s, the basic principles have not changed too much. The early PLC-s had to be[3]:

- flexible and easily reprogrammable, like a PC;
- easily maintainable and programmable in line with the so-called ladder logic;
- resistant to dirt, moisture, vibration, which are common in industrial environment;
- modular and easily expandable.

In the viewpoint of this paper, the next important step was the invention of remote IO-s. The first Remote IO was the production of Allen Bradley in 1976.[4] The remote IO-s simplified the communication networks significantly. In this new hierarchical structure, the PLC controlled the remote IO-s, which were connected to the actuators and the sensors. (There was no longer any need for a PLC to connect the devices to be controlled.) Today, most PLC-based control systems contain a PLC and lots of remote IO-s, but the idea behind the remote IO-s is the same as in 1976: The PLC is the only intelligent device in the network, the remote IO-s just execute the got instructions. Only the communication methods evolved. (The most popular communication methods are Ethernet/IP or Profibus based but in new systems the Ethernet/IP-based ProfiNet is preferred.)

With the use of remote IO-s, the price and complexity of an industrial control network greatly reduced, but there are some drawbacks, too. In the industrial control systems, the main focus is on the failure handling, because a small disruption (some minutes long) in the production can cause huge material loss. (Not to mention the chain reaction of failures: A small disruption of a utility system can cause failures across the whole plant.) The remote IO-s (because of their low price) are not as sophisticated devices as the PLC, in the case of network error they can set their outputs only some predefined default state independently from the inputs. This behaviour is sometimes enough (for example, stopping a motor can be a good choice in the case of network loss), but in some complicated situations, it can damage the equipment (for example, see figure 2).

Today, the industrial productions and needs are more complex to handle them with the original principles of the third revolution. This was recognised by the German Federal Ministry of Education and Research when they published an article about the future of industry and the fourth industrial revolution, the so-called Industry 4.0.

II. The advantages of decentralised control networks according to industry 4.0

Industry 4.0 (or Industrie 4.0 in German-speaking countries) is not an exact concept, more like an umbrella term with

M. LŐRINCZ, "The open research areas in distributed wireless industrial monitoring and control network" in *PhD Proceedings Annual Issues of the Doctoral School, Faculty of Information Technology and Bionics, Pázmány Péter Catholic University – 2016.* G. Prószéky, P. Szolgay Eds. Budapest: Pázmány University ePress, 2016, pp 131– 134.

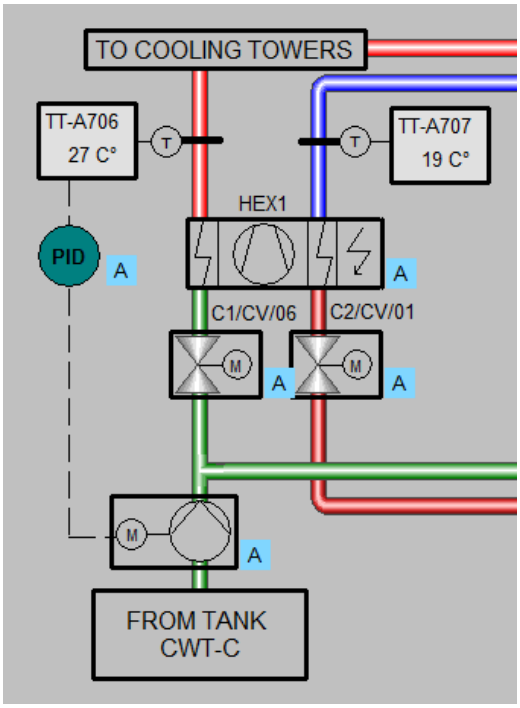

Fig. 2. This is a part of a cooling circuit. In the primer pipeline (with temperature meter TT-A706) the water is circulated from CWT-C tank to cooling towers via two heat exchangers (HEX1 and HEX2, but the last one is not presented on this image trim) by the pump on the bottom. In the seconder pipeline (with temperature meter TT-A707) the water flows between the production equipments and the HEX-s. To prevent the damage of the HEX-s after an emergency stop, the primer water circuit's pump has to continue the circulation until the *TT-A706* temperature sensor's value falls below a critical level. After that, the *C1/CV/06* valve has to close to prevent the reflux. This stopping sequence is too complex for a remote IO.

some design principles. The fallowing definition was given by Herman, Pentek and Otto in their review article[6]:

> Industrie 4.0 is a collective term for technologies and concepts of value chain organization. Within the modular structured Smart Factories of Industrie 4.0, CPS [Cyber Physical Systems] monitor physical processes, create a virtual copy of the physical world and make decentralized decisions. Over the IoT [Internet of Things], CPS communicate and cooperate with each other and humans in real time. Via the IoS [Internet of Services], both internal and crossorganizational services are offered and utilized by participants of the value chain.

To make decentralised decisions, we need lots of small controllers with local responsibility organised in a **Programmable Control Network**. The functional model of a PCN goes against the currently widespread practice, but a distributed, decentralised architecture has lots of advantages:

- Local responsibility means also modularity. Respecting the interfaces, the independent systems can be replaced without any side effects.
- It's easier to customise a product on a decentralised architecture, because the different parts of the recipe (or *batch*) can be modified independently and with local batch, the decisions can be made locally[7].
- In a distributed factory, it's even possible to store the customised batch on the product. (For example, in an RFID chip[8] or in a more sophisticated built-in controller.)

Of course there are difficulties to be solved, because the common programming methods in the industry are based on assumptions, like

- controllers run a single-threaded, real-time operation system;
- subprograms are synchronised and serialised;
- communication paths are well-defined and constant;
- the borders and responsibilities of different programs are clear, because they are running on different controllers.

To design marketable control networks (which can compete with the PLC-s), we need a toolset containing techniques, protocols and methods to eliminate (or at least reduce) the drawbacks and help maximise the advantages.

III. The desired toolset of a PCN

In general, a PCN is a network composed of heterogeneous nodes connected by various reliable routes. All of the members have well-defined resources (like memory and CPU speed), physical IO-s connected to sensors and actuators (which can be modelled as resources, too) and a communication neighbourhood set.

A. The programming of PCN

The network can be described by two matrices: A connection and a resource matrix. The connection matrix is an adjacency matrix written on the graph of the network. (To support moving nodes, the connection matrix can be time-dependent.) The resource matrix assigns all the resources (including actuators and sensors) to the nodes. Its elements are non-negative numbers or ∞. Non-negative numbers can represent the computing capacity, the available memory, battery capacity or any finite resources consumed by the tasks. The ∞ elements represent the actuators and sensors (see on fig. 3).

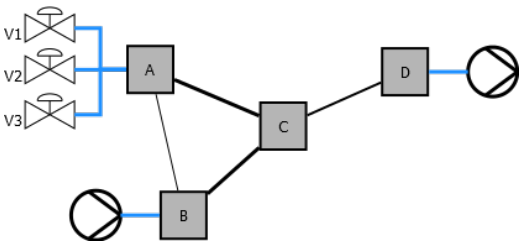

	A	B	C	D
A	0	1	3	0
B	1	0	3	0
C	3	3	0	2
D	0	0	2	0

	A	B	C	D
CPU	3	2	10	2
MEM	40	25	60	25
V1	∞	0	0	0
V2	∞	0	0	0
V3	∞	0	0	0
M1	0	∞	0	0
M2	0	0	0	∞

Fig. 3. Above is a simple control network, to the right is the network's connection matrix and to the left is the resource matrix.

The programming of PCN comprises the following three steps:

1) Divide the specification into weakly dependent processes.

In most cases, this is the easiest step, because the specification given by the customer already contains some kind of separation. Two process is weakly dependent on each other, if they communicate trough only status bits. This is not an exact step, but the good separation of the processes will facilitate the further steps. (This step is also important for a traditional PLC program. For example RSLogix 5000 use the term *Program*[9] for these processes.)

2) Identify the atomic tasks and their communication needs. The atomic task is a group of unparallelisable instructions. Its inputs and outputs are streams and it can read or write status bits. A task is connected to an other if it needs a stream generated by the other.
3) Distribute the tasks between the nodes of PCN. A task can run on a node, if the node have enough resources. Of course if two tasks connect to each other, they should run on nearby nodes to minimise the communication overhead.

To allow the PCN to be marketable, the developers need a toolset which makes the previous three steps optimal and as easy as possible. The remainder of this chapter will discuss the implementation of the last two steps. (The first step is not PCN-specific.)

B. A programming language to describe atomic tasks

Identifying the atomic tasks can be a complex problem if the programmer uses a traditional language, but if he or she gets the proper language to describe the tasks and relations, it can be automated. The easiest would be to ask for a data flow graph because each node of the graph is an atomic task, but would be too complex for a human even in simple cases.

My solution for this problem is a two-level language which can describe the data flow graph with high-level programming structure. A full presentation of the language is not possible for space reasons but I will show a simple examples. The current version of the language is text-based with a Python-like syntax, but it's easy to compile it to a Labview-like box-logic.

A Cooley-Tukey FFT algorithm[10] can be seen on figure 4. On the top of the figure is a part of the box-logic with recursion and branching. A box can contain two different kind of logic:

- it can call other boxes, like in this case box *DFT* call box *Split array*, itself and box *Combine array* if parameter $length > 1$ (high level), or
- a box can contain some kind of code in some traditional language (low level).

The compiler (which generate the data flow graph) will start from the top level box with given parameters, execute the control operations (like cycles or branches) and fallows three simple rules:

- If it finds a code block, it generates an atomic task (node of the data flow graph).
- If it finds called boxes, it continues the run.
- If it finds mixed code and box calles, it raises an error.

This language ease the generation of data flow graph and the programmer has full control over the content of its nodes.

C. The task-distributor algorithm

After we have the data flow graph of our application, we have to assign each atomic task to a node of the control network respecting some constraints.

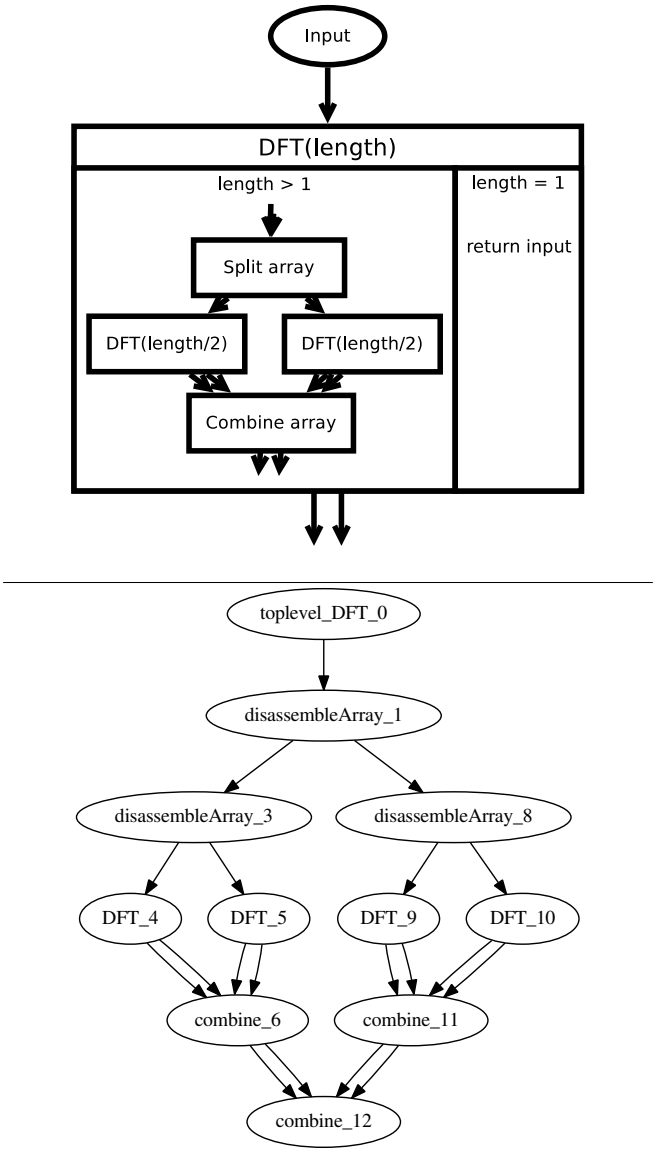

Fig. 4. Above is a high-level parametrised description of FFT, below is a realised data flow graph with parameter length=8.

Firstly, the assignment must not overload any node. Every atomic task has a resource requirements and each g node and its H' tasks must be satisfied that

$$\forall i \sum_{h \in H'} k_i(h) \leq k_i(g)$$

where $k_i(h)$ is the need of task h from the ith resource and $k_i(g)$ is the g node's capacity from the ith resource. This is a physical constraint. An assignment satisfying this is just realisable but not necessarily optimal.

An optimal assignment has to map the interdependent atomic tasks close to each other. On figure 3 that means, that *DFT_5* and *combine_6* should be run on the same (or at least adjacent) nodes. To formulate this constraint we have to define a metric on the task graph, an other metric on the control graph and some weight-function to calculate the goodness of an assignment. This can't be done regardless of the application.

Finally, because an industrial application must be robust, we have to preserve the redundancy of the control network during the assignment. This means that a node can have an atomic

task exclusively, if and only if its failure would destroy the network anyway. (It has an application-critical sensor or the control network falls apart without it.)

Creating an assignment with the constraints above is an NP-complete problem but with some simplifications, it can be solved by a graph partitioning algorithm.

IV. Solving the task-distributing as graph partitioning problem

The graph partition problem is defined on a graph $G = (V, E)$ (where V is the set of vertices and E is the set of edges). The goal is to partition G into smaller components with specific properties. Most commonly, the optimisation condition is to minimise the number (or weight) of edges between the partitions and there may be additional criteria to the maximum size of partitions.

This section shows how to simplify the original task-distributing problem so it can be handled with a graph partitioning algorithm. However these simplifications will make the resultant solutions moderately usable in real-life applications, they are useful to find an appropriate polynomial algorithm, because GPP is a well-known problem.[11]

A. Reducing atomic task distribution to GPP

In atomic task distribution (ATD) the solution is a function which maps the nodes of the task graph to the nodes of the control network. This mapping function (call it m) have to minimise the edges between interdependent tasks mapped into different nodes of the control network without overloading them. It also has to provide the redundancy of tasks mapped into dispensable nodes.

There are two main difference between GPP and ATD:

1) the mapping is disjoint in GPP but not in ATD because of the redundancy;
2) in GPP the maximum size of a partition is a well-defined integer but in case of ATD the quantity of tasks assigned to the same node determined by multidimensional resource vectors.

To eliminate these differences, we have to ignore the redundancy criterion and use only one dimensional resource vectors. In some simple application, this mitigation is acceptable and with them, we can handle the ATD with the algorithmic toolset of GPP.

V. Conclusion

The new demands of industry will sooner or later trigger a new industrial revolution where the decentralised decisions and control will have great importance. As this goes completely against the current practice, we need use and customise solutions from other areas to create the control system meeting the new demands.

In this paper, I presented the concept of Programmable Control Networks as a possibly successors of the traditional PLC. To design a marketable product (especially a successor), we can't just throw away every current methodology and except the users to learn a new technology. With a new, two-level programming language, the programmer can describe the connections between the atomic tasks with a graph-based language and can use ladder logic or any traditional language to define the tasks.

After the programmer finishes the program, the compiler must optimise for the current (maybe dynamic) control network. Due to the huge size and heterogeneity of the network an ideal optimiser is unrealisable. We need to use some kind of heuristic. Since this step has similarities to the Graph Partitioning Problem, we can use and improve its solutions.

Although there are still many open questions, the concept of PCN looks promising.

References

[1] David S. Landes, *The Unbound Prometheus.*, Press Syndicate of the University of Cambridge Massachusetts, p. 40. 1969.

[2] Controldesign (2014. 11. 13) Terminal/PLC Combo to Rise in Popularity [Online] http://www.controldesign.com/industrynews/2012/terminal-plc-combo-to-rise-in-popularity/

[3] PLCDev (2014. 11. 13) The birth of PLC [Online] http://www.plcdev.com/the_birth_of_the_plc

[4] Rockwell automation (2016. 04. 12) Allen Bradley history pages [Online] http://www.rockwellautomation.com/en_IN/news/allen-bradley-history-pages.page

[5] Bundesministerium für Bildunk und Forschung (2016. 04. 12) [Online] Zukunftsprojekt Industrie 4.0 https://www.bmbf.de/de/zukunftsprojekt-industrie-4-0-848.html

[6] Hermann, Pentek, Otto, "Design Principles for Industrie 4.0 Scenarios" presented at the 2016 49th Hawaii International Conference on System Sciences (HICSS)

[7] Hompel, M. and B. Otto, 2014: Technik für die wandlungsfähige Logistik. Industrie 4.0. 23. Deutscher Materialfluss-Kongress.

[8] Schlick, J., P. Stephan, M. Loskyll, and D. Lappe, 2014: Industrie 4.0 in der praktischen Anwendung. In: Bauernhansl, T., M. ten Hompel and B. Vogel-Heuser, eds., 2014: Industrie 4. 0 in Produktion, Automatisierung und Logistik. Anwendung, Technologien und Migration, 75.

[9] Rockwell automation (2016. 05. 15) Logix5000 Controllers Tasks, Programs, and Routines [Online] http://literature.rockwellautomation.com/idc/groups/literature/documents/pm/1756-pm005_-en-p.pdf

[10] Cooley, James W.; Tukey, John W. (1965). "An algorithm for the machine calculation of complex Fourier series". Math. Comput. 19: 297–301.

[11] Buluç, Aydin, et al. "Recent advances in graph partitioning." CoRR, abs/1311.3144 (2013).

Dual-pixel CMOS APS architecture for intra-frame speed measurement

Máté NÉMETH
(Supervisor: Dr. Ákos ZARÁNDY)
Pázmány Péter Catholic University, Faculty of Information Technology and Bionics
50/a Práter street, 1083 Budapest, Hungary
nemeth.mate@itk.ppke.hu

***Abstract*—A dual-pixel APS sensor architecture is proposed in this paper, for vision based speed measurement applications. The proposed sensor integrates two separate imaging element on pixel level, and is designed to generate two separate images: the primary sensor generates a good quality image of the scene for vehicle identification, while the secondary sensor is used for speed measurement, based on the intra-frame displacement of the vehicle. A scaling process is also shown for the sensitivity of the secondary sensor for a specific illuminance value.**

***Keywords*-CMOS Sensor; Global Shutter Efficiency; Multi exposure; Motion Blur; Speed Estimation; Dual-pixel**

I. Introduction

Speed measurement plays an important role in traffic management and control, which enables authorities to manage the traffic flow. The most common devices used for speed measurement, are based on active sensing technologies, like RADAR or LIDAR speed guns. According to US Department of Transportation National Highway Traffic Safety Administration[1], these devices measure the movement speed of the vehicles with high precision, with only a +2, -3 km/h tolerance in the measurement. On the other hand, these tools are expensive, and thus not suitable for example, to monitor the whole road network of a city, which would require a large number of sensing nodes. In addition, a camera is used along with these devices to perform the license plate recognition, to identify the vehicles. In this work, we present an alternative solution, in the form of a vision based speed measurement concept, which has an advantage of using a single sensor for both the speed measurement and the license plate recognition. Vision-based displacement calculation methods can be divided into two categories: inter-, and intra-frame. Inter-frame methods, like optical-flow based algorithms calculate the displacement of certain objects between two frames, or image sequences. On the other hand, intra-frame methods[2], [3], [4], [5], [6] measure the displacement during the exposure, thus capable of providing speed estimates based on a single image. For the latter case, there are only a few publications available[2], [3], [4]. In these papers, the authors utilize the fast shutter speed and the high resolution of the selected camera, to achieve 2% measurement error, with a deblurring method. Our approach is based on a different measurement principle, using a low-end image sensor, which provide similar accuracy, with better image quality in the region of interest, without the need for deblurring, as described in [5] and [6].

The paper is composed in the following way. The measurement concept and the double-exposure method is described in Section II, as well as the results of preliminary work using low global shutter efficiency imagers. Section III contains the description of the novel dual-pixel architecture, and design considerations related with photodiode scaling based on a given luminous intensity value, and the specifications of the selected technology. Section IV gives a short summary of the work.

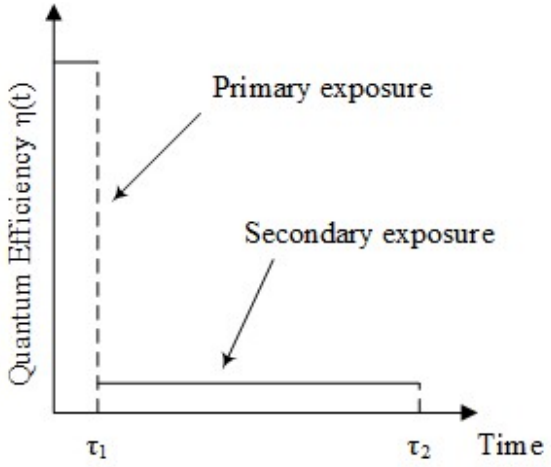

Fig. 1. Exposure-control scheme of the proposed method, with the primary [0,τ_1] and the secondary [τ_1,τ_2] exposure having different QE values.

II. Intra-frame Speed Measurement Concept

The proposed intra-frame speed measurement concept is based on a modification of the sensor shutter, which ensures sufficient image quality for the license plate recognition, while still holding information describing the intra-frame motion of the vehicles. To achieve such an image, a multi-exposure method has been developed. The modified shutter cycle contains three states of the electronic shutter: open state (primary exposure), semi-open-state (secondary exposure), and the close states. We modeled these integration intervals with different Quantum Efficiency (QE) values, as you can see in Fig. 1. Quantum Efficiency describes the photon to electron conversion efficiency of a sensor in the following way:

$$\eta = \frac{Jh\nu}{\Psi q} \tag{1}$$

where J is the incident photon generated current density, q is the elementary charge, Ψ is the optical power density, while $h\nu$ represents the energy of one photon. This means, that in the case of the secondary exposure, much more incident light power is required to generate the same signal on the sensor. As a result of this double-exposure method, we get a superimposed image. The short primary exposure generates a sharp image, and the longer secondary exposure with lower QE results in a motion blurred image, where only the brightest

M. NÉMETH, "Dual-pixel CMOS APS architecture for intra-framespeed measurement" in *PhD Proceedings Annual Issues of the Doctoral School, Faculty of Information Technology and Bionics, Pázmány Péter Catholic University – 2016.* G. Prószéky, P. Szolgay Eds. Budapest: Pázmány University ePress, 2016, pp 135– 138.

Fig. 2. Superimposed image acquired with the low-GSE Aptina MT9M021 CMOS sensor. The saturated trace represents the movement of the headlights during the readout phase.

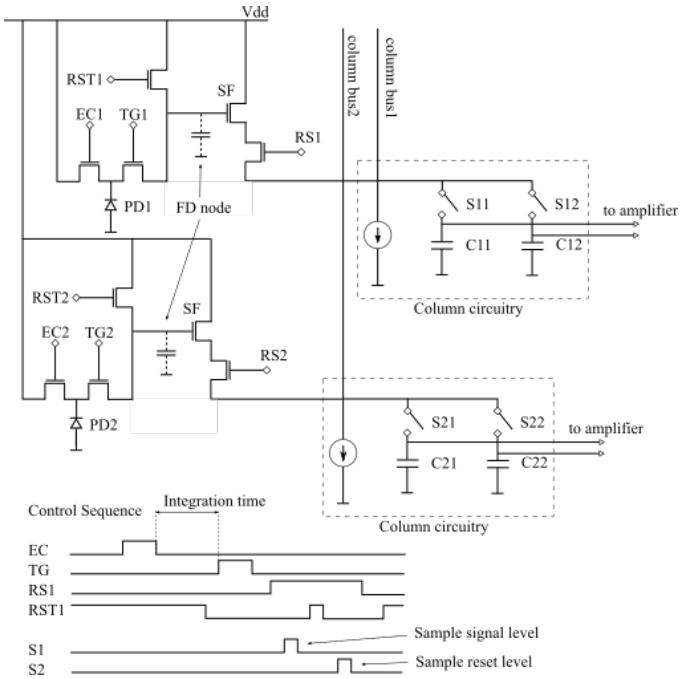

Fig. 3. Pixel architecture is based on a conventional 5T APS pixel. A 5T pixel consists of a photodiode, a floating diffusion (FD - analog storage node) and five transistors. S1X and S2X signals represent the two switches, which perform the double sampling, and sample the signal and reset levels in the analog storage node respectively.

regions of the scene will appear (Fig. 2). If we consider a measurement situation, where there is a moving vehicle in front of the camera system with the headlights turned on, light traces will appear on the image, representing the movement of the headlights during the secondary exposure. The length of the traces will be proportional with the movement speed of the vehicle, thus the speed measurement can be interpreted as length measurement on the image plane. If the exact spatial geometry of the measurement setup, and the length of the secondary exposure is known, we can calculate the movement speed of the vehicles. The problem formulation and the calculation of speed estimates can be found in [5] and [6], as well as error analytics and the description of the measurement method itself.

A. Speed measurement with low GSE CMOS sensor

In our previous works [5] and [6], we used a suitable, commercially available sensor for the measurements, featuring low global shutter efficiency. Global shutter efficiency (GSE) is a term, which describes the electrical and optical isolation of the in-pixel memory node, and is defined as a ratio of photodiode (PD) sensitivity to in-pixel store parasitic sensitivity. Global shutter pixel arrays start the integration of incident photons at the same time for all pixels in the array, and the readout is performed in a row-by-row manner. At the end of the integration, the collected charge is transferred to an in-pixel storage node (Fig. 3.). This memory node functions as a parasitic photodiode, incident photons will generate electron-hole pairs in the analog storage also. The PD to storage leakage current and the diffusion current outside of the memory node also contribute to the parasitic current. These effects will modify the stored photocharge until it is read out, so improving optical and electrical isolation (improving GSE) is essential in most CMOS imagers. There are some special applications however, where a sensor with low GSE can be beneficial, for example in the field of optical speed measurement. The impact of the low GSE on an image is similar to that of the secondary exposure phase of the double-exposure method (described in Section II), except the length of the light trace depends on its vertical position on the image, and can be controlled through the readout frequency. We developed an FPGA based test framework, capable of controlling multiple imager modules. The cameras use the Aptina MT9M021 CMOS sensor chip, which features the early 3rd generation 3.75μm global shutter pixel technology of Aptina[7]. These sensors have relatively low GSE (approx. 1/200), which enables us to use them for the speed measurement. The proof of concept measurements and the complete description of the measurement method, based on these sensors can be found in [5] and [6]. The fundamental problem with this method is that the length measurement of the traces has an inherent uncertainty. As you can see in Fig. 2, there is a saturated area around the starting point of the trace, which depends on the headlight geometry. In [6], we proposed a method using two synchronized cameras to overcome this problem, but the exact measurement, using a single sensor remained unsolved.

III. Sensor Architecture

CMOS technologies enable the designers to implement various pixel level control and processing innovations, as prototyping of custom ASIC designs with different technologies (including opto technologies, with anti-reflective coating, dedicated to CMOS imager design) are available for universities and research laboratories. We selected a suitable technology for our design, namely the 0.35μm AMS C35O, which is a dedicated opto technology. Our goal is to develop an imager capable of separating the saturated region of the headlight and the light trace on a hardware level, making the trace length measurement more accurate.

A. Dual-pixel Sensor

The challenge in this design remains the same as in the previous implementations. The requirements are to provide an

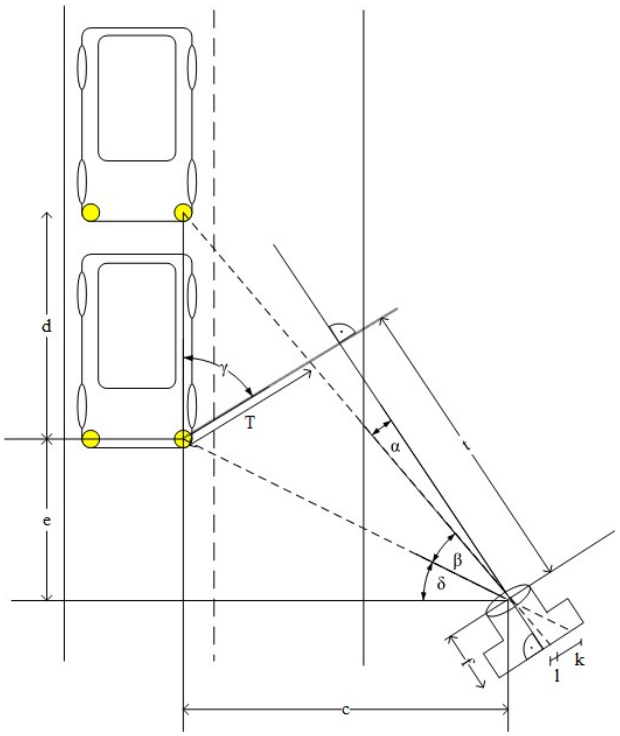

Fig. 4. Geometry of the measurement setup.

adequate quality image for license plate recognition, as well as to generate an image, which holds information regarding the intra-frame motion of the vehicle. To satisfy both conditions, we proposed a dual-pixel structure (Fig. 3). Every pixel in the array contains two PD, one of them is responsible for the good quality image of the scene, the other one, with much less sensitivity (QE), will be used to measure the intra-frame movement of the vehicle. The pixel structure is based on a conventional 5T active pixel sensor (APS) pixel with double sampling[8]. As both primary and secondary sensors have similar readout circuitry, one pixel contains 10 transistors. This means, that two architecturally similar sensor elements are integrated in a pixel of the proposed dual-pixel sensor. The pixel-level integration is important, because of the integrity of the spatial and temporal features of the scene. The 5T pixel consists of an exposure control (EC) gate, a transfer gate (TG), a reset (Rst), a source follower (SF) and a row select (RS) transistor. The shutter functionality is implemented with EC and TG, while SF act as a buffer amplifier to isolate the sensing node, and RS selects the pixel in the readout phase. Both PDs have separate exposure control, since the exposure has to satisfy different conditions in both cases. In the case of the primary sensor, the exposure control is similar to conventional imagers, the integration time depends on the illuminance of the scene. Our goal is to adapt to the lighting conditions, to generate a sharp image of the scene. However in the case of the secondary sensor, the exposure conditions remain the same for every measurement situation, since only the brightest spots of the scene - often the headlights - will appear on the secondary image, and the illuminance of a headlight can be specified from the isolux diagrams provided by manufacturers. As a result, we can scale the sensitivity of the secondary PD to a specified illuminance level.

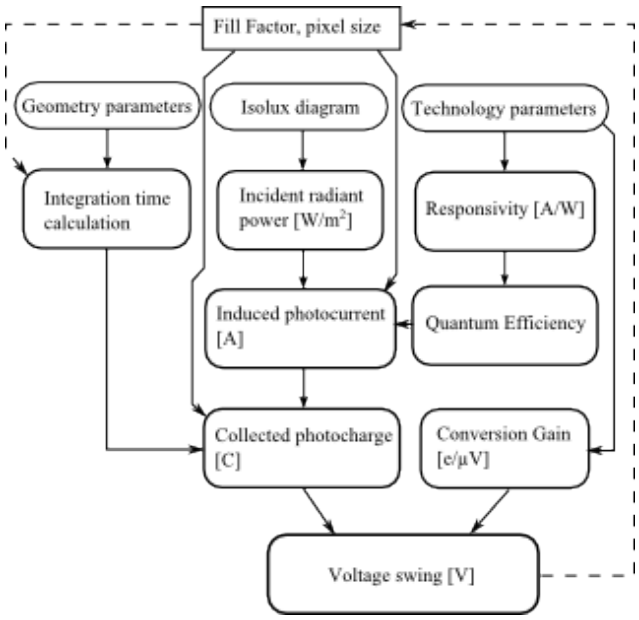

Fig. 5. Flowchart of the PD scaling process based on the geometry parameters, the technology parameters and the isolux diagram of a selected headlight.

B. Integration time calculation for the secondary PD

Based on the parameters of the spatial measurement geometry (Fig. 4.) along with the characteristics of the optical system and the sensor itself, we can calculate the length of the light trace on the image plane in pixels for a given vehicle movement speed. For example, in an urban traffic situation, the speed of the vehicles is typically around 50km/h. Based on the regulations specified in Section 1, in this case, +4, -6% relative error is accepted in the measurements. This specification can be directly transferred to our interpretation of the speed measurement, as the length measurement of the light trace on the image corresponds to the movement speed. As a result, the previously described error range applies to the aliasing error caused by the pixelization also, which affects the accuracy of the length measurement on the image plane, so we can define the required minimum length of the light trace on the image for the given accuracy. After this, based on a pinhole camera model and the geometry setup (Fig. 4), we can specify the integration time for the secondary sensor, based on 2 and 3

$$vt_{int} = d = c(\tan\gamma - \alpha - \tan\gamma - \alpha - \beta) \tag{2}$$

$$l_{trace}s_{pix} = k = f\frac{T}{t} \tag{3}$$

where l_{trace} is the length of the light trace in pixels and s_{pix} is the pixel size. Connection between T and d can be expressed with trigonometric functions from the geometry.

$$\frac{\sin\left(\frac{\pi}{2} - \alpha\right)}{d} = \frac{\sin\left(\frac{\pi}{2} - \alpha - \beta - \gamma\right)}{T} \tag{4}$$

The calculation of the integration time can be performed iteratively, since the initial pixel size is affected by later stages of the sensor design.

C. Secondary PD scaling based on isolux diagram

The challenge in the secondary sensor design is that we have to ensure that only the brightest regions of the scene

have significant impact on the image, so scaling the sensitivity of the sensor is crucial. In the previous subsection, the integration time has been specified based on the spatial geometry. Another starting point of the scaling is the isolux diagram of a headlight. The isolux diagram provides the contours of equal illuminance or luminous intensity in lux or candelas respectively, from a specified position. This diagram can be used to analyze the power distribution characteristics of a headlight and to determine lighting levels in selected directions[9]. The most important steps of the scaling process are highlighted in Fig. 5. Because in many cases, the structure of the PD is pre-defined by the technology, the only features the designers have, to control the sensitivity of the sensor is the fill factor (FF=photoactive area (PD size)/pixel size), and the reverse bias voltage of the PD. In this paper, we focus on the fill factor, the effect of a variable reverse bias voltage on the output through the conversion gain will be discussed in another paper. Based on the luminous intensity provided by the isolux diagram at an angle specified from the geometry, we can calculate the incident radiant power density reaching the surface of the sensor in W/m2 after photometric-radiometric conversion. On the other hand, technology parameters define the spectral responsivity function of the PD. After rewriting 1, we obtain the following equation for the QE[10]

$$\eta(\lambda) = R(\lambda)\frac{h\nu}{q} \tag{5}$$

where $R(\lambda) = \frac{I_d}{P_{pix}}$ denotes the responsivity, I_d is the photocurrent, and P_{pix} is the radiant power [W] reaching the surface of the PD. As a result, we can calculate the photocurrent

$$I_d = \frac{q\eta P_{pix}}{h\nu} \tag{6}$$

Taking into consideration the spectral power density distribution of the light source (denoted with $f(\lambda)$), the photocharge cumulated during the previously defined integration time can be obtained as follows

$$Q = A_{eff} t_{int} \int R(\lambda) f(\lambda) d\lambda \tag{7}$$

where A_{eff} denotes the photoactive area of the pixel. The electron to voltage conversion gain can be calculated from the technology parameters,

$$C_{gain} = \frac{q}{C_{jdep}} \tag{8}$$

where C_{jdep} is the area dependent junction capacitance of the PD. After combining 7 and 8, we get an equation for the voltage swing at the pixel output, for the given illuminance.

$$V = \frac{Q}{C_{jdep}} = \frac{A_{eff} t_{int} q}{C_{jdep}} \int \frac{\lambda}{hc} \eta(\lambda) f(\lambda) d\lambda \tag{9}$$

The value of the voltage swing on the pixel output can be controlled with the FF. This method can be performed iteratively, until the voltage swing range meets the specifications, since it is hard to estimate the size of the readout circuitry prior to the actual design process. This will affect the size of the pixels and in the end, the integration time and the fill factor also. The lower fill factor due to extra devices will be compensated by microlens.

IV. Conclusions

We are developing a novel speed measurement CMOS imager, based on dual-pixel architecture. Some of the most important design considerations are described in this paper. The sensitivity of the secondary, speed measurement sensor is designed for a specific exposure value, based on the luminous intensity of a vehicle headlight. This way, we can ensure that intra-frame motion information will only be extracted from the brightest regions of the scene.

Acknowledgements

The support of the KAP-1.5-14/006 grant and the advices of László Orzó are greatly acknowledged, as well as the kind help and cooperation of ON Semiconductor (formerly Aptina) customer service.

References

[1] US Department of Transportation National Highway Traffic Safety Administration, *Speed-Measuring Device Performance Specifications*, 2015, http://www.theiacp.org/portals/0/pdfs/IACPLidarModule.pdf.

[2] H.-Y. Lin, K.-J. Li, and C.-H. Chang, *Vehicle speed detection froma singlemotion blurred image*, Image and Vision Computing, vol. 26, no. 10, pp. 1327–1337, 2008.

[3] H.-Y. Lin and C.-H. Chang, *Automatic speed measurements of spherical objects using an off-the-shelf digital camera*, in Proceedings of the IEEE International Conference on Mechatronics (ICM '05), pp. 66–71, Taipei, Taiwan, July 2005.

[4] M. Celestino and O. Horikawa, *Velocity measuerment based on image blur*, ABCM Symposium Series in Mechatronics, vol. 3, pp. 633–642, 2008.

[5] M. Nemeth and A. Zarandy, *New sensor concept for intraframe scene and speed capturing*, in Proceedings of the European Conference on CircuitTheory and Design (ECCTD '15), pp. 1–4, IEEE, Trondheim, Norway, August 2015.

[6] Mate Nemeth and Akos Zarandy, *Intraframe Scene Capturing and Speed Measurement Based on Superimposed Image: New Sensor Concept for Vehicle Speed Measurement*, Journal of Sensors, vol. 2016, Article ID 8696702, 10 pages, 2016. doi:10.1155/2016/8696702

[7] S. Velichko, G. Agranov, J. Hynecek et al., *Low noise high efficiency 3.75μm and 2.8μm global shutter CMOS pixel arrays*, in Proceedings of the International Image Sensor Workshop (IISW '13), Snowbird,Utah, USA, June 2013.

[8] Chenghan Li, Christian Brandli, Raphael Berner, Hongjie Liu, Minhao Yang, Shih-Chii Liu, Tobi Delbruck, *An RGBW Color VGA Rolling and Global Shutter Dynamic and Active-Pixel Vision Sensor*, in Proceedings of the International Image Sensor Workshop (IISW '15), Vaals, The Netherlands, June 2015.

[9] M. A. Laughton, D. F. Warne, Electrical Engineer's Reference Book, Sixteenth edition, Elsevier Science, 2003, pp. 21/6-7.

[10] O. Yadid-Pecht and R. Etienne-Cummings, CMOS Imagers From Phototransduction to Image Processing, Kluwer Academic, 2004.

Portfolio optimization with memory

Zsolt Nika
(Supervisors: Miklós Rásonyi and Péter Szolgay)
Pázmány Péter Catholic University, Faculty of Information Technology and Bionics
50/a Práter street, 1083 Budapest, Hungary
nika.zsolt@itk.ppke.hu

***Abstract*—In portfolio optimization the classical problem is to trade with assets so as to maximize some kind of utility of the investor. We investigate the problem, where assets depend on exogenous variable and its past values as well. Though the literature covers several problems where exogenous process is involved, considering the effect of memory is waiting for deeper study.**

For easier interpretation of our model we find similarities with regulators from control theory, where similar models are used. Moreover, we choose our class of strategies in such a way that it resembles us to a linear quadratic regulator. The formulation of the model is discrete in time and uses power utility function, while optimum is yielded by numerical simulation.

Keywords – portfolio theory; investment strategy; stochastic processes; memory; factor model; risk sensitive

I. Introduction

Modern portfolio optimization started with Markowitz's theory [1] in 1952, barely 20 years after that Kolmogorov had set the basics of probability theory [2], which we usually use nowadays. The most important property of a portfolio is its price, but it is not evident how to take it into consideration. To maximize its value (or its expected value, since we regard every price in the future as a random variable) seems an obvious idea, but this approach avoids to think about risk: from two portfolios with the same profit we would choose the one with less risk. Common practice is to maximize the expected value of the portfolio value via a function, called *utility* function, which determines the investor's sensitivity to risk through its parameters.

Some typical features of assets' and portfolios' prices is that they are time-dependent and heavily oscillate, they need to be modelled as stochastic processes made up by a smooth *drift* part and a noise (*volatility*). For instance, consider the stock prices of Facebook on figure 1, although we can see a growth trend in its price, thanks to the noise, it is impossible to know the price in the next day in advance.

The task also can be formulated as a *control problem* (regulator), where the dynamical system is the stock price process, the control is our decision on how many assets we buy or sell at a given time point and the aim is to maximize the expected utility of the portfolio (mathematically it is called *objective function*). Because decision is involved, it is also called *decision problem*. The model can be built up either in continuous or discrete way, but the value of the processes are usually continuous variables. So we can say, that portfolio optimization is a stochastic control theory problem with a *linear exponential quadratic Gaussian control* (linearity refers to the decision), see below.

Dynamical systems usually indicate that the state variables are evolving in time by a linear differential equation, also in the stochastic case by a stochastic differential equation. These models implicitly assume, that it is enough to know the structure of the dynamics and the actual state to make calculations for the future (i.e. the Markovian property is assumed). The theory of controlling or investment management is well studied in this case, where the current state holds all the information, even if there are still a lot to investigate. On the other side it seems a strong restriction: why should we not take into account any information from the past if we have data?

To study the price's behavior it is common to use the increments instead of the process itself (the *returns*) in order to get rid of the drift and see only the noise part (the volatility). The above mentioned systems assume that the noise does not have any time correlation but studies have shown in the 90s [3]–[5] that correlation exists and not at a negligible level. A very good overview about statistical properties of returns can be found in [6]. To show this, we use the same time series from Facebook on figure 2. Our model has its main focus on this property. [1]

Another stylized fact is that economic quantities like broadly used indices, interest rates or inflation can have a deep impact on stock prices. Bielecki and Pliska [7] worked out a model where economic factors are taken into consideration in the drift, and 3 years later Kuroda and Nagai [8] improved this with correlation in the volatility. Moreover, they use risk-sensitive approach via the optimization function, hence it is suitable for extensions to processes with memory. Davis and

[1]Correlation in time is measured by autoforrelation (ACF). ACF(τ):=correlation($X(t), X(t+\tau)$). It shows a linear connection of a sign between its value at time t and at $t+\tau$.

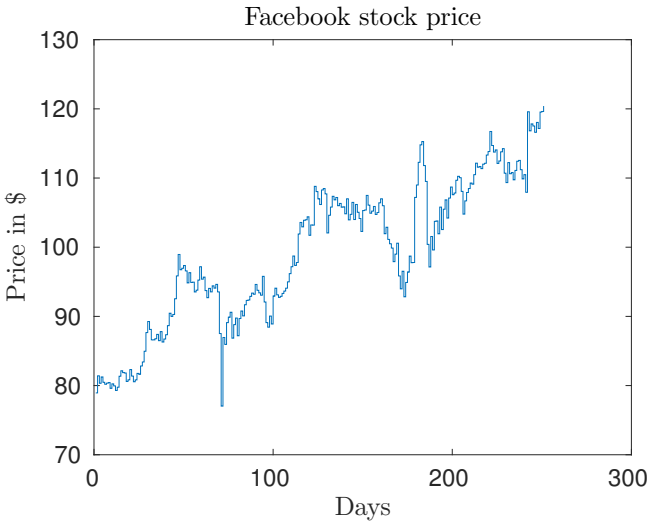

Fig. 1. Stock prices (daily openings) of Facebook in the last one year: noisy and time-dependent behavior

Zs. NIKA, "Portfolio optimization with memory" in *PhD Proceedings Annual Issues of the Doctoral School, Faculty of Information Technology and Bionics, Pázmány Péter Catholic University – 2016.* G. Prószéky, P. Szolgay Eds. Budapest: Pázmány University ePress, 2016, pp 139– 142.

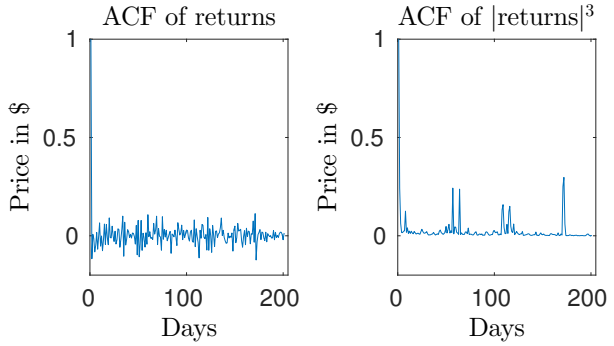

Fig. 2. Autocorrelation of Facebook's stock price openings. The left image could suggest independent increments, but the right image refutes it: higher power of absolute returns has strong correlation in time.

Lleo wrote a good survey about these models in [9].

In the following our model is an extension of Bielecki and Pliska's model with memory effect in the noise term, therefore it contains time-correlation, economic factor correlation and risk-sensitivity of the investor, for this, see equations (7) below in section III.

II. Regulators with exogenous variable

A. A class of control problems

Our problem is complex to solve it explicitly, but there is a class of control problems similar to ours, where the optimal control is obtained by a linear function of the variables. Hence, at first we briefly look at this class and then proceed to our strategy class where the optimum is obtainable only by numerical methods.

The basic example about regulators is the LQR model, where the (state) process $x(t)$ evolves by a linear differential equation with a control action $u(t)$. The output can be a linear transformation of the state process, but we choose the following model:

$$\begin{aligned} \dot{x}(t) &= Ax(t) + Bu(t) \\ y(t) &= x(t), \end{aligned} \tag{1a}$$

and for simplicity the system is written in one dimension. The function which ought to be optimized (called *value function* or *performance criterion*) is the following:

$$J(x,u) = \frac{1}{2}\int_0^T Qx(t)^2 + Ru(t)^2 dt,$$

where x is the initial condition of $x(t)$ and u is the chosen control. The problem is solved if we find the optimum (u^*) among all possible controls: $J^*(x) = min_u\{J(x,u)\}$. The reason why we present this model is its solution, which can be deduced easily with calculus of variations. The surprising about the optimal strategy is that it is achieved by a simple linear function of the state process: $u^*(t) = \alpha_1(t)x(t)$. The linear factor $\alpha_1(t)$ is the solution of a *Ricatti differential equation* (the form of the equation is unimportant, but well known, D. H. Jacobson wrote a very good survey about it in [10]). Maybe more surprisingly, this strategy is also optimal in a Linear Quadratic Gaussian regulator case (LQG), where the only difference with LQR is the dynamics: $\dot{x}(t) = Ax(t) + Bu(t) + \sigma w(t)$, and $w(t)$ is a white noise.

Sometimes, in finance, the criteria function is the integral not the quadratic term but its exponential: $J(x,u) = \int_0^T \exp(Qx(t) + Ru(t)^2)dt$. Without white noise term (i.e. $\sigma = 0$) the optimal solution is again yielded by the same $u^*(t) = \alpha_2(t)x(t)$ form, but if $\sigma \neq 0$, the optimal strategy changes to a different coefficient $\alpha_2(t)$, which is also a solution of a slightly modified Ricatti equation. Our model, as pointed out in the Introduction, contains random processes (i.e. $\sigma \neq 0$, $w(t)$ is a noise, but not necessarily a white one) and the state variable depends on an exogenous variable.

B. Financial setting

The state variable in finance is the stock price $S(t)$, or the log price $X(t)$, they are random processes. To simplify as much as possible, we regard only one stock and one bond ($S_0(t)$), the latter is a deterministic process, it can be a bank deposit. The portfolio with value $V(t)$ is made of these two assets, and every time point we can sell and buy them *in a self-financing way* – this is the control, or *investment strategy*.

Mathematically it is more precise if we use the time integral of the differential equations and we note, the integral of white noise is the Brownian motion $W(t)$, and these are called *Stochastic Differential Equations* and have the following form:

$$dX(t) = \mu(X(t),t)dt + \sigma(X(t),t)dW(t),$$

where the first term in the RHS $\mu(\cdot,\cdot)$ is the drift characterizing an average behavior of the process and $\sigma(\cdot,\cdot)$ is the volatility, the oscillation around it.

We assume the following stock and bond price dynamics:

$$\frac{dS_0(t)}{S_0(t)} = (a_0 + A_0 Y(t))dt \tag{2a}$$

$$\frac{dS(t)}{S(t)} = (a + AY(t))dt + \sigma_1 dW_1(t) + \sigma_2 dW_2(t), \tag{2b}$$

$$dY(t) = BY(t)dt + \lambda dW_2(t), \tag{2c}$$

with initial conditions $S(0) = s$, $Y(0) = y$. The variable $Y(t)$ is the exogenous process usually referred as *economic factor*. It has effect not only on the drift part, since one of the driving Brownian motion in the price $W_2(t)$ appears also in the equation of $Y(t)$ which results a correlation in their volatility terms. The portfolio is a combination of $S_0(t)$ and $S(t)$ and if the value at t is $V(t)$, then we can invest $u(t)V(t)$ into stock and $(1-u(t))V(t)$ into bonds which gives the following equation:

$$\frac{dV(t)}{V(t)} = u(t)\frac{dS(t)}{S(t)} + (1-u(t))\frac{dS_0(t)}{S_0(t)}. \tag{3}$$

In the Section III. we investigate a similar model with $a_0 = 0$ and $A_0 = 0$ where we use the logarithm of the price and value processes. In this case the explicit formulas for the price of the stock and the portfolio helps to understand our model:

$$\begin{aligned} V(t) =& V(0)\exp\left\{\int_0^t u(s)(\sigma_1 dW_1(s) + \sigma_2 dW_2(s)) \right. \\ &\left. + \int_0^t \left[u(s)\left(a + AY(s)\right) - \frac{u(s)^2(\sigma_1^2+\sigma_2^2)}{2}\right] ds\right\}, \end{aligned} \tag{4a}$$

$$\begin{aligned} S(t) =& S(0)\exp\left\{\int_0^t \sigma_1 dW_1(s) + \sigma_2 dW_2(s) \right. \\ &\left. + \int_0^t \left[a + AY(s) - \frac{\sigma_1^2+\sigma_2^2}{2}\right] ds\right\} \end{aligned} \tag{4b}$$

From equation (4a) it is clear that the problem is quadratic in the exponential.

The risk-sensitive criterion function is the following:

$$J_\theta(y,u,T) = -\frac{1}{\theta}\ln \mathbf{E}\left[V(T)^{-\theta}\right], \tag{5}$$

where θ is the parameter of the risk sensitivity, y is the initial condition of $Y(t)$ and $\mathbf{E}[\cdot]$ denotes the expected value. The maturity T is the end time when the investing finishes. As we gave the explicit formula for the process $V(t)$ which is actually an exponential function, it is easy to take its power $-\theta$. Equation (5) also defines the utility function in this case: it is a power function $utility(V(t)) = V(t)^{-\theta}$. The optimum has a linear form again: $u^*(t) = \alpha_3(t)Y(t) + \beta(t)$, see [8]. From theoretical point of view another performance function is investigated where the maturity T goes to infinity and we are searching for an average optimal:

$$J_\theta(y,u) = \liminf_{T\to\infty} -\frac{1}{\theta T}\ln \mathbf{E}\left[V(T)^{-\theta}\right]. \tag{6}$$

Its optimal solution has also linear form (under suitable assumptions), but thanks to the infinite T, the solution does not depend on t, hence $u^*(t) = \alpha Y(t) + \beta$.

III. Model

From the two effects we consider in this paper the correlation between a factor variable and the price already involved in Bielecki and Pliska's work as in equation (2). The other effect, the memory should also take into account, therefore we change one of the Brownian motion in equation (2b) into a process that depends on its past. Due to this, it is impossible to calculate the optimal strategy explicitly and we have to optimize numerically. Generally it is very difficult, since $u(t) \in \mathbf{R}$ for every $t \in [0,T]$ and if we discretize in time into N time points, then the optimal solution lays in the N-dimensionl $\mathbf{R}^N$ space. To reduce the problem we use the same parameter class as in section II. and we look at an infinite horizon problem, equation (6), i.e. the optimum $u^*(t) = \alpha^* Y(t) + \beta^*$, which simplified the optimum searching in a two-dimensional problem: $(\alpha^*, \beta^*) \in \mathbf{R}^2$.

We use a discretized version of the equation (2) using the logarithm of the variables [2]: log-price $X(t) = \log(S(t))$ and log-portfolio value: $W(t) = \log(V(t))$. It is generally used in simulation because the numerical model is more stable in this case. The time steps are unit length, $t \in \{1,2,\dots\}$ and for simplicity $a_0 = A_0 = 0$ (it does not change the results fundamentally). The following dynamics can be deduced easily from equation (4):

$$\begin{aligned}
X(t+1) - X(t) =& (a + AY(t)) - \frac{1}{2} \\
&+ \sigma_1\xi(t) + \sigma_2\eta(t), && \text{(7a)}\\
Y(t+1) - Y(t) =& b + BY(t) + \lambda\xi_2(t), && \text{(7b)}\\
W(t+1) - W(t) =& u(t)(X(t+1) - X(t)) \\
&+ \left(\frac{u(t)}{2} - \frac{u(t)^2}{2}\right)\frac{\sigma_1^2+\sigma_2^2}{2}, && \text{(7c)}\\
J_\theta(y,u) =& \liminf_{T\to\infty} -\frac{1}{\theta T}\ln \mathbf{E}\left[\exp\{-\theta W(t)\}\right]. && \text{(7d)}
\end{aligned}$$

If $\eta(t) = \xi_2(t)$ were, this would be the discretization of Bielcki ans Pliska's model mentioned in equation (2). The constants $(a, A, b, B, \sigma_{1,2}, \lambda)$ have the same role as in equation (2),

[2]We disregard here of the deduction of the difference equation, it is required the Ito's lemma and due to lack of space we do not expound it here.

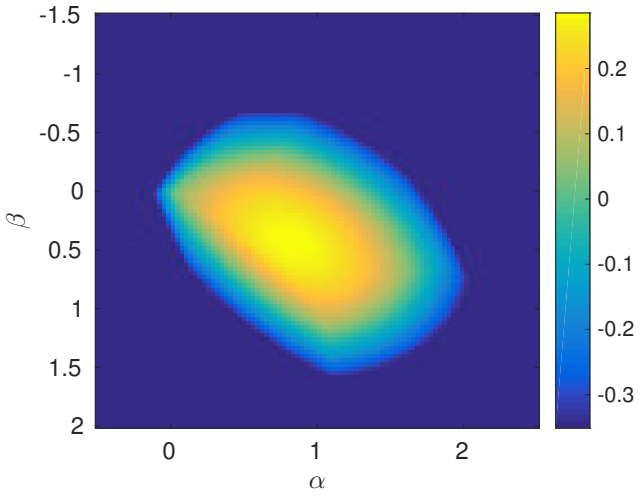

Fig. 3. Only a small domain on $\mathbf{R}^2$ gives feasible solution and it is enough to search the optimal parameters in it.

while $\xi_{1,2}(t), \eta(t) \sim \mathcal{N}(0,1)$ replace the Brownian motions. The noise terms $\xi_{1,2}$ are uncorrelated white noises, and the third one $\eta(t)$ carries information from the past, moreover it is correlated with $\xi_2(t)$, i.e. the price and the economic factors are correlated in their volatility.

In the next section we are investigating two cases. First, when $\eta(t) = \xi_2(t)$; secondly, $\eta(t) = \sum_{k=0}^{\infty}(k+1)^{-\kappa}\xi_2(t-k)/c(\kappa)$ what is a moving-average process (MA(∞)). The latter carries memory which is in our focus here. It should be noted, that we choose $c(\kappa)$ such that $\eta(t)$ has unit variance.

IV. Results

To understand more the relation between the log-price $X(t)$ and the factor variable $Y(t)$, we choose the volatilities such that $\sigma_1^2 + \sigma_2^2 = 1$, therefore the correlation between the volatilities is σ_2. In the second case the strength of memory is descried by $\kappa > 1/2$. When $\kappa \to \infty$, the memory vanishes and we get back the $\xi_2(t) = \eta(t)$ case.

The expectation function $\mathbf{E}$ is approximated by Monte Carlo method and the optimal strategy (α^*, β^*) is searched on a mesh in the $\mathbf{R}^2$ space. We are mainly interested in the changes of the optimal parameters when $\kappa \in (1/2, \infty)$ is increasing. The parameter space is not unbounded, the problem is feasible only in a small bounded domain where the system is stable. This constraint comes from the Ricatti differential equation

We set the following parameters: $\theta = 1$, $a = 0.5$, $A = 1$, $B = -0.5$, $\lambda = 1$, $\sigma_1 = \sigma_2 = \sqrt{2}$ for the dynamics and $T = 400$, $N = 1000$ for the simulations, where T is the number of the steps in time and N is the number of threads of the Monte Carlo method. On figure (3) we display region of the feasible solution for memory parameter $\kappa = 2$. Its shape slightly depends on the memory κ as well as on the dynamics.

On figures (4) and (5) we show some examples at two different risk sensitivity levels $\theta = -0.5$ and $\theta = 1$. Three artifacts are obvious on these figures. Firstly, as the system looses its memory ($\kappa \to \infty$), the optimal values $J^*(\kappa)$ converge to the Markov case, when $\eta(t) = \xi_2(t)$. Secondly, when $\kappa > 1$, the optimal values decrease, perhaps due to the information loss, the optimal investment cannot be as good as with more information. Thirdly, when $0.5 < \kappa < 1$, it is the

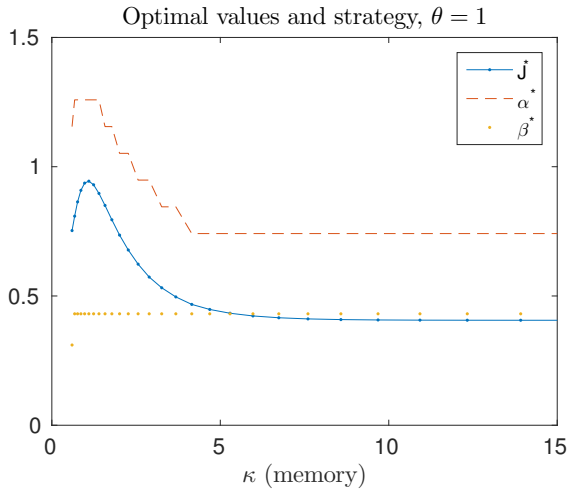

Fig. 4. Optimal values and strategies as a function of memory when $\theta = 1$.

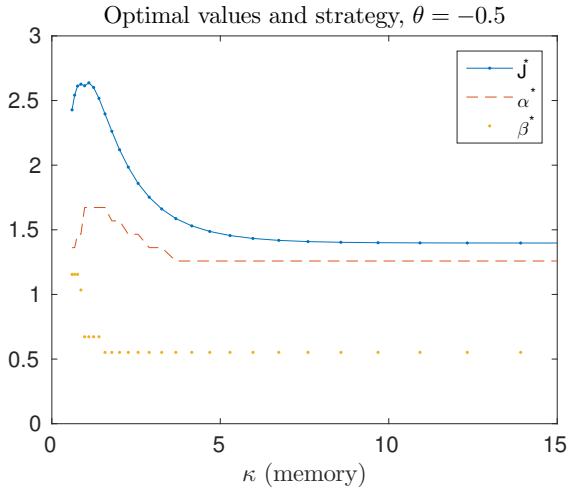

Fig. 5. Optimal values and strategies as a function of memory when $\theta = -0.5$.

opposite, which is a non-trivial phenomenon requiring further investigations.

V. Future work

There are a lot of directions where we can proceed with our work and we only show a few of them:

- Using different type of noise process in $\eta(t)$, for example fractional Brownian noise.
- In this paper the time correlated noise drives the log-price. It could drive the factor process instead.
- The power utility function we used here is close to a real investor, but other utility functions, for example log-utility has the advantage to have a more elaborate theory.

Acknowledgements

The author would like to thank Dr. Miklós Rásonyi for his guidance in this research project.

References

[1] H. Markowitz, "Portfolio selection," *The journal of finance*, vol. 7, no. 1, pp. 77–91, 1952.
[2] A. N. Kolmogorov, "Foundations of the theory of probability. 1956," *Translation of Grundbegriffe der Wahrscheinlichkeitsrechnung*, 1933.
[3] Z. Ding, C. W. Granger, and R. F. Engle, "A long memory property of stock market returns and a new model," *Journal of empirical finance*, vol. 1, no. 1, pp. 83–106, 1993.
[4] T. G. Andersen and T. Bollerslev, "Intraday periodicity and volatility persistence in financial markets," *Journal of empirical finance*, vol. 4, no. 2, pp. 115–158, 1997.
[5] T. G. Andersen, T. Bollerslev, F. X. Diebold, and P. Labys, "The distribution of realized exchange rate volatility," *Journal of the American statistical association*, vol. 96, no. 453, pp. 42–55, 2001.
[6] R. Cont, "Empirical properties of asset returns: stylized facts and statistical issues," *Quantitative Finance*, vol. 1, no. 2, pp. 223–236, 2001.
[7] T. R. Bielecki and S. R. Pliska, "Risk-sensitive dynamic asset management," *Applied Mathematics and Optimization*, vol. 39, no. 3, pp. 337–360, 1999.
[8] K. Kuroda and H. Nagai, "Risk-sensitive portfolio optimization on infinite time horizon," *Stochastics: An International Journal of Probability and Stochastic Processes*, vol. 73, no. 3-4, pp. 309–331, 2002.
[9] M. H. Davis and S. Lleo, *Risk-sensitive Investment Management*. World Scientific, 2014.
[10] D. H. Jacobson, "Optimal stochastic linear systems with exponential performance criteria and their relation to deterministic differential games," *Automatic Control, IEEE Transactions on*, vol. 18, no. 2, pp. 124–131, 1973.

Morphological evidence supporting retrograde endocannabinoid signalling between GnRH neurons and their kisspeptin afferents in mice

Tamás WILHEIM
(Supervisor: Dr Imre KALLÓ)
Pázmány Péter Catholic University, Faculty of Information Technology and Bionics
50/a Práter street, 1083 Budapest, Hungary
wilheim.tamas@koki.mta.hu

***Abstract*—The GnRH network gives the main output of the reproduction control circuitry. It was previously shown by our lab, that GnRH cells can modulate their GABAergic afferents via the endocannabinoid retrograde signalling pathway. The kisspeptin (KP) network gives one of the main excitatory inputs to the GnRH neurons. We investigated, if it is possible, that the GnRH cells can modulate their input coming from the KP cells via the endocannabinoid pathway. By using immunohistochemical triple labelling, we have identified KP-immunoreactive (IR) axon varicosities in apposition to GnRH neurons IR either for GAD65, the marker of GABAergic neurons, or VGLUT2, the marker of glutamatergic neurons, or the type 1 endocannabinoid receptor (CB1). We used confocal imaging and 3D reconstruction to analyse the data. We have found, that 70$\pm$0.98% of the KP afferent to GnRH perykaria contains CB1 receptor, and 59$\pm$3.53% of KP-IR fibres in apposition to GnRH processes were found to be IR for CB1. 52$\pm$1.56% of KP-IR fibres in apposition to GnRH perikarya and 47$\pm$2.72% of KP-IR fibres in apposition to GnRH processes were found to be also IR for VGLUT2. 31$\pm$0.70% of KP-IR fibres in apposition to GnRH perikarya and 40$\pm$2.38% of KP-IR fibres in apposition to GnRH processes were found to be also labelled for GAD. Since it is a well-known fact, that GnRH neurons synthetize 2-AG, one of the endocannabinoids secreted by the nervous system, our data shows, that it is possible, that GnRH neurons can influence their inputs via the endocannabinoid retrograde signalling pathway.**

***Keywords*-GnRH; kisspeptin; VGLUT2; GAD65; retrograde signalling; afferents; 3D reconstruction;**

I. Introduction

The GnRH network gives the main output of the hypothalamic reproductive regulation circuitry by producing the GnRH hormone, secreted into the portal vessels of the hypophysis. KP neurons provide an important excitatory input for the GnRH network in the hypothalamus [1-6]. Without KP, e.g. in kisspeptin knock out animals, GnRH release is absent, causing underdeveloped gonads, and infertility [7]. In rodents, two distinct KP populations exist: one, in the rostral periventricular area of the third ventricle (RP3V), and one in the arcuate nucleus (ARC) [8,9]. It was previously described, that GnRH neurons are capable to modulate their synaptic input from presynaptic GABA terminals expressing cannabinoid type 1 receptor (CB1). This is an important regulation mechanism, because due to the elevated chloride levels in the adult GnRH cells, the GABA transmission causes depolarization in GnRH neurons, resulting that GABA, the classical inhibitory neurotransmitter is excitatory on GnRH neurons [9,10].

It was also shown, that KP is released only when the KP neuron is stimulated with a higher frequency (5-10Hz). Low frequency ($<$1Hz) resulted in classic neurotransmitter release. [12] Due to these properties of the GnRH cells, it is important that some inhibitory regulation is employed in the network. The aims of this study were to determine (1) whether KP afferents onto GnRH neurons contain either of the classical neurotransmitters (GABA or glutamate) and (2) whether GnRH neurons are targets of endocannabinoids and immunoreactive for CB1. Triple labelling immunohistochemistry was used in brain sections of mice expressing cre enzyme and GFP in KP and GAD65 neurons [13-16]. To visualize the KP or GAD65 cell membrane, an adeno-associated virus construct was injected either into the preoptic area, or into the arcuate nucleus carrying channel rhodopsin and YFP. With this construct, the YFP is sorted into the cell membrane, making it possible to visualize the whole cell compartment, compared to the direct KP/GAD65 immunolabelling, where only the KP/GAD65 containing compartments are visible.

II. Materials and methods

A. Animals

Adult, female Kiss1-CreGFP mice, or GAD2-CRE-GFP mice were used. The Kiss1-CreGFP mouse expresses Cre recombinase and GFP under the endogenous Kiss1 promoter, making it possible to see GFP only when Kiss1 is expressed. These animals received a viral construct AAV-EF1a-DIO-hChR2(H134R)-EYFP injection into the anteroventral periventricular nucleus (AVPV) to label the KP and GAD65 neurons. The animals were housed under controlled lighting(12:12h light-dark cycle; lights on at 07:00h, and temperature (22 $\pm$ 2 °C), with access to food and water ad libitum. All studies were carried out with permission from the Animal Welfare Committee of the Institute of Experimental Medicine (No. 2285/003) and in accordance with legal requirements of the European Community (Decree 86/609/EEC). Surgery was performed on animals under deep anaesthesia induced by an intraperitoneally injected cocktail of ketamine (25mg/kg b.w.), xylavet (5mg/kg b.w.) and pipolphen (2.5mg/kg b.w.) in saline.

B. Tissue Preparation for Confocal Microscopy

The animals were injected with adeno-associated virus carrying cre-dependent channel rhodopsin, and YFP in the AVPV. The animals were perfused transcardially with phosphate-buffered saline (PBS; 0.1M) containing 4% paraformaldehyde (PFA). The brain was removed, postfixed for 24 hours, and transferred into 30% sucrose for cryoprotection, then 30μm thick coronal sections were cut on a freezing microtome. After the endogenous peroxidase activity had been quenched

T. WILHEIM, "Morphological evidence supporting retrograde endocannabinoid signalling between GnRH neurons and their kisspeptin afferents in mice" in *PhD Proceedings Annual Issues of the Doctoral School, Faculty of Information Technology and Bionics, Pázmány Péter Catholic University – 2016.* G. Prószéky, P. Szolgay Eds. Budapest: Pázmány University ePress, 2016, pp 143– 146.

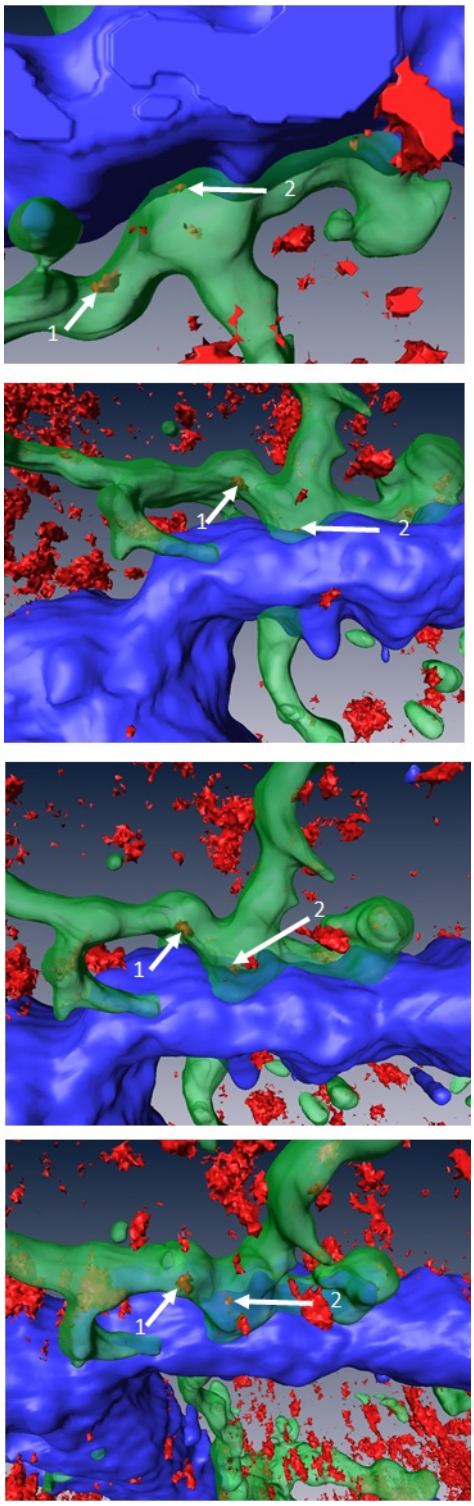

Fig. 1. 3D reconstruction of the representative confocal stack. The green marked KP varicosity is apposed to the blue marked GnRH cell. The VGLUT2 immunoreactivity is marked in red, but seen as orange when it is inside the KP structure. The 3D model was rotated for better viewing. The VGLUT2 IR that is visible inside the KP varicosity is marked with arrows. The same numbers across images mean the same IR.

with 0.5% hydrogen peroxide (20 min), sections were permeabilised with 0.5% Triton X-100 (23,472-9, Sigma, 20min). Finally, 2% normal horse serum was applied (20min) to reduce non-specific antibody binding. Subsequent treatments and interim rinses in PBS (3×5min) were carried out at room temperature, except for incubation in the primary antibody or fluorochrome.

C. Triple Immunofluorescence

Sections from the RP3V and pre-optic region of the virus injected KP-cre animals were incubated (72h) in a cocktail of the guinea pig anti GnRH (#1018, Hrabovszky, 1: 50,000)[18] and rabbit anti-GFP (1: 2,000, AB10145 Millipore), and either goat anti CB1([17], 1:600), or mouse anti VGLUT2 (#5504, Chemichon, 1:2000) primary antibodies. Sections from the RP3V and pre-optic region of the virus injected GAD2-cre animals were incubated (72h) in a cocktail of the guinea pig anti GnRH (#1018, Hrabovszky, 1: 50,000)[18] and rabbit anti-GFP (1: 2,000, AB10145 Millipore), and sheep anti KP (#053, Alain Caraty, 1:10000). For the kisspeptin afferents, GnRH immunoreactivity was visualised with CY5-conjugated donkey anti-guinea pig IgG (#706-175-148, Jackson ImmunoResearch Laboratories, 1: 2,000, 2h). To visualise the KP-IR structures, the sections were incubated in FITC-conjugated donkey anti-rabbit (#711-095-152, Jackson ImmunoResearch Laboratories, 1: 1,000, 2 h). To visualise the CB1-IR structures, the sections were incubated in CY3-conjugated donkey anti-goat (#706-165-147, Jackson ImmunoResearch Laboratories, 1: 2,000, 2 h). VGLUT2 IR was visualized with CY3-conjugated donkey anti-mouse (#715-165-151, Jackson ImmunoResearch Laboratories, 1: 3,000, 2 h). The virus labelled GAD65 was visualized with FITC-conjugated donkey anti-rabbit (#711-095-152, Jackson ImmunoResearch Laboratories, 1: 1,000, 2 h).

D. Confocal Laser Analysis and 3-D Reconstruction of GnRH-IR Afferents

The triple-labelled sections were analysed using a Nikon A1R confocal microscope (Nikon, Japan). Multiple stacks of optical slices (1024×1024 pixels, z-steps $0.15\mu m$) were obtained by scanning all of the KP-IR neurons unilaterally in each of the selected coronal sections using a $60\times$ oil immersion objective. The FITC, CY3, and CY5 fluorochromes were detected with laser lines 488nm, 561nm, and 641nm laser excitation. The separately recorded green, red and the artificially blue coloured far red channels were merged and displayed with the ImageJ software [19] running on an IBM-compatible personal computer. The images acquired with the confocal laser microscope were further investigated using three dimensional (3D) analyses. The stack of optical slices were loaded into the visualisation software Amira (6.0, Visual Imaging Group) and the three channels containing images of consecutive optical slices were deconvolved with the built in deconvolution module, then rendered in three dimensions with surfaces generated from above threshold immunoreacitvity. The threshold was set individually for each image and colour channel to minimise any noise, while maintaining the proper cellular boundaries. The surfaces generated from the three channels in the same optical volume were visualised to check for cell-to-cell contacts, and the presence of CB1 receptor immunoreactivity. This enabled verification of the findings from the two dimensional confocal image analyses.

E. Quantitative analysis

Optical slices were analyzed to obtain a quantitative estimate about the extent of CB1/VGLUT2/GAD65 positive KP varicosities in apposition to GnRH cell bodies or processes. Representative photomicrographs were taken from regions in

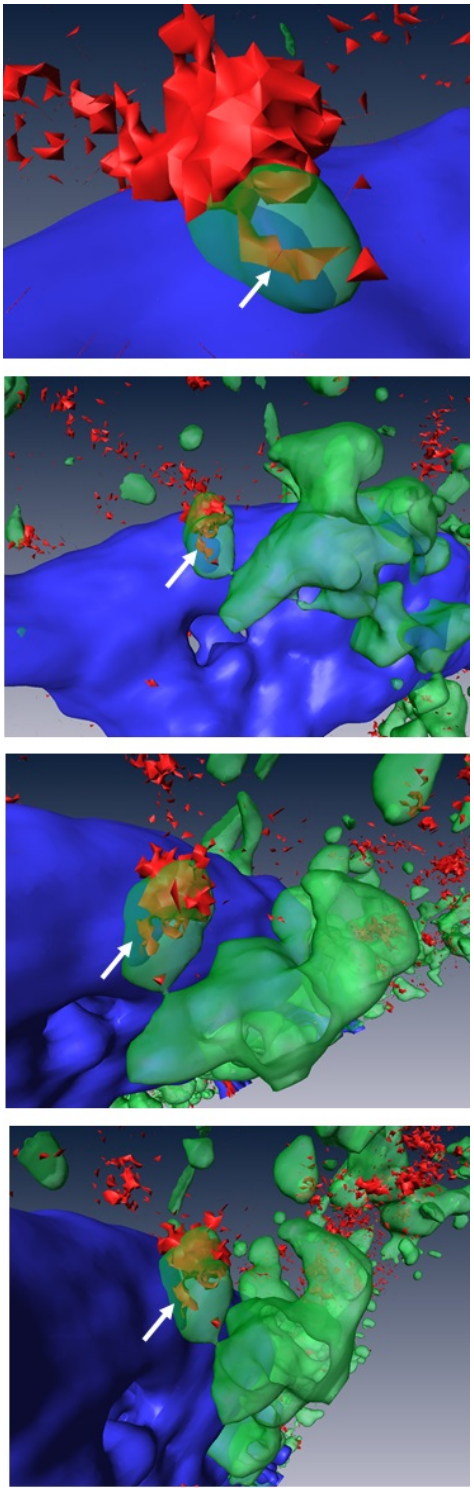

Fig. 2. 3D reconstruction of the representative stack. The blue marked GnRH cell receives GAD65 (marked in green) appositions. The GAD65 processes were made transparent to show the KP immunoreactivity inside (visible in orange as in Fig1). The 3D model is rotated for better visibility. The KP IR that is visible inside the GAD65 varicosity is marked with arrows. The same numbers across images mean the same IR from different directions.

the pre-optic area and OVLT, where GnRH neuron cell bodies can be found. Results were expressed as percentages of the CB1/VGLUT2/GAD65 positive varicosities.

III. Results

The presence of cannabinoid receptor in the afferent terminal is necessary for the retrograde signalling pathway that inhibits synaptic input via releasing endocannabinoids that are detected by the CB1 receptors on the afferent terminal membrane. [10,11] First, I have tried triple labelling immunohistochemistry to visualize CB1 in the KP afferents of GnRH cells with labelling the kisspeptin directly, and was able to show KP immunoreactive terminals in close apposition to GnRH that showed CB1 labelling. However, we did find this approach suboptimal, since the KP does not fill the whole anatomical structure, because in the processes or terminals KP is packed into dense core vesicles trafficking, or waiting to be released in the terminal. The CB1 is a membrane receptor, it is expected mainly in the membrane, but with the direct KP labelling, only the kisspeptin containing parts of the cell can be visualised. To overcome this problem, I used the virus construct to enable labelling the plasma membrane. The channel rhodopsin encoded by this virus is also a membrane protein, and it directs the YFP to the membrane, thus making the whole cell visible. With this method, it can be decided if the visible CB1 signal is part of the KP varicosity or not, and also the KP afferent's classical neurotransmitter content can be determined. The quantitative analyses showed 70% of KP fibres in apposition to GnRH perikarya from 33 total contacts, and 59% of KP fibres in apposition to GnRH processes to be immunoreactive for CB1 out of 154 total contacts. 52% of the counted 29 KP-IR fibres in apposition to GnRH perikarya, and 47% of the counted 107 KP-IR fibres in apposition to GnRH processes were found immunoreactive for VGLUT2. 31% of the counted 13 GAD65-IR fibres in connection with GnRH perikarya, and 40% of the counted 70 GAD65-IR fibres in apposition to GnRH processes were identified as GAD65-positive axons. It still remains to be seen, whether the GABA- or glutamatergic KP afferents of the GnRH cells are expressing CB1 receptors.

Acknowledgements

The project was founded by National Science Foundation of Hungary K101326, K115984 grant.

References

[1] Li XF, Kinsey-Jones JS, Cheng Y, Knox AM, Lin Y, Petrou NA, Roseweir A, Lightman SL, Milligan SR, Millar RP, O'Byrne KT: *Kisspeptin signalling in the hypothalamic arcuate nucleus regulates GnRH pulse generator frequency in the rat.*, PLoS One 2009; 4:e8334.

[2] Kinoshita M, Tsukamura H, Adachi S, Matsui H, Uenoyama Y, Iwata K, Yamada S, Inoue K, Ohtaki T, Matsumoto H, Maeda K: *Involvement of central metastin in the regulation of preovulatory luteinizing hormone surge and estrous cyclicity in female rats.*, Endocrinology 2005; 146: 4431–4436.

[3] Adachi S, Yamada S, Takatsu Y, Matsui H, Kinoshita M, Takase K, Sugiura H, Ohtaki T, Matsumoto H, Uenoyama Y, Tsukamura H, Inoue K, Maeda K: *Involvement of anteroventral periventricular metastin/kisspeptin neurons in estrogen positive feedback action on luteinizing hormone release in female rats.* J Reprod Dev 2007; 53: 367–378.

[4] Clarkson J, d'Anglemont de Tassigny X, Moreno AS, Colledge WH, Herbison AE: *Kisspeptin-GPR54 signaling is essential for preovulatory gonadotropin-releasing hormone neuron activation and the luteinizing hormone surge.* J Neurosci 2008; 28: 8691–8697.

[5] Roseweir AK, Kauffman AS, Smith JT, Guerriero KA, Morgan K, Pielecka-Fortuna J, Pineda R, Gottsch ML, Tena-Sempere M, Moenter SM, Terasawa E, Clarke IJ, Steiner RA, Millar RP: *Discovery of potent kisspeptin antagonists delineate physiological mechanisms of gonadotropin regulation.* J Neurosci 2009; 29: 3920–3929.

[6] Pineda R, Garcia-Galiano D, Roseweir A, Romero M, Sanchez-Garrido MA, Ruiz-Pino F, Morgan K, Pinilla L, Millar RP, Tena-Sempere M: *Critical roles of kisspeptins in female puberty and preovulatory gonadotropin surges as revealed by a novel antagonist.* Endocrinology 2010; 151: 722–730.

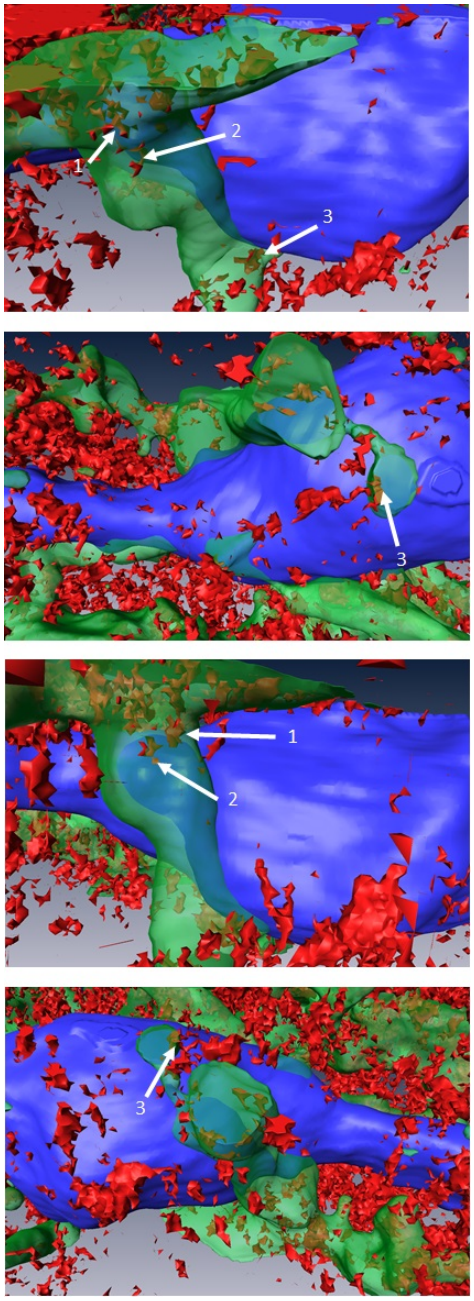

Fig. 3. 3D reconstruction of representative confocal stack. The green marked KP varicosity is apposed to the blue marked GnRH cell. The KP processes were made transparent to show the CB1 immunoreactivity inside (visible in orange as in Fig1). The 3D model rotated. The CB1 IR that is visible inside the KP varicosity is marked with arrows. The same numbers across images mean the same IR.

[7] Uenoyama Y, Nakamura S, Hayakawa Y, Ikegami K, Watanabe Y, Deura C, Minabe S, Tomikawa J, Goto T, Ieda N, Inoue N, Sanbo M, Tamura C, Hirabayashi M, Maeda KI, Tsukamura H.: *Lack of pulse and surge modes and glutamatergic stimulation of luteinising hormone release in Kiss1 knockout rats.*, Neuroendocrinology 2015;98:187-197

[8] A. S. Kauffman, J. T. Smith: *Kisspeptin Signaling in Reproductive Biology* Springer Science+Business Media, ISBN 978-1-4614-6198-2

[9] Kalló I, Vida B, Bardóczi Z, Szilvásy-Szabó A, Rabi F, Molnár T, Farkas I, Caraty A, Mikkelsen J, Coen CW, Hrabovszky E, Liposits Z.: *Gonadotropin-Releasing Hormone Neurones Innervate Kisspeptin Neurones in the Female Mouse Brain*, Neuroendocrinology 2013;98:281-289

[10] Farkas I., Kalló I., Deli L., Vida B., Hrabovszky E., Fekete C., Moenter S. M., Watanabe M., Liposits Zs.: *Retrograde endocannabinoid signaling reduces GABAergic synaptic transmission to gonadotropin-releasing hormone neurons* Endocrinology. 151(12):5818-5829.

[11] Glanowska K. M., Moenter S. M.: *Endocannabinoids and prostaglandins both contribute to GnRH neuron-GABAergic afferent local feedback circuits* J Neurophysiol. 106(6):3073-81.

[12] Liu X, Porteous R, d'Anglemont de Tassigny X, Colledge WH, Millar R, Petersen SL, Herbison AE.: *Frequency-dependent recruitment of fast amino acid and slow neuropeptide neurotransmitter release controls gonadotropin-releasing hormone neuron excitability.*, J Neurosci 2011;31:2421-2430

[13] Gottsch ML, Popa SM, Lawhorn JK, Qiu J, Tonsfeldt KJ, Bosch MA, Kelly MJ, Ronnekleiv OK, Sanz E, McKnight GS, Clifton DK, Palmiter RD, Steiner RA.: *Molecular properties of Kiss1 neurons in the arcuate nucleus of the mouse.*, Endocrinology 2011;152:4298–4309

[14] Navarro VM, Gottsch ML, Wu M, García-Galiano D, Hobbs SJ, Bosch MA, Pinilla L, Clifton DK, Dearth A, Ronnekleiv OK, Braun RE, Palmiter RD, Tena-Sempere M, Alreja M, Steiner RA.: *Regulation of NKB pathways and their roles in the control of Kiss1 neurons in the arcuate nucleus of the male mouse.*, Endocrinology 2011;152:4265–4275

[15] Popa SM, Moriyama RM, Caligioni CS, Yang JJ, Cho CM, Concepcion TL, Oakley AE, Lee IH, Sanz E, Amieux PS, Caraty A, Palmiter RD, Navarro VM, Chan YM, Seminara SB, Clifton DK, Steiner RA.: *Redundancy in Kiss1 Expression Safeguards Reproduction in the Mouse.*, Endocrinology 2013;154:2784–2794

[16] Piet R, de Croft S, Liu X, Herbison AE.: *Electrical properties of kisspeptin neurons and their regulation of GnRH neurons.*, Frontiers in Neuroendocrinology 2015;36:15-27

[17] Makara J, Katona I, Nyíri G, Nemeth B, Ledent C, Watanabe M, de Vente J, Freund T, Hájos N: *Involvement of nitric oxide in depolarization-induced suppression of inhibition in hippocampal pyramidal cells during activation of cholinergic receptors.*, 2007 J Neurosci 27:10211–10222

[18] Hrabovszky E, Molnár CS, Sipos MT, Vida B,Ciofi P, Borsay BA, Sarkadi L, Herczeg L,Bloom SR, Ghatei MA, Dhillo WS, Kalló I, Liposits Z: *Sexual dimorphism of kisspeptin and neurokinin B immunoreactive neurons in the infundibular nucleus of aged men and women.*, Front Endocrinol (Lausanne) 2011;2:80

[19] Rasband, W.S., *ImageJ*, U. S. National Institutes of Health, Bethesda, Maryland, USA, http://imagej.nih.gov/ij/, 1997-2014.

Program 3

Feasibility of Electronic and Optical Devices, Molecular and Nanotechnologies, Nano-architectures, Nanobionic Diagnostic and Therapeutic Tools

Head: Árpád CSURGAY

GPU-based image compression for multi-view microscopy data

Bálint BALÁZS[1,2]
(Supervisors: Lars HUFNAGEL[1], Balázs RÓZSA[2])
[1]European Molecular Biology Laboratory, Cell Biology and Biophysics Unit
Meyerhofstraße 1, 69117 Heidelberg, Germany
[2]Pázmány Péter Catholic University, Faculty of Information Technology and Bionics
Práter utca 50/a, 1083 Budapest, Hungary
balba@digitus.ppke.hu

***Abstract*—Multi-view light-sheet microscopy is one of the best tools to investigate early embryonic development due to its inherent optical sectioning, fast imaging speed, and low phototoxicity. Evaluating, or simply just storing the data, however, is an extremely challenging step, since each experiment can generate terabytes of data. Furthermore, this data has to be pre-processed before any evaluation step can be performed, i.e. multiple views have to be fused to create a single, high quality image.**

Here we present a fast, GPU-based image preprocessing pipeline that is capable of fusing opposing views instantly during acquisition, thus completely eliminating the need for a separate fusion step. Furthermore, the pipeline also includes a real-time image compression step to further reduce necessary storage space. Both lossless and near-lossless compressions are available, achieving up to 7 and 20-fold compression ratios, respectively. The compression filter is also implemented as an HDF5 plugin, offering compatibility for many existing applications.

***Keywords*-image processing; GPU computing; light-sheet microscopy**

I. Introduction

Imaging embryonic development over large spatial and temporal scales have always been a great desire for developmental biologists, and a great challenge for optics developers. Single-Plane Illumination Microscopy [1] provides a convenient and effective way to image such processes [2], utilizing dedicated optics for illumination which generates a light-sheet in the focal plane of the detection objective, thus providing true optical sectioning. This illumination scheme allows for fast imaging times while keeping laser exposure and thus phototoxicity to the smallest possible level [3].

Depending on the optical realization, single plane illumination microscopy is well suited for a variety of samples spanning a large scale from micrometers to even centimeters. It has been applied to image the neuronal network in whole mouse brain [4], to reconstruct the early devlopment in zebrafish embryos [5], and *Drosophila melanogaster* embryos [6], [7], and to study the early differentiation processes in the mouse embryo [8].

Because light-sheet microscopy uses a simple wide-field detection scheme, it is also possible to combine it with other imaging techniques that further improve image quality, such as RESOLFT [9], structured illumination [10], Bessel beams [11], 2-photon excitation [12], and the combination of these [13].

Despite the advantages, imaging optically opaque samples, such as the *Drosophila m.* embryo can be still challenging due to scattering effect inside the tissue, and refractive index mismatches from the mounting medium. A straightforward way to improve image quality for such samples is to record multiple views from different directions, and later stitch these views to create a single, high quality stack. This can be easily achieved by rotating the sample, however this can be already to slow for certain processes.

The recently introduced Multi-View Single-Plane Illumination Microscope [6], which was developed in our lab, together with the Simultaneous Multiview Light-sheet Microscopy [7] provide an elegant solution for multi-view imaging. These setups utilize two illumination and two detection objectives, to give altogether four different combinations of illumination and detection, *i.e.* four different views. Although this is enough to fully visualize an opaque sample, several image preprocessing steps are necessary before any evaluation can be performed to combine the four stacks to a single, high quality 3D image.

By combining scanned light-sheet [5] witch confocal slit detection on the camera chip [14], [15], one can exclude out of focus, scattered illumination light. This way it's already possible to illuminate simultaneously, which leaves us with only two views, the views of the two opposing cameras. In last year's report [16] I introduced a GPU-based image preprocessing pipeline, that is capable of fusing these opposing views in real time, which already reduces the necessary data storage by half.

II. B^{3}D image compression algorithm

In order to address the challenges presented in the previous section, in this paper we introduce a novel compression algorithm to significantly reduce data sizes already during image acquisition. The algorithm supports both lossless and near lossless modes, where the acceptable amount of loss can be specified as the function of the photon shot noise. This makes the algorithm especially suitable for scientific imaging applications, such as light-sheet microscopy.

The other motivation to develop a new algorithm was to also improve compression speed, to accomodate the use of high-speed cameras, and enable real-time compression during data acquisition. To achieve this, we built a massively parallel algorithm using the Compute Unified Device Architecture (CUDA) [17], to run the compression on a Graphics Processing Unit (GPU). Our algorithm combines the features of lossless JPEG (predictors and Huffman coding) [18] and JPEG-LS (near lossless mode) [19], and is built on the optimized image compression library, cudaCompress [20], [21].

B. BALÁZS, "GPU-based image compression for multi-view microscopy data" in *PhD Proceedings Annual Issues of the Doctoral School, Faculty of Information Technology and Bionics, Pázmány Péter Catholic University – 2016.* G. Prószéky, P. Szolgay Eds. Budapest: Pázmány University ePress, 2016, pp 149– 152.

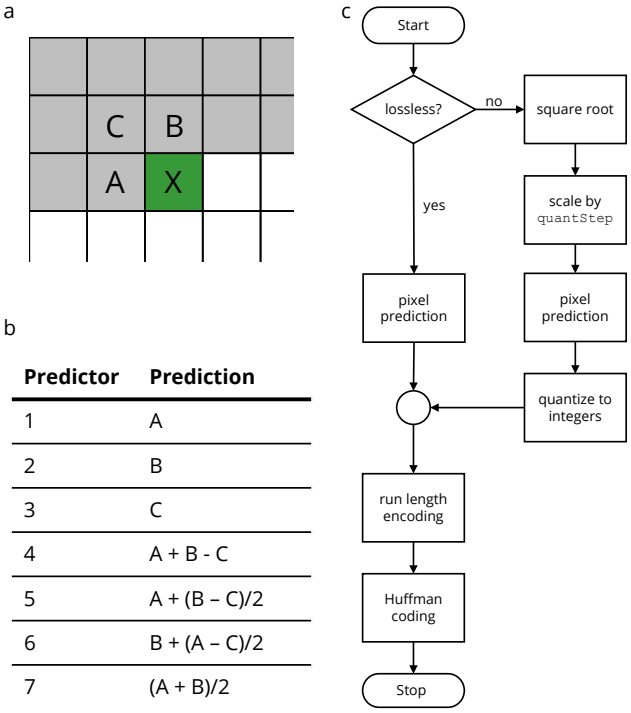

Fig. 1. Compression algorithm schematics. a) Prediction context for pixel X, the next sample to be encoded. b) Possible predictions based on the neighboring pixels. c) Complete algorithm flowchart depicting the main stages of the compression.

A. Lossless compression

To make the algorithm as fast as possible, we were willing to sacrifice on compression ratio, by omitting a few computationally intensive and/or inherently serial parts of the algorithm, such as context modeling and Golomb parameter adaptation that is included in the JPEG-LS standard. Other compression methods such as SFALIC [22] and FLIC [23] already explored these possibilities with promising results. However, these were implemented on the CPU, and while they achieved significant increase in the compression speed, it was still not enough for real-time compression of light-sheet images.

In order to effectively compress the images, the data is first decorrelated by predicting the value of each pixel based on it's neighbors (Fig. 1. a,b), and only storing the prediction error ϵ. Since most flourescence images are continuous tone, this prediction error will be relatively small compared to the original values, making it much more efficient to compress them. After the prediction run length encoding is performed followed by Huffman coding to effectively reduce the data size. Finally, the output stream from the Huffman coder is saved as the compressed file (Fig. 1. c).

B. Within noise lossless compression

In order to further push the capabilities of the compression algorithm, we also propose a near lossless, or within noise lossless (WNL) mode of operation. Usually for lossy image compression algorithms it is not possible to control the amount of information loss, because most of them include a quantization step in a transformed space (such as Fourier transform or Wavelet transform). This makes these methods incompatible with scientific imaging, where preserving data integrity is of the utmost importance. However, if the information loss is

TABLE I
COMPARISON OF B^{3}D PERFORMANCE WITH JPEG2000 AND PBZIP

algorithm	ratio	compression speed	decomp. speed
JPEG2000	8.40	6.56 MB/s	14.6 MB/s
pbzip (8 cores)	7.56	78.9 MB/s	163 MB/s
B^{3}D lossless	7.00	570 MB/s	532 MB/s
B^{3}D WNL	21.92	335 MB/s	526 MB/s

controlled in a way that it is guaranteed to be smaller than the standard deviation of the image noise, than the resulting image will be statistically equivalent to the original, uncompressed data. For a scientific complementary metal-oxide semiconductor (sCMOS) sensor, we can model the recorded intensity as a random variable X as the sum of two random variables:

$$X = X_c + X_f \tag{1}$$

where X_c is the camera noise (read noise + dark current), while X_f is the detected fluorescence. Since X_c is camera dependent, it is difficult to estimate it's parameters, except for the mean, which is just the average of dark images. For this reason, we only consider the noise arising from X_f, the fluorescence itself, which is also called the shot noise. Since this is a Poisson process, it's standard deviation is equal to the square root of its mean:

$$\sigma(X_f) = \sqrt{\mu(X_f)} \tag{2}$$

This can be estimated by subtracting the average camera dark image ($i.e.$ $\mu(X_c)$) from the original:

$$\sigma(X_f) = \sqrt{X - \mu(X_c)} \tag{3}$$

Because of this, if we quantize the square root of the images instead of the original images, by selecting an appropriate quantization step q, we can ensure that the compressed image will not differ from the original by more than the standard deviation of the shot noise.

To find q, for any pixel p_{ij}, let $I = a^2$ be the corresponding intensity. To quantize a, let's represent it in the following form:

$$a = pq + r \tag{4}$$

where $q \in \mathbb{R}^+$ is the previously mentioned quantization step, $p \in \mathbb{N}$, and $r \in [-q/2, q/2)$ is the remainder. During the quantization step, we discard the remainder, so the reconstructed intensity will be:

$$\hat{I} = (pq)^2 = (a - r)^2 \tag{5}$$

From here, the difference arising from the quantization:

$$\delta = |I - \hat{I}| = |a^2 - (a - r)^2| = |2ar - r^2| \tag{6}$$

and to satisfy our previous requirement, we have to make sure that

$$\delta = |2ar - r^2| < a \tag{7}$$

From here we can calculate, that if

$$q < 2(\sqrt{2} - 1) \approx 0.82 \tag{8}$$

then the difference δ arising from the quantization will always be smaller than the standard deviation of the shot noise.

III. Evaluation methods and results

We evaluated the algorithm by comparing it's compression ratio to a widely used lossless compression standard, JPEG2000, and a relatively new format, KLB [24], which is based on pbzip, and was specifically developed for fast compression of microscopy data. For all algorithms we measured the compression ratio $r = size_{original}/size_{compressed}$, compression speed and decompression speed on 3 different datasets (*Drosophila melanogaster*, *Danio rerio*, and *Phallusia mammilata* embryos). Speed measurements were performed in system memory to exclude hard drive overhead, and was repeated 5 times and averaged to get a robust reading (Table I.).

In the lossless mode although the compression ratio slightly decreased compared to both JPEG2000 and pbzip (7.0 vs. 8.4 and 7.56 respectively), the massive increase in compression speed (570 MB/s vs. 6.56 MB/s and 78.9 MB/s) makes this algorithm superior for high-speed microscopy applications. In the case of WNL mode the compression ratio massively increases to 21.92, while still maintaining a considerable advantage in the compression speed. Although theoretically in this case the compressed images will not be exactly equal to the original ones, in practical terms the difference is negligible (Fig. 2.).

To further evaluate the effects of the WNL compression we compared the segmentation results of uncompressed and compressed images. In order to do this we imaged a *Drosophila melanogaster* embryo in the cellularization phase exhibiting an H2Av-mCherry fluorescent marker every 10 seconds 5 times. Since this is such a short timeframe, the biological processes can be considered stationary, and the same biologically relevant information can be obtained from all 5 of these stacks. In this scenario, the only differences can be resulting from the shot noise between each stack.

We compressed all stacks, and trained the interactive image segmentation tool ilastik [25] on the first original stack (O1) and segmented the nuclei in all of the stacks.

To measure the segmentation overlap of different stacks, we used MATLAB [26] to calculate the Sørensen–Dice coefficient [27], [28] for all stack pairs:

$$QS = \frac{2|A \cap B|}{|A| + |B|} \tag{9}$$

where A and B are segmented regions from two different stacks. QS is the quotient of similarity which ranges from 0 (no overlap) to 1 (perfect overlap). The results are show in a heatmap in Fig. 3.

As expected for the original stacks (O1–O5) the Sørensen–Dice coefficient is very high, ranging from 0.93 to 0.96, however for any original stack and it's compressed counterpart it's even higher, averaging 0.996, which means that the compression has actually less effect on the segmentation than imaging the same stack a few seconds later.

IV. Conclusions

As light-sheet microscopy continues to advance, data storage and even just data visualization is becoming a bigger and bigger challenge [29]. In this paper we introduced a novel compression algorithm, B^{3}D , which is capable of addressing this problem by effectively compressing the images during acquisition by utilizing the parallel architecture of the modern GPU. It can compress data more than 80 times faster than JPEG2000, and using the within noise lossless mode it can reduce image sizes by more than a factor of 20.

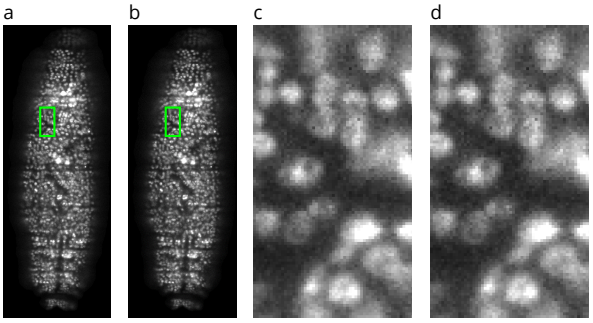

Fig. 2. A representative comparison of an original and a compressed image. a) Original image, b) Compressed image, c) Original image zoomed in to the region show in a), d) Compressed image zoomed in to the region show in b)

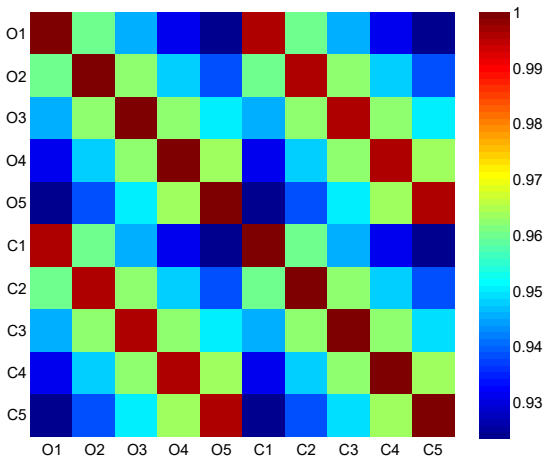

Fig. 3. Comparing segmentation results for the same stack imaged 5 times at 10 s intervals(O1-O5), and their near lossless compressed counterparts (C1-C5). The automatic segmentation was trained on the first original stack, O1, and applied to all 10 stacks. The heatmap shows the overlap of different segmentations, calculated by the Sørensen–Dice coefficient.

We included the B^{3}D compression to our already existing GPU-based real-time image preprocessing pipeline (Fig. 4.) and combined with live fusion and background masking we achieved more than a factor of 40 data reduction, while keeping the biologically relevant information intact. This not only reduces the necessary amount of storage (180 GB vs 7.5 TB per experiment), but also reduces processing time, since data transfer to different processing machines is also dramatically reduced.

We also implemented the compression algorithm as a plugin for HDF5 [30] to make is easily accessible from several different image processing and image visualization environments. HDF5 is already supported by MATLAB, Fiji, LabVIEW, Python, ilastik, and more software, which greatly facilitates adopting this format in wider use.

Acknowledgments

This research was funded by the EMBL International PhD Programme. Special thanks to Marvin Albert, Gustavo de Medeiros, Nils Norlin and Dimitri Kromm.

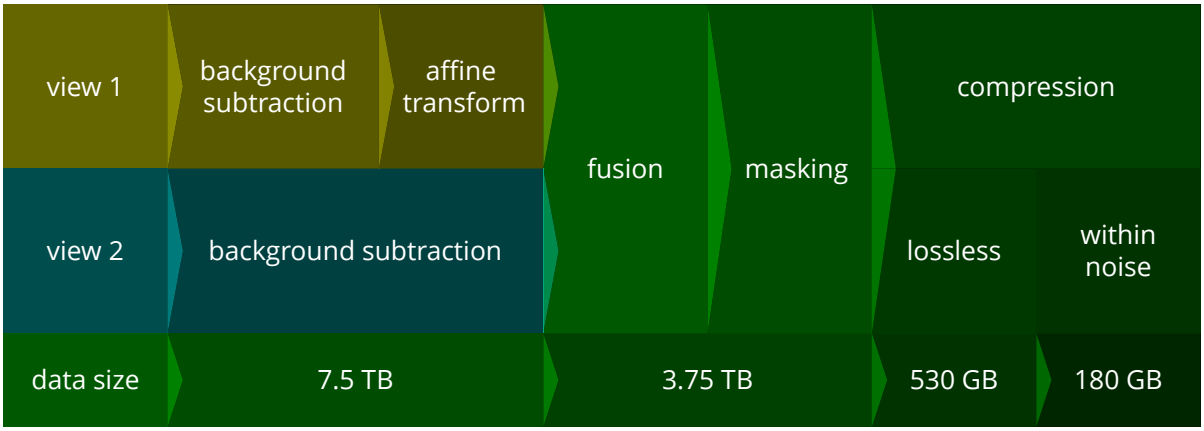

Fig. 4. Real-time image processing pipeline, showing the data reduction after each step. First the average camera background is subtracted from both views, then the images are fused with a weighted average (1:2 reduction). The images are then masked, and the background pixels are set to 0. Finally, the images are compressed either lossless to achieve a further 1:7 reduction, or allowing some compression differences while staying under the shot noise level. Altogether the data size can be massively reduced to 1:40 of its original size.

References

[1] J. Huisken, J. Swoger, F. Del Bene, J. Wittbrodt, and E. H. K. Stelzer, "Optical Sectioning Deep Inside Live Embryos by Selective Plane Illumination Microscopy," *Science*, vol. 305, no. 5686, pp. 1007–1009, 2004.

[2] M. Weber and J. Huisken, "Light sheet microscopy for real-time developmental biology," *Current Opinion in Genetics & Development*, vol. 21, no. 5, pp. 566–572, 2011.

[3] E. G. Reynaud, U. Kržič, K. Greger, and E. H. Stelzer, "Light sheet-based fluorescence microscopy: more dimensions, more photons, and less photodamage," *HFSP Journal*, vol. 2, no. 5, pp. 266–275, Oct. 2008.

[4] H.-U. Dodt, U. Leischner, A. Schierloh, N. Jährling, C. P. Mauch, K. Deininger, J. M. Deussing, M. Eder, W. Zieglgänsberger, and K. Becker, "Ultramicroscopy: three-dimensional visualization of neuronal networks in the whole mouse brain," *Nature Methods*, vol. 4, no. 4, pp. 331–336, Mar. 2007.

[5] P. J. Keller, A. D. Schmidt, J. Wittbrodt, and E. H. K. Stelzer, "Reconstruction of Zebrafish Early Embryonic Development by Scanned Light Sheet Microscopy," *Science*, vol. 322, no. 5904, pp. 1065–1069, Nov. 2008.

[6] U. Krzic, S. Gunther, T. E. Saunders, S. J. Streichan, and L. Hufnagel, "Multiview light-sheet microscope for rapid in toto imaging," *Nature Methods*, vol. 9, no. 7, pp. 730–733, Jul. 2012.

[7] R. Tomer, K. Khairy, F. Amat, and P. J. Keller, "Quantitative high-speed imaging of entire developing embryos with simultaneous multiview light-sheet microscopy," *Nature Methods*, vol. 9, no. 7, pp. 755–763, Jul. 2012.

[8] P. Strnad, S. Gunther, J. Reichmann, U. Krzic, B. Balazs, G. de Medeiros, N. Norlin, T. Hiiragi, L. Hufnagel, and J. Ellenberg, "Inverted light-sheet microscope for imaging mouse pre-implantation development," *Nature Methods*, vol. advance online publication, Dec. 2015.

[9] P. Hoyer, G. d. Medeiros, B. Balázs, N. Norlin, C. Besir, J. Hanne, H.-G. Kräusslich, J. Engelhardt, S. J. Sahl, S. W. Hell, and L. Hufnagel, "Breaking the diffraction limit of light-sheet fluorescence microscopy by RESOLFT," *Proceedings of the National Academy of Sciences*, vol. 113, no. 13, pp. 3442–3446, Mar. 2016.

[10] P. J. Keller, A. D. Schmidt, A. Santella, K. Khairy, Z. Bao, J. Wittbrodt, and E. H. K. Stelzer, "Fast, high-contrast imaging of animal development with scanned light sheet-based structured-illumination microscopy," *Nature Methods*, vol. 7, no. 8, pp. 637–642, Aug. 2010, light-sheet structured illumination.

[11] T. A. Planchon, L. Gao, D. E. Milkie, M. W. Davidson, J. A. Galbraith, C. G. Galbraith, and E. Betzig, "Rapid three-dimensional isotropic imaging of living cells using Bessel beam plane illumination," *Nature Methods*, vol. 8, no. 5, pp. 417–423, May 2011.

[12] T. V. Truong, W. Supatto, D. S. Koos, J. M. Choi, and S. E. Fraser, "Deep and fast live imaging with two-photon scanned light-sheet microscopy," *Nature Methods*, vol. 8, no. 9, pp. 757–760, Sep. 2011.

[13] B.-C. Chen, W. R. Legant, K. Wang, L. Shao, D. E. Milkie, M. W. Davidson, C. Janetopoulos, X. S. Wu, J. A. Hammer, Z. Liu, B. P. English, Y. Mimori-Kiyosue, D. P. Romero, A. T. Ritter, J. Lippincott-Schwartz, L. Fritz-Laylin, R. D. Mullins, D. M. Mitchell, J. N. Bembenek, A.-C. Reymann, R. Böhme, S. W. Grill, J. T. Wang, G. Seydoux, U. S. Tulu, D. P. Kiehart, and E. Betzig, "Lattice light-sheet microscopy: Imaging molecules to embryos at high spatiotemporal resolution," *Science*, vol. 346, no. 6208, p. 1257998, Oct. 2014.

[14] E. Baumgart and U. Kubitscheck, "Scanned light sheet microscopy with confocal slit detection," *Optics Express*, vol. 20, no. 19, pp. 21 805–21 814, 2012.

[15] G. de Medeiros, N. Norlin, S. Gunther, M. Albert, L. Panavaite, U.-M. Fiuza, F. Peri, T. Hiiragi, U. Krzic, and L. Hufnagel, "Confocal multiview light-sheet microscopy," *Nature Communications*, vol. 6, p. 8881, Nov. 2015.

[16] B. Balázs, "GPU-based live fusion of multi-view microscopy data," in *PhD Proceedings*. Budapest: Pázmány University ePress, Jun. 2015.

[17] J. Nickolls, I. Buck, M. Garland, and K. Skadron, "Scalable Parallel Programming with CUDA," *Queue*, vol. 6, no. 2, pp. 40–53, Mar. 2008.

[18] W. B. Pennebaker and J. L. Mitchell, *JPEG: Still Image Data Compression Standard*. Springer Science & Business Media, Dec. 1992.

[19] M. Weinberger, G. Seroussi, and G. Sapiro, "The LOCO-I lossless image compression algorithm: principles and standardization into JPEG-LS," *IEEE Transactions on Image Processing*, vol. 9, no. 8, pp. 1309–1324, Aug. 2000.

[20] M. Treib, F. Reichl, S. Auer, and R. Westermann, "Interactive Editing of GigaSample Terrain Fields," *Computer Graphics Forum*, vol. 31, no. 2pt2, pp. 383–392, May 2012.

[21] M. Treib, K. Burger, F. Reichl, C. Meneveau, A. Szalay, and R. Westermann, "Turbulence Visualization at the Terascale on Desktop PCs," *IEEE Transactions on Visualization and Computer Graphics*, vol. 18, no. 12, pp. 2169–2177, Dec. 2012.

[22] R. Starosolski, "Simple fast and adaptive lossless image compression algorithm," *Software: Practice and Experience*, vol. 37, no. 1, pp. 65–91, Jan. 2007.

[23] Z. Wang, M. Klaiber, Y. Gera, S. Simon, and T. Richter, "Fast lossless image compression with 2d Golomb parameter adaptation based on JPEG-LS," in *Signal Processing Conference (EUSIPCO), 2012 Proceedings of the 20th European*, Aug. 2012, pp. 1920–1924.

[24] F. Amat, B. Höckendorf, Y. Wan, W. C. Lemon, K. McDole, and P. J. Keller, "Efficient processing and analysis of large-scale light-sheet microscopy data," *Nature Protocols*, vol. 10, no. 11, pp. 1679–1696, Nov. 2015.

[25] C. Sommer, C. Straehle, U. Köthe, and F. A. Hamprecht, "Ilastik: Interactive learning and segmentation toolkit," in *2011 IEEE International Symposium on Biomedical Imaging: From Nano to Macro*, Mar. 2011, pp. 230–233.

[26] MATLAB, *R2016a*. Natick, Massachusetts: The MathWorks Inc., 2016.

[27] T. J. Sørensen, *A method of establishing groups of equal amplitude in plant sociology based on similarity of species content and its application to analyses of the vegetation on Danish commons.* København: I kommission hos E. Munksgaard, 1948.

[28] L. R. Dice, "Measures of the Amount of Ecologic Association Between Species," *Ecology*, vol. 26, no. 3, pp. 297–302, Jul. 1945.

[29] J. M. Perkel, "The struggle with image glut," *Nature*, vol. 533, no. 7601, pp. 131–132, Apr. 2016.

[30] The HDF Group, "Hierarchical Data Format, version 5," 1997. [Online]. Available: http://www.hdfgroup.org/HDF5/

Correlation-based scan conversion of ultrasound images

Gergely CSÁNY
(Supervisor: Miklós GYÖNGY PhD)
Pázmány Péter Catholic University, Faculty of Information Technology and Bionics
50/a Práter street, 1083 Budapest, Hungary
csany.gergely@itk.ppke.hu

***Abstract*—Ultrasound imaging generally relies on *scan conversion*, that is, converting sets of 1D data into 2D or 3D images, which requires knowledge of the relative position of these 1D data. Following a brief review of scan conversion techniques, the so-called data-based scan conversion is presented, which in the current context relies on measuring decorrelation between 1D data. The current work shows our efforst in characterizing this decorrelation for a spherically focussed single element transducer. The results show opportunities for obtaining the calibration curve without using specific and complex phantoms.**

***Keywords*-ultrasound; correlation; decorrelation; scan conversion**

I. Introduction

Ultrasound images are generally obtained from 1D lines of ultrasonic signals. In the pulse-echo technique, a mechanical (sound) wave pulse is sent from a transducer; this pulse propagates through the examined media of and gets reflected and/or refracted at the boundaries of media with different acoustic impedances. Inhomogenities of a medium that cause scattering of the sound wave are called scatterers. The receiving transducer (which can be identical to the transmitting transducer) collects information in a certain direction – along a 1D line – by measuring amplitude changes of pressure in time, thus collecting information of the received reflected or scattered pressure waves along that certain line. These temporal signals in t can be converted into a spatial signal in z using the equation $z = ct/2$, where c is the assumed speed of sound. By the technique of envelope detection, biphasic raw A-line signals can also be converted and represented as a 1D series of image pixels in which color or intensity (in case of a gray-scale representation) of a pixel corresponds to the enveloped amplitude of the backscattered signal (and thus to the strength of scattering in that certain point in space, which point is calculated from time and sound speed as described previously). In order to get a 2D image, several A-line envelopes (created in the above described way) should be put beside each other considering their spacial dispositions relative to each other. 3D images are usually created in a similar way from 2D images (in this case, 2D images are put side by side with proper spatial positioning).

As can be seen from the above description, 2D or 3D ultrasound imaging requires a sequence of lower dimensional data with known relative positions to be placed alongside each other. This process is termed scan conversion, and requires the ultrasound system to acquire data (or scan) in different directions. Currently used scanning methods can be summarized in the following groups [1]:

1) Electronic scanning,
2) Mechanical scanning,
3) Free-hand scanning with position sensors,
4) Free-hand scanning without position sensors.

A. Scanning methods for ultrasound imaging

The following is a review of different scanning methods for ultrasound imaging. For further information, the reader is referred to [1], [2].

1) Electronic scanning: Image dimension can be incremented without any movement when using a multiple element transducer. In the case of a 'linear array transducer', multiple transducer elements are arranged along a line. The beam of these multi-element transducers can be focused in several directions along a plane. In a similar way, the focus of the transducer can be varied using different delay profiles before signal summation in the receive mode – in this way, multiple axial scans (A-lines) can be collected in the lateral direction.

Considering the case of transducer elements being placed on a plane, 3D images can be scanned electronically in a similar way (by varying the delay profile on the 2D array of elements).

The great advantage of electronic scanning is that it is a real-time method for multidimensional scanning with precisely known information of the spacing of scans and without any physical movement needed. However, array transducers require complex electronics and multiple transducer elements, hence they are not cost-effective [1].

2) Mechanical scanning: A widely used approach for incrementing image dimension is to move a transducer physically in a direction in which dimension increment is desired. However, in order to avoid distortion it is necessary to know the relative location and orientation of the single (lower-dimensional) scans are necessary to know. Mechanical scanning techniques use a motorized mechanical apparatus to physically move a transducer with precisely known location and orientation [1].

Linear mechanical scanners move a transducer along a line in order to acquire a series of parallel images. Besides its spatial precision, this method has the advantage of collecting images with equal spacing, thus a smooth resolution can be obtained. As a disadvantage, a mechanical scanner apparatus is a bulky device, hence it is not very convenient to use [1].

Another commonly used approach is to tilt a transducer, obtaining fan-like images with equal angular spacing [1]. Tilt scanners are convenient to use and not bulky (as compared to the linear scanner devices), but have the disadvantage of uneven resolution in different depths [1].

A third possible technique is rotational scanning in the case of 3D imaging. In this method, rotation is performed along the axial axis. Rotational scanning has similar advantages and disadvantages to tilt scanning, having the disadvantages of a more complex resolution distribution and also a risk of

G. CSÁNY, "Correlation-based scan conversion of ultrasound images" in *PhD Proceedings Annual Issues of the Doctoral School, Faculty of Information Technology and Bionics, Pázmány Péter Catholic University – 2016.* G. Prószéky, P. Szolgay Eds. Budapest: Pázmány University ePress, 2016, pp 153–156.

having artefacts based on possible motion of axis of rotation in addition [1].

In summary, mechanical scanning has the advantage of precise position determination and fast reconstruction time [1], but also has the general disadvantages of potential failure of the motorized system and of physical limitations of the area (or volume) in which scanning can be performed.

3) Free-hand scanning with position sensors: In order to get rid of the above disadvantages and limitations, free-hand scanning can be used, providing more convenience and freedom. Determination of the relative locations and orientations of single scans is achieved in most of the cases by the usage of position sensors. There are several types of sensors successfully combined with ultrasound transducers.

In the case of using acoustic sensors, (low-frequency ultra)sound is emitted from three separate locations on the transducer surface and measured by three microphones (located somewhere near the object of examination). One of the main disadvantages of this technique is that the line between the transducer and the microphones should be left free. The other one is that sound speed varies with humidity in the air [1].

Another approach uses articulated arms. In this case, relative movements are measured by potentiometers located in the joints of the arms. Larger flexibility of the arms leads to worse resolution of position sensing. However, by decreasing the length of the arms (in order to reduce flexibility) leads to another disadvantage: a reduced maximum size of scanning area or volume [1].

Probably the most successful position sensors for free-hand scanning are the magnetic sensors. These little sensors provide convenience and freedom. However, the magnetic field distortion of ferrous metals can cause artefacts when using these systems [1].

4) Free-hand scanning without position sensors: There is an interesting possibility for position estimation even without additional sensors or external devices. Speckles are common and usually artefactual features in ultrasound images. The speckle pattern evolves from interference caused by interaction of the ultrasound field and the scatterers [1]. While it is commonly treated as an artefact, speckle patterns may contain important information about the imaging system and the examined medium [3]. Data-based scan conversion, makes use of the speckle pattern of ultrasound images. The idea is based on the correlation between two parallel images or A-lines. If the images or lines are close enough to each other, the speckle pattern causes a high correlation between the images or lines. When moving away from a certain line, the calculated correlation value is decreasing even in homogeneous media, again, due to the presence of the speckle pattern. There is a specific dependence between distance and correlation, which can be described by the so-called decorrelation function (in terms of distance).

B. Data-based scan conversion approaches

In order to perform scan conversion based on correlation, an accurate calibration curve should be obtained. The term *calibration curve* refers to a function, that describes a one-to-one relation between distance and correlation. Much research focuses on the proper determination of this function. Conventional methods use a nominal decorrelation curve obtained from an (ideal) fully developed speckle [4]. The nominal decorrelation curve is stable for a certain transducer [5].

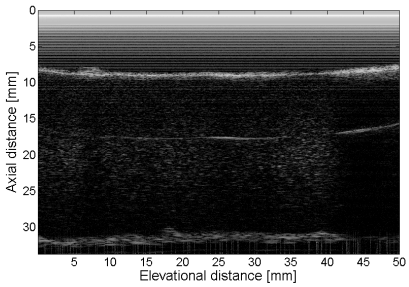

Fig. 1. B-mode ultrasound image made of a 3% agar – 4 % lead homogeneous phantom by mechanically scanning an Olympus V317 single-element transducer (with 19 mm focus). 5000 A-lines were collected with an equal 10 μm spacing.

Furthermore, several adaptive algorithms exist [6] that use an ideal phantom for obtaining the nominal decorrelation curve and then use adaptive models to get dynamic decorrelation curves [7]. There are techniques for speckle tracking without fully developed speckle using modeling of the raw ultrasound signals generated by speckles [3]. Several studies perform statistics on the image data in order to get a more suitable calibration curve (based on some statistical features of the examined object and the signals generated by the imaging system). It has been shown that estimation of the envelope statistics allows characterization of tissue regularity and thus estimation of the calibration curve [5].

II. Materials and Methods

A. Experimental setup

For investigation of data-based 1D to 2D scan conversion, experiments as well as simulations we collected experimental and simulated data from a spherically focused single element transducer with 20 MHz center frequency. Olympus V317 transducers were used with f# = 3, 6.3 mm aperture, 20 MHz central frequency and 10 MHz –6 dB bandwidth. This type of transducer has a (geometrical) focus at 19 mm (from transducer surface).

An experimental setup was built using a precision mechanical motion system from Thorlabs. During experiments, the transducer was scanned mechanically along a line being perpendicular to the axial direction. In this way, several thousands of adjacent A-lines were collected with an equal (and precisely known) 10 μm spacing. See Fig. 1 for an illustration.

B. Simulations

Simulations were performed using the Field II software (which is capable of calculating the ultrasound image response for arbitrary transducer geometries and scattering fields) [8].

Parameters of the Olympus V317 transducer (which are described in the previous subsection) were used for the simulations. As for the related experiments, several thousands of parallel A-lines with equal 10 μm spacing were collected and stored in each simulation of a homogeneous phantom.

Before creating homogeneous computer phantoms, the size of the (2D) resolution cell of the transducer was determined from simulations. A single scatterer was placed at the focus of the transducer. The response to this single scatterer gave the point spread function (PSF) of the transducer. The resolution cell was defined as the smallest 2D spatial region which contains the part of the enveloped (2D) PSF for which

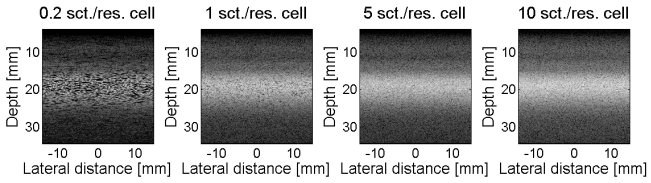

Fig. 2. Resulting B-mode images (with 60 dB dynamic range) of homogeneous phantoms with 0.2, 1, 5 and 10 scatterers/resolution cell densities, respectively. The simulated imaging system was a single element Olympus V317 transducer moved along the lateral dimension, collecting A-lines with an equal 10 μm spacing.

amplitude was greater than –6 dB. For the simulations, the resolution cell of the transducer was determined to have 84.7 μm and 210 μm sizes in the axial and lateral (or elevational) directions, respectively. 30 mm $\times$ 30 mm quasi-homogeneous phantoms were simulated with 0.2, 1, 5 and 10 randomly placed scatterers per resolution cell (Fig. 2).

In order to assess our ability to predict the calibration curve from a limited number of scatterers, a series of simulations were also performed with scatterers being placed along an axial line near the transducer focus. Odd numbers of single scatterers were placed with an equal spacing centered around the focus, with 1 to 35 scatterers with 1 mm spacing, and 1 to 69 scatterers with 500 μm spacing.

C. Calibration curve calculation

Calibration curves were obtained by calculating a modified Pearson's correlation coefficient between pairs of raw A-lines. Multiple decorrelation curves were calculated, each showing the correlations between a certain reference A-line and a series of the following (adjacent) A-lines (in one direction). The length of these decorrelation curves (the distance between the reference line and the farthest line to be considered) was set to 600 μm – as an empirically chosen distance being long enough for reaching (roughly) zero correlation.

After the decorrelation curves were calculated for every possible reference line, the calibration curve was obtained as the mean of these lines.

Calibration curves were also normalized – in order to get correlation (absolute) values between 0 and 1. Taking into account that the highest value of these curves should be the first value (which should be normalized to 1), normalization is simply done by dividing the curve by its first value.

In cases where a significant amount of noise was present that affected the beginning of the calibration curve, division was done by the second value – as the drop from the first to the second value of a decorrelation curve generally refers to the content of noise [9] – (and the first value was set to 0) when performing normalization.

III. Results

Calibration curves were calculated (in the way described in Subsection II/C) for homogeneous phantoms with all four types of scatterer densities (0.2, 1, 5 and 10 scatterers/resolution cell). For all four phantoms, some noise according to 60 dB, 40 dB, 20 dB and 0 dB signal-to-noise ratio (SNR) values were added. Thus, calibration curves were calculated for 16 phantoms with different scatterer densities and different SNR. The results showed practically equal calibration curves, for all of these cases (see Fig. 3 and Table I, the

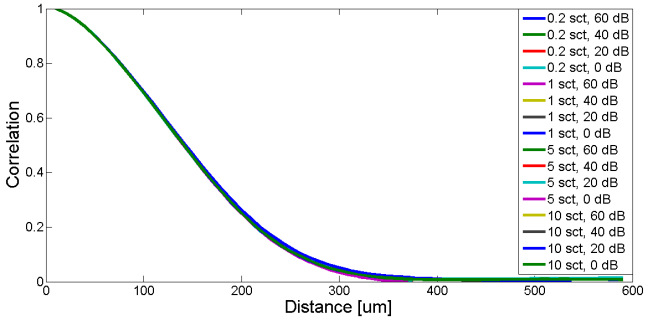

Fig. 3. Calibration curves obtained for simulated homogeneous phantoms of all combinations of 0.2, 1, 5, 10 scatterers/resolution cell densities and 60 dB, 40 dB, 20 dB, 0 dB SNR. Results show a great and significant correlation between all of these curves.

TABLE I
NRMSE between calibration curves of homogeneous phantoms (with different densities of scatterers; SNR = 60 dB)

sct./res. cell	0.2	1	5
0.2	0	0.0072	0.0142
1	0.0072	0	0.0118
5	0.0142	0.0118	0

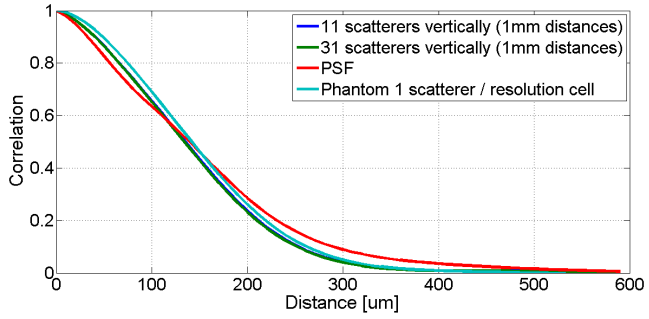

Fig. 4. Calibration curves calculated for PSF, 11 scatterers and 31 scatterers around transducer focus (along an axial line) and for a homogeneous phantom with 1 scatterer/resolution cell density.

TABLE II
NRMSE between calibration curves of homogeneous phantoms and of several scatterers (around transducer focus)

	PSF	11 scatterers	31 scatterers
0.2 sct./res. cell	0.0350	0.0116	0.0184
1 sct./res. cell	0.0343	0.0122	0.0209
5 sct./res. cell	0.0420	0.0173	0.0193

latter showing normalized root-mean-square errors (NRMSE) calculated for pairwise calibration curves in order to quantify their similarity).

Calibration curves were also calculated for PSF and for images of scatterers placed around the focal point with an equal (1 mm) spacing, axially. In Fig. 4 calibration curves calculated for PSF, 11 scatterers and 31 scatterers (along a line) are compared with the calibration curve calculated for homogeneous phantoms (in this case, the curve for phantom with 1 scatterer/resolution cell is present). Table II shows the normalized root-mean-square errors calculated pairwise for calibration curves of different scattering conditions.

As can be seen in NRMSE values (Table II), the calibration curve of 11 individual scatterers is closer to all homogeneous

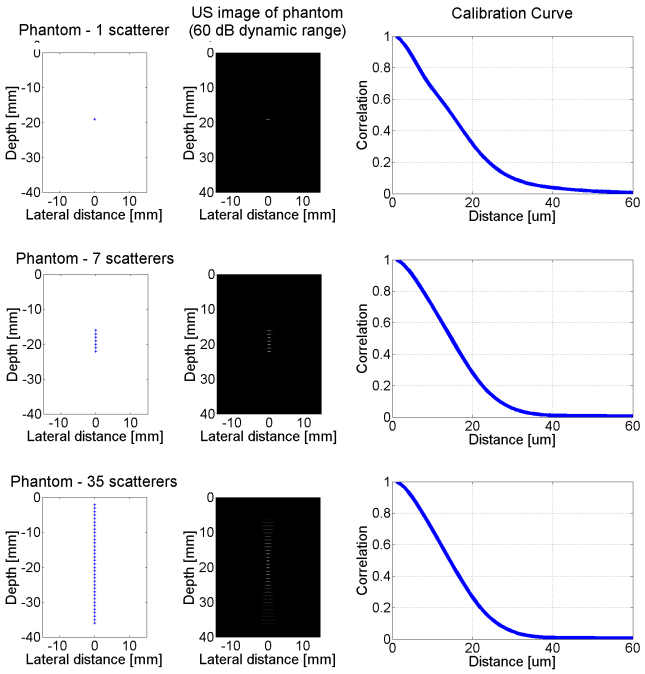

Fig. 5. Scatterer positions, simulated B-mode images and calibrated curves for 1, 7 and 35 individual scatterers (placed around transducer focus with an equal 1 mm axial spacing).

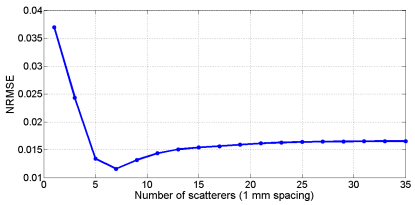

Fig. 6. Normalized root-mean-square error between calibration curves for different (odd) numbers of individual scatterers placed around transducer focus with an equal 1 mm axial spacing.

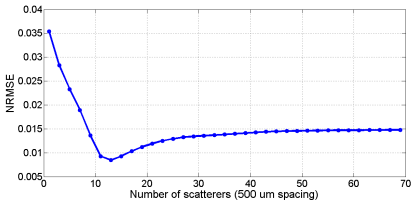

Fig. 7. Normalized root-mean-square error between calibration curves for different (odd) numbers of individual scatterers placed around transducer focus with an equal 500 μm axial spacing.

phantom calibration curves than either the one of the PSF or that of 31 scatterers. In order to obtain the optimal number of scatterers, odd numbers of scatterers were placed around the focus of the transducer (one of the scatterers being at the focus point) as described in Section II/B. After simulation of ultrasound imaging for all these cases, calibration curves were determined and NRMSE values were calculated between these curves and the calibration curve of a homogeneous phantom. The results showed that there is an optimal axial region around the focus into which placing a few scatterers, a calibration curve practically identical to the calibration curves of homogeneous phantoms can be obtained.

Fig. 5 shows a few extreme examples for the number of scatterers, their (simulated) images and the calibration curves calculated for each one of them (here, the spacing between adjacent scatterers was 1 mm). In Fig. 6 NRMSE values are shown for a series of phantoms with scatterers with 1 mm spacing, while NRMSE values of Fig. 7 were calculated for 500 μm spacing of scatterers in order to obtain a better resolution of this function. Spacing scatterers with a distance being lower than this value, however, would lead to undesirable interference. Results showed – in accordance with each other – that the optimal region (for calibration) is around 6.5 mm long, which is significantly close to the calculated depth-of-field length of the transducer. The can be seen in Fig. 5 that the scattering region in Fig. 5b shows the depth-of-field (as compared with Fig. 5a and Fig. 5c).

IV. Discussion

It was shown in the above results that for homogeneous phantoms, the calibration curve is robust enough for different scatterer densities and SNR (variation of these parameters did not affect the calibration curve significantly). We can also conclude that – based on the simulation results – complex 'ideal phantoms' may be substituted by a few scatterers placed in the depth-of-field region for calibration purposes of a correlation-based sensorless freehand scan conversion algorithm.

Future work includes comparison and validation of these simulation results with experimental results as well as validation and improvement of the scan conversion algorithm based on the investigated calibration curves and described in detail in [2] – both of which are currently under investigation with partial results.

Statement of Originality

This report describes the work of the doctoral student during the educational year 2015/2016, parts of which are under preparation for submission at international journals and conferences.

References

[1] Aaron Fenster, Dónal B Downey and H Neale Cardinal, *Three-dimensional ultrasound imaging*, Physics in Medicine and Biology, Volume 46, Number 5, pp. R67–R99, 2001.

[2] Miklós Gyöngy, Gergely Csány, *Method of generating ultrasound images and computer storage device*, Patent, P 15 00299, 2015.

[3] N. Afsham, M. Najafi, P. Abolmaesumi, R. Rohling, *Out-of-plane motion estimation based on a Rician-Inverse Gaussian model of RF ultrasound signals: speckle tracking without fully developed speckle* Medical Imaging 2012: Ultrasonic Imaging, Tomography, and Therapy, Proc. of SPIE Vol. 8320 832017-1, 2012.

[4] Hassenpflug P, Prager R W, Treece G M, *Speckle classification for sensorless freehand 3-D ultrasound*, Ultrasound in Medicine and Biology, 31(11): 1499-1508, 2005.

[5] Dong Fang, Zhang Dong, Yang Yan, Yang Yue, Qin Qianqing, *Distance Estimation in Ultrasound Images Using Specific Decorrelation Curves*, Wuhan University Journal of Natural Sciences, Vol.18 No.6, 517-522, 2013.

[6] Gee A H, Housden R J, Hassenpflug P, *Sensorless freehand 3D ultrasound in real tissue: speckle decorrelation without fully developed speckle*, Medical Image Analysis, 10(2): 137-149, 2006.

[7] Catherine Laporte, Tal Arbel, *Measurement Selection in Untracked Freehand 3D Ultrasound*, MICCAI 2010, Part I, LNCS 6361, pp. 127–134, 2010.

[8] Jørgen Arendt Jensen, Peter Munk, *Computer phantoms for simulating ultrasound B-mode and CFM images*, Acoustical Imaging, vol. 23, pp. 75-80, 1997.

[9] Craig K. Abbey, Min Woo Kim, Michael F. Insana, *Perfusion Signal Processing for Optimal Detection Performance*, 2014 IEEE International Ultrasonics Symposium Proceedings, pp. 2253—6, 2014.

Computer simulated examples for quantum systems in QuTiP

Máté HANDBAUER
(Supervisor: Prof. Árpád CSURGAY, D.Sc.)
Pázmány Péter Catholic University, Faculty of Information Technology and Bionics
50/a Práter street, 1083 Budapest, Hungary
handbauer.mate@itk.ppke.hu

***Abstract*—Numerical simulation of quantum physical systems is known to be a demanding computational problem, particularly dealing with large regimes. However, quantum simulations provide great assets for the development of new quantum technologies such as quantum sensors or creation of a universal quantum computer. Furthermore, they are also applicable in various other related fields, e.g. condensed-matter physics, high-energy physics, atomic physics or quantum chemistry. The creation of a simple computational model may contribute to the understanding of a given problem before the actual implementation using quantum computers, or simpler, analog quantum simulators, such as ions, polar molecules, electrons in semiconductors, quantum cavities and oscillators, nuclear spins or photons. The Quantum Toolbox in Python (QuTiP) is well suited for the numerical simulations. Inter alia it is an appropriate framework for example in quantum optics or in circuit quantum electro dynamics (C-QED), while it also possesses potential for educational purposes. This preliminary study presents simple models and simulation examples illustrating the capabilities of the QuTiP framework.**

***Keywords*-python; quantum systems; simulations**

I. Introduction

It can be stated, that in general an analytical description of the system dynamics is hardly manageable for Hamiltonians of more advenced physical systems. Considering the solution of these problems, one must confine themselves to numerical simulations of the equations of motion. If these simulations are to be carried out using classical computers instead of quantum computers, the exponentially increasing dimensionality of the inherent Hilbert space sternly limits the simulation efficiency of the system [1]. However, in many fields such as trapped ions [2], nanomechanics [3], quantum optics and circuits [4] using a small number of effective components is sufficient for composing few-level quantum systems and harmonic oscillators excited by a small number of quanta, in a simplified Hilbert space. These are manageable with classical simulation techniques. The Quantum Toolbox in Python (QuTiP) is an open-source software designed to be a general framework for solving the aforementioned quantum mechanical problems ie. for simulating the dynamics of open quantum systems [5].

This article briefly presents the main concepts of numerical simulations for quantum models using QuTiP in particular of quantum mechanical light-matter interactions (Section II), while Sections III delineate the simulation model and a simulation example. Finally, in Section IV, the paper closes with conclusions and outlines the main aspects of the author's subsequent scientific work.

II. Concepts

QuTiP, as mentioned above, is a python package for calculations and numerical simulations of quantum systems. The key difference between classical and quantum mechanics lies in the use of operators instead of numbers as variables. Moreover, one must specify state vectors and their properties. Therefore, for computing of the dynamics of quantum systems a given data structure is needed, which is capable of encapsulating the properties of a quantum operator. QuTiP accomplishes this by defining the quantum object class using matrix representation. This is a basic facility for representing and doing calculations with state vectors (wave-functions), as bras, kets and density matrices, quantum operators of single and composite systems, and useful for defining master equations. It also includes solvers for a time-evolution of quantum systems, according to: Schrodinger equation, von Neuman equation, master equations, Floquet formalism, Monte-Carlo quantum trajectories, experimental implementations of the stochastic Schrodinger/master equations.

The Jaynes-Cummings model is the simplest possible model for quantum mechanical light-matter interactions, describing a single two-level atom interacting with a single electromagnetic cavity mode[6]. The Hamiltonian that describes the full system consists of the free field Hamiltonian, the atomic excitation Hamiltonian, and the Jaynes–Cummings interaction Hamiltonian:

$$\hat{H} = \hat{H}_{field} + \hat{H}_{atom} + \hat{H}_{JC} \tag{1}$$

$$\hat{H}_{field} = \hbar\omega_c \hat{a}^\dagger \hat{a};\ \hat{H}_{atom} = \hbar\omega_a \frac{\hat{\sigma}_z}{2};\ \hat{H}_{int} = \frac{\hbar\Omega}{2}\hat{E}\hat{S} \tag{2}$$

Where ω_c and ω_a are the frequencies of the cavity and the atom, respectively, and Ω represents the interaction strength. The JC interaction Hamiltonian with the quantized radiation field is taken to consist of a single bosonic mode with the field operator $\hat{E} = \hat{a} + \hat{a}^\dagger$, where the operators $\hat{a}^\dagger$ and $\hat{a}$ are the bosonic creation and annihilation operators, while the atom is coupled to the field through its polarization operator $\hat{S} = \hat{\sigma}_+ + \hat{\sigma}_-$, where the operators $\hat{\sigma}_+$ and $\hat{\sigma}_-$ are the raising and lowering operators of the atom. The operator $\hat{\sigma}_z$ is the atomic inversion operator.

To get a solvable model, when $|\omega_c - \omega_a| \ll \omega_c + \omega_a$ the quickly oscillating "counter-rotating" terms can be ignored. This is referred to as the rotating wave approximation. The JC Hamiltonian is thus written as:

$$\hat{H}_{JC} = \hbar\omega_c \hat{a}^\dagger \hat{a} + \hbar\omega_a \frac{\hat{\sigma}_z}{2} + \frac{\hbar\Omega}{2}\left(\hat{a}\hat{\sigma}_+ + \hat{a}^\dagger\hat{\sigma}_-\right) \tag{3}$$

Electromagnetic signals are always composed of photons, although in the circuit domain those signals are carried as voltages and currents on wires, and the discreteness of the photon's energy is usually not evident. However, by coupling a

M. HANDBAUER, "Computer simulated examples for quantum systems in QuTiP" in *PhD Proceedings Annual Issues of the Doctoral School, Faculty of Information Technology and Bionics, Pázmány Péter Catholic University – 2016.* G. Prószéky, P. Szolgay Eds. Budapest: Pázmány University ePress, 2016, pp 157– 159.

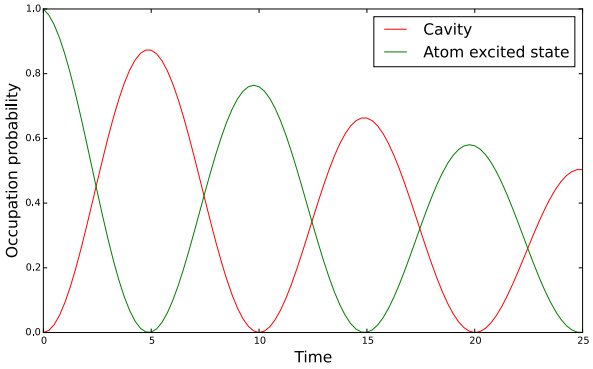

Fig. 1: Vacuum Rabi oscillations in the Jaynes-Cummings model. Occupation probabilities in the function of time for the cavity (red) and for the atom excited state (green).

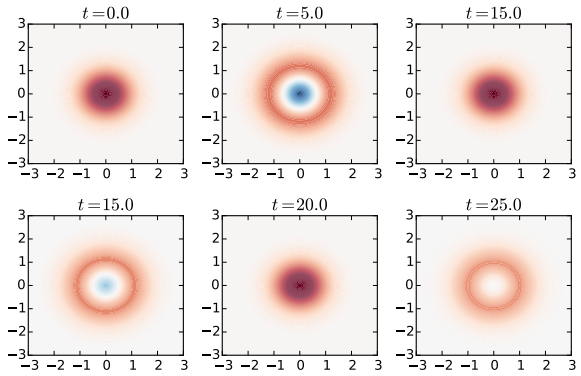

Fig. 2: Wigner quasi-probability distribution in the Jaynes-Cummings model. Positive values with red, and negative values with blue. For $t = 5$ and $t = 15$ the Wigner function has negative values, indicating a truly quantum mechanical state.

superconducting quantum bit (qubit) to signals on a microwave transmission line, it is possible to construct an integrated circuit in which the presence or absence of even a single photon can have a dramatic effect. Such a system can be described by circuit QED—the circuit equivalent of cavity QED, where photons interact with atoms or quantum dots.

III. Simple models and simulations

A. Jaynes-Cummings model

It is useful for computational purposes to write Equation 1-3 into matrix (and vector) representation form. So it can easily be implemented for numerical calculations, after setting up the parameters (using some robust approximations), the operators and the initial conditions. Furthermore using collapse operators one can describe a simple dissipation of the system. The built-in Lindblad master equation solver in QuTiP can solve this. Figure 1 shows excitation probabilities of the cavity and the atom. We can clearly see how energy is being coherently transferred back and forth between the cavity and the atom.

The Wigner quasi-probability distribution (Wigner function) provides additional insights considering the nature of the state of the resonators. To calculate it, one can first recalculate the evolution without specifying any expectation value operators, which will result in that the solver return a list of density matrices for the system for a given time (Figure 2). At $t = 0$,

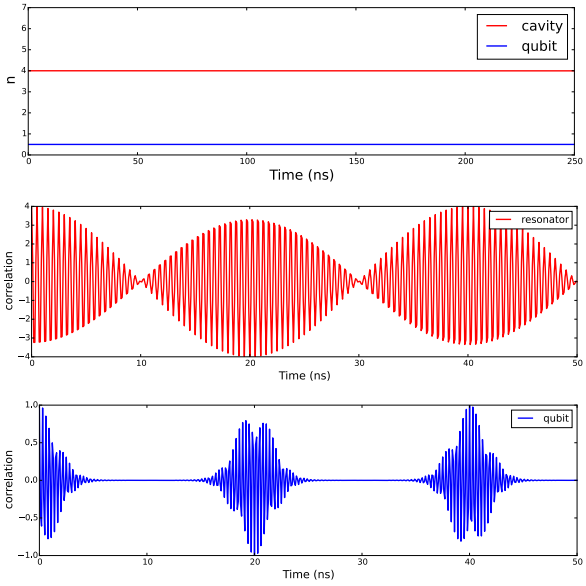

Fig. 3: Qubit-resonator with dispersive regime. Top: the systems do not exchange any energy, because the off-resonance with each other, middle and bottom: correlation functions for the resonator (red) and of the qubit (blue).

the cavity is in its ground state. At $t = 5, 15, 25$ it reaches its maximum occupation in this Rabi-vacuum oscillation process. It can be noted that for $t = 5$ and $t = 15$ the Wigner function has negative values, indicating a truly quantum mechanical state. At $t = 25$, however, the Wigner function no longer has negative values and can therefore be considered as a pure classical state.

B. C-QED in the dispersive regime

A qubit-resonator system can be described based upon the Hamiltonian shown in Equation 1-3. An interesting regime appears in this system when the resonator and the qubit is far-off resonance, $\Delta \gg \Omega$, where $\Delta = \omega_r - \omega_q$ is the detuning between the resonator and the qubit, and ω_r and ω_q are the bare frequencies of the resonator and qubit. This is the dispersive regime, where even a single photon has a large effect on the qubit without ever being absorbed [7]. In the dispersive regime the system can be described by the Hamiltonian:

$$\hat{H} = \omega_r \hat{a}^\dagger \hat{a} - \omega_q \frac{\hat{\sigma}_z}{2} + \chi \left(\hat{a}^\dagger \hat{a} + 1/2\right) \hat{\sigma}_z \qquad (4)$$

where $\chi = \Omega^2/\Delta$. It can be clearly seen that the last term is a correction of the resonator frequency that depends on the qubit state, or a correction to the qubit frequency that depends on the resonator state. In experiments the dispersive regimes were used to resolving the photon number states of a microwave resonator by monitoring a qubit that was coupled to the resonator[7]. In Figure 3 top, there is seen that the systems do not exchange any energy, because of they are off-resonance with each other, however there is oscillation, the middle and the bottom pictures show the correlation function for the resonator (red) and the correlation function of the qubit (blue) respectively. If we look at the cavity wigner function (Fig. 4) we can see that after interacting dispersively with the qubit, the cavity is no longer in a coherent state, but in a superposition of coherent states.

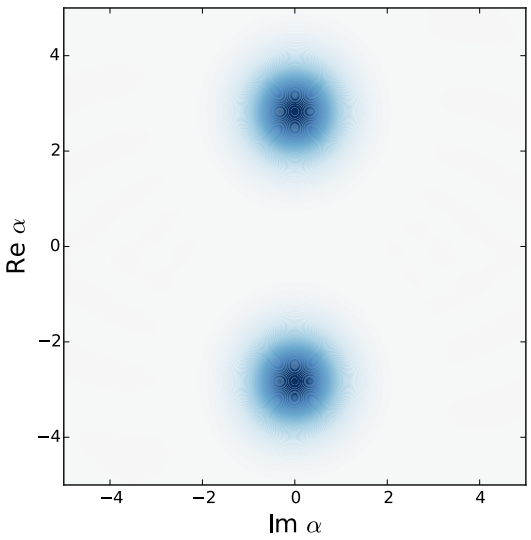

Fig. 4: Wigner quasi-probability distribution. After interacting dispersively with the qubit, the resonator is in a superposition of coherent states.

IV. Conclusion

This study introduced basic simulation programs in Python (using QuTiP) based on simple quantum physical models, that enabled basic investigation of light-matter interactions. In order to illustrate the capabilities of the simulator, some simulation examples were presented. According to the plans of the author a new C-QED model will be set up with parameters of physically relevant values in order to model real systems or published experiments. Additionally, further investigations should be made as the model is developed by using more complex systems and more sophisticated approaches of the system–environment interaction.

Acknowledgements

The author would express deep gratitude to his supervisor, Árpád Csurgay DSc for guidances he gave and the promotion of the doctoral research work. In addition, the author wish to express thanks to Imre Juhász, for his advices, and for his encouragements.

References

[1] R. P. Feynman, "Simulating physics with computers," *International Journal of Theoretical Physics*, vol. 21, no. 6, pp. 467–488, 1982.

[2] y. Leibfried, R. Blatt, C. Monroe, and D. Wineland, "Quantum dynamics of single trapped ions," *Reviews of Modern Physics*, vol. 75, no. 1, p. 281, 2003.

[3] M. Y. Zhao, S. M. Yu, X. Xiao, and Y. B. Gao, "Vacuum Rabi Splitting in Nanomechanical QED System with Nonlinear Resonator," p. 5, mar 2016.

[4] J. You and F. Nori, "Atomic physics and quantum optics using superconducting circuits," *Nature*, vol. 474, no. 7353, pp. 589–597, 2011.

[5] J. Johansson, P. Nation, and F. Nori, "QuTiP: An open-source Python framework for the dynamics of open quantum systems," *Computer Physics Communications*, vol. 183, pp. 1760–1772, aug 2012.

[6] E. T. Jaynes and F. W. Cummings, "Comparison of quantum and semiclassical radiation theories with application to the beam maser," *Proceedings of the IEEE*, vol. 51, pp. 89–109, Jan 1963.

[7] D. Schuster, A. Houck, J. Schreier, A. Wallraff, J. Gambetta, A. Blais, L. Frunzio, J. Majer, B. Johnson, M. Devoret, *et al.*, "Resolving photon number states in a superconducting circuit," *Nature*, vol. 445, no. 7127, pp. 515–518, 2007.

An overview of sparsity-based super-resolution algorithms for medical images

Ákos MAKRA
(Supervisor: dr. Miklós GYÖNGY)
Pázmány Péter Catholic University, Faculty of Information Technology and Bionics
50/a Práter street, 1083 Budapest, Hungary
makra.akos@itk.ppke.hu

Statement of originality: This report describes the work of the doctoral student during the educational year 2015/2016. Parts of this work are under submission to academic conferences and journals, notably 2016 IEEE Ultrasonics Symposium and/or the IEEE Transactions UFFC.

***Abstract*—Imaging modalities of any kind have a theoretical limit on their feasible resolution. The object of the super-resolution algorithms is to break this boundary obtaining a higher quality image with the same hardware. The aim of this work is to review on the existing solutions of the problem, comparing their practicability and effectiveness. We concentrate on the so-called stippling algorithm, originally applied in arts, but nowadays with increasing impact on science. Considering these properties an algorithm is developed, which could be applied for ultrasound images - a modified, decision-tree based stippling algorithm is presented for extracting the possible point scatterers. The results achieved so far proved to be promising, meaning that further investigation of the topic could be beneficial. However, care needs to be taken to evaluate the resulted stippling points as a real point scatterer arrangement.**

***Keywords*-ultrasound; super-resolution; medical images**

I. Motivation

There has always been a great demand on creating images, which have higher and higher resolution, whether it is about security cameras, satellites, professional photography or even the HUBBLE space telescope. The same rules apply for medical purposes: the higher the resolution of an image is, the more precise diagnosis can be established. There are two different ways to enhance the image: by constructing a better hardware with the capability of delivering(achieving) greater resolution or by an algorithm, which pushes the resolution limits of the imaging system beyond its physical boundaries (like the diffraction limit) to achieve super-resolution (SR). The algorithm can be used either real-time when the image is acquired(usually by taking more than one picture i.e. capturing sub-pixel-shifted frames and stacking them later) or as a post-processing step (depending on the algorithm even one frame can be satisfactory). The use of SR techniques provides the possibility of receiving a more detailed image at a lower cost compared to the expensive and time-consuming process of building a new hardware capable of delivering the same quality.

This paper is mainly concentrated on ultrasound (US) images, however, the algorithms to be presented can also be adapted to other imaging modalities as well. US imaging is a cost-effective, safe and portable method for medical examinations. On the other hand, along with other imaging modalities (such as MR, CT or light microscopy) its resolution is heavily dependent on the wavelength (higher frequency, thus shorter wavelength leads to better resolution) what in the case of sound is a lot poorer than that of the light or X-ray. The transducer and its frequency also determines the penetration depth (the higher the frequency the smaller the mentioned depth is) [1, p. 116]. To be able to examine deeper layers of the medium lower frequencies (therefore lower resolution) should be used. Taking into account the benefits of US imaging it would be worthwhile if the image resolution and signal-to-noise quality could be improved by post-processing methods.

II. Overview of methods

In the physical model the measured image arises as the scatterer map gets convolved with the point-spread function (PSF) of the transducer, and some noise will add to it because of the imperfection of the system:

$$x * PSF + N = y, \tag{1}$$

where x is the scatterer-map, $*$ means the convolution operator, the PSF is the point-spread function, N is the noise and y is the actual ultrasound image.

There are different well-known techniques to achieve SR. The conventional methods – like deconvolution, least square estimation, Wiener-filters, – are usually dependent on estimating the PSF of the imaging system, what always introduces an estimation error to the calculations. Furthermore, these algorithms are really sensitive to noise, not to mention their inability to recover frequency components outside of the frequency range of the PSF. In these cases extrapolation for higher frequencies in the frequency domain can be used to enhance the fine structure of the image [2]. Nevertheless, extrapolation is an estimation in itself, introducing a new source of error to our model. Therefore, it sheds light on the need of new algorithms or a different way to approach the problem.

Another way of dealing with the problem of SR is to define a dictionary of functions, and to find a combination of them which could estimate our measured image with a maximum level of error. These usually iterative decomposition algorithms will therefore have steps for maximizing the data fidelity and terms for introducing a regularization of some sense (eg. sparsity or smoothness of the result). A US image reflects point scatterers' additive response, meaning that a simple signal builds up the whole image, a sparse decomposition algorithm could come into view to overcome the aforementioned disadvantages of the conventional deconvolution algorithms, Therefore, a sparse dictionary can be used with the $\ell 1$- or $\ell 2$ - norm for regularization, either compressing and sparsity or smoothness can be achieved, respectively, by minimizing

Á. MAKRA, "An overview of sparsity-based super-resolution algorithms for medical images" in *PhD Proceedings Annual Issues of the Doctoral School, Faculty of Information Technology and Bionics, Pázmány Péter Catholic University – 2016.* G. Prószéky, P. Szolgay Eds. Budapest: Pázmány University ePress, 2016, pp 161– 164.

the following equation:

$$\min_f \sum_{i=1}^{n} (V(f(\hat{x}_i), \hat{y}_i) + \lambda \cdot R(f))), \tag{2}$$

where V is a cost function for the difference of the measured function, y and its prediction $f(x)$, $R(f)$ is the regularization term, usually some penalty for the complexity of f, and $lambda$ is the factor responsible for the importance of the regularization.

Another approach to both enhance the details and eliminate noise, Markov Random Fields (MRF) can be used [3]. The image is described by a Markov model, where the pixel values depend only on their neighbours but are independent from any other pixel value. By introducing a cost/energy function which has two terms: one of them penalizes discrepancy between the measurement and the prediction, while the other one penalizes any big difference between neighbouring pixel values to avoid high frequency changes between adjacent pixels to redound smoothness. An IIR filter can be designed using the constructed energy function, which filter can be applied to the measured image., However, this method can easily blur small differences making two (or more) adjacent point scatterers' response indistinguishable.

III. Definition of stippling problem

To find the point scatterers in an US image, we would like to use the so-called stippling algorithm. Our goal is to automatically detect and represent with single dots the important structures of the image, thus predicting the original scatterer map as precisely as possible. Stippling is an algorithm, which is about placing small dots proportional to the intensity of an area in a picture but having random distribution at the same time. The darker the area is, the more dots are drawn to visually provide the same result as the original one. The arising image made of dots should preserve the structures of the original image (see Fig. 1 as an example). This technique was first presented in drawing and painting, while later it was used for saving ink during printing and to re-size images with less error. (Note: it is very similar to pointillism but not the same) Using this method it is possible to describe any scatterer object as a set of uniformly weighted point scatterers, hopefully leading to the same, or a similar enough US image.

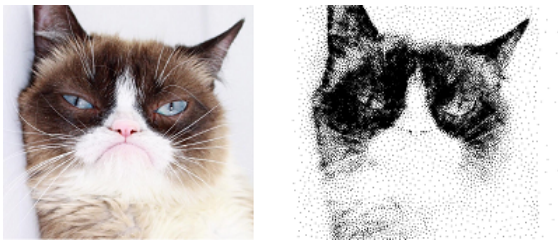

Fig. 1. Stippling method example. Left: original picture, right: stippled image. Image processing tool was downloaded from http://wiki.evilmadscientist.com/StippleGen

Originally these images were drawn by hand, which process can take days. However, because of the usefulness of the method, many automatization techniques have been developed since the use of computers.

IV. Existing solutions to the stippling problem

Traditional/Original

The easiest interpretation is to place dots on the image in a random manner, defining a maximum distance between them depending on the color of the given area. So in every case we draw a new position, we have to decide on keeping it by calculating the distance between this and the previously drawn points. This method is usually computationally expensive and time-consuming (leads to a quadratic problem), and do not preserve structures like edges in general (dart throwing algorithm [4]). This method draws the attention to the following problem: we can observe, that even using a random method, inner patterns easily arise (the human eye is very good at picking up these patterns), which could also influence the goodness of our predicted scatterer map. This led to the conclusion, that the so-called blue noise should be achieved during the process, which lacks these inner patterns. To do so, the Poisson-Disc sampling can be effectively used.

Voronoi diagrams

In order to achieve blue noise, still spacing the dots evenly, the so-called weighted Voronoi algorithm can be used. On a Voronoi diagram we define cells around previously specified seed points in such a manner, that every point of the cell is closer to its seed than to any other using some metric (usually the $\ell 2$-norm or the so-called Euclidean distance). A special form of the problem is when the seed point is registered to the centroid of the cell. The centroid of the cell is defined as

$$C_i = \frac{\int_{A_i}(x\rho(x)dA)}{\int_{A_i}(\rho(x)dA)}, \text{(eq. centroid)} \tag{3}$$

where C_i is the centroid of the ith cell, A_i is the area of the given cell, x is the position of the point, and $\rho(x)$ is the value of the density function at the given point. The density function can be defined using the gray-scale intensity of the give area on the picture. This means, that seeds will be denser on a darker area, and sparser on a lighter area. Starting from a beforehand defined set of seed points, the so-called Lloyd's relaxation algorithm [5]can be used to achieve the above mentioned criteria. The steps of the algorithms are as follows: Calculating the Voronoi cells (using the 3D graphics hardware-based algorithm of Hoff, or the sweeping Fortune's algorithm for example), Compute the centroids of the cells (eq. centroid) reposition the seed points to the centroids Repeat from step 1.) until the average path of the repositioning reaches a lower limit. The algorithm has a high-quality result, but its computational need is also extremely high.

Graph theory-based

A similar, area-dependent algorithm uses graph theory. The image is transformed into a weighted graph, where every pixel is connected to its 8 neighbours, The nodes' value is calculated from its gray-level and gradient, while the edges are weighted with the average of the nodes it connects. Starting from an arbitrary seed point we expand the region around the seed point, calculating the distance between the seed and the area boundary points using Dijkstra's algorithm, until the path length reaches a threshold. At the frontier point with highest gradient we place a new stipple point, with 0 distance from the previous stipple(s), so the expansion will preferably continue from here. When there is no remaining region of the image

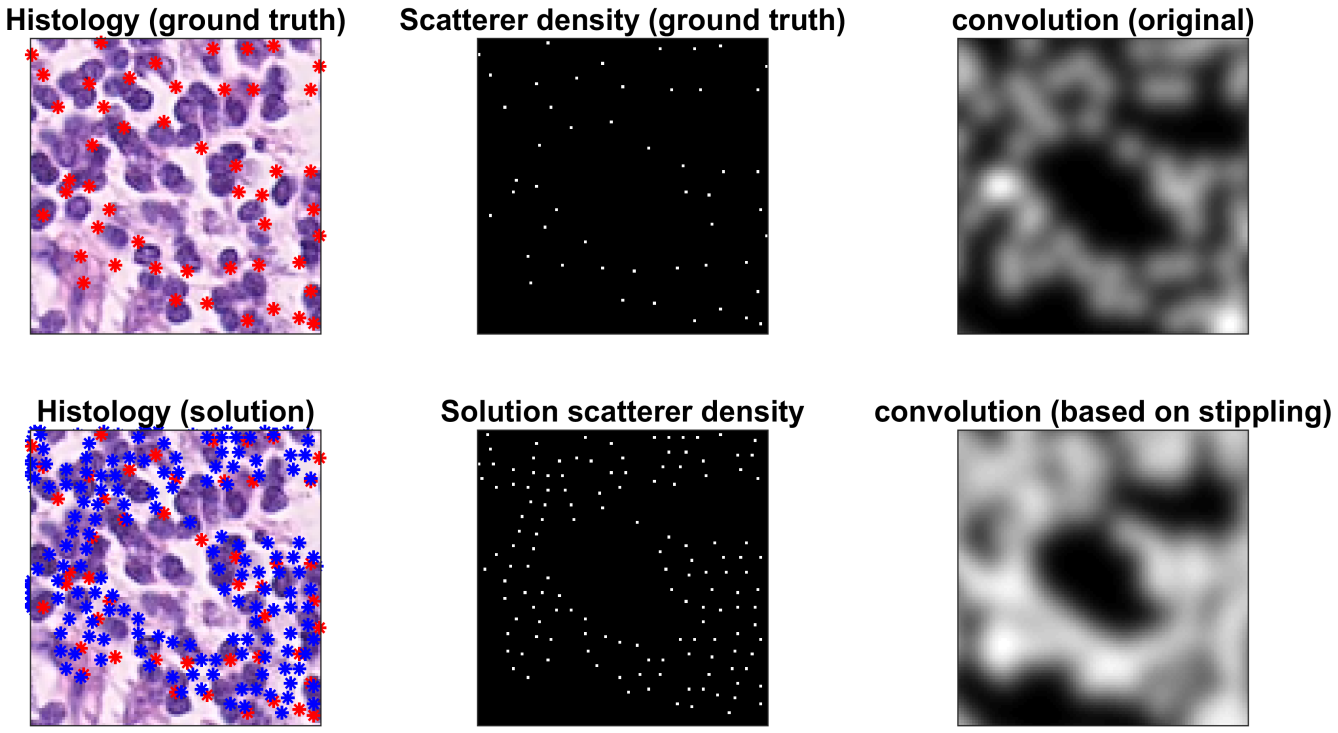

Fig. 2. Ground truth vs. stippling solution. In the top row data the original (annotated) data can be seen, while the bottom row shows the result of our method. Red markers indicate the annotated nuclei, while the blue ones are provided by our stippling method. It can be observed that our method places the point scatterers on the edges too, which is most likely the result of the binary intensity categorization and the accepted small gradient-levels. Both of these causes leads to a greater acceptable region for placing stipples in the vicinity of the maximum. The achieved similarity between the convolved images was $R^2 = 0.63$, which is satisfactory based on the visual conformity between the images.

to be expanded, the algorithm stops. The node values will account for the density of stipple points, while the positioning of new stipples depending on the gradient helps to preserve edge structures. However, as Dijkstra's algorithm is greedy, with increasing image size the run time can get utterly slow.

Decision tree

A fast, but less precise method can be constructed using decision trees. These methods usually have the most threshold parameters. Decision values calculated from the grey levels and gradients of the input image are used in the initial positioning of stipple point. New threshold values have to be defined in the next step, when we decrease the number of these points to achieve the desired densities - the probability of deleting points should be higher at lighter, and evenly toned input areas and lower at dark, and edge regions. This means, that the quality of the output strictly depends on these thresholds, so for different input images we can get very different results. In ideal case, the algorithm should calculate these parameters using the input image.

V. Method of current work

For testing the effectiveness of stippling, an algorithm was needed which is fast, easily adjustable, and a high level of similarity can be achieved with it. The code was adapted from [6] and re-implemented with modifications in MATLAB (Mathworks, Natick, MA).

It is based on a decision tree, starting with computing the vertical and horizontal gradient image and placing stipple points to every location where the gradient value reaches the input threshold value. In the next step stipple points are randomly removed: the more stipple points are found in the vicinity of the examined point, the more likely will it be preserved.

This method, however, has multiple disadvantages. First of all, it focuses only on the edges, neglecting the different tones of an input image, leading to the fact that the structures will be enhanced, but in case a scatterer object with a uniformly toned area was present, only the edges of that region would be detected. Furthermore, its structure would also have a very different response image: assuming that the PSF has a given radius, stipples placed on the edge of this PSF would produce a response image with twice of the radius (half of the resolution). It leads to the assumption that edge detection is rather disadvantageous in our case.

To overcome these problems, a simple binary tone recognition was included in the algorithm. First of all stipples are placed to locations where the gradient is smaller than the input threshold, thus uniformly toned regions will be preferred over sharp edges (which, for instance could be easily produced by noise speckles). However, the background would also be covered by stipples following our previous rule, so intensities under a second threshold are penalized. Apart from the fact that dark regions and speckles will be stipple-free, this second rule also helps to limit the stipples to the brighter, inner region of a structure. In the following step stipples are similarly removed, as in the original workflow. The resulting image, however would have far too many stipple points. Randomly decreasing their numbers would be dangerous as complete scatterers easily could be lost. In regions where the number of stipple points exceeds a limit, those points are substituted with one point with one point in the centroid of the others. This step will also help to obtain more concentrated groups

of the stipples.

VI. Results

For testing the algorithm a simulation environment was set up. An arbitrary input image (taken from [7], showing H&E stained histology picture of colorectal adenocarcinoma) is taken where coordinates of point scatterers (nuclei) are known and is convolved with a PSF. For the PSF a precalculated two-dimensional Gauss-signal with 0 expected value and 0.5 standard deviation was used. As dealing with point scatterers, no scattering was taken into account from any other cell parts. By performing the mentioned convolution a simulated US image was obtained. To extract the original location of the scatterers, the above presented algorithm is used on the US image. The located stipple points are convolved with the PSF again, and the result is compared to the original input image. For the latter the well-known R^2 metric is used.

The results can be seen in Fig. 2. Top row indicates ground-truth-based data, while the bottom row shows the stippling methods' result. Red markers indicate the annotated nuclei (ground truth), while the blue ones are provided by our stippling method. It can be observed that our method places the point scatterers on the edges too, which is most likely the result of the binary intensity categorization and the accepted small gradient-levels. Both of these causes leads to a greater acceptable region for placing stipples in the vicinity of the maximum. The achieved similarity between the convolved images was R^2 = 0.63, which is satisfactory based on the visual conformity between the images.

VII. Conclusion

It would be too early to draw a conclusion whether stippling methods in general could solve or not the problem of finding the point scatterers in an US image. For finding that out, different approaches like clustering the points with the Voronoi diagrams, or setting the threshold values from local and global properties of the image could improve the performance. It is also obvious, that the intensity of the regions contains more information in our case than the gradient, so further experiments should be carried out in this direction. The described method provides a solution to this inverse problem, however, care needs to be taken to evaluate the dot arrangement as a possible, real-life scatterer position layout.

Furthermore, a proper metric could be used to compare point scatterers of the ground truth data and stippling, even in case of different amount of scatterers. To reduce the stippling points either a proper thresholding or a better (even adaptive) "substitution window" could be used.

Last, but not least, stippling methods could be used on any other imaging modalities.

Acknowledgements

The author would like to thank Janka Hatvani, Dr. András Horváth and Dr. Miklós Gyöngy for their help during the research process.

References

[1] Thomas L. Szabo, *Diagnostic ultrasound imaging*. Elsevier Academic Press, 2004.

[2] A. Papoulis and C. Chamzas, "Improvement of range resolution by spectral extrapolation," *ULTRASONIC IMAGING*, vol. 1, pp. 121 – 135, 1979.

[3] K. Kutulakos, "Foundations of computer vision: Markov random fields." [Online]. Available: http://www.cs.toronto.edu/~kyros/courses/2503/Handouts/mrf.pdf

[4] R. L. Cook, "Stochastic sampling in computer graphics," *ACM Transactions on Graphics*, vol. 5, pp. 51–72, 1986.

[5] B. B. Atsuyuki Okabe and K. Sugihara, *Spatial Tessellations: Concepts and Applications of Voronoi Diagrams*. John Wiley & Sons, New York, 1992.

[6] M. Snider and K. Chan, "Stippling algorithm (Python)." [Online]. Available: https://github.com/msilvprog7/Python-Image-Manipulation/blob/master/stipple2.py

[7] S. et al., "Locality sensitive deep learning for detection and classification of nuclei in routine colon cancer histology images," *IEEE Transactions on Medical Imaging*, 2016.

Spin-wave-based signal processing

Ádám PAPP*†
(Supervisors: Árpád CSURGAY*, György CSABA†, Wolfgang POROD†)
*Pázmány Péter Catholic University, Faculty of Information Technology and Bionics
50/a Práter street, 1083 Budapest, Hungary
†Center for Nano Science and Technology (NDnano), University of Notre Dame
Notre Dame, IN, USA
papad@digitus.itk.ppke.hu

***Abstract*—We demonstrate the use of spin-wave interference in patterned magnetic films for spectral decomposition of microwave signals. In particular, we propose the use of the so called Rowland circle arrangement which is widely used in optical and X-ray spectroscopy. Our design's simplicity (the spin-wave generation, the grating and the focusing device are all realized by one patterned edge of the magnetic film) enables exceptionally straightforward fabrication and a very compact device. We believe that the idea can be generalized and we envision devices where the signal is first converted from long wavelength waves to sub-micron wavelength spin waves, so that signal processing may be realized by a compact on-chip device. Our designs were verified by means of micromagnetic simulations.**

***Keywords*-YIG; spin wave; spectrum analyzer; Rowland circle; concave grating**

I. Introduction

Spin-wave-based computing devices are promising CMOS-alternative candidates for low-power and high-speed applications. A number of devices has been proposed that use spin waves to realize Boolean logic gates [1] or non-Boolean computing primitives [2][3]. In this paper we present a different application area for spin waves: by means of micromagnetic simulations we demonstrate the operating principles of a spin-wave-based spectrum analyzer for microwave signals. Microwave spectral analysis is a fundamental part of many telecommunication systems as well as scientific lab equipment. The typical realization of a spectrum analyzer consist of a filter bank with a large number and often bulky filters and/or a digital signal processor with relatively large power consumption and considerable delay. Our design uses analog signals and wave interference to produce the spectral decomposition.

A similar arrangement were proposed in [4] but in that arrangement beams of magnetic waves are deflected by a flat grating created by surface acoustic waves.

II. Spin waves

Spin waves (often called magnons if quantized) are excitations of the magnetization in magnetic materials. There are multiple differences between spin waves and electromagnetic waves: spin waves are bound to magnetic media, they are nonlinear and spin waves only exist in the gigahertz-terahertz range. The most important difference for us is the difference in dispersion properties as spin waves has much lower wavelengths at the same frequency (spin waves can have wavelengths from a few nanometers to several micrometers). This enables a much more compact integration of spin-wave devices compared to the bulky microwave devices. In fact, spin waves can have wavelengths comparable to the visible light at microwave frequencies. This inspired us to realize optical computing arrangements using spin waves.

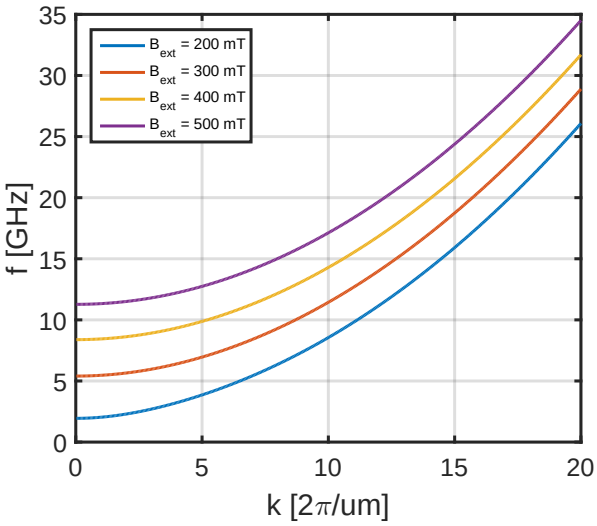

Fig. 1. Calculated dispersion curves in YIG at various biasing fields.

Spin waves also have anisotropic dispersion, i.e. the spin-wave wavelength depends on the angle between the magnetization and the wave propagation. In case of thin magnetic films if the magnetization is perpendicular to the film plane this angle is 90° at every direction in the plane of the film, thus this out-of-plane magnetization is preferred over the in-plane magnetization. Fig. 1 shows typical dispersion curves in yttrium iron garnet (YIG) at different bias fields. The direction of the magnetization is out of plane.

III. Rowland circle arrangement

The Rowland arrangement [5] is used in X-ray and optical spectroscopy. Its main element is a patterned, reflecting surface, acting as a combination of a diffraction grating and a concave mirror. In this geometry, waves are diffracted by the grating, depending on their wavelength and at the same time focused by the concave mirror on different points of the Rowland circle. Different wavelengths correspond to different foci, thus the frequency components of the signal become spatially separated. A spin-wave-based implementation for the Rowland geometry is shown in Fig. 2. This depicts the result of a micromagnetic simulation of an approx. 3 x 2.5 micrometer size Permalloy film. For micromagnetic simulations the well established OOMMF code[6] were used. The bottom of the film is patterned in such a way that it performs the diffracting, focusing and wave generation functions. The spin waves are generated on the edge of the magnetic film by the magnetic field of a microstrip line. The magnetic field of the microstrip line were calculated using HFSS EM simulator, and applied

Á. PAPP, "Spin-wave-based signal processing" in *PhD Proceedings Annual Issues of the Doctoral School, Faculty of Information Technology and Bionics, Pázmány Péter Catholic University – 2016.* G. Prószéky, P. Szolgay Eds. Budapest: Pázmány University ePress, 2016, pp 165– 166.

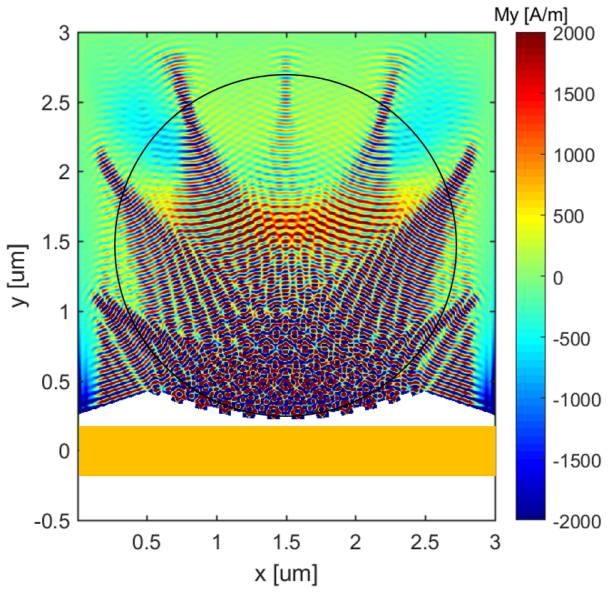

Fig. 2. Micromagnetic simulation of the spin-wave spectrum analyzer. The colormap represents a magnetization snapshot of the magnetic film. Along the Rowland circle different diffraction orders of one frequency component can be seen.

in the magnetic simulation assuming a sinusoidal time dependence.

The resulting structure is significantly simpler than our earlier proposal for a spin-wave lens [7], as it requires no non-uniform magnetic fields for the manipulation of spin-waves. A static uniform external magnetic field is still required to set the magnetic film to a single-domain state, and this magnetic field is also used to define the cutoff frequency and the dispersion relation for spin waves. This external bias field can be realized by an additional fixed magnet, a coil, a built in anisotropy in the magnetic field or the combination of these. It is possible to change the operation frequency band of the device by changing the external bias field. At the same time the resolution of the device is determined by this external bias field due to the nonlinear spin-wave dispersion curve in magnetic materials. It is possible to achieve megahertz resolution at gigahertz frequencies by choosing the proper bias field, however the size of the device will limit the achievable bandwidth.

The intensity peaks of the spin-wave intensity distribution along the Rowland circle correspond to the frequency components of the excitation. In an actual device these peaks may be picked up by magnetoresistive or inductive sensors placed on the Rowland circle. The size of these sensors limits the smallest spin-wave wavelength that can be used in the device.

While the Rowland circle can be implemented in ferromagnetic metallic films (such as Permalloy or CoFe), YIG films enable long-range spin-wave propagation and the formation of complex interference patterns since YIG has one of the lowest damping among the known magnetic materials, with damping coefficient as low as $\alpha = 2.3 \times 10^{-4}$ and decay lengths of several hundreds of nanometers [8]. This enables to realize spectrometers up to a millimeter size at micrometer spin-wave wavelengths, thus increasing the resolution and bandwidth.

IV. Conclusion

We presented a design for a spin-wave-based spectrum analyzer for microwave signals. Our estimations suggest that the device could significantly outperform its digital and filter-bank-based counterparts in terms of power consumption, chip area and delay at several gigahertz frequency. Further considerations are needed to determine the overhead added by the readout circuitry. Spin-wave optical devices, such as the presented device, may enable the replacement of surface acoustic wave (SAW) devices or perform the processing functions of complex, power-hungry high-frequency circuitry.

Acknowledgment

The authors are grateful to Gary H. Bernstein, Jonathan Chisum (Notre Dame) and Giovanni Carlotti (University of Perugia) for motivating discussions. This work was supported by the NSF/SRC grant 'Nanoelectronics Beyond 2020'.

References

[1] T. Schneider, A. A. Serga, B. Leven, B. Hillebrands, R. L. Stamps, and M. P. Kostylev, "Realization of spin-wave logic gates," *Applied Physics Letters*, vol. 92, no. 2, p. 022505, 2008.

[2] A. Khitun, "Magnonic holographic devices for special type data processing," *Journal of Applied Physics*, vol. 113, no. 16, p. 164503, 2013.

[3] F. Gertz, A. Kozhevnikov, Y. Filimonov, and A. Khitun, "Magnonic Holographic Memory," *IEEE Transactions on Magnetics*, pp. 1–1, 2014.

[4] S. Hanna, "Apparatus and method for diffracting MSW in a garnet film using SAW," Oct. 1991.

[5] M. C. Hutley, *Diffraction gratings*. No. 6 in Techniques of physics, London: Academic Press, 1982.

[6] M. J. Donahue and D. G. Porter, *OOMMF User's Guide, Version 1.2a3*. National Institute of Standards and Technology, Gaithersburg, MD, 1999. Interagency Report NISTIR 6376.

[7] G. Csaba, A. Papp, and W. Porod, "Spin-wave based realization of optical computing primitives," *Journal of Applied Physics*, vol. 115, p. 17C741, May 2014.

[8] H. Yu, O. d. Kelly, V. Cros, R. Bernard, P. Bortolotti, A. Anane, F. Brandl, R. Huber, I. Stasinopoulos, and D. Grundler, "Magnetic thin-film insulator with ultra-low spin wave damping for coherent nanomagnonics," *Scientific Reports*, vol. 4, p. 6848, Oct. 2014.

Program 4

HUMAN LANGUAGE TECHNOLOGIES, ARTIFICIAL UNDERSTANDING, TELEPRESENCE, COMMUNICATION

Head: Gábor PRÓSZÉKY

HuQ corpus

Zijian Győző YANG
(Supervisor: Dr. Gábor PRÓSZÉKY)
Pázmány Péter Catholic University, Faculty of Information Technology and Bionics
50/a Práter street, 1083 Budapest, Hungary
yang.zijian.gyozo@itk.ppke.hu

***Abstract*—Quality estimation for machine translation is an important task. The standard automatic evaluation methods that use reference translations cannot perform the evaluation task well enough. These methods produce low correlation with human evaluation for English-Hungarian. Quality estimation is a new approach to solve this problem. This method is a prediction task estimating the quality of translations for which features are extracted from only the source and translated sentences. Quality estimation systems have not been implemented for Hungarian before, thus there is no such training corpus either. In this study, we created a dataset to build quality estimation models for English-Hungarian. We also did experiments to optimize the quality estimation system for Hungarian. In the optimization task we did research in the field of feature engineering and feature selection. We created optimized feature sets, which produced better results than the baseline feature set.**

***Keywords*-quality estimation; machine translation**

I. Introduction

The measurement of the quality of translation output has become necessary especially in the field of machine translation (MT). A reliable quality score for MT could save a lot of time and money for translators, companies, researchers and ordinary users. Knowing the quality of machine translated segments can accelerate the translators' work, or can help human annotators in their post-edit tasks, or can filter out and inform about unreliable translations. Last but not least, quality indicators can help MT systems to combine the translations to produce better output. There are two kinds of evaluation methods for MT. The first type uses reference translations, i.e. it compares machine translated sentences to human translated reference sentences, and measures the similarities or differences between them. To evaluate the quality of MT, after an automatic translation, we also have to create a human translated sentence (for the sentences of the test set) to compare it to the machine translated output. Creating human translations is expensive and time-consuming, thus these methods, such as BLEU and other methods based on BLEU, TER, HTER etc., cannot evaluate in run-time, and the correlation between the results of these methods and that of human evaluation is very low in the case of translations from English to Hungarian. A completely new approach is needed to solve these problems, i.e. a method which can predict translation quality in real-time and does not need reference translations.

The other type of evaluation methods is called Quality Estimation (QE). This is a supervised approach that does not use reference translations. This method addresses the problem by evaluating the quality of machine translated segments as a prediction task. Using QE we can save considerable time and money for translators, human annotators, researchers, companies and ordinary users.

In this study, we use the QuEst framework [1], developed by Specia et al., to train and apply QE models for Hungarian, which to our knowledge has not been done before. Hence, first, we needed to create a QE corpus for Hungarian. Then, using this corpus we built different kinds of optimized English-Hungarian QE models. For optimizing we developed new semantic features using WordNet and word embedding models.

The structure of this paper is as follows: First we will shortly introduce the QE approach. Then, we will present the corpus we created for English-Hungarian QE. Finally, our experiments, optimizations and results in the task of QE are described.

II. Related Work

In the last couple of years there have been several WMT workshops with quality estimation shared tasks,[1] which provided datasets for QE researches. The datasets are evaluated with HTER, METEOR, ranking or post-edit effort scores. But, unfortunately, there is no dataset for Hungarian. In this research we created a QE dataset for English-Hungarian. For human judgement we used the Likert scoring scale.

Recently, in the field of QE, research has focused on feature selection using a variety of machine learning algorithms and feature engineering. In feature selection task, Beck et al. tried more than 160 features in an experiment for English-Spanish to predict HTER. Other key aspects in field of QE are: a.) providing larger datasets; b.) feature selection using a variety of machine learning algorithms and feature engineering for word-level, sentence-level and document level QE; c.) exploring differences between sentence-level and document-level prediction; d.) analyzing training data size and quality [2].

In our research we did experiments for Hungarian QE in providing a dataset, word-level feature engineering and feature selection.

III. Quality Estimation

In the QE task, we extract different kinds of features as quality indicators from the source and translated sentences. Following the research of Specia et al., we can separate the features in different kinds of category [1]. From the source sentences, complexity features can be extracted. From the translated sentences, we extract fluency features. From the comparison between the source and the translated sentences, adequacy features are extracted. We can also extract indicators from the MT system, these are the confidence features. From another point of view, we can also divide the features into two main categories: "black-box" features (independent from the MT system) and "glass-box" features (MT system-dependent). Since in our experiments we have translations from different MT systems, we did use only the "black-box" features. After feature extraction, using these quality indicators, we can build

[1] http://www.statmt.org/wmt15/quality-estimation-task.html

Z. YANG, "HuQ corpus" in *PhD Proceedings Annual Issues of the Doctoral School, Faculty of Information Technology and Bionics, Pázmány Péter Catholic University – 2016.* G. Prószéky, P. Szolgay Eds. Budapest: Pázmány University ePress, 2016, pp 169– 172.

Adequacy	Fluency
1: none	1: incomprehensible
2: little meaning	2: disfluent Hungarian
3: much meaning	3: non-native Hungarian
4: most meaning	4: good Hungarian
5: all meaning	5: flawless Hungarian
0: I do not understand this English sentence	

TABLE I
ADEQUACY AND FLUENCY SCALES FOR HUMAN EVALUATION

QE models with machine learning methods. The aim is that the predictions of the QE models are highly correlated with human evaluations. Thus, the extracted quality indicators need to be trained on human judgments.

IV. HUQ CORPUS

To build the English-Hungarian QE system, we needed a training corpus. In our experiments, we created a corpus called Hungarian QE (HuQ). The HuQ corpus contains 1500 English-Hungarian sentence pairs. To build the HuQ corpus, we used 300 English sentences of mixed topics from the Hunglish corpus [3]. We translated these 300 sentences into Hungarian with different MT systems. After the translation, to create human judgements, we evaluated these translated segments with human annotators. For creating human scores, we developed a website[2] with a form for human annotators to evaluate the translations. In this website we can see an English source sentence and its Hungarian translation, originating from one of the translation sources. However, the evaluates were not aware of the origin of the translation. The annotators could give quality scores from 1 to 5, from two points of view: adequacy and fluency (see Table I). We added a 0 score (*I do not understand the English sentence*) to filter out wrong evaluations. All the 1500 sentences were evaluated by 3 human annotators: L, M and T. All the annotators were native Hungarian speakers who have minimum B2 level English language skill. The 3 annotators have different evaluation attitudes:

- L: linguist,
- M: MT specialist,
- T: language technology expert.

To follow and control the annotators effectively, or to discuss the annotation aspects with the annotators personally, to avoid misunderstandings, we did not use crowdsourcing for the evaluation. In order to ensure a consistence annotation scheme, the 3 annotators evaluated a set of 50 translations in a personal meeting. These translations are not included in the training set.

There are 3 topics in the HuQ corpus: subtitles, literature and law. The subtitles are simple daily used sentences containing a high ratio of slang words. The language of literature has more complex grammatical constructions with many rare words used. The segments from law are official texts with complex grammar.

We used 5 different translations for each of the 300 sentences. One of them is human translation from the Hunglish corpus, the remaining translations are from 4 different MT systems: MetaMorpho [4] rule based MT system, Google Translate, Bing Translator and MOSES statistical MT toolkit [5].

[2]http://nlpg.itk.ppke.hu/node/65

The Google Translate and the Bing Translator are statistical MT systems. The main advantage of these two systems is that these are trained on huge corpora. Thus, the commonly used phrases will be translated in high quality, but in the case of unseen or rare segments or word forms, the quality will be low. In contrast, the MetaMorpho rule based MT system can handle numerous grammatical forms. Thus, it can gain high quality both in adequacy and fluency. The MOSES MT toolkit was trained on the Hunglish corpus, which contains $\sim$1.1 million English-Hungarian sentence pairs, which is not big enough to produce high quality translations. There is a typical difference between statistical MT systems and rule based MT systems for English-Hungarian. In Table II we can see an example: *Smith turned the question over in his mind*. The main difficulty for automatic MT systems in this sentence is that not Smith turned over, but the question turned over (by Smith). The MetaMorpho system, using the grammatical analyzer could handle this problem correctly, but the statistical systems could not, because the probability of "Smith turning over" is higher than a "question turning over". This problem appears in the human evaluation scores as well. We can see in Table II, in the case of Google Translation, that the 3 annotators gave 3 different scores. One reason for the difference is that the 3 annotators had different attitudes, another reason is the ambiguity. If we translate the Hungarian sentence back, it means: *Smith turned around in his mind, above the question*. Thus, L gave 1 because this translation is totally different from the source sentence. But T gave 5, because these phrases: "in mind" , "turn question" , together definitely have the main meaning that Smith analyzed the question, which has the same meaning as the source sentence. M agrees with both L and T, he is halfway between them.

For building the QE models, we used the arithmetic mean of the scores of the 3 annotators: AD: arithmetic mean of the adequacy scores, FL: arithmetic mean of the fluency scores and AF: arithmetic mean of the AD and FL scores.

We also created classification scores, because there are many cases, when we do not need 5 grades. For instance, the companies and translators need only 2 or 3 classes: need post-edit – do not need post edit; correct – need correction, etc. We created 3 classes from the AD, FL and AF scores:

- BAD: $1 \leq x \leq 2$,
- MEDIUM: $2 < x < 4$,
- GOOD: $4 \leq x \leq 5$,

where: $x = AD,\ FL\ or\ AF$. The classification scores are: CLAD: classification scores from AD, CLFL: classification scores from FL and CLAF: classification scores from AF.

V. METHODS, EXPERIMENTS AND OPTIMIZATION

Using the HuQ corpus with AD, FL, AF, CLAD, CLFL and CLAF, we built the QE models. For building the QE model, features as quality indicators are needed to be extracted from the corpus. Then, with a machine learning method, human or automatic evaluation scores are used to build the QE model. To create the quality indicators from features, we used the QuEst framework. In this study, 103 features (103F) were extracted from the corpus. The set of 103 features contains 76 features implemented by Specia et al. and 27 additional features developed by us. In the 103F, there are adequacy features, fluency features and complexity features. The 27F contains 3 dictionary features and 24 features using WordNet and word embedding models.

MT system	Example	Adequacy			Fluency		
		L	M	T	L	M	T
Source	Smith turned the question over in his mind.						
Reference	Smith megvizsgálta a kérdést.						
MetaMorpho	Smith a kérdést forgatta a fejében. (Smith turned the question in his mind.)	2	5	5	4	5	5
Google	Smith megfordult a kérdés felett a fejében. (Smith has turned in his mind above the question.)	1	3	5	5	3	4
Bing	Smith megfordult a kérdés a fejében. (Smith the question turned in his mind.)	4	5	4	4	4	4
MOSES	Cyrus smith a kérdést. (Cyrus smith the question.)	1	1	1	1	1	4

TABLE II
EXAMPLE OF TRANSLATION DIFFERENCE

The first task was doing evaluations with differently-sized portions of the HuQ corpus. Secondly, we evaluated the HuQ corpus with standard automatic metrics. Thereafter, we built different QE models for English-Hungarian. First, we tried the 17 baseline features (17F) [1] for Hungarian. The 17F is language and language tool independent. Then we performed experiments with the 103F (17F is subset of 103F).

For the machine learning task, we used the Weka system [6]. We created 7 classifiers with 10 fold cross-validation: Gausian Processes with RBF kernel, Support Vector Machine for regression with NormalizedPolyKernel (SMOreg), Bagging (with M5P classifier), Linear regression, M5Rules, M5P Tree and for classification we used Support Vector Machine with NormalizedPolyKernel (SMO). We only show the results of the SMOreg and SMO, because these gained the best results. For evaluating the performance of our methods, we used the statistical correlation, the MAE (Mean absolute error), the RMSE (Root mean-squared error) and the Correctly Classified Instances (CCI) evaluation metrics. The correlation ranges from -1 to +1, and the closer the correlation to -1 or +1, the better it is. In the case of MAE and RMSE the closer the value to 0, the better.

We developed 27 new word-level semantic features. Our aim was to quantify the similarity and relatedness of the topic or meaning of the source and the target sentences. We created bag of words (BOW) from the source and the target segments.

We used 3 features extracted from an English-Hungarian dictionary used by the MetaMorpho system, which contains 365000 entries. We created noun, verb, adjective BOW from the source and the target sentences, then we counted the source-target word pairs from the BOW, which are included in the dictionary. After all, we divided the matches by the length of the source sentence, the length of the target sentence and we counted the F1 score of them.

We developed an additional 24 features using WordNet and word embedding models. We used the Princeton WordNet 3.0 [7] and the Hungarian WordNet [8]. We collected the synsets of the nouns in the source and the target segments. Then, we collected the hypernyms of the synsets up to two levels. Using the collected synsets and hypernym synsets we counted the weighted intersection of synsets of the source and the target words. Features are extracted from the result synsets. We counted the instances of the result synset and divided the sum with the length of the source sentence, the length of the target sentence, the number of nouns in the source sentence, the number of nouns in the target sentence and we counted the F1 score of them. Using these counts, we also created features with the verbs, the adverbs and the adjectives.

However, if looking up words in WordNet did not provide any results, which is quite often the case because of the small coverage of the Hungarian WordNet, we used word embedding models to substitute synset results. Thus, first we trained a CBOW model with 300 dimensions on a 3-billion-word lemmatized Hungarian corpus. The reason for using the lemmatized version was to have set of semantically related words, rather than syntactically related ones. Due to the agglutinating behaviour of Hungarian, building an embedding model from the raw text would have provided syntactically similar groups of words, and only a second key of similarity would have been their semantic relatedness. However, in the lemmatized model, this problem was eliminated. Thus, if there was no result for a word from WordNet, its top 10 nearest neighbours were retrieved from this embedding model, resulting in a list of quasi synonyms, and used the same way as WordNet synsets. However, as these lists did not necessarily correspond to exact synonyms of the original word, the weight of this feature was lower (set to 0.1).

The experiment with human scores needed to be optimized for English-Hungarian. For optimizing, we used the forward selection method.

We carried out experiments for four different settings:

1) task (T1): we did statistical and inter-annotator agreement measurements on the HuQ corpus.
2) task (T2): we compared and evaluated the quality of the MT systems.
3) task (T3): using the HuQ corpus and the 103F, we built QE models with different portions of the HuQ corpus trained on AF: 100, 500, 1000 and 1500 sentence pairs.
4) task (T4): using the HuQ corpus, the 17F and the optimized feature sets, we built the QE models trained on the AD, the FL, the AF, the CLAD, the CLFL and the CLAF scores.

VI. RESULTS AND EVALUATION

In Table III we can see the inter-rater agreement found in T1. Because of the ambiguities described in Section 4, the Fleiss Kappa values of inter-annotator agreement between the 3 annotators is moderate.

In T2 (see Table IV), as we expected, MOSES achieved the lowest result and MetaMorpho performed best.

According to CLAF scores, we counted the ”GOOD” classes. There are 780 instances of GOOD, which means 52% of the HuQ corpus contains correct or close to correct translations. According to AF scores, we counted the perfect

	AD	FL	CLAD	CLFL	CLAF
Fleiss Kappa	0.357	0.463	0.44	0.521	0.493
Krippendorff Alpha	0.357	0.463	0.44	0.521	0.493
Average Pairwise Cohen's Kappa	0.360	0.464	0.444	0.522	0.494
Average pairwise percent	52.467%	61.222%	70.022%	74.444%	70.6%

TABLE III
EVALUATION OF ANNOTATOR-RATER AGREEMENT

	AD mean	FL mean	AF mean
MetaMorpho	3.8707	3.8651	3.8679
MOSES	3.0175	3.1872	3.1024
Google	3.6395	3.5729	3.6062
Bing	3.2166	3.2256	3.2211

TABLE IV
QUALITY OF MT SYSTEMS

translations (score value = 5), there are 387 instances of perfect translation, which means 25.8% of HuQ are correct translations.

In T3, as we can see in Table V, increasing the size of HuQ, we got better results: the AF-500 could gain ∼24% higher correlation than the AF-100, the AF-1000 could gain ∼3% higher correlation than the AF-500 and the AF-1500 could gain ∼1.5% higher correlation than the AF-1000.

In T4, first, we used 103 features to build QE models trained on AD, FL, AF, CLAD, CLFL and CLAF human scores. Then, we optimized the models to Hungarian. After optimizing, as we can see the results in Table VI and in Table VII, the optimized features for Hungarian could gain ∼14% (optimized AD - 29 features), ∼10% (optimized FL - 32 features), ∼12% (optimized AF - 26 features), ∼6% (optimized CLAD - 21 features), ∼5% (optimized CLFL - 10 features) and ∼4% (optimized CLAF - 12 features) higher correlation than the baseline features. The optimized AD set contains 5, the optimized FL set contains 8, the optimized AF contains 5, the optimized CLAD contains 2, the optimized CLFL contains 1 and the optimized CLAF contains 2 semantic features developed in this research. As we can see in the results of the optimization, each optimized feature set contains semantic features developed in this research, which means that the semantic features are important features for QE.

	Correlation	MAE	RMSE
AF-100	0.2700	0.8159	1.0613
AF-500	0.5155	0.8478	1.0603
AF-1000	0.5480	0.8147	1.0481
AF-1500	**0.5618**	**0.7962**	**1.0252**

TABLE V
EVALUATION OF T4

	Correlation	MAE	RMSE
AD-17F	0.3832	0.9429	1.1990
Optimized AD	**0.5245**	**0.8397**	**1.0869**
FL-17F	0.5400	0.8229	0.8345
Optimized FL	**0.6413**	**0.7440**	**0.9878**
AF-17F	0.4931	0.8345	1.0848
Optimized AF	**0.6100**	**0.7459**	**0.9775**

TABLE VI
EVALUATION QE USING THE HUMAN JUDGEMENTS

	CCI	MAE	RMSE
CLAD-17F	0.5493	0.3590	0.4591
Optimized CLAD	**0.6093**	**0.3370**	**0.4346**
CLFL-17F	0.5887	0.3434	0.4419
Optimized CLFL	**0.6407**	**0.3299**	**0.4262**
CLAF-17F	0.5780	0.3433	0.4417
Optimized CLAF	**0.6180**	**0.3299**	**0.4263**

TABLE VII
EVALUATION OF QE USING THE CLASSIFICATION METRICS

VII. CONCLUSION

We created the HuQ corpus for quality estimation of English-Hungarian machine translation. The corpus contains 1500 quality scores of translations, which are given by human annotators. Then, using the HuQ corpus, we built different QE models for English-Hungarian translations. In our experiments, we used automatic metrics and human judgements as well. In the experiments we tried 103 features including 27 newly developed semantic features using WordNet and word embedding models. Then, we optimized the quality models to English-Hungarian. In the optimization task, we used forward selection to find the best features. We could produce optimized sorted feature sets, which produced more than 10% better correlation than the baseline set. In our experiments, our HuQ corpus and QE models can be used for predicting the quality of machine translation outputs for English-Hungarian.

In the future, we would like to enlarge the corpus. We also would like to examine the effect of utilizing crowdsourcing to increase the size of HuQ. Last, but not least, we will do experiments and evaluations in a ranking task.

REFERENCES

[1] L. Specia, K. Shah, J. G. de Souza, and T. Cohn, "Quest - a translation quality estimation framework," in *Proceedings of the 51st Annual Meeting of the Association for Computational Linguistics: System Demonstrations*, (Sofia, Bulgaria), pp. 79–84, Association for Computational Linguistics, August 2013.

[2] O. Bojar, R. Chatterjee, C. Federmann, B. Haddow, M. Huck, C. Hokamp, P. Koehn, V. Logacheva, C. Monz, M. Negri, M. Post, C. Scarton, L. Specia, and M. Turchi, "Findings of the 2015 workshop on statistical machine translation," in *Proceedings of the Tenth Workshop on Statistical Machine Translation*, (Lisbon, Portugal), pp. 1–46, Association for Computational Linguistics, September 2015.

[3] P. Halácsy, A. Kornai, L. Németh, B. Sas, D. Varga, T. Váradi, and A. Vonyó, "A Hunglish korpusz és szótár.," in *III. Magyar Számítógépes Nyelvészeti Konferencia*, Szegedi Egyetem, 2005.

[4] A. Novák, L. Tihanyi, and G. Prószéky, "The metamorpho translation system," in *Proceedings of the Third Workshop on Statistical Machine Translation*, StatMT '08, (Stroudsburg, PA, USA), pp. 111–114, Association for Computational Linguistics, 2008.

[5] P. Koehn, H. Hoang, A. Birch, C. Callison-Burch, M. Federico, N. Bertoldi, B. Cowan, W. Shen, C. Moran, R. Zens, C. Dyer, O. Bojar, A. Constantin, and E. Herbst, "Moses: Open source toolkit for statistical machine translation," in *Proceedings of the 45th Annual Meeting of the ACL on Interactive Poster and Demonstration Sessions*, ACL '07, (Stroudsburg, PA, USA), pp. 177–180, Association for Computational Linguistics, 2007.

[6] M. Hall, E. Frank, G. Holmes, B. Pfahringer, P. Reutemann, and I. H. Witten, "The weka data mining software: An update," *SIGKDD Explor. Newsl.*, vol. 11, pp. 10–18, Nov. 2009.

[7] C. Fellbaum, *WordNet: An Electronic Lexical Database*. Bradford Books, 1998.

[8] M. Miháltz, C. Hatvani, J. Kuti, G. Szarvas, J. Csirik, G. Prószéky, and T. Váradi, "Methods and results of the hungarian wordnet project," in *Proceedings of the Fourth Global WordNet Conference GWC 2008*, pp. 310–320, 2008.

APPENDIX

PROGRAM 1: Bionics, Bio-inspired Wave Computers, Neuromorphic Models	
Name	**Supervisor**
Sándor BABIK	Zoltán GÁSPÁRI PhD
Flóra BÁLINT	Zsolt LIPOSITS MD DSc, Imre FARKAS MD PhD
Virág BOKODI	István ULBERT MD DSc, Dániel FABÓ MD PhD
Réka DÉNES	Zsolt RÓNAI MD PhD, Zoltán GÁSPÁRI PhD
Dániel DUDOLA	Zoltán GÁSPÁRI PhD
Bálint FILE	István ULBERT MD DSc, Dániel FABÓ MD PhD
Edit GYŐRI	István ULBERT MD DSc, Dániel FABÓ MD PhD
Márton HARTDÉGEN	Kristóf IVÁN PhD
Anett HINSENKAMP	Zoltán GÁSPÁRI PhD
János JUHÁSZ	Sándor PONGOR MHAS
Ágnes KANDRÁCS	István ULBERT MD DSc
Annamária KISS-TÓTH	Zoltán GÁSPÁRI PhD
Kinga KOCSIS	István ULBERT MD DSc
Tamás LASZLOVSZKY	Balázs HANGYA PhD
Eszter LEELŐSSYNÉ TÓTH	Péter FÜRJES PhD, Kristóf IVÁN PhD
Domokos MESZÉNA	István ULBERT MD DSc
Vivien MICZÁN	István KATONA DSc, András HORVÁTH PhD
Tamás MOLNÁR	Loránd ERŐSS MD PhD, Kristóf KARACS PhD
György PERCZEL	Loránd ERŐSS MD PhD, László GERENCSÉR PhD, Zsuzsanna VÁGÓ PhD
Sára SÁRAY	Szabolcs KÁLI, Tamás FREUND
Beáta Tünde SZABÓ	István WINKLER, István ULBERT MD DSc
Csilla SZABÓ	Lucia WITTNER, István ULBERT MD DSc
Balázs SZÉKY	Sarolta KÁRPÁTI, Miklós GYÖNGY PhD
Ádám György SZÉLIG	Kristóf IVÁN PhD
Dóra SZEPES	István ULBERT MD DSc
Zsófia SZTYÉHLIKNÉ BÉRCES	Kristóf IVÁN PhD, Anita PONGRÁCZ PhD

PROGRAM 2: Computer Technology Based on Many-core Processor Chips, Virtual Cellular Computers, Sensory and Motoric Analog Computers	
Name	**Supervisor**
Bernadett ÁCS	Gábor SZEDERKÉNYI DSc
Sándor FÖLDI	György CSEREY PhD, Péter SÓTONYI MD PhD
Márton Áron GODA	Ferenc KOVÁCS PhD
Balázs György JÁKLI	György CSEREY PhD
Máté LŐRINCZ	András OLÁH PhD
Máté NÉMETH	Ákos ZARÁNDY DSc
Zsolt NIKA	Miklós RÁSONYI PhD, Péter SZOLGAY DSc
Tamás WILHEIM	Imre KALLÓ MD PhD

PROGRAM 3: Feasibility of Electronic and Optical Devices, Molecular and Nanotechnologies, Nano-architectures, Nanobionic Diagnostic and Therapeutic Tools	
Name	**Supervisor**
Bálint BALÁZS	Balázs RÓZSA PhD
Gergely CSÁNY	Miklós GYÖNGY PhD
Máté HANDBAUER	Árpád CSURGAY MHAS
Ákos MAKRA	Miklós GYÖNGY PhD
Ádám PAPP	Árpád CSURGAY MHAS

PROGRAM 4: Human Language Technologies, Artificial Understanding, Telepresence, Communication	
Name	**Supervisor**
Zijian Győző YANG	Gábor PRÓSZÉKY DSc